



HAL
open science

Chemical surface modification of silica nanoparticles for the labeling of DNA in lipoplexes

Nora Maria Elisabeth Reinhardt

► **To cite this version:**

Nora Maria Elisabeth Reinhardt. Chemical surface modification of silica nanoparticles for the labeling of DNA in lipoplexes. Material chemistry. Université Sciences et Technologies - Bordeaux I, 2013. English. NNT : 2013BOR14820 . tel-01208139

HAL Id: tel-01208139

<https://theses.hal.science/tel-01208139>

Submitted on 2 Oct 2015

HAL is a multi-disciplinary open access archive for the deposit and dissemination of scientific research documents, whether they are published or not. The documents may come from teaching and research institutions in France or abroad, or from public or private research centers.

L'archive ouverte pluridisciplinaire **HAL**, est destinée au dépôt et à la diffusion de documents scientifiques de niveau recherche, publiés ou non, émanant des établissements d'enseignement et de recherche français ou étrangers, des laboratoires publics ou privés.



THÈSE

PRÉSENTÉE A

L'UNIVERSITÉ BORDEAUX 1

ÉCOLE DOCTORALE DES SCIENCES CHIMIQUES

Par Nora Maria Elisabeth REINHARDT

POUR OBTENIR LE GRADE DE

DOCTEUR

SPÉCIALITÉ : Physico-Chimie de la Matière Condensée

Chemical surface modification of silica nanoparticles for the labeling of DNA in lipoplexes

Soutenue le : 24 juillet 2013

Devant la commission d'examen formée de :

M. Durand, Jean Olivier Mme Ménager, Christine	Directeur de Recherche, CNRS Professeur, Université Pierre et Marie Curie	Rapporteurs
M. Roux, Stéphane M. Maglione, Mario	Professeur, Université de Franche Comté Directeur de Recherche, CNRS	Examineur Président
M. Ravaine, Serge M. Mornet, Stéphane	Professeur, Université de Bordeaux 1 Chargé de Recherche, CNRS	Directeurs de thèse

"Fortune is arranging matters for us better than we could have shaped our desired ourselves, for look there, friend Sancho Panza, where thirty or more monstrous giants present themselves, all of whom I mean to engage in battle and slay, and with whose spoils we shall begin to make our fortunes; for this is righteous warfare, and it is God's good service to sweep so evil a breed from off the face of the earth."

L'Ingénieux Noble Don Quichotte de la Manche, Miguel de Cervantes

Cette thèse est dédiée à tous ceux qui se lancent dans la recherche, parce que chacun de nous se bat au moins une fois contre des moulins à vent avant de prendre le bon chemin.

REMERCIEMENTS

Ce travail a été réalisé au sein de l'équipe « chimie des nanomatériaux » (ICMCB) et de l'équipe « Nano-Ingénierie colloïdale, Chimie et Emulsions – NICE » (CRPP) sous la direction de **Stéphane Mornet** et **Serge Ravaine** à qui j'exprime ma plus profonde gratitude pour m'avoir choisi pour mener à bien cette thèse. Je vous remercie pour vos idées, votre audace, votre patience et vos critiques, qui ont fait progresser mon travail et mon esprit au cours de cette thèse. Particulièrement je remercie **Stéphane Mornet** pour tout le temps et l'énergie qu'il a investi à me former, me guider et me motiver : Merci de m'avoir fait découvrir l'univers passionnant dans lequel j'espère pouvoir continuer à évoluer dans les années futures. Merci de m'avoir poussé à toujours aller plus loin, de m'avoir montré ce qu'est le bon sens du travail scientifique et de m'avoir permis de développer et d'améliorer mes compétences professionnelles.

J'adresse mes plus sincères remerciements aux membres du jury pour avoir accepté d'évaluer ma thèse; Monsieur **Jean Olivier Durand** et Madame **Christine Ménager** rapporteurs de ma thèse et messieurs **Stéphane Roux** et **Mario Maglione** examinateurs de ma thèse. Je vous remercie vivement pour votre intérêt sincère à mon travail et pour la discussion vivante et passionnante lors de ma soutenance de thèse.

Je remercie le Professeur **Etienne Duguet**, directeur du groupe V à l'ICMCB de m'avoir accueilli dans son équipe. Je remercie également **Claude Delmas**, ancien directeur du laboratoire ICMCB, **Mario Maglione** directeur de l'ICMCB à présent, ainsi que **Phillipe Richetti** directeur du CRPP de m'avoir permis de travailler au sein de leurs instituts de recherche.

Je remercie tout les permanents qui ont participé à mon travail et qui m'ont permis d'obtenir des bons résultats de mesure et de caractérisation, des clichés de microscopie focalisés et hautement résolus et des conseils. J'exprime mes remerciements envers **Alexandre Fargues**, **Laetitia Etienne**, **Phillipe Dagault**, **Dominique Denux** et **Stéphane Toulin** (ICMCB).

Je remercie **Alain Brisson** et **Olivier Lambert** qui m'ont permis d'accomplir une partie de mon travail au CBMN particulièrement **Sisareuth Tan**, **Céline Gounou**, **Nicolas Arraud**, **Pierre Bonafouss** et **Marion Decossas**.

Je remercie **Anne-Laure Gaillard** et **Nicolas Guidolin** du LCPO, qui m'ont permis de conduire des mesures de caractérisation sous leur responsabilité.

Egalement je remercie les permanents du CRPP qui m'ont permis de travailler dans leur laboratoires ; **Isabelle Ly** et **Wilfried Neri** pour leur support technique, **Nadine Laffarque** pour son bonne humeur, ainsi que **Elisabeth Hortolland** et **Josyane Parzych** pour leur aide précieux concernant mes missions en Italie et au Japon. Particulièrement je remercie **Claude Coulon** et **Rodolphe Clérac**, qui m'ont accueilli dans leur équipe en tant que stagiaire ERASMUS. C'est grâce à vous que j'ai développé le souhait de faire une thèse, que j'ai commencé à aimer la science et de croire en moi, merci pour votre soutien.

Je remercie tout particulièrement les membres actuels ou antérieurs du **groupe V** qui de part la diversité de leurs compétences m'ont été d'une aide précieuse durant toute ma thèse. Merci à **Lydia Roudier** qui a

garanti le bon fonctionnement du laboratoire qu'est la base de tout travail réussi. Merci à **Etienne Durand** pour sa bonne volonté de me fournir des résultats de mesure important. Je remercie également l'ensemble des permanents du groupe V et notamment les permanents de la zone E pour leurs conseils et leurs engagement : **Graziella Goglio, Mona Treguer-Delapierre, Guy Campet** et **Marie-Hélène Delville**.

J'exprime ma gratitude envers **Laurent Adumeau**, qui a travaillé pour moi au sein de son stage M2 et qui ma apporté un soutien énorme. Je remercie également mes collègues post-doc du « labo Bio » **Julien Boudon** pour son aide et sa compagnie au début de ma thèse et **Hélène Gehan** pour ses conseils pendant ma rédaction. Mes collègues de bureau **Anthony Desert, Hakim Moulki, Aurelie LeBeulze, David Sallagoity** et **Cyril Chomette** je vous remercie pour vos conseils, votre bonne humeur et la bonne ambiance de travail que vous avez créé. Merci également à **Thomas Alnasser, Quentin LeTrequesser, Isabelle Trenque, Pascal Massé, Miguel Spuch, Stéphanie LeSturgez, Brice Basly, Iona Moog** et **Romain Epherre** : Vous m'avez fait rire plus qu'une fois, votre présence a permis mon intégration dans le groupe et m'a appris mille choses sur la culture françaises et l'art de vivre. Je vous remercie également pour toutes les discussions scientifiques qui m'ont aidé à mener ce projet de thèse.

Je remercie tout les maitres de conférences et professeurs qui m'ont permis d'enseigner leurs étudiants et qui ont fait équipe avec moi, en particulier **Dany Carlier, Laurence Maille, Jérôme Roger, Mona Treguer-Delapierre, Manuel Goudon** et **Frédéric Nallet**. Merci de m'avoir fait découvrir ce coté de l'université, j'ai apprécié vos conseils et votre confiance.

Je remercie **Etienne Pousin** pour m'avoir supporté et soutenu pendant tous les trois ans de ma thèse, tu m'as aidé de garder l'équilibre entre vie et travail autant que c'était possible. Mille mercis. J'adresse également mes remerciements à mes amis au CRPP, particulièrement à **Ludivine Malassis** et **Clémence Tallet**. Ces trois ans de thèses ont été enrichissant pour mon cœur grâce à vous.

Mes derniers remerciements s'adressent aux membres de ma famille, qui me soutiennent toujours n'importe ce que je décide de faire et qui font tout pour moi sans de rien demander en retour. Merci !

SUMMARY

Résumé de thèse en français	9
References	17
List of Abbreviations.....	18
List of reagents	21
Introduction.....	25
Chapter I – State of the art	27
1. Imaging modalities currently used for biomedical applications	28
2. Multifunctional nanoparticles applicable for multimodal imaging <i>in vivo</i> or <i>in vitro</i>	35
2.1 Different architectures and utilities of multimodal hybrid nanoparticles	35
2.2 Nanomaterials suitable for multimodal imaging and their physical properties	38
3. Colloidal surfaces as frontiers between inorganic and biologic matter	49
3.1 The chemical functionalization of nanoparticle surfaces	52
3.2 Biofunctionalization of colloidal surfaces.....	56
3.3 The biological fate of nanoparticles destined for theragnostic applications.....	64
4. The context of the study	65
4.1 The exploration of the transfection of therapeutic DNA into living cells.....	65
4.2 Condensation of DNA to functionalized nanoparticles	67
4.3 Strategies to functionalize nanoparticles destined for DNA labeling.....	68
References	73
Chapter II – Synthesis of silica nanoparticles bearing quaternary ammonium groups on their surface	79
1. Synthesis and characterization of exemplary silica nanoparticles serving as body material for chemical modifications.....	80
2. Synthesis of quaternary ammonium group bearing silica surfaces by chemical surface modification with an organofunctional silane coupling agent.....	88
2.1 General information about the silanization process and the choice of a quaternary ammonium group bearing silane coupling agent	88
2.2 Exemplary reaction protocols to undergo chemical surface modification of silica nanoparticles with the silane coupling agent TMAPS.....	91
2.3 Influence of the amount of TMAPS during the chemical surface modification of silica nanoparticles on the final TMAP coverage	94

2.4	Investigation of the surface density of TMAPS-coated silica nanoparticles obtained by chemical surface modification at different pHs	96
2.5	Investigation of the zeta potential of TMAPS-coated silica nanoparticles obtained by chemical surface modification at different pHs	99
2.6	Influence of temperature and duration time of the thermal treatment on the condensation of TMAPS oligomers on silica NPs	105
2.7	The execution of end-capping reactions on TMAPS modified nanoparticles	108
2.8	Steric effects on the organization of TMAPS oligomers on silica	110
2.9	Conclusions	112
3.	Quaternization of surface-aminated silica nanoparticles	114
3.1	Implementation of a reaction protocol to obtain quaternization of aminated silica nanoparticles and verification of its achievement	115
3.2	Attempts to estimate the surface density of quaternary ammonium groups on quaternized silica nanoparticles	124
3.3	Surface potential and colloidal stability of EDPS modified and quaternized EDPS modified silica nanoparticles	131
3.4	Conclusions	134
	References	135
	Chapter III – Study of the interactions taking place between quaternized silica surfaces, lipids and DNA	139
1.	Investigating the adsorption of liposomes on bare, aminated or quaternized silica surfaces	141
1.1	The formation of supported lipid bilayers on silica surfaces	141
1.2	Formation of supported lipid bilayers on silica surfaces bearing primary and secondary amines or quaternary ammonium groups	148
1.3	Conclusions	155
2.	Investigating the adsorption of DNA on aminated or quaternized silica surfaces	156
2.1	The formation of nanoparticle/DNA complexes during cosedimentation assays	156
2.2	The investigation of the pH dependence of DNA adsorption on differently modified cationic silica surfaces	161
2.3	Salt concentration as a parameter influencing the adsorption of DNA to cationic surfaces	167
2.4	Conclusions	171
3.	Towards the assembly of nanoparticle labeled lipoplexes.	172
3.1	Following of the adsorption of cationic liposomes on DNA layers formed on modified silica surfaces by QCM-D	173

3.2	Investigation of the formation of lipoplexes including nanoparticle labeled DNA.....	179
3.3	Conclusions and prospects.....	185
	References	188
	Overall conclusion.....	191
	Annex	194
	Annex 1: Characterization protocols	194
	Annex 2: Tables	197
	Annex 3: Calculations	201
	Annex 4: IUPAC names and structures of lipids and cationic transfection agents.....	202
	Annex 5: Supplementary Cryo-TEM and TEM pictures	204

RESUME DE THESE EN FRANÇAIS

Grâce à leurs propriétés physiques les nanoparticules (NPs) fonctionnalisées sont des outils puissants utilisés en tant qu'agent bioimagerie comme agent de contraste et de marquage. Permettant le marquage de biomolécules ciblées des nanoparticules sont utilisées pour la détection de protéines, d'ADN ou de lipides afin de comprendre les procès biologiques auxquels les composés marqués participent et de réaliser des diagnostics. Les nanoparticules fonctionnalisées peuvent servir au ciblage de cellules cancéreuses ainsi permettant la localisation de tissus tumoraux et de métastases^[1]. Dans la circulation sanguinaire de nanoparticules, fonctionnalisées afin de détecter des anticorps spécifiques, sont utilisées pour la diagnostique de maladies auto-immunes comme la sclérose en plaques^[2]. Des surfaces de nanoparticules peuvent également être ajustées afin de détecter des facteurs rhumatoïdes permettant le diagnostique d'arthrites^[3] ou être conçues pour la détection de facteurs cardiovasculaires^[4].

Aujourd'hui des techniques d'imagerie multiples sont disponibles afin de visualiser des tissus, des cellules ou même des biomolécules en utilisant des nanoparticules fonctionnalisées comme agent de contraste ou comme sondes moléculaires. Certaines techniques comme l'imagerie de résonance magnétique (IRM), la tomographie d'émission de positrons (TEP), l'échographie, la radiographie ou l'imagerie optique dans le proche infrarouge sont adaptées afin d'étudier des systèmes biologiques *in vivo*. D'autres techniques comme la microscopie optique ou la microscopie électronique à transmission (MET) sont employées afin d'explorer des processus biologique *in vitro*. Chaque de ces techniques à ses propres avantages ainsi que ses limitations intrinsèques. Pour cette raison, l'utilisation de techniques d'imagerie complémentaires. La combinaison d'une technique possédant une grande résolution spatiale et d'une deuxième permettant la détection d'une cible avec une grande sensibilité facilite la visualisation et diagnostique de la situation biologique à l'endroit ciblé^{[5],[6]}. L'utilisation simultanée de différentes techniques d'imagerie peut également permettre d'analyser un phénomène biologique à différentes échelles. La visualisation d'une situation biologique de l'échelle tissulaire jusqu'à l'échelle cellulaire permet d'analyser un processus biologique plus précisément, qui permettrait de mieux le comprendre (FIGURE 0.0-1).

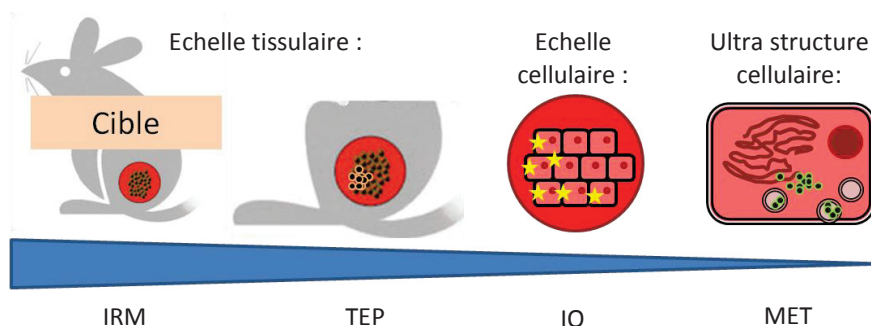


FIGURE 0.0-1 Des modalités d'imageries complémentaires permettent de visualiser une pathologie à différentes échelles, ce suivi permet de mieux analyser la situation biologique du site ciblé et de diagnostiquer plus précisément des anomalies apparentes.

Afin de synthétiser des nanoparticules multimodales la silice est appropriée comme matrice hôte afin d'incorporer des agents d'imagerie différents. Ce matériau n'adsorbe pas de lumière ni dans le spectre de l'UV visible ni dans le spectre du proche-infrarouge et s'affiche comme photostable. La matrice d'une particule de silice peut être dopée avec des fluorophores et simultanément incorporer des particules cœur avec des propriétés magnétiques ou plasmoniques et désormais former un outil de marquage multimodal. La taille, la morphologie et la porosité d'une nanoparticule de silice peuvent être précisément contrôlées. En outre la silice est une matrice de support pour des modifications de surfaces chimiques permettant la fonctionnalisation des nanoparticules multimodales afin de pouvoir intervenir comme sonde moléculaire. Des nanoparticules avec un cœur de magnétite et une écorce de silice dopée avec de la fluorescéine ont été synthétisées^[7] (FIGURE 0.0-2) et peuvent être visualisées par IRM, par imagerie optique de fluorescence et par microscopie électronique à transmission.

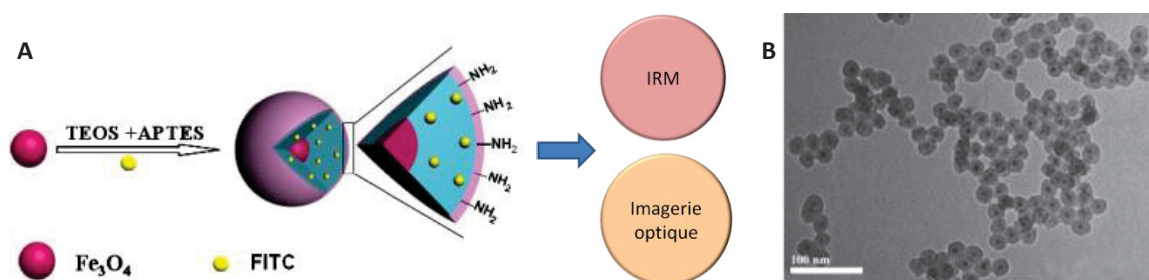


FIGURE 0.0-2 Illustration de nanoparticules possédant un cœur de magnétite et une écorce de silice dopée avec un fluorophore afin de permettre de l'imagerie multimodale **A** : Une nanoparticule de magnétite (Fe_3O_4) et de la fluorescéine ont été incorporées dans de la silice. Cette nanoparticule multimodale a été modifiée de plus avec un agent de couplage silanique (APTES). **B** : Image MET des nanoparticules magnétite@ SiO_2 synthétisées^[7].

Des biomolécules peuvent être fixées à la surface de nanoparticules de différentes manières (FIGURE 0.0-3). Le marquage d'une biomolécule peut être acquis par la formation d'une liaison covalente ainsi que par des interactions électrostatiques ou des interactions de type van der Waals^[8]. La nature combine ces interactions selon les besoins stériques des protéines afin de créer des systèmes interagissant avec une grande spécificité et affinité comme des couples d'anticorps/antigène ou d'enzyme/substrat^[9]. On dit que ces interactions suivent le principe serrure/clé. Un exemple pour un couple enzyme substrat est le couple streptavidine/biotine, qui possède une constante de dissociation de 10^{15} M^{-1} ^[10]. Dans le but de marquer des biomolécules, non seulement les propriétés physiques des nanoparticules mais également les propriétés physicochimiques de leur surface doivent être contrôlées. En effet les propriétés physicochimiques d'une surface colloïdale sont les paramètres clés déterminant les interactions, qui auront lieu à l'interface entre la particule et une biomolécule ciblée. La surface agit comme interface solide-liquide et constitue la frontière entre le nanomatériau et l'environnement biologique^[11,12]. Les ligands présents en surface d'une nanoparticule peuvent augmenter la spécificité de la particule envers une biomolécule. Le contrôle des caractéristiques de la surface colloïdale comme le potentiel de surface, la fonctionnalité de la surface, la densité des ligands ainsi que la balance hydrophile/hydrophobe est un des objectifs majeurs afin de contrôler les futures interactions avec des biomolécules, qui auront lieu.

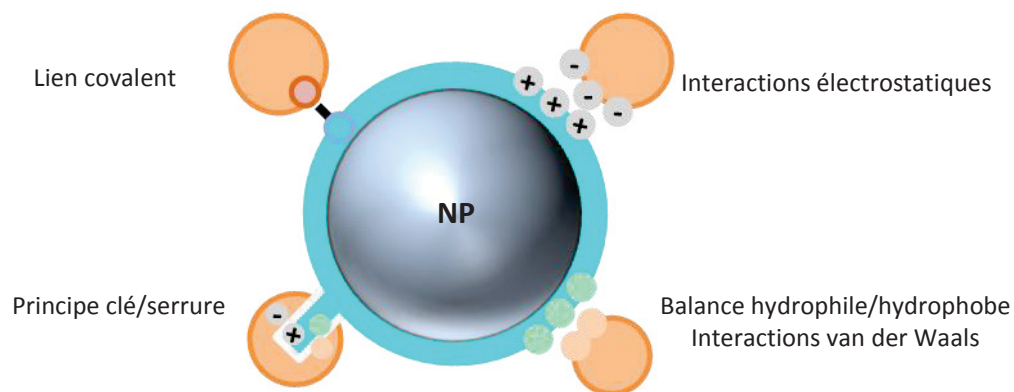


FIGURE 0.0-3 Cette illustration montre les différentes possibilités d'attacher une biomolécule à la surface d'une nanoparticule : la biomolécule peut être attachée par une liaison covalente par une molécule bifonctionnel ou être adsorbée à la surface grâce aux interactions électrostatiques, van der Waals et la balance hydrophile/ hydrophobe. Egalement des biomolécules peuvent interagir avec des protéines greffées en surface en combinant ces interactions par le principe clé/serrure.

Une étude antérieure à cette thèse^[13] essayait d'employer des nanoparticules multimodales afin de suivre la transfection de l'ADN par des agents de transfection lipidiques à l'échelle cellulaire. L'objectif était de déterminer les mécanismes de transfection d'ADN par des lipides cationiques. Dépendant de la composition des lipides les mécanismes d'internalisation de l'ADN dans une cellule changent considérablement. En analysant et comprenant les étapes critiques de la transfection d'ADN on espère pouvoir améliorer l'efficacité des agents transfectant lipidiques. Pourtant le suivi de l'ADN marqué par des nanoparticules aminées n'a pas pu être effectué jusqu'au noyau, dû au fait que l'ADN se dissociait des nanoparticules modifiées dans le cytosol^[13]. En conséquence de cette étude nous voudrions synthétiser des nanoparticules nous permettant de suivre la transfection d'ADN par des agents de transfection lipidiques jusqu'à l'internalisation de l'ADN dans le noyau. Afin d'atteindre ce but, nous souhaitons de développer une fonctionnalisation de surface, qui permet de lier l'ADN en surface des nanomarqueurs plus fortement afin de pouvoir suivre le processus complet de la transfection d'ADN.

L'attache d'ADN à des nanoparticules d'or fonctionnalisées avec des groupements d'ammonium quaternaire est montrée d'être forte et suffisante afin d'inhiber la transcription d'ADN adsorbés en surface des nanoparticules^[14]. Goodman^[15] et collaborateurs ont montré que des groupements d'ammonium quaternaire lient l'ADN non seulement par des interactions électrostatiques mais également par des interactions hydrophobes renforçant ainsi la liaison. L'implémentation des groupements d'ammonium quaternaires sur des surfaces de silice de nanoparticules multimodales est désormais notre objectif principal dans le but final de synthétiser une nanoparticule permettant le suivi d'ADN pendant toutes les étapes de la transfection. Idéalement de l'ADN étant complexé par des agents de transfection lipidiques sous forme de lipoplexe se trouvait marqué par des nanoparticules de silice multimodales et en même temps par des nanoparticules d'or afin de suivre de l'ADN même au cas où il dissocierait d'une des composantes marquantes (**FIGURE 0.0-4**).

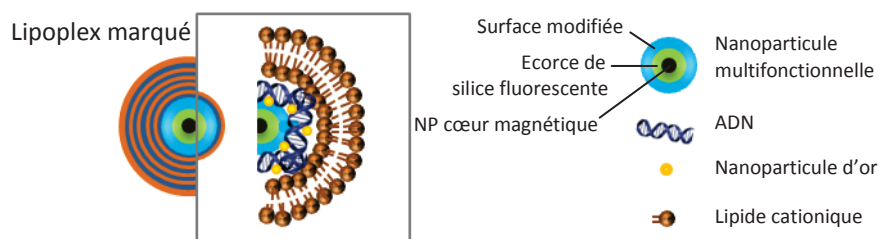


FIGURE 0.0-4 L'illustration montre le nano-objet idéal d'un lipoplexe contenant de l'ADN marqué par des nanoparticules multimodales de silice et d'or fonctionnalisées avec des groupements d'ammonium quaternaires.

La fonctionnalisation d'une nanoparticule est soumise à plusieurs contraintes. Il est important que les particules modifiées soient colloïdalement stable pendant le processus de modification chimique ainsi que dans leur milieu d'application en présence de sels et selon le pH des milieux physiologiques. Afin de synthétiser des nanoparticules de silice portant des groupements d'ammonium quaternaire en surface nous avons exploré une stratégie de modification de surface d'une nanoparticule de silice avec un agent de couplage silanique organofonctionnel contenant un groupement d'ammonium quaternaire. Nous avons étudié la silanisation des colloïdes de silice en utilisant les agents de couplage silanique comme le chlorure de *N*-triméthoxysilylpropyl-*N,N,N*-triméthylammonium (TMAPS) ou le chlorure de *N*-triméthoxysilylpropyl-*N,N,N*-tributylammonium (TBAPS) (**FIGURE 0.0-5**).

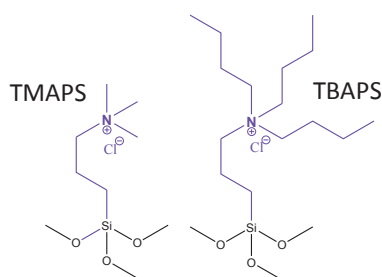


FIGURE 0.0-5 Structure des agents de couplage silaniques TMAPS : chlorure de *N*-triméthoxysilylpropyl-*N,N,N*-triméthylammonium (TMAPS) et TBAPS : chlorure de *N*-triméthoxysilylpropyl-*N,N,N*-tributylammonium.

La silanisation est réalisée par des réactions d'hydrolyse des agents de couplage et de condensation des silanes aux surfaces de silice. Nous avons pu montrer que la densité de greffage du silane employé augmente avec la quantité d'agent de couplage ajoutée dans le milieu réactionnel. Au delà une concentration de 60 μmol de TMAPS dans le milieu réactionnel la densité de greffage vaut 7.91 $\mu\text{mol}/\text{m}^2$ ce qui constitue un maximum de greffage : il ne peut plus être augmenté en modifiant des surfaces des nanoparticules de silice en utilisant des concentrations de TMAPS supérieures. Ceci est dû à une saturation de la surface des nanoparticules modifiée à partir du moment où l'agent de couplage est disponible en quantité suffisante afin d'adsorber à la totalité de la surface développée des nanoparticules. En conséquence de ce résultat, la concentration des silanes utilisés pendant un processus de modification a été fixée à 100 $\mu\text{mol}/\text{m}^2$ de surface développée par des nanoparticules de silice destinées à être chimiquement modifiées par silanisation. En changeant des paramètres clés des processus de modification comme le catalyseur, le pH, la durée et la température nous avons pu optimiser la modification de surface par silanisation avec des agents de couplage silaniques organofonctionnels contenant un groupement d'ammonium quaternaire. Nous obtenons des

nanoparticules modifiées avec du TMAPS possédant un potentiel de surface de 25 mV à pH 7,4 et un point isoélectrique à pH 8,4 (FIGURE 0.0-6).

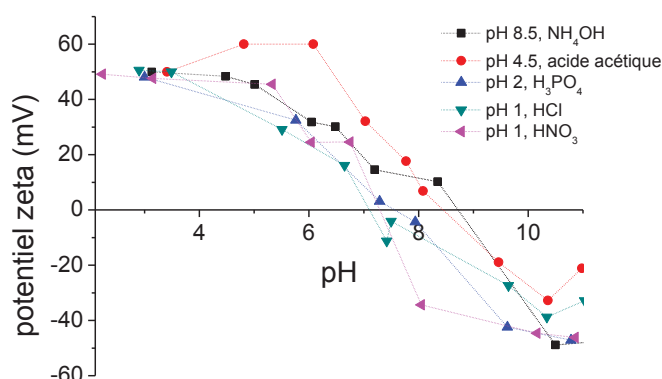


FIGURE 0.0-6 Ce graph montre les potentiels zeta de nanoparticules modifiées avec du TMAPS sous différentes conditions (conditions 006,009-012, voir TABLE 03, annexe 2, chapitre II).

Néanmoins le potentiel de surfaces des nanoparticules fonctionnalisées par cette voie de modification de surface n'est pas suffisamment haut à pH 7,4 afin de pouvoir garantir la stabilisation des colloïdes par répulsion électrostatique en milieu physiologique. La zone de floculation des nanoparticules fonctionnalisées avec du TMAPS se situe entre pH 6,5 et pH 10. Quand les nanoparticules sont sous forme d'agglomérats, il est possible de mesurer la densité optique du sol, car en effet le signal mesurer en spectrométrie est d'autant important que la taille des agrégats est grande (FIGURE 0.0-7). Des résultats semblables ont pu être observés pour des nanoparticules modifiées avec TBAPS.

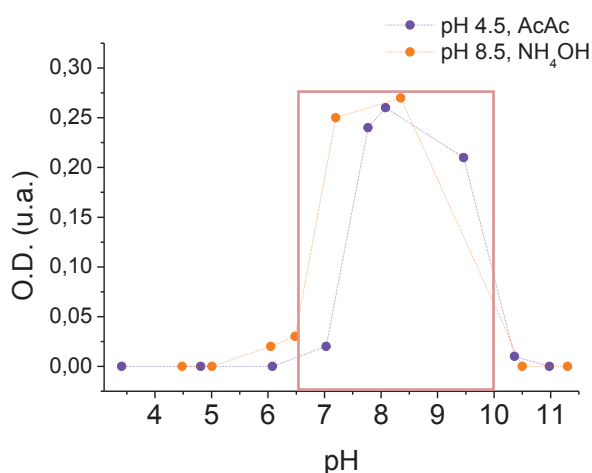


FIGURE 0.0-7 La zone de floculation (encadré rouge) de nanoparticules de silice modifiées avec du TMAPS a été déterminée en mesurant la densité optique d'un sol de particules modifiées à différents pHs. Les nanoparticules forment des agglomérats, qui plus qu'elles sont grandes plus elles diffusent de la lumière comme on a pu mesurer par spectrométrie à 800 nm.

Nous avons identifié la tendance des groupements d'ammonium quaternaire à interagir avec des silanolates demeurant à la surface des nanoparticules de silice modifiées en quantité suffisante afin d'influencer le point isoélectrique des nanoparticules fonctionnalisées comme problématique principale handicapant l'implémentation de groupements d'ammonium quaternaires en surface de colloïdes de silice par silanisation directe avec du TMAPS ou alors du TBAPS.

Par conséquent nous avons changé notre stratégie de modification de surface. Au lieu de passer par une silanisation directe d'une surface de silice avec un agent de couplage silanique comme le TMAPS ou TBAPS afin d'implémenter des groupements d'ammonium quaternaire en surface de particules de silice, nous avons accompli une étape de fonctionnalisation des nanoparticules de silice avec un aminosilane comme le *N*-[3-(Triméthoxysilyl)propyl]éthylènediamine (EDPS) suivi par une alkylation chimique des amines en surface des particules modifiées menant à la présence d'ammoniums quaternaires. Nous avons réussi à développer un protocole de quaternisation d'amines par la réaction de Mentschutkin, qui nous permet de garder une bonne stabilisation colloïdale de particules aminées pendant le processus de modification. Nous sommes capables de synthétiser des nanoparticules de silice portant environ 3.7 μmol d'ammonium quaternaire par m^2 de surface développé et possédant un potentiel de 36 mV à pH 7.4 et un point isoélectrique à pH 10.5 (FIGURE 0.0-8). La zone de floculation de ces nanoparticules se situe entre pH 9 et pH 11.5, ce qui garantit leur stabilisation colloïdale même en milieu physiologique.

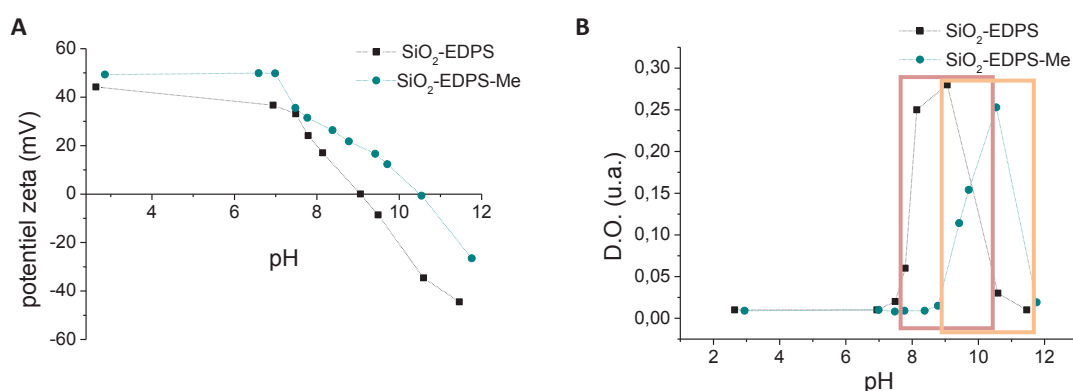


FIGURE 0.0-8 A: Comparaison des profils de potentiel zeta des nanoparticules modifiées avec de l'EDPS avant et après la quaternisation des fonctions d'amines. **B:** Les encadrés rouge et orange marquent les zones de floculations de nanoparticules modifiées avec de l'EDPS avant et après la quaternisation des fonctions d'amines déterminées par la mesure des densités optiques des sols de nanoparticules modifiées à différents pH.

Après l'obtention de ces nanoparticules, qui sont colloïdalement stables dans un milieu physiologique, nous avons commencé à explorer les interactions de ces nanoparticules avec des biomolécules comme des lipides et de l'ADN afin d'estimer leur potentiel afin d'être incorporées dans des lipoplexes en marquant de l'ADN. Nous montrons que pour complexer la même quantité d'ADN à pH 9 nous avons besoin d'une quantité de nanoparticules quaternisées qui correspond à seulement de $\frac{3}{5}$ de la quantité de nanoparticules aminées utilisées (FIGURE 0.0-9).

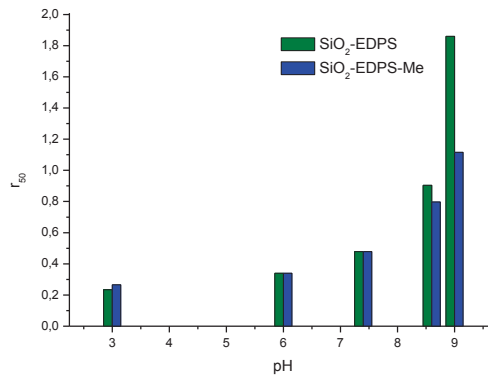


FIGURE 0.0-9 Quantité de nanoparticules dont on a besoin afin de complexer 50 % de l'ADN mis à disposition pendant des essais de cosédimentation (r50) en fonction du pH.

Des mesures de QCM-D ont également pu montrer qu'en présence de sel des surfaces de silice quaternisées sont en mesure d'adsorber une quantité d'ADN plus importante que des surfaces aminées. Sous des conditions d'assemblages favorisant les interactions électrostatiques nous avons pu constater que des surfaces quaternisées adsorbent de l'ADN dans une conformation plus rigide que des surfaces aminées. Ces résultats montrent que des surfaces de silice portant des ammoniums quaternaires réussissent à mieux condenser l'ADN que des surfaces modifiées seulement avec des amines primaires et secondaires. Nous avons réussi à former de multicouches d'ADN et des bicouches lipidiques en conséquence du fait que les couches d'ADN adsorbées étaient suffisamment rigides afin d'agir comme support d'une bicouche de lipides cationiques (**FIGURE 0.0-10**).

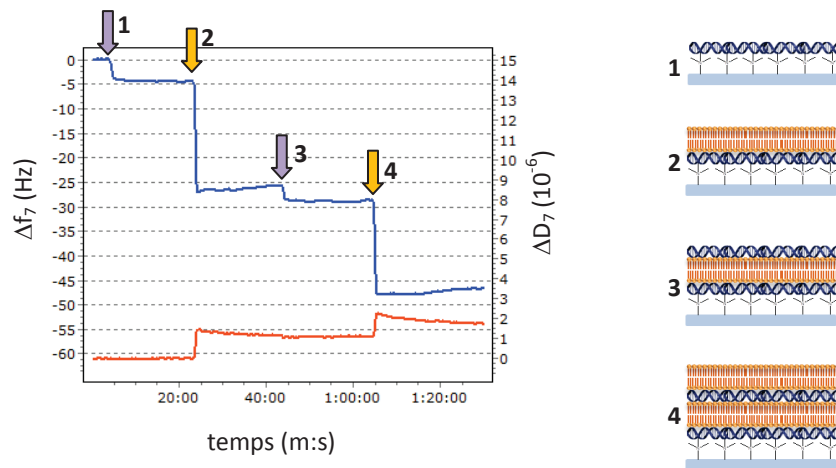


FIGURE 0.0-10 En absence de sel des multicouches ADN/DOTAP forment sur des surfaces de silice quaternisées à pH 7.4. Le signal de la fréquence résonante est affiché en bleu alors que la dissipation est représentée par la ligne orange. Les injections d'ADN sont signalées par des flèches violettes, les injections de lipides cationiques par des flèches jaunes.

L'accomplissement de tests d'assemblages supramoléculaires d'ADN, de lipides cationiques et de nanoparticules de silices portant des groupements d'ammoniums quaternaires à leur surface montraient que les nanoparticules quaternisées sont appropriées pour marquer de l'ADN incorporé

dans des lipoplexes grâce à des interactions électrostatiques. La formation de complexes tripartites nanoparticules quaternisées/ADN/lipides a même été possible en présence de 150 mM de sel à pH 8.6 alors que sous les mêmes conditions des nanoparticules aminées ne sont plus intégrées dans des structures de lipoplexes mais interagissent uniquement avec des lipides cationiques, qui forment une bicouche supportée à leur surface dû à des interactions van der Waals (FIGURE 0.0-11).

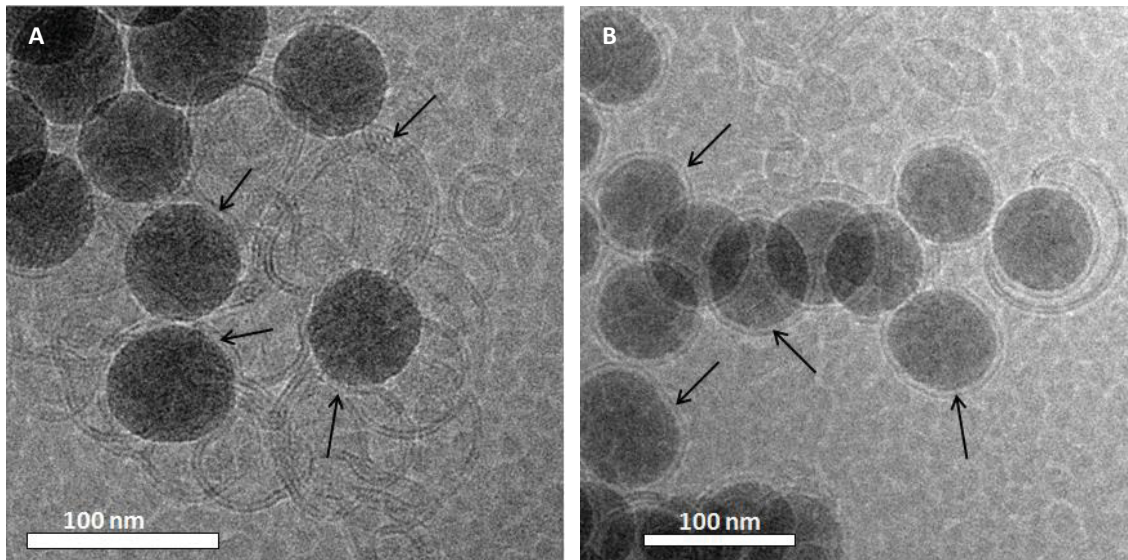


FIGURE 0.0-11 A : Image Cryo-MET d'une agglomération NP/lipoplex assemblées en utilisant des nanoparticules quaternisées, de l'ADN et BGTC/DOPE liposomes à 150 mM NaCl dans un tampon borate (10 mM, pH 8.6). **B :** En réalisant l'assemblage supramoléculaire sous les mêmes conditions mais en utilisant des nanoparticules aminées nous n'obtenons pas de complexes tripartites mais des nanoparticules supportant des bicouches lipidiques.

Pendant cette étude, nous avons été capables d'installer des groupements d'ammoniums quaternaires en surface des nanoparticules de silice. Nous avons montré que les surfaces de silice quaternisées adsorbent de l'ADN de manière plus efficace que des nanoparticules aminées même en présence de sel et à des pHs basiques. En conséquence de notre étude, nous sommes maintenant capables de fonctionnaliser des nanoparticules de silice multimodales afin de marquer de l'ADN. Nous espérons pouvoir effectuer des études de suivi de la transfection d'ADN par des agents de transfection lipidiques *in vitro* et *in vivo* dans un futur proche.

REFERENCES

- [1] A. G. Rockall, S. A. Sohaib, M. G. Harisinghani, S. A. Babar, N. Singh, A. R. Jeyarajah, D. H. Oram, I. J. Jacobs, J. H. Shepherd, R. H. Reznek, *JCO* **2005**, *23*, 2813–2821.
- [2] S. A. Anderson, J. Shukaliak-Quandt, E. K. Jordan, A. S. Arbab, R. Martin, H. McFarland, J. A. Frank, *Ann. Neurol.* **2004**, *55*, 654–659.
- [3] A. Wunder, R. H. Straub, S. Gay, J. Funk, U. Müller-Ladner, *Rheumatology* **2005**, *44*, 1341–1349.
- [4] F. A. Jaffer, P. Libby, R. Weissleder, *Circulation* **2007**, *116*, 1052–1061.
- [5] D.-E. Lee, H. Koo, I.-C. Sun, J. H. Ryu, K. Kim, I. C. Kwon, *Chem. Soc. Rev.* **2012**, *41*, 2656–2672.
- [6] J. L. Vivero-Escoto, R. C. Huxford-Phillips, W. Lin, *Chem. Soc. Rev.* **2012**, *41*, 2673.
- [7] G. Zhang, J. Feng, L. Lu, B. Zhang, L. Cao, *J. Colloid Interface Sci.* **2010**, *351*, 128–133.
- [8] A. E. Nel, L. Mädler, D. Velegol, T. Xia, E. M. V. Hoek, P. Somasundaran, F. Klaessig, V. Castranova, M. Thompson, *Nat. Mater.* **2009**, *8*, 543–557.
- [9] T. Pellegrino, S. Kudera, T. Liedl, A. Muñoz Javier, L. Manna, W. J. Parak, *Small* **2005**, *1*, 48–63.
- [10] M. L. B. Magalhães, C. M. Czekster, R. Guan, V. N. Malashkevich, S. C. Almo, M. Levy, *Protein Sci.* **2011**, *20*, 1145–1154.
- [11] L. Y. T. Chou, K. Ming, W. C. W. Chan, *Chem. Soc. Rev.* **2011**, *40*, 233–245.
- [12] X. Xue, F. Wang, X. Liu, *J. Mater. Chem.* **2011**, *21*, 13107–13127.
- [13] O. Le Bihan, R. Chèvre, S. Mornet, B. Garnier, B. Pitard, O. Lambert, *Nucleic Acids Res.* **2011**, *39*, 1595–1609.
- [14] C. M. McIntosh, E. A. Esposito 3rd, A. K. Boal, J. M. Simard, C. T. Martin, V. M. Rotello, *J. Am. Chem. Soc.* **2001**, *123*, 7626–7629.
- [15] C. M. Goodman, N. S. Chari, G. Han, R. Hong, P. Ghosh, V. M. Rotello, *Chem. Biol. Drug. Des.* **2006**, *67*, 297–304.

LIST OF ABBREVIATIONS

AcAc	Acetic acid
AcCheE	Acetylcholine esterase
ANTA	Amino-nitrilotriacetic acid
APES	(3-Aminopropyl)triethoxysilane
APS	(3-Aminopropyl)trimethoxysilane
APTES	(3-Aminopropyl)triethoxysilane
BET	Brunauer-Emmett-Teller
BGTC	(Bis(guanidinium)-trencholesterol)
β -OG	<i>N</i> -octyl- β -D-glucoside
bp	DNA base pair
BSA	Bovine serum albumin
CBMN	Chimie et Biologie des membranes et des nanoobjets
CCD	Charge coupled device
CHI	Chitosan
CRPP	Centre de Recherche Paul Pascal
CytC	Cytochrome C
CTAB	Cetyl trimethylammonium bromide
DLS	Dynamic light scattering
DMF	Dimethylformamid
DMSO	Dimethylsulfoxid
DNA	Deoxyribonucleic acid
DNTB	5,5'-Dithiobis-(2-nitrobenzoic acid) (Ellman's reagent)
DOPA	Di-n-octylphosphinic acid
DOPC	1,2-dioleoyl- <i>sn</i> -glycero-3-phosphocholine
DOPE	1,2-dioleoyl- <i>sn</i> -glycero-3-phosphocholine
DOPG	1,2-dioleoyl- <i>sn</i> -glycero-3-phospho-(1'- <i>rac</i> -glycerol)
DOPS	1,2-dioleoyl- <i>sn</i> -glycero-3-phospho-L-serine
DOTAP	1,2-dioleoyl-3-trimethylammonium-propane
DRIFT	Diffuse reflectance infrared fourier transform
EDBE	2,2-(ethylenedioxo)bis(ethylamine)
EDC	1-ethyl-3-(3-dimethylamino)-propylcarbodiimide
EDPS	<i>N</i> -[3-(Trimethoxysilyl)propyl]ethylenediamine
FITC	Fluorescein isothiocyanate
FRET	Förster resonance energy transfer
GFP	Green fluorescing protein
HA	Hyaluronic acid
HEPES	4-(2-hydroxyethyl)-1-piperazineethanesulfonic acid
HPA	Hexyl phosphonic acid

ICP	Inductive coupled plasma
ICMCB	Institut de Chimie de la Matière Condensée de Bordeaux
IR	Infrared
LDL	Low density lipoprotein
LUV	Large unilamellar vesicles
MeEDPS	<i>N</i> -[3-(Trimethoxysilyl)propyl]dimethylammonium ethyltrimethylammonium iodide
MES	2-(<i>N</i> -morpholino)ethanesulfonic acid
MLV	Multilamellar vesicles
MOPA	Mono- <i>N</i> -octyl-phosphinic acid
MRI	Magnetic resonance imaging
MS	Mass spectrometry
MUTAB	(11-mercaptoundecyl)- <i>N,N,N</i> -trimethylammonium bromide
m/v	Mass per volume; weight percent
NHS	<i>N</i> -hydroxy succinimide
NIR	Near infrared
NMR	Nuclear magnetic resonance
NTA	Nitrilotriacetic acid
NP	Nanoparticle
NQ	Quaternary ammonium ion
OI	Optical imaging
PAMAM	Polyamidoamine
PDI	Polydispersity index
PEG	Polyethylene glycol
PEI	Polyethyleneimine
PEM	Polyelectrolyte multilayer
PET	Positron emission tomography
PMIDA	<i>N</i> -phosphonomethyl imidodiacetic acid phosphonate
PVP	Polyvinylpyrrolidone
QCM-D	Quartz crystal microbalance with dissipation monitoring
QD	Quantum dot
RhB	Rhodamine B
RNA	Ribonucleic acid
SAM	Self assembled monolayer
SDS	Sodium dodecylsulfate
SEF	Surface enhanced fluorescence
SERS	Surface enhanced raman scattering
SLB	Supported lipid bilayer
SPDP	<i>N</i> -succinimidyl-3-[2-pyridyldithio]-propionate
SPIO	Small iron oxide particle
SUV	Small unilamellar vesicle

TBAPS	<i>N</i> -trimethoxysilylpropyl- <i>N,N,N</i> -tributylammonium chloride
TEM	Transmission electron microscopy
TEOS	Tetraethylorthosilicate
TG	Thermogravimetry
TGA	Thermogravimetric analysis
THF	Tetrahydrofuran
TMAPS	<i>N</i> -trimethoxysilylpropyl- <i>N,N,N</i> -trimethylammonium chloride
TMAP	Organic part (C ₅ H ₁₅ N) of the silane coupling agent TMAPS
TOPO	Trioctylphosphine oxide
UV-VIS	Ultraviolet-visible
USPIO	Ultrasmall iron oxide particle
VdW	Van der Waals
v/v	Volume per volume; volume percent

LIST OF REAGENTS

Manufacturer	Product
Sigma-Aldrich (St. Louis, USA) (Lyon, France)	Acetic acid (glacial), ReagentPlus [®] , ≥99%
Atlantclabo-ics (Bruges, France)	Hydrochloric acid (37 % w/v)
Atlantclabo-ics (Bruges, France)	Phosphoric acid (85 % w/v)
Atlantclabo-ics (Bruges, France)	Nitric Acid (69 % w/v)
Atlantclabo-ics (Bruges, France)	Perchloric acid (70 % w/v)
Atlantclabo-ics (Bruges, France)	Hydrofluoric acid (40 % w/v)
Aldrich	(3-Aminopropyl)triethoxysilane (99 % w/v)
Aldrich	(3-Aminopropyl)trimethoxysilane (97 % w/v)
Synthesized at CBMN (O. Lambert)	(Bis(guanidinium)-trencholesterol)
Sigma-Aldrich	<i>N</i> -octyl-β-D-glucoside ≥98% (GC)
Sigma-Aldrich	Citric acid (99 % w/v)
Sigma	<i>N,N</i> -Dimethylformamide for molecular biology, ≥99%
Sigma	Dimethyl sulfoxide BioReagent, ≥99.9%
Sigma	Deoxyribonucleic acid from herring sperm
Avanti Polar Lipids, Inc. / Coger (Alabaster, USA) / (Paris, France)	1,2-dioleoyl- <i>sn</i> -glycero-3-phosphocholine
Avanti Polar Lipids, Inc.	1,2-dioleoyl- <i>sn</i> -glycero-3-phospho-(1'- <i>rac</i> -glycerol)
Avanti Polar Lipids, Inc.	1,2-dioleoyl- <i>sn</i> -glycero-3-phospho-L-serine
Avanti Polar Lipids, Inc.	1,2-dioleoyl-3-trimethylammonium-propane
Aldrich	<i>N</i> -[3-(Trimethoxysilyl)propyl]ethylenediamine (97 % w/v)
Thermo Scientific/ Pierce Protein Biology products (Rockford, USA)	Fluorescein isothiocyanate
Aldrich	(11-mercaptoundecyl)- <i>N,N,N</i> -trimethylammonium bromide 95 % (w/v)
Sigma	Rhodamine B isothiocyanate mixed isomers, BioReagent, suitable for protein labeling
Sigma-Aldrich	Sodium dodecylsulfate BioXtra, ≥99.0% (GC)
abcr GmbH & Co. KG (Karlsruhe, Allemagne)	<i>N</i> -trimethoxysilylpropyl- <i>N,N,N</i> -tributylammonium chloride
Aldrich	Tetraethylorthosilicate ≥99.0% (GC)
abcr GmbH & Co. KG (Karlsruhe, Allemagne)	<i>N</i> -trimethoxysilylpropyl- <i>N,N,N</i> -trimethylammonium chloride
Sigma-Aldrich	Iron(III) chloride hexahydrate puriss. p.a., Reag. Ph.

	Eur., ≥99%
Sigma-Aldrich	Iron(II) chloride tetrahydrate puriss. p.a., ≥99.0% (RT)
Sigma-Aldrich	Silver nitrate ACS reagent, ≥99.0%
Sigma-Aldrich	Sodium chloride BioXtra, ≥99.5% (AT)
Sigma	4-(2-hydroxyethyl)-1-piperazineethanesulfonic acid
Sigma	2-(<i>N</i> -morpholino)ethanesulfonic acid BioReagent, ≥99.5%
Sigma-Aldrich	Sodium tetraborate decahydrate BioXtra, ≥99.5%
Atlantclabo Inc.	Ammonium hydroxide (28-30 % w/v)
Sigma-Aldrich	Sodium hydroxide reagent grade, ≥98%, pellets (anhydrous)
Sigma-Aldrich	Sodium dihydrogen phosphate BioXtra, ≥99.0%
Fluka	Phosphotungstic acid hydrate for microscopy
Fluka	Uranyl acetate puriss. p.a., ACS reagent, ≥98.0% (T)
Thermo Scientific	Gene ruler™ 1kb DNA ladder
Invitrogen / Life Technologies SAS (St. Aubin, France)	SYBR® green I nucleic acid gel stain
Sigma-Aldrich	Iodomethane, ReagentPlus®, 99%
Atlantclabo-ics (Bruges, France)	Ethanol
Fluka	Ethanol puriss. p.a., ACS reagent, absolute alcohol, without additive, A15 o ¹ , ≥99.8%
Atlantclabo-ics (Bruges, France)	Acetone
Fluka	Potassium dichromate for 1L standard solution, 1/60 M K ₂ Cr ₂ O ₇ (0.1N)
Aldrich	Iron(III) nitrate nonahydrate ≥99.999% trace metals basis
Fluka	Chlorotrimethylsilane puriss., ≥99.0% (GC)
Aldrich	Glycidol 96%
Sigma-Aldrich	Triethylamine ≥99%
Sigma-Aldrich	Chloroform anhydrous, ≥99%
Atlantclabo	Diethyl ether Anhydrous, J.T.Baker® Stabilized
Sigma-Aldrich	Tetrahydrofuran anhydrous, ≥99.9%
Sigma-Aldrich	Hexane anhydrous, 95%
Sigma-Aldrich	Acetonitrile anhydrous, 99.8%
Sigma-Aldrich	Potassium carbonate ACS reagent, ≥99.0%
Sigma	Tin(II) chloride <i>ReagentPlus</i> ®, ≥99%
Sigma-Aldrich	Mercury(II) chloride ACS reagent, ≥99.5%
Sigma-Aldrich	Potassium bromide FT-IR grade, ≥99% trace metals basis
Sigma-Aldrich	Bromphenol blue ACS reagent
Sigma	Xylene cyanol for molecular biology, BioReagent
Sigma	Ficoll® 400 BioXtra, Type 400-DL
Sigma	Dextran sulfate sodium salt from <i>Leuconostoc</i> spp. for

	molecular biology, average $M_w > 500,000$
Sigma-Aldrich	Polyvinylpyrrolidone average mol wt 55,000
Sigma	5,5'-dithiobis-2-nitrobenzoic acid $\geq 98\%$ (TLC), BioReagent
Sigma-Aldrich	Hydrogen peroxide solution 30 wt. % in H_2O , ACS reagent
Sigma	L-Ascorbic acid BioXtra, $\geq 99.0\%$, crystalline
Sigma-Aldrich	Glycerol $\geq 99.5\%$

INTRODUCTION

Nanoparticles or colloids are defined as being of sizes in the range from 1 nm to 1 μm in at least one dimension and existing dispersed in a surrounding medium^[1]. They can consist of different materials as metals, metal oxides, semiconductors or silica and possess unique physical properties leading to a wide range of applications in material science, biotechnology and biology. Depending on their composition nanoparticles show specific optical properties, fluorescence or magnetic behavior. The utility of nanoparticles in biology arises from their properties as well as their size, which is similar to the size of biomolecules as proteins or DNA. They find application in the fields of drug and gene delivery, biosensing and bioimaging^[2].

The labeling of biomolecules as proteins, DNA or lipids is of increasing interest for biologists interested in the exploration of biological processes. Multimodal nanoparticles allow the following of biomolecules and biological actions at different scales on the tissue, cellular and subcellular level. Subsequently the development of multifunctional and multimodal nanoparticles serving as bioimaging tools is a hot spot of actual science.

To improve the efficiency of gene transfer by lipidic transfection agents biologists aspire after the understanding the pathway of DNA-transfection via lipoplexes^[3]. The present study examines the synthesis and surface modification of silica nanoparticles, which are used as markers for DNA. Silica matrixes provide a good platform for the creation of multimodal nanoparticles due to the fact that they don't absorb light in the near-infrared (NIR), visible, and ultraviolet regions neither interfere with magnetic fields and permits the inclusion of different markers and nanoobjects^[4].

In the first chapter we present the state of the art concerning the use and the synthesis of multimodal nanoparticles and their possibilities to interact with or to be conjugated to biomolecules of interest. The second chapter explores the surface modification of silica nanoparticles via silane coupling agents and chemical modifications. The surface modification of a nanoobject is the key step permitting to control its surface properties, which guide the interactions between the biomolecule of interest and the nanoparticle. Inspired from modification protocols in literature we explore different ways to install quaternary ammonium groups on the surface of silica nanoparticles using different silane coupling agents and chemical modification processes.

Quaternary ammonium groups are supposed to interact electrostatically with negatively charged DNA strands. In the third chapter we investigate their capacity to bind to DNA in comparison to nanoparticles modified with grafts containing primary and secondary amine groups. We also discuss results of self assembly experiments leading to the formation of nanoparticle-labeled cationic lipoplexes and analyze the adsorption of DNA and cationic lipids on modified silica surfaces by quartz crystal microbalance with dissipation monitoring (QCM-D).

CHAPTER I – STATE OF THE ART

This first chapter permits to get an overview of the research context within which the present study is situated. In the following paragraphs we will first introduce several imaging techniques which allow the use of nanoparticles as biomarkers. Secondly we will exemplify several nanomaterials which are suitable for acting as markers. Thirdly we will focus on the colloidal surface of these nanoparticles, which defines the solid liquid interface that permits interaction with biomolecules and therefore the labeling of bio-entities. In the last section we will highlight a problem, relating to the objectives of the present study, which consists in the elaboration of a multimodal nanoparticle suitable for the labeling of DNA; furthermore we will pinpoint the goal of the study.

1. IMAGING MODALITIES CURRENTLY USED FOR BIOMEDICAL APPLICATIONS

Functionalized nanoparticles (NPs) are interesting tools for bioimaging, because their physical properties allow their use as contrast and labeling agents. Their small size, similar to that of biological entities, enables the labeling of biomolecules of interest. The labeling of biomolecules such as proteins, DNA or lipids is of increasing interest for biologists longing to understand biological processes. They are also used for diagnostic applications. Nanoparticles functionalized to target tumor cells permit the localization of tumoral tissues and metastases^[1]. Functionalized nanoparticles detecting specific antibodies in the blood circulation can be used to diagnose autoimmune diseases like multiple sclerosis^[2] and can also be functionalized to detect rheumatoid factors, which make the diagnosis of rheumatoid arthritis^[3] possible, or vascular growth factors to explore cardiovascular diseases^[4].

Multiple techniques are used today to visualize tissues, cells or biomolecules of interest with the assistance of functionalized nanoparticles acting as contrast agents or molecular probes. Some techniques such as magnetic resonance imaging (MRI), positron emission tomography (PET), single photon emission computed tomography (SPECT), optoacoustic imaging using ultrasound signals (US), X-ray computed tomography (CT) or near-infrared (NIR) imaging are most valuable for exploring a biosystem *in vivo*. Other techniques such as optical microscopy and electronic microscopy are suitable for exploring biosystems *in vitro*. Each of these techniques has its advantages but also limitations (see FIGURE 1.0-1).

A complementary use of imaging modalities with high sensitivity and imaging modalities with high spatial resolution can facilitate the visualization of an abnormal state of the body and in the same time the biological situation of the target site^[5]. The exploitation of different imaging techniques applied for diagnosis of one target permits a more precise diagnosis of a disease. Multifunctional nanoparticles which are multimodally applicable are therefore biomarkers of considerable interest. They make it possible to regard a target of interest combining for example the high sensitivity of PET imaging for the exploration of biochemical processes of interest with the possibility of magnetic resonance imaging to provide 3D images of affected tissues^[6].

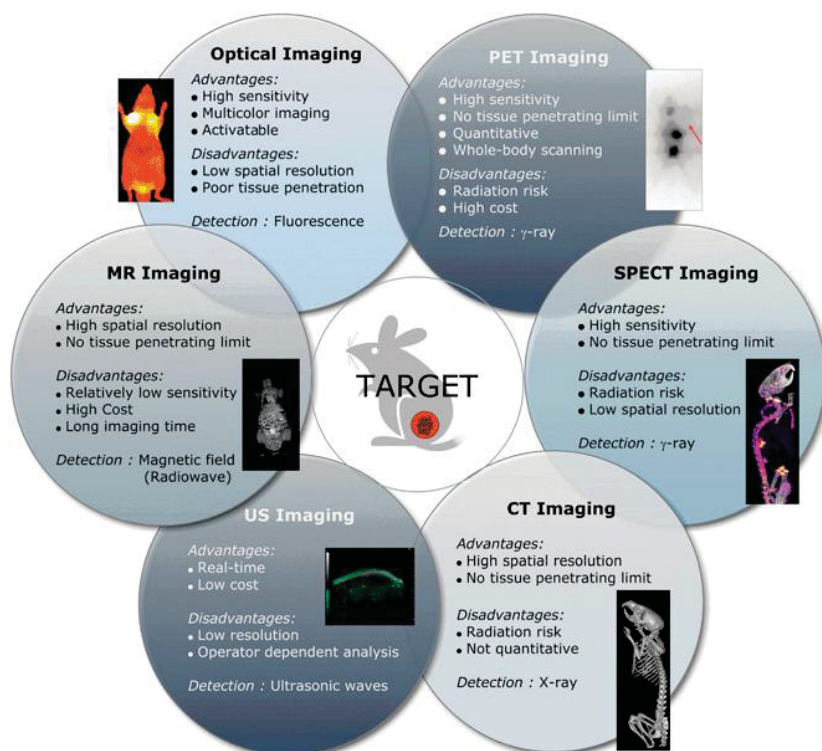


FIGURE 1.0-1 The illustration gives an overview of the characteristics of some imaging modalities currently used for biomedical applications^[5].

The different imaging techniques enable the following of biomolecules on different scales. The visualization of a biologic situation from the tissue down to the cellular scale allows a complete view of the phenomenon in question and enables a precise diagnosis and understanding of the observed pathology. In the following section we will present some of the imaging techniques mentioned, which provide information about a problem of interest on different scales (see **FIGURE 1.0-2**). We focus on imaging modalities requiring the use of nanoparticles as signal-enhancing agents. For imaging on the tissue scale we will introduce two complementary techniques the magnetic resonance imaging (MRI) and the positron emission tomography (PET). We will discuss optical fluorescence imaging (OI) focalizing on its potential to visualize the special distribution of labeled biomolecules at the cellular scale and subsequently introduce transmission electron microscopy (TEM) as an imaging modality enabling us to follow labeled biomolecules on the scale of the cellular ultrastructure.

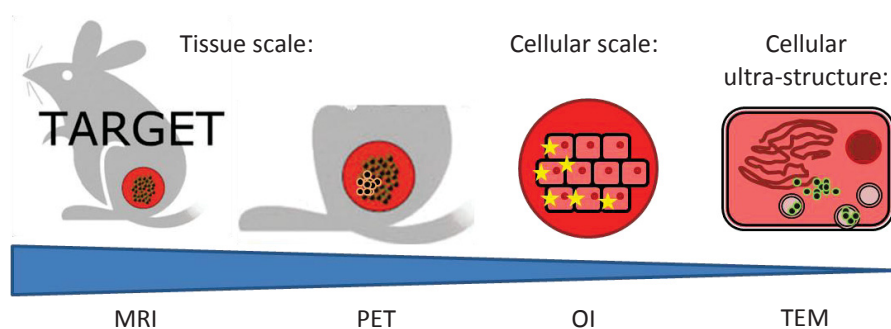


FIGURE 1.0-2 Different imaging modalities permit the visualization of an abnormal state of the body at different scales, which allows a better understanding of the biological situation of the target site.

a) Magnetic resonance imaging

Magnetic resonance imaging (MRI) is an imaging technique, which permits *in vivo* imaging on the tissue scale of animals such as rats, cats, dogs and humans. It provides images of soft tissue and enables a distinction between liquids, fats and different tissues such as brain, muscle, healthy or pathological tissue in comparison to each other. MRI shows a spatial resolution of 3.5 mm³ to 0.5 mm³ and a penetration depth of several millimeters^[7].

It is based on the principle of NMR spectroscopy and exploits the fact that all these tissues contain large quantities of water molecules. By the application of an electromagnetic field the magnetic moments of H₂O protons align to the magnetic field. If radiofrequency impulses of the resonance frequencies of the protons in different tissues are applied, the spins of the H₂O protons are deflected. After the radiofrequency pulse the deflected proton spins return in their original spin states and realign through the magnetic field^[8]. This relaxation of deflected spins of hydrogen atoms situated in the living tissues is traceable due to an emitted radiofrequency signal and displayed.

The spin relaxation is reciprocal to relaxation time and split up to a spin-lattice longitudinal relaxation time T₁ and a transverse relaxation time T₂. These relaxation times depend on the nature of the examined tissue. They influence the imaging signal which can be collected from examined tissue as well as the hydrogen spin density^[9], viscosity and temperature of the examined tissues. This leads to a contrast between different tissues such as pathological and healthy tissue. To enhance the contrast between tissues of interest and other tissue the spin relaxation times T₁ and T₂ can be artificially manipulated by the use of contrast agents.

Superparamagnetic materials such as ultrasmall iron oxide nanoparticles act as T₂ contrast agents. Due to their instantaneous appearing magnetization in a magnetic field they create non-uniformities in the field around them. Water molecules diffusing through these regions suffer from accelerated spin phase shifts, which lead to a decreased T₂ relaxation time. By diminishing the T₂ relaxation time they enhance the negative contrast of the MRI image and enable the biodistribution and agglomeration of the marked biomolecules to be followed^[10,11].

Paramagnetic materials like metallic ions as Fe³⁺, Mg²⁺, Co²⁺, Mn²⁺, Cu²⁺, Gd³⁺, La³⁺ or Eu³⁺ facilitate the T₁ relaxation. Unlike superparamagnetic contrast agents they need direct contact with the water molecules to influence their relaxivity by a dipolar interaction between their magnetic moment and the magnetic moment of a water molecule. They permit positive contrast enhancement. Mn²⁺, Co²⁺, Gd³⁺, La³⁺ or Eu³⁺ ions need to be applied in a chelate complexed form to shield their toxicity and may be encapsulated to nanoparticles^[12,13].

In **FIGURE 1.0-3** examples for T₂ and T₁ weighted TEM micrographs are shown to illustrate the utility of negative and positive contrast enhancements.

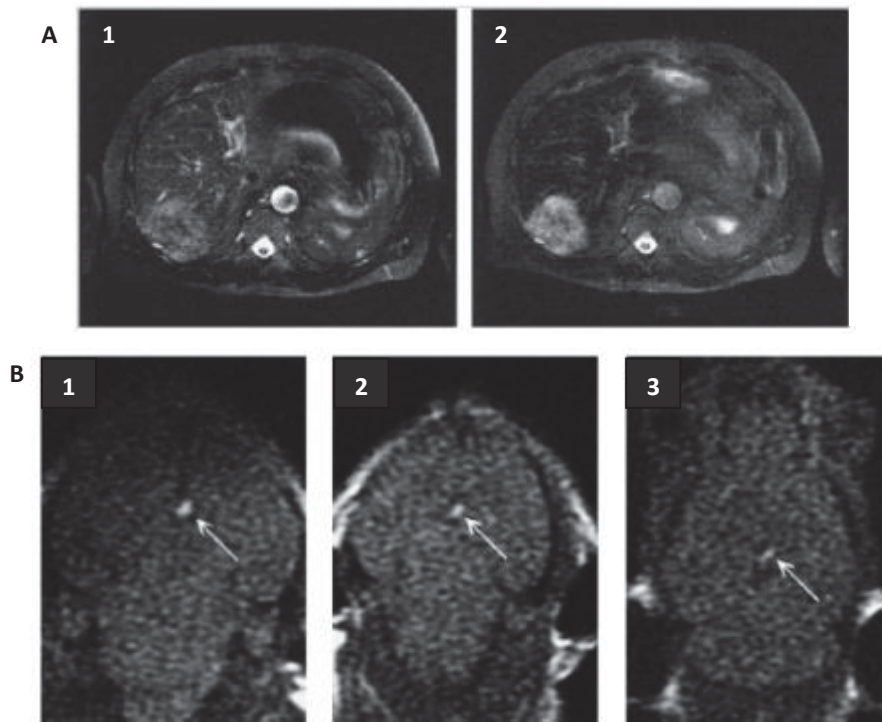


FIGURE 1.0-3 A: T_2 weighted MRI images of a liver affected by metastases. **1:** Natural contrast **2:** Injected iron oxide nanoparticles accumulate in the healthy parts of the liver and provide a negative contrast enhancement, which enables pathological tissue to be identified^[14]. **B:** T_1 weighted MRI images of a mouse brain. **1:** day 0, **2:** day 7, and **3:** day 14 after the injection of gadolinium chelate containing nanoparticles to the midline of high brain stem (indicated by white arrows) providing a positive contrast enhancement^[15].

b) Positron emission tomography

Positron emission tomography (PET) is an *in vivo* imaging technique, which permits the following of radiolabeled biomolecules on the tissue scale, providing images with a resolution of 3.6 mm to 5 mm^[16]. Radiopharmaceutical agents are used to specifically label a biomolecule of interest. Often the targeted biomolecule has a known biochemical function. Its radiolabeling permits the precise and quantitative measuring of specific physiological quantities of the labeled target. PET can therefore be used to display physiologic functions such as blood flow, glucose metabolism or receptor binding characteristics^[17].

A radiolabeled biomolecule is detected by the emission of positron, due to a beta decay of the labeling radioisotope. This positron annihilates with an electron, which leads to the emission of two high energy gamma photons (511keV). These photons are detected within a short timing window (10 ns). The emitted photons pass a collimator, which aligns them along parallel paths, a crystal scintillator, which converts the photons to visible light and a photomultiplier. Summing up the detected photon signals gives information about the radioisotope distribution; the detected signals are converted to an image by a CCD camera^[16].

Radionuclides used in PET imaging usually have short half times such as ^{11}C , ^{13}N , ^{15}O , ^{18}F , ^{82}Rb or ^{124}I . Due to their short life time (<20 min) ^{11}C , ^{13}N and ^{15}O are used less frequently for clinical applications than ^{18}F , which possesses a half time of 110 minutes. The most frequently used fluorine-tagged radiopharmaceutical is fluorodeoxyglucose, which is used to detect cancer cells due to their increased metabolism^[18]. Normandin et al.^[19] used ^{18}F -fluoropropyl-dihydrotetrabenazine to show the dysfunction of β -cells in diabetes I patients. They showed that the tracer-specific binding per unit volume of pancreas tissue was reduced by 40 % in patients with a diabetes I pathology compared to healthy individuals. The repartition of the radiotracer is shown in **FIGURE 1.0-4**.

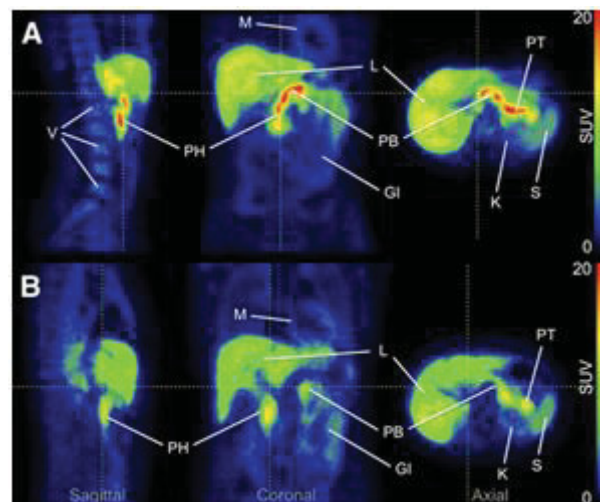


FIGURE 1.0-4 Representative ^{18}F -FP-(+)-DTBZ PET images. **A:** Image acquired for healthy control subject showed high uptake of tracer in pancreas. **B:** Pancreas uptake was reduced in type 1 diabetes patient. Both images represent PET data summed from 0 to 90 min after injection and are displayed on a common scale (0–20 SUV that is, radioactivity normalized by injected dose and body weight). GI = gastrointestinal tract; K = kidney; L = liver; M = myocardium; PB = pancreas body; PH = pancreas head; PT = pancreas tail; S = spleen; V = vertebrae^[19].

c) Optical fluorescence microscopy

Optical fluorescence imaging permits the localization of fluorescent probes on the scale of the cellular structure. It has a spatial resolution of several micrometers; the depth resolution of optical imaging in the UV-VIS range is limited to 1-2 mm. This limit can be overcome by the employing of fluorescent probes usable at NIR wavelengths (650-950 nm) allowing a deeper anatomical penetration^[6]. The labeling of biomolecules with fluorescent or luminescent markers allows their detection by confocal microscopy from the cellular up to the tissue level in small animals such as mice or rats^[20,21].

Optical fluorescence microscopy usually starts by the exciting of a fluorescent probe by the supply of monochromatic filtered light corresponding to the absorption wavelength of the fluorescent material. A second filter is employed to ensure that only the light emitted due to fluorescence is observed. The emitted light is then imaged by an optical microscope, which is connected to a CCD camera. To increase the optical resolution of the recorded micrographs confocal microscopy is used. In contrast to classical optical microscopy, where the whole sample is illuminated, confocal microscopy uses point illumination. The illumination of a small part of the sample and the collection of light through a

pinhole in an optically conjugate plane in front of the detector makes it possible to eliminate the detection of optical signals out of the focal plane.

An advantage of optical imaging is its ability to follow the spatial distribution of differently labeled organelles as shown in **FIGURE 1.0-5**.

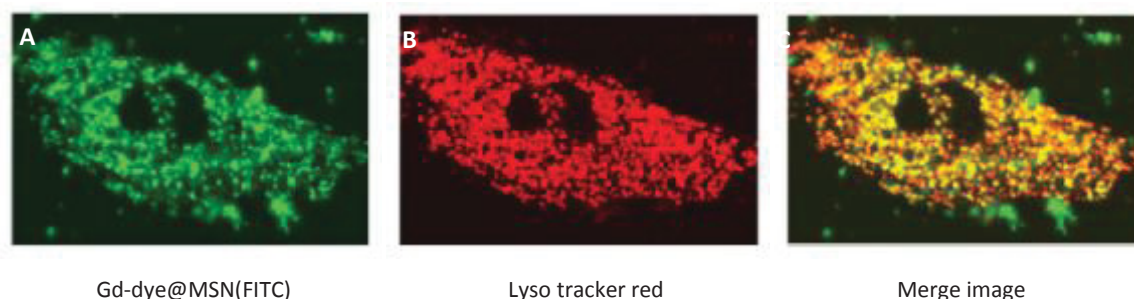


FIGURE 1.0-5 Confocal microscopy images of differently labeled compounds enabling tracking of their spatial distribution: human mesenchymal stem cells treated with different fluochromes. The cellular distribution of **A**: green fluorescent Gd-Dye@silica nanoparticles and **B**: Lyso Tracker Red-labeled organelles (late endosomes/lysosomes) were analyzed. **C**: Co-localization of green fluorescent Gd-Dye@silica NPs with late endosomes/lysosomes^[15].

Confocal fluorescence microscopy has been used to analyze biological events in single cells such as enzyme activity, protein dynamics and interactions. Biomolecules of interest may be labeled by different types of fluorescent molecules such as fluorescent proteins, synthetic organic dyes or fluorescent nanoparticles. Organic fluorophores coupled to oligonucleotide sequences have been used to localize the production of specific RNA fragments^[22,23].

Fluorescent proteins like GFP (238 bp, 26.9 kDa) from the jelly fish *Aequorea Victoria*^[24] and its mutants provide proteins, which fluoresce in a spectral emission range from 505 nm to 525 nm^[25]. There are blue fluorescent proteins such as mTagBFP^[26] as well as proteins which emit fluorescence in the near-infrared range, as the protein Katushka or eqFP650^[27] with a maximal emission wavelength at 635 nm. They may be fused to proteins of interest like kinase proteins to follow their enzymatic activity by FRET^[28].

Labeling two different biomolecules separately enables the dissociation of a marked bio entity from nanoparticles to be followed by observing the Förster resonance energy transfer (FRET) (see **FIGURE 1.0-6**). The observed fluorescence signal depends on the distance between the two fluorescent compounds. If the distance between them is smaller than the so called Förster distance the observed fluorescence changes. This phenomenon is caused by energy transfer between two chromophores which takes place when the emission and absorption spectra of the different fluorophores overlap^[29,30]. This phenomenon can be used to display protein interactions^[31].

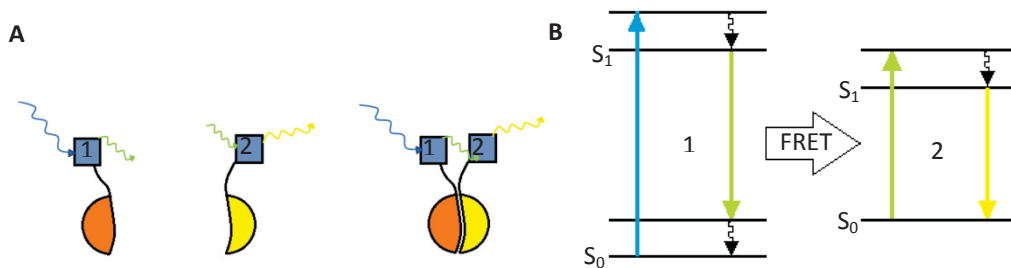


FIGURE 1.0-6 Schematic illustration of the FRET effect. **A:** The FRET effect takes place while two biomolecules (red bulk and yellow bulk) are interacting^[31]. Fluorophore 1 acts as a donor, fluorophore 2 acts as acceptor. **B:** Jablonski diagram illustrating the Förster resonance energy transfer (FRET). One electron of the first fluorophore has been excited by blue light from the basic state to its first electronically excited state. It emits green light. The second fluorophore is excited by a Förster Resonance Energy Transfer absorbing the green light, which has been emitted before.

d) Transmission electron microscopy

Transmission electron microscopy offers the necessary precision for the display of intracellular actions at the level of the cellular ultra-structure. Due to the small de Broglie wavelength of electrons it shows a spatial resolution in the nanometer scale and permits the clear distinction of different cell compartments of eukaryotic cells as cell membranes, cytosol, endoplasmatic reticulum, golgi apparatus, intracellular vesicles and nucleus.

On the top of the microscope an electron source like a tungsten filament connected to a high voltage source delivers an electron beam, which travels through a vacuum column and is focused by electromagnetic quadrupole or hexapole lenses before it reaches the sample^[32]. The high voltage electron beam is transmitted through a thin sample, which depending on the electron density of the material, either lets pass or scatters the beamed electrons^[33]. The detection of the electron beam transmitted at different intensities and the conversion of the signal to an image are accomplished by a screen-coupled CCD camera. Different materials can be observed by transmission electron microscopy. Inorganic materials are relatively electron dense and provide a good contrast during the microscopy observations^[34]. Due to their lower electron density organic materials, of which the cell is composed, can't be observed as distinct as inorganic materials.

In general the specimen is prepared by depositing a thin film of the sample which needs to be observed on a copper grid which has previously been covered with a carbon film. This is generally achieved by the desiccation of a solvent droplet containing observable objects of interest. To obtain a sharp image of organic cell compartments they are negatively stained with solutions of dilute osmium tetroxide, phosphotungstate or uranyl acetate during the sample preparation^[35].

To observe organic cell compartments in their native environment without desiccation^[36] a sample, deposited as a thin liquid film on a holey carbonated copper grid, is frozen in liquid nitrogen or liquid ethane before the observation. Cryo-TEM makes it possible to observe the cellular ultra structure without the need for coloration. To prevent water crystallization and rearrangement of material,

which can occur during the warming of a cryo-sample, the frozen samples are kept under liquid cryogen until they are examined^[37] or embedded and frozen in gel like media such as polyethylene glycol, polyvinyl alcohol or an epoxy resin and sliced to sections of 60 nm^[38].

In FIGURE 1.0-7 two TEM pictures are shown, providing an example of the high resolution which can be obtained. The cellular ultra-structure of sections of eukaryotic Kupfer cells as well as internalized nanoparticles can be clearly distinguished. The electron dense nanoparticles give a darker signal than the cell compartments, due to higher electron scattering.

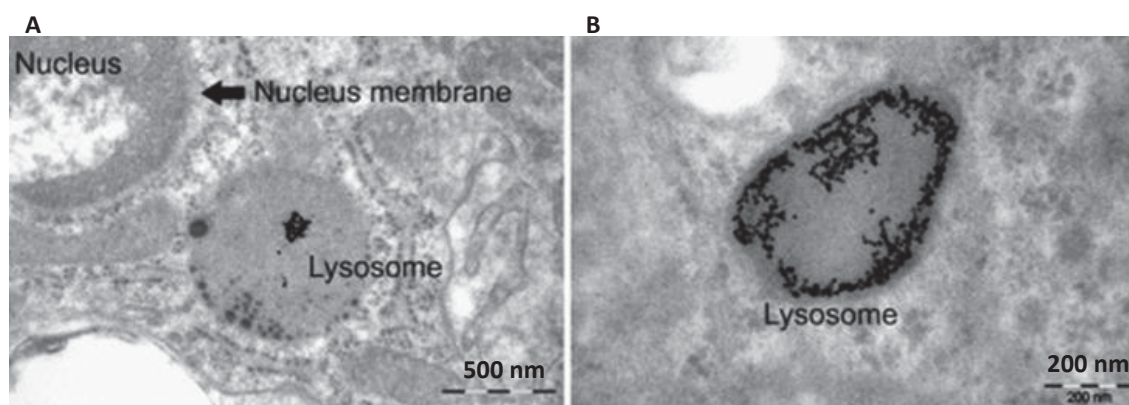


FIGURE 1.0-7 TE microscopy is used to show the cellular ultrastructure of eucariotic cells on the nanoscale. **A, B:** Images of sections of Kupfer cells after injection of gold nanoparticles at different magnifications^[38]. Nanoparticles are entrapped to a lysosome.

The design of multifunctional nanoparticles permitting the combination of imaging modalities underlies rational constraints. Although the use of multimodal imaging probes enables a more precise and detailed diagnosis than it could be provided from a single imaging technique, the combination of the modalities which can be employed by the use of a multimodal imaging tool need to complement their advantages and to compensate their drawbacks. The sensitivity of the combined modalities should be taken into account to maximize synergistic effects and to guarantee the successful employment of multifunctional nanoparticles as imaging probes.

2. MULTIFUNCTIONAL NANOPARTICLES APPLICABLE FOR MULTIMODAL IMAGING *IN VIVO* OR *IN VITRO*

2.1 Different architectures and utilities of multimodal hybrid nanoparticles

After dealing with a few imaging modalities we will now show a selection of multifunctional nanoparticles used as multimodal imaging agents. Hybrid nanoparticles combining different materials have been developed to serve as multimodal imaging agents. Their architectures differ from each other and the possibilities for combining several imaging agents in one particle system are various. With the

help of such particle systems it is possible to explore biological systems by locating nanoparticle labeled biomolecules from the ultracellular up to the tissue level. Furthermore the development of platforms serving as diagnostic and therapeutic agents at the same time is of remarkable interest. Particles providing imaging and therapeutic facilities are called “theragnostic”, which is a term that relies on the combination of diagnostic and therapeutic features. In the following section we will present some examples of multimodal and multifunctional nanoparticles and their architecture.

MRI active dextran coated magnetite nanoparticles can interact with PET active complexes (see FIGURE 2.1-1). These nanoparticles are dual imaging agents and have in addition a therapeutic function because the magnetic cores are used to exterminate cancer cells by hyperthermia.

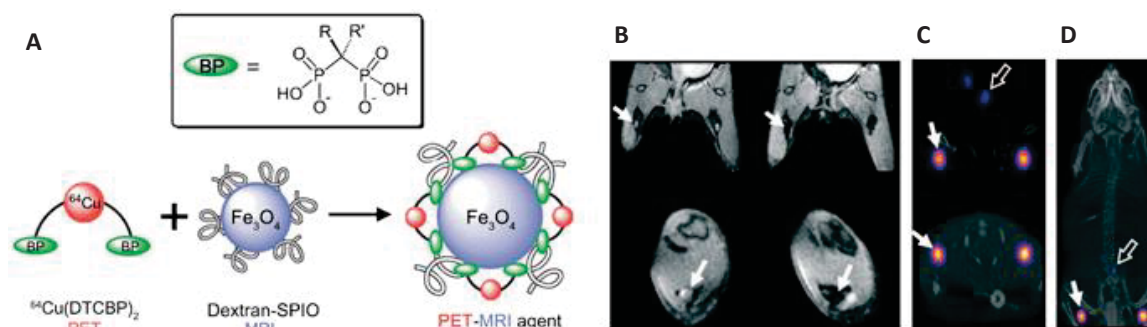


FIGURE 2.1-1 Iron oxide nanoparticle functionalized on its surface to bind a second imaging agent. **A:** Schematic illustration of an iron oxide particle, which is interacting with a copper complex to form a multimodal PET-MRI imaging tool. **B:** T-2 weighted MR images before (left) and after (right) footpad injection of [⁶⁴Cu-(DTCBP)₂]-Endorem. **C:** PET images from coronal (top), short-axis (bottom). **D:** Whole body PET-CT image^[39].

Often silica is used as a host matrix permitting loading with imaging agents. One main strategy is the synthesis of core shell nanoparticles. The encapsulation of biosensing nanoparticles in a silica shell is one type of approach. Magnetic (see FIGURE 2.1-2) or plasmonic cores can be encapsulated in fluorophore-doped silica shells, which allow further functionalization with organosilanes on their surface.

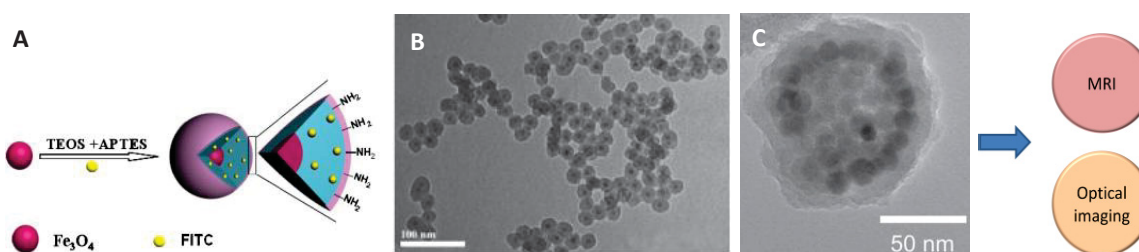


FIGURE 2.1-2 Nanoparticles with magnetic metal oxide cores and fluorescent silica shell allow dual imaging: **A:** Magnetite nanoparticles and fluorescein are encapsulated into the silica shell. The nanoparticle is further modified by the grafting of an aminosilane on its surface. **B:** TEM picture of the MRI-OI active magnetite@SiO₂ nanoparticles^[40]. **C:** Multicore-shell nanoparticle containing Mn-doped ferrite nanoparticles as core and a near-infrared dye incorporated into the silica shell^[41].

Other particle architectures exist, such as for instance a fluorochrome doped silica core surrounded by a plasmonic shell (see FIGURE 2.1-3). Such particles are detectable by optical imaging (OI) due to

surface enhanced fluorescence (SEF) and are suitable for surface enhanced raman scattering (SERS) imaging. Plasmonic metal coated silica nanoparticles can also provide NIR absorption; the plasmonic absorption wavelength can be tuned by variation of the shell thickness. At moderate intensity NIR irradiation these nanoparticles show a photothermal effect. Heating up they thus induce the apoptosis of cancer cells located near to them.

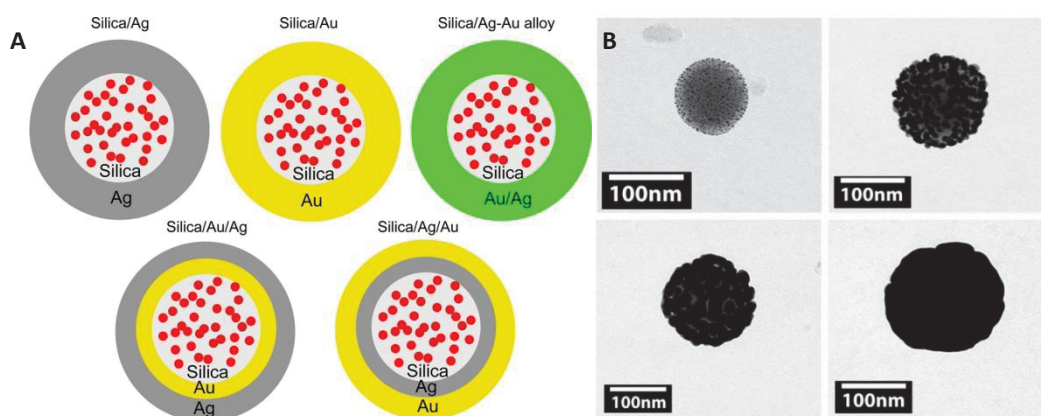


FIGURE 2.1-3 Schematic illustration of multimodal nanoparticles with silica core and metal shell. **A:** Geometries of monometallic and bimetallic shells with the $\text{Ru}(\text{bpy})_3^{2+}$ (red point)-doped silica spheres as the cores; monometallic shells include the silver and gold shells, and bimetallic shells include the homogeneous bimetallic alloy shells and heterogeneous bimetallic shells^[42]. **B:** Representative transmission electron micrographs (TEM) of fluorescent silica particles with a gold shell grown by step-wise synthesis^[20].

Ma et al.^[43] have elaborated the synthesis of ellipsoidal $\text{Fe}_3\text{O}_4@\text{SiO}_2@\text{Au}$ nanoparticles (see **FIGURE 2.1-4**). These nanoparticles are functionalized internally as well as on their surface; they are multimodal and multifunctional. Using a mesoporous silica matrix as shell, which encloses an ellipsoidal magnetite core, these particles allow the incorporation of therapeutic drugs such as doxorubicin as well as the therapy of cancerous cells by photothermic and magnetically induced hyperthermia treatments.

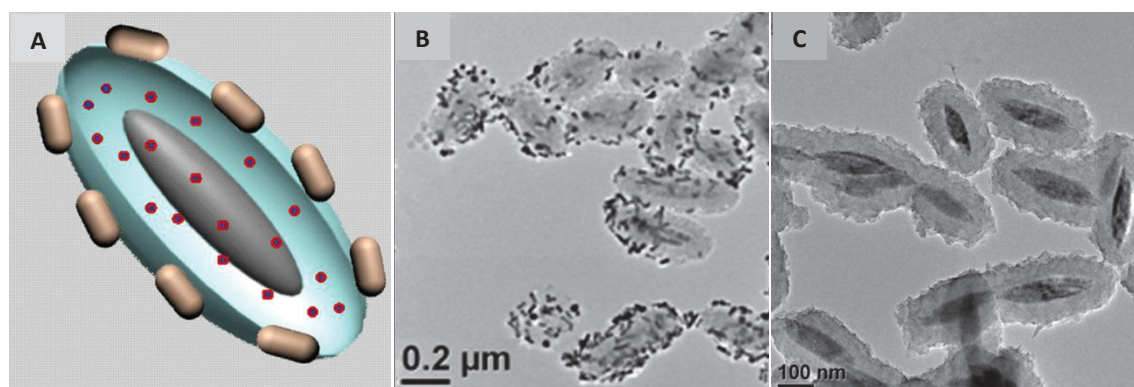


FIGURE 2.1-4 A multimodal and multifunctional nanoparticle possesses a sophisticated architecture. **A:** Schematic illustration of an ellipsoid $\text{Fe}_3\text{O}_4@\text{SiO}_2@\text{Au}$ nanoparticle. The inner grey compartment corresponds to the Fe_3O_4 core, the blue compartment indicates the mesoporous SiO_2 shell, the red dots illustrate encapsulated doxorubicin and the outer grey rods signify attached gold nanoparticles. **B** and **C:** TEM pictures of the synthesized ellipsoids, the different magnifications permit the identification of each constituent^[43].

The ellipsoidal $\text{Fe}_3\text{O}_4@\text{SiO}_2@\text{Au}$ nanoparticles have been tested *in vivo* as drug delivery agents. Due to their magnetic core, injected particles reach their target by “magnetofection”, which means that their migration and biodistribution is controlled by the application of an external magnetic field^[44]. The nanoparticles can be used for therapeutic and diagnostic applications at the same time. It has proved possible to localize them on different scales, from the ultra-cellular up to the tissue level (see FIGURE 2.1-5)^[43]. TEM measurements made it possible to follow the cellular uptake and the localization of the particles in the cell. Optical microscopy allowed following the release and repartition of the red fluorescent doxorubicin in the cytosol. MRI permitted the detection of the cancerous tissues and made it possible to control the success of the cell targeting. The migration of the nanoparticles and the delivery of internalized drugs have been followed in detail.^{45]}

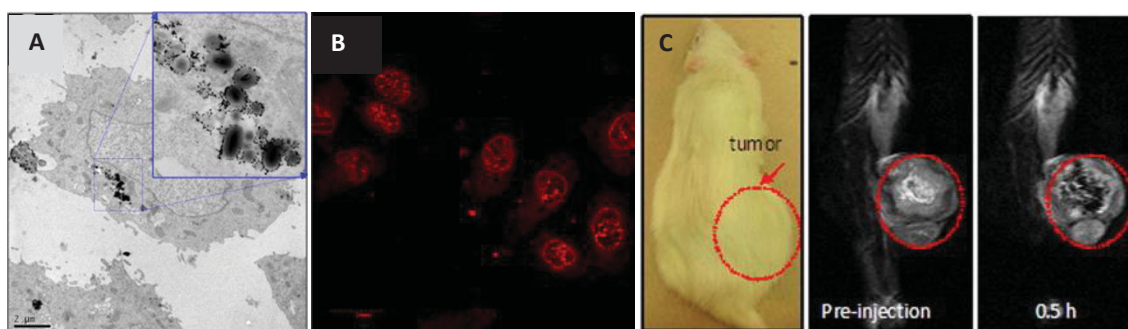


FIGURE 2.1-5 The internalization, uptake and biodistribution of a multimodal nanoparticle can, as well as the release of a fluorescent drug, be followed by bioimaging techniques. **A:** TEM image of $\text{Fe}_3\text{O}_4@\text{SiO}_2@\text{Au}$ nanoparticles internalized to breast cancer MCF 7 cells. **B:** Release of doxorubicin in the cytosol after incubation of MCF 7 cells with the ellipsoid nanoparticles for 4h imaged by confocal microscopy. **C:** Tumor location by MRI, before (on the left) and after (on the right) magnetic attraction of injected particles to the tumor tissue^[43].

The previous examples showed that the combination of chemically different materials with singular physical properties in the same nanoobject renders it multimodal and multifunctional.

2.2 Nanomaterials suitable for multimodal imaging and their physical properties

The physical properties of different materials allow their use as markers during imaging processes. Properties like magnetism, fluorescence, plasmonic resonance and electron density determine for which imaging technique a material is suitable. In the following section the properties and syntheses of superparamagnetic iron oxide, plasmonic and fluorescent nanoparticles will be discussed to understand why they can be combined in order to synthesize multimodal nanoparticles.

a) Superparamagnetic iron oxide nanoparticles

Superparamagnetic iron oxide nanoparticles can be used as contrast agents for MRI. They are applied in biomedicine and are used for experiments aimed at magnetic extraction^[46], the formulation of drug carriers such as magnetoliposomes^[47], the magnetofection of labeled compounds^[44] or hyperthermia^[48].

These nanoparticles consist of inversed spinel ordered ferrimagnetic iron oxide materials as magnetite (Fe_3O_4) or maghemite ($\gamma\text{-Fe}_2\text{O}_3$). Depending on their size they are divided into superparamagnetic iron oxide (SPIO) nanoparticles existing in the size range of 20-100 nm and ultrasmall superparamagnetic iron oxide (USPIO) nanoparticles which are smaller iron oxide clusters possessing sizes in the range from 2 nm to 20 nm^[49].

Superparamagnetism is a form of magnetism, which occurs in ferromagnetic or ferrimagnetic nanomaterials. SPIO nanoparticles consist of several Weiss domains, each of them keeping spins oriented in a different direction. Under application of a magnetic field the spin states of the iron atoms are directed through the field. After the magnetic field is switched off the magnetization of the material persists as the spin relaxation takes place very slowly due to its high anisotropy K. This relaxation is called Néel relaxation, the time required for it to take place is expressed by the equation:

$$\tau_N = 10^{-9} \exp\left(\frac{KV}{kT}\right)$$

EQUATION 2.2-1 Expression of Néel relaxation time

For a ferromagnetic material the anisotropic energy $E_a = KV$ (K anisotropy constant, V domain volume) is higher than the thermic energy kT (k Boltzmann constant, T temperature).

As we can see, the anisotropic energy depends directly on the volume of the magnetic domain: chemical composition, crystallographic structure and shape therefore influence the anisotropy of a nanoparticle. At ambient temperature the anisotropic energy of small iron oxide nanoparticles (<50 nm) becomes smaller than the thermic energy kT , which results in a fast spin relaxation after an external magnetic field is switched off^[50]. The difference between ferromagnetic and superparamagnetic compounds can be illustrated by the fact that in contrast to ferromagnetic nanoparticles superparamagnetic colloids don't show a hysteresis loop (see **FIGURE 2.2-1**), due to the fast and complete relaxation of their spin orientations.

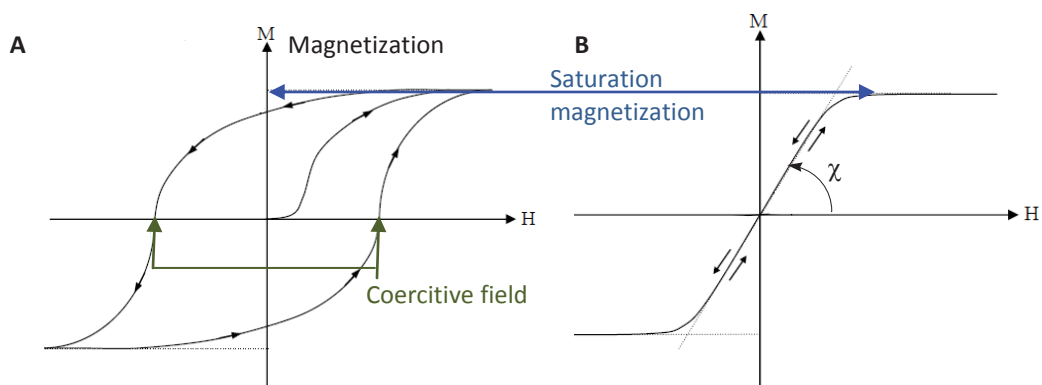


FIGURE 2.2-1 Comparison of the magnetic behavior of a ferromagnetic and a superparamagnetic material at room temperature. **A:** Hysteresis loop obtained by the application of an external magnetic field on a ferromagnetic compound. The ferromagnetic material keeps its magnetization even after the external field is switched off. **B:** Superparamagnetic compounds show magnetic behavior exclusively under the application of an external magnetic field. At each moment spins will orient themselves exactly on the applied field, while after switch-off no magnetization remains.

The magnetization of superparamagnetic nanoparticles follows the Langevin equation. The transverse relaxation time T_2 of such superparamagnetic iron oxide nanoparticles is extremely short, which permits their use as negative contrast agents in MRI^[51].

SPIO or USPIO nanoparticles can be synthesized in multiple ways. One way is the alkaline co-precipitation of magnetic nanoparticles using FeCl_3 and FeCl_2 in a stoichiometric ratio^[52]. The main advantages of this synthesis are its conducting under moderate temperatures in aqueous media, its rapidity, cost effectiveness and applicability to create large quantities of SPIOs or USPIOs. A second way to form iron oxide nanoparticles, leading to highly monodisperse USPIO particles, is their formation in protein cages^[53] or reverse micelles. Nanoparticles can be formed in inverse water in oil micro-emulsions with the use of ionic or unionic surfactants. One example is the synthesis of 7 nm sized iron oxide nanoparticles in sodium bis(2-ethylhexylsulfosuccinate micelles in toluene^[54]. The synthesis of iron oxide nanoparticles by high temperature reactions is based on the reaction of organic iron precursors such as $\text{Fe}(\text{CO})_5$ or $\text{Fe}(\text{acac})_3$ in the presence of organic surfactants. In the presence of octyl ether and oleic acid iron oleate can be formed from a $\text{Fe}(\text{CO})_5$ precursor. Refluxing of the iron oleic complex at 300 °C finally leads to the formation of iron oxide nanoparticles^[55]. A further possibility of synthesis is the creation of iron oxide nanoparticles by hydrothermal procedures^[56] in aqueous media. They take place in reactors or autoclaves, where the pressure can be up to 7000 bar and the temperature up to 650 °C. The formation of $\gamma\text{-Fe}_2\text{O}_3$ nanoparticles from a sol-gel process can also be implemented by heating a three-dimensional iron oxide wet gel at high temperature^[50]. A special form of sol-gel synthesis is the formation of nanoparticles in polyols such as ethyleneglycol and polyethyleneglycols, which act as solvents, reducing agents and particle stabilizing compounds. An iron precursor such as $\text{Fe}(\text{acac})_3$ becomes solubilized in a polyol mixture and forms an intermediate, which is reduced to form metal nuclei leading to nanoparticle growth at high reaction temperatures^[57].

The morphology of the synthesized iron oxide nanoparticles depends on the method of their synthesis. Nanoparticles synthesized by thermolysis are monodisperse and may have different morphologies. Nanoparticles synthesized by coprecipitation are spherical but less regular as shown in **FIGURE 2.2-2**.

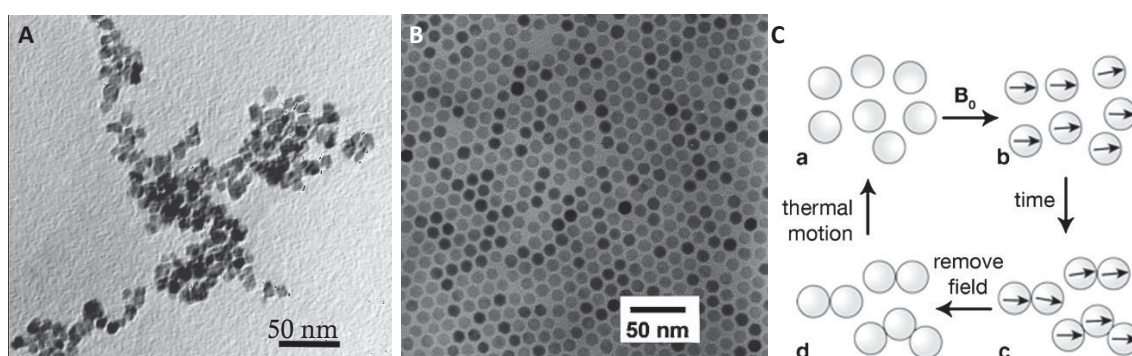


FIGURE 2.2-2 Differently synthesized iron oxide nanoparticles and an exemplary illustration of magnetically induced aggregation are shown. **A:** TEM picture of polydisperse USPIOs prepared by coprecipitation^[58]. **B:** TEM picture of monodisperse hexagonal assembled USPIOs prepared by thermolysis^[55]. **C:** When dispersed magnetic particles (a) are exposed to an external magnetic field their magnetic moments will align (b). With time, the particles form aggregates (c), which disperse again due to thermal motion (a) and loss of magnetisation (d) if the magnetic field is removed^[59].

In general SPIOs need to be protected from aggregation, which can occur under physiological conditions, pH values around the isoelectric point, high salt concentration or their magnetization. To prevent the aggregation of iron oxide nanoparticles they are most often coated with aminosilanes, dextrans or PEG moieties. The stabilization is achieved either by electrostatic or steric repulsion of the nanoparticles among each other. In the case of superparamagnetic nanoparticles magnetically induced aggregation is reversible. If an external magnetic field is applied to a ferrofluid the nanoparticles are magnetized; they move and align in relation to the applied magnetic field. A schematic of magnetically induced nanoparticle aggregation is shown in **FIGURE 2.2-2**. The rotation of entire particles in a global magnetic field is characterized as the Brownian component of the phenomenon of superparamagnetism. It contributes to the relaxation time of the particle magnetization and is expressed by the Brownian relaxation time equation:

$$\tau_B = \frac{3V\eta}{kT}$$

τ_B – Brownian relaxation time

V – volume of the nanoparticle

η – viscosity of the nanoparticle dispersing solvent

EQUATION 2.2-2 Equation characterizes the extrinsic superparamagnetism according to Brown.

b) Plasmonic nanoparticles

Plasmonic nanoparticles may consist of metals, alloys or semiconductors if the materials possess a negative real and small positive imaginary dielectric constant such as for example Al, Cu or noble metallic materials like Au and Ag. Their physical properties enable them to support surface plasmon resonance, which is defined as a coherent oscillation of the surface conduction electrons. The collective oscillation of the electrons, which are situated in the conduction band, leads to the appearance of an electric field located on the metallic surface (see **FIGURE 2.2-3**).

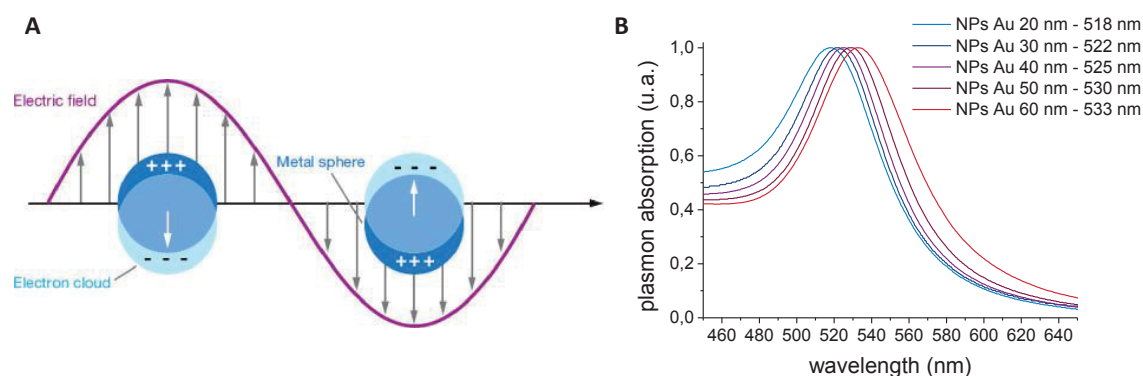


FIGURE 2.2-3 Representation of the surface plasmon of a spherical metal nanoparticle and UV-VIS spectrum illustrating the size dependence of the plasmon absorption band. **A:** Electrons of the conducting band have been excited to oscillation at the resonance frequency of the adsorbed wavelength. While the electron cloud oscillates on the metallic surface, it creates an electric field which follows its oscillation^[60]. **B:** UV-VIS spectrum of spherical gold nanoparticles of different sizes. It can be seen that with increasing particle size the plasmon absorption band shifts to higher wavelength.

The oscillation of the conducting electrons is initiated by electromagnetic fields commonly light. The excited electrons oscillate at the resonance frequency of the absorbed excitation wavelength (electromagnetic field). The resonance frequency of the surface plasmon resonance of a metallic nanoparticle is highly dependent on its material, size and shape which influence the mode of oscillation.

For bioimaging Au and Ag nanoparticles are used due to the fact, that their surface plasmon absorption bands are situated in the UV-VIS and near-infrared (NIR) spectral regions^[61] (see **FIGURE 2.2-3**). Such plasmonic nanoparticles can be used for sensing applications using UV-VIS or near-infrared spectroscopy to follow labeled compounds. Gold nanoparticles are applied as contrast agents in X-ray measurements permitting *in vivo* detection of labeled biomolecules^[62]. Plasmonic resonators are also used as contrast agents during photoacoustic computed tomography measurements.

One technique frequently applied *in vitro* and *in vivo* for the detection of biomolecules is the surface enhanced raman scattering (SERS). This technique is based on the observation that molecule adsorbed or close to the surface to a plasmonic materials will have their Raman signal enhanced. The electric field located on the plasmonic surface (see **FIGURE 2.2-3**)^[63] induces the excitation of the Raman modes and magnifies the signal.

Plasmonic nanoparticles can be used for optical imaging, due to the possibility of the surface plasmon created electric field to induce an enhancement of the brightness and photo stability of fluorescent organic dyes. This phenomenon is called surface enhanced fluorescence (SEF)^[61]. The increased density of photonic states in the proximity of metallic colloids leads to excitation and subsequently a shortening of the spontaneous emission time of the organic dye, which increases the number of absorption-emission cycles and accordingly to an enhanced fluorescence signal.

Both the plasmonic enhancement of the fluorescence and the Raman signal enhancement are phenomena taking place on the nanoscale. The excitation of a fluorophore or a Raman detectable species can only occur when the molecule in question is at an extremely close distance (5 - 30 nm)^[61] to the plasmonic metal.

The use of metallic nanoparticles such as gold or silver colloids for biosensing applications can be synthesized at extremely small sizes permitting a labeling of biomolecules without having an extensive impact on the investigated biosystem. The synthesis of gold or silver nanoparticles can be performed by templating, electrochemical and chemical seeded growth methods^[64]. Seeded growth methods induce the growth of metallic nanoparticles by reducing metal ions using reductive agents. For example methods to synthesize spherical gold nanoparticles use the reduction of Au³⁺ ions, which are provided from the dissolved salt HAuCl₄, with hydroxylamine, sodium citrate, ascorbic acid or NaBH₄ to form Au clusters serving as seeds.

The growth process consists of adding a precise quantity of seeds into a growth aqueous solution containing metallic salt. Particles with diameters from 5 to 100 nm can be synthesized during the growth process. To control growth and avoid secondary nucleation the addition rate of the metal seeds

to the reducing agent and the metal salt solution need to be controlled. In addition pH, temperature and the reduction potential of the reducing reagent influence the kinetics of the particle growth^[64].

By controlling the growth conditions it is possible to control the morphology of the synthesized particles. The use of weak reducing agents such as ascorbic acid is advantageous to obtain a homogenous growth of monodisperse nanoparticles. The addition of AgNO₃ to the reaction environment, the control of pH, the use of sodium borohydride reduced by citrate moieties as well as the presence of CTAB can lead to the growth of gold nanorods^[65-67]. The mechanism by which Ag⁺ ions modify the Au nanoparticle shape is matter of debate. Nikoobakht and El-Sayed^[65] suggest that silver ions form AgBr, which caps CTAB surfactant molecules leading to a decreased charge density in these, hence to decreased steric repulsion and the subsequent elongation of the soft CTAB template. In contrast Murphy et al.^[66,67] consider a rigid structure of CTAB monomers and proclaim that AgBr adsorbs differentially to the facets of gold nanoparticles and hence restricts the particle growth to a rod-like shape.

Further morphologies such as branched spheres, octaedric and triangle-shaped particles can be obtained by the application of different growth conditions and the use of various surfactants during the synthesis (see FIGURE 2.2-4).

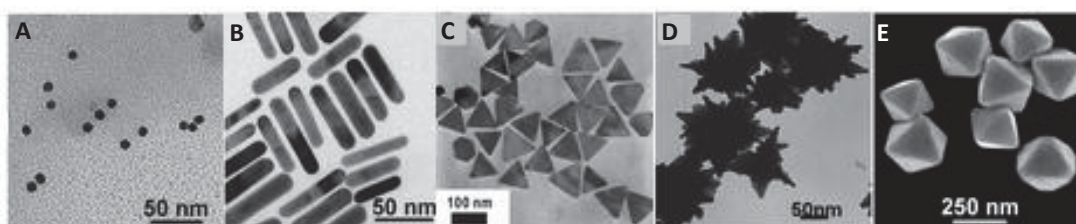


FIGURE 2.2-4 TEM pictures of gold nanoparticles with different shapes show **A:** spheres, **B:** rods, **C:** triangles, **D:** branched spheres, **E:** octahedra^[68].

c) Fluorescent and luminescent nanoparticles

Light-emitting nanoparticles can be used in optical imaging. Depending on their emission wavelength they are suitable for different bioimaging purposes (see FIGURE 2.2-5). Nanoparticles emitting light in the UV-VIS range of the electromagnetic spectrum are used for cellular and assay labeling or as marker during microbiology experiments. Fluorescence is used to create a FRET effect (see FIGURE 1.0-6), which makes it possible to observe the interactions and spatial distances between labeled objects. Nanoparticles emitting in the near-infrared range are predestined as labels for *in vivo* imaging. There are different kinds of light emitting nanoparticles suitable for the use in bioimaging tasks.

One species of luminescent nanocrystals is called quantum dots. Quantum dots are semiconducting materials, which show a bright stable luminescence across a broad range of frequencies, due to the electronic characteristics related to their size and shape. Quantum dots are stable to photobleaching and have narrow emission spectra.

Fluorescent nanoparticles consist of nanoparticles bonding to classical fluorophores. Either they can bind fluorophores like fluorescein or rhodamine on their surface or incorporate them into their matrix. In contrast to the steadily fluorescent quantum dots organic dyes suffer from photobleaching, self-quenching and broad emission spectra, but they are less toxic than quantum dots and therefore advantageous for biomedical use^[20,69].

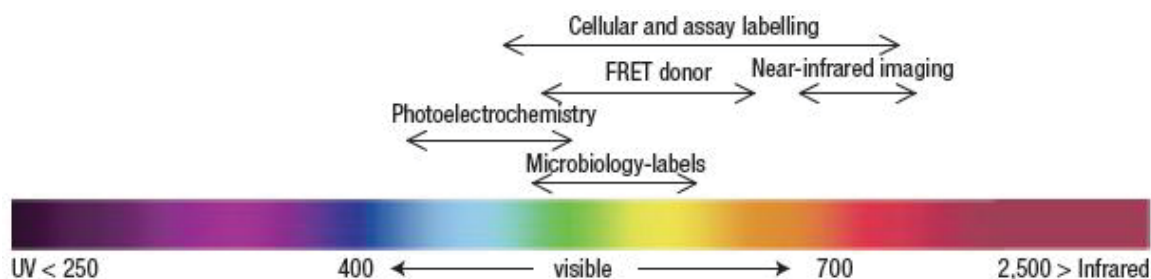


FIGURE 2.2-5 Bioimaging applications use fluorescence at different wavelengths: Optical bioimaging applications of interest require multiple nanocompounds emitting at different wavelengths. The majority of them depend on the existence of fluorescence with an emission range from visible UV to near-infrared^[70].

In the following section we will discuss the two types of particles – luminescent quantum dots and fluorescent silica nanoparticles.

i) Luminescent quantum dot nanocrystals

Quantum dots can consist of semiconducting materials. Compositions of atoms from the periodic groups II-VI and III-V of elements such as ZnS, ZnSe, CdS, CdSe, PbS, PbSe and others build up this kind of material. The size, shape and composition of quantum dot nanoparticles define their photoelectronic properties. For example, CdSe nanocrystals are most interesting for optical imaging in the UV-VIS range, whereas PbS nanocrystals are functional imaging tools in the near-infrared range (see **FIGURE 2.2-6**). Particles of the same composition change their emission peak depending on their size (see **FIGURE 2.2-8**).

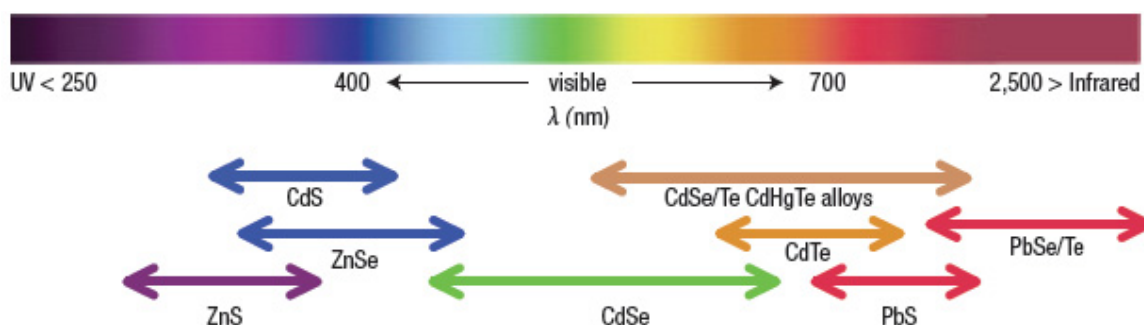


FIGURE 2.2-6 The fluorescence of different QDs covers a large range of the electromagnetic spectrum: Partially core materials determine the emission wavelength of a quantum dot and define their field of action in bioimaging. Dots of the same material vary their emission spectra in depending on their size and shape^[70].

Quantum dots of various compositions are synthesized in hot organic solvents (250 °C - 300 °C) in the presence of surfactants such as trioctylphosphine oxide (TOPO) and a phosphine like tributyl- or trioctylphosphine. Furthermore the mixtures of stabilizing surfactants can contain alkyl amines such as oleylamines, phosphonic or carboxylic acids such as hexyl phosphonic acid (HPA), di-*N*-octylphosphinic acid (DOPA), mono-*N*-octylphosphinic acid (MOPA) and oleic acid^[71].

To form CdSe quantum dots the adding of atomic species precursors like e.g. phosphine complexed Se, organic acid complexed Cd²⁺ or dimethyl cadmium is implemented at high temperature, where the precursors decompose and release Cd and Se atoms. Cd and Se species bind rapidly to each other and form huge aggregates in the absence of surfactants. The present surfactants bind to facets of the nanocrystals via their polar electron donating headgroup and can be seen as Lewis bases^[72]. The nature and quantity of surfactants determine the size and shape of the growing nanoparticles, because of their ability to complex the semiconductor ions in solution and to bind on specific facets of the surface of the growing nanocrystals, which permits them to regulate the particle growth.

Both particle size and particle shape can be regulated making it possible to synthesize CdSe nanocrystals with spherical, rod and teardrop morphologies (see **FIGURE 2.2-7**).

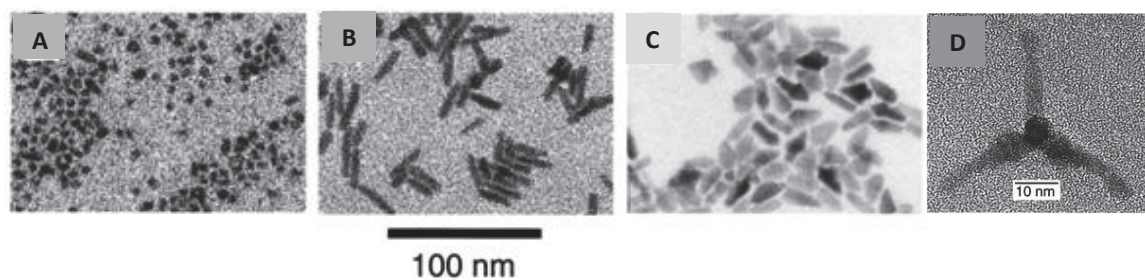


FIGURE 2.2-7 QDs can show different morphologies: TEM pictures of CdSe nanocrystals with **A**: spherical, **B**: rod, **C**: teardrop morphologies and **D**: a typical tetrapod-shaped CdSe nanocrystal, looking down the [001] direction of one arm providing from syntheses under the same reaction conditions but different TOPO/HPA ratios^[73] (HPA - hexyl phosphonic acid).

Quantum dots have the advantage that they can be synthesized at relatively small sizes. They show a bright, photostable luminescence with a wide absorption range and narrow emission peaks. These properties are due to the physical properties causing their luminescence. The bright luminescence of quantum dots is due to an energetic gap between the valence band and the conduction band of the semiconducting core materials. The energy an electron needs to pass through the gap depends on the size of the quantum dot and is due to quantum confinement effects; hence the gap energy is inversely proportional to the size of the nanoparticles^[74]. The dot absorbs all photons with energy higher than its band gap energy. This leads to the excitation of an electron of the valence band to pass through the gap and leaves behind a positively-charged electron hole. When the electron relapses into its original state the electron and hole recombine emitting energy as light.

At the surface of a semiconductor nanocrystal reconstructions in the atomic positions of Cd²⁺ and Se²⁻ atoms are possible and hence surface defects occur, which are able to energetically trap electrons or

holes within energetically forbidden states^[74]. Subsequent this fluorescence quantum yield is decreased at about 10 %. Under continuous excitation quantum dots also suffer from photoblinking, which has been explained by Auger ionization^[70]. However, for bioimaging their main inconvenience is the fact, that they are mostly composed of heavy metals and therefore highly toxic. Because of their high toxicity quantum dots are often included in host matrixes such as SiO₂ or ZnS, shielding the biologic environment from its toxic core, which considerably increases their size^[63,75,76]. Encapsulation into a ZnS matrix (see FIGURE 2.2-8) has instead the further advantage that the encapsulation of a core material to a semiconducting material with a larger band gap passivates the surface of the core by protecting it from oxidation or chemical degradation and by reducing surface defects, which leads to an increase in the photoluminescence yield^[70].

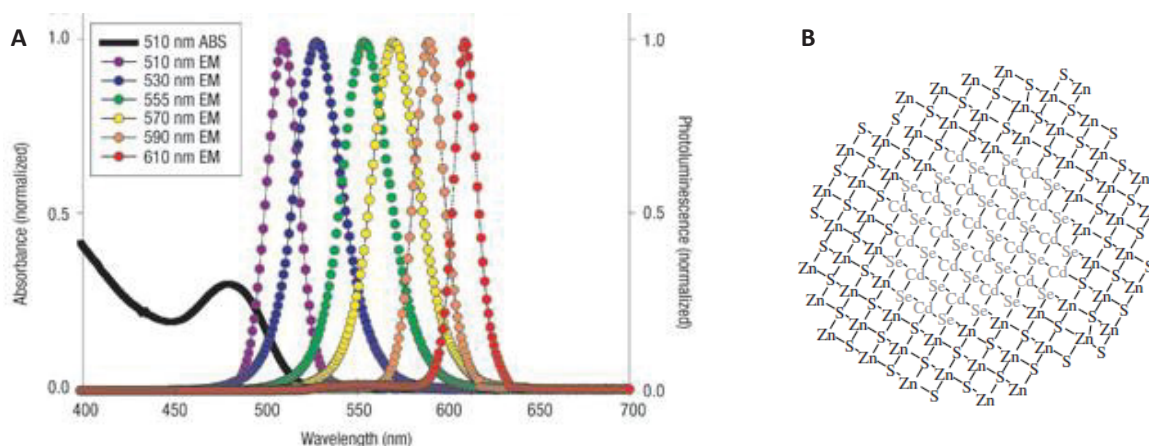


FIGURE 2.2-8 Illustration of the frequency shift, which the fluorescence undergoes with increasing QD size: **A:** Absorption and emission spectra of CdSe quantum dots of different sizes (13.5, 14.5, 17.5, 19, 21.5, 24 nm from left to right)^[70]. The emission spectra are narrow and symmetric. **B:** Schematic illustration of a ZnS shell shielding the environment from a toxic QD core and passivating its surface^[8].

ii) Fluorophore labeled silica nanoparticles

Fluorescent silica-nanoparticles are used as markers for biomolecules to follow their movements *in vitro* or *in vivo*. Depending on the incorporated fluorophores they can be applied as fluorescent ratiometric nanosensors. Different fluorophores can be encapsulated at the same time, either equally distributed in the silica matrix or in different matrix compartments leading to a core-shell architecture, which permits sensing applications using one fluorophore as a reference and the second one as a sensing dye. Fluorophores can act not only as a pH indicator^[77-79] or O₂ indicator^[80,81], but also as an indicator for cations as Pb²⁺, Zn²⁺, Mg²⁺ and K⁺^[82]. Furthermore they can serve as an indicator for temperature fluctuations^[83,84].

Silica (SiO₂) consists of a three-dimensional framework of SiO₄ entities. In crystalline silicate structures Si atoms show tetrahedral coordination with four oxygen atoms. In a silicate network the tetrahedrons are vertex linked so that their oxygen atoms are shared between Si atoms of the silica network leading to the net formula of SiO₂. The material itself doesn't absorb light neither in the UV-VIS range nor in the near-infrared spectrum. It is photophysically stable. The size, morphology and

porosity of silica nanoparticles can be precisely tuned. A silica nanoparticle can be doped with or surface bound to many different kinds of organic fluorophores. As a result nanoparticles fluorescent at a required wavelength have been produced.

To enclose fluorophores in a silica matrix they are usually covalently attached to a silane coupling agent, which co-condenses with TEOS during the formation of the silica matrix^[85]. This synthesis process has the advantage that it permits different NP architectures, where the fluorophore can be located inside the silica matrix or on the particle surface. Different fluorescent chromophores such as fluorescein, tetramethylrhodamine, rhodamineB, Alexa Fluor, near-infrared dyes as purchasable from the Cy dye and the DY dye series or coumarin dyes can - via a functionalization as isothiocyanate or a succinimidyl ester - be coupled to the amine-function of a silane coupling agent such as (3-Aminopropyl)triethoxysilane APTES^[86,87]. Functionalized with a maleimide-group they can be conjugated to mercaptopropyltriethoxysilanes^[88].

Different methods exist for synthesizing spherical monodisperse silica nanoparticles. One method is the so called Stöber process. This synthesis is accomplished under basic catalysis of ammonia in a hydro-alcoholic reaction medium^[89]. The most frequently used precursor is tetraethylorthosilicate (TEOS), which polymerizes in the presence of water. The polymerization is achieved by a hydrolysis/condensation mechanism^[90]. First a hydrolysis of the ethoxy group takes place; ethanol is freed and in its former position a silanol group is obtained. At one moment the solution is saturated of the emerging silicic acid. When the saturation limit is exceeded the solution is called supersaturated. It is in this supersaturated state that a nucleation of silica clusters begins. The polymerization of TEOS can be accelerated by an acidic or basic catalysis. In both cases the catalyzed hydrolysis follows an S_N2 mechanism (see FIGURE 2.2-9).

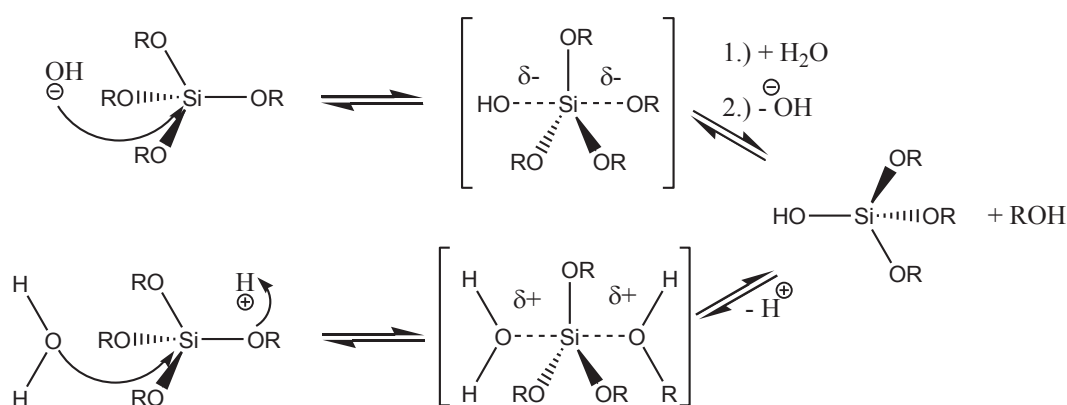


FIGURE 2.2-9 Basic and acidic catalysis of the hydrolysis of TEOS. R – ethylchain.

The production of the hydrolyzed monomer silicic acid is rate limiting during the growth process. The concentration and the ratio of ammonia and water determine the ionic strength of the reaction medium and the ratio of hydrolysis as well as the condensation processes taking place in the same time. The nucleating silica clusters grow to nanoparticles - while low concentrations of ammonia in the reaction medium lead to a fast colloidal stabilization of small particles, high concentrations of ammonia conduct the growth of nanoparticles to higher diameters^[91].

A second possibility for synthesizing spherical silica NPs is to conduct the formation of silica nanoparticles in a reverse micro-emulsion. Aqueous micelles form small spherical reactors determining particle size^[92,93]. Bagwe et al.^[94] synthesized dye doped silica nanoparticles in a reverse micro-emulsion which they composed of adequate amounts of surfactant, co-surfactant and organic solvent, aqueous solution of dye, water and aqueous ammonia. As surfactants they used Triton X-100, sodium dodecyl sulfate (SDS), dioctyl sulfosuccinate (Aerosol-OT) and Igepal CO-520 or polyoxyethylene nonylphenol ether (NP-5).

On the other hand the accomplishment of sol-gel procedures in oil-in-water emulsion has been performed to obtain silica-materials possessing a regular hexagonal pore distribution^[95,96] (see **FIGURE 2.2-10**). These syntheses use surfactants such as the ammonium salt cetyltrimethyl ammonium bromide (CTAB) as a structure directing agent in alkaline media to condense TEOS around formed micelles, which leads to silica nanoparticles with mesopores in the dimension of three to four nanometers^[97].

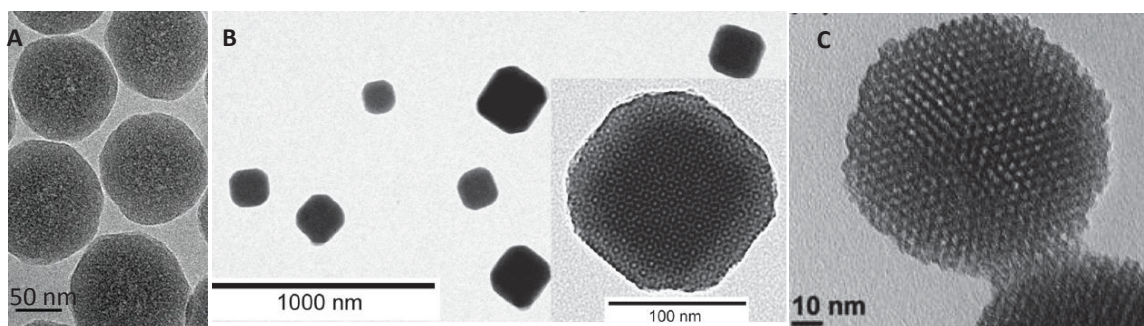


FIGURE 2.2-10 Silica nanoparticles synthesized by different methods: **A** TEM picture of colloidal silica spheres synthesized by the Stöber method^[98]. **B** TEM picture of mesoporous nanoparticles with cubic symmetry synthesized by a sol-gel process in a CTAB microemulsion^[97]. **C** High resolution TEM picture of a mesoporous nanoparticle with pores of a diameter of 4 nm^[96].

Even if organic fluorophores encapsulated to silica matrixes suffer from photo induced chemical destruction upon exposure to fluorescence exciting light known as photobleaching^[99], fluorophore doped silica nanoparticles have the advantage that compared to quantum dots their synthesis is cost effective and undergone at ambient temperature. Silica nanoparticles have the further advantage that they can incorporate metal or metal oxide nanoparticles into their matrix. As well they permit the deposition of metal layers on their surface. Silica is therefore an ideal host matrix for the construction of a multifunctional nanoparticle serving as multimodal imaging tool.

3. COLLOIDAL SURFACES AS FRONTIERS BETWEEN INORGANIC AND BIOLOGIC MATTER

With the goal of labeling biomolecules not only the chemical and physical properties but also the physicochemical characteristics of the nanoparticles must be taken in account. In fact their physicochemical properties mainly govern all interactions with targeted biomolecules. They take place on the colloidal surface acting as solid-liquid and at the same time as a nano-bio interface^[100,101]. Moreover grafted ligands present on the particle surface may enhance the specificity of an inorganic nanomaterial towards biological systems. Scientists tend to control surface properties such as surface potential, surface functionality, the density of grafted residues and the hydrophilic hydrophobic balance (see **FIGURE 3.0-1**) of nanoparticles. These parameters are the key parameters, which control the interactions happening at the nanoparticle surface.

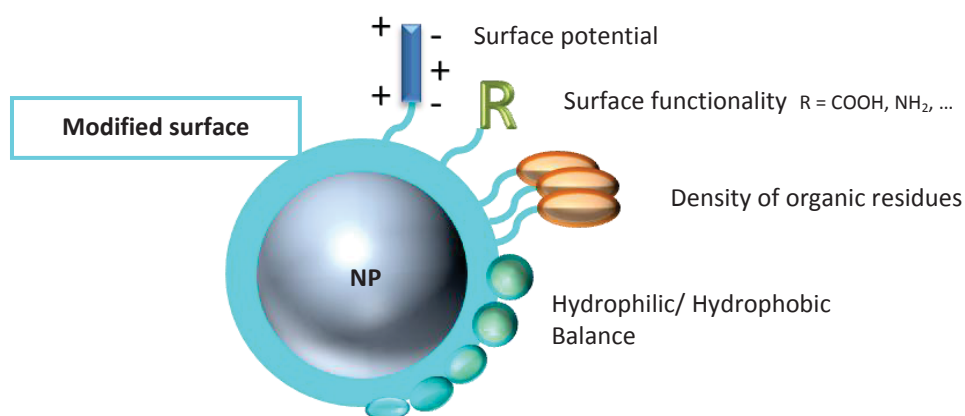


FIGURE 3.0-1 Parameters to be considered when designing nanoparticle surfaces intended to interact with biomolecules: Surface potential, functionality and density of the grafted organic residues as well as the hydrophilic and hydrophobic balance.

The functionalization of the surface of inorganic nanoparticles underlies some constraints. During the modification process the colloidal stability of the nanoparticles has to be maintained. Nanoparticles able to proceed a successful self-assembly with other colloidal entities, as which biomolecules can also be described due to their similar size, need to perpetuate their colloidal stability under physiological conditions at 37 °C in an aqueous medium where the pH is 7.4 and the ionic strength is equivalent to 150mM NaCl. The colloidal stability of functionalized nanoparticles can be provided by electrostatic or steric repulsion.

a) Colloidal stability by electrostatic repulsion

The interactions between colloidal particles which determine their colloidal stability depend on the attractive van der Waals (vdWs) forces and on the repulsive forces appearing between equally charged particles. Introduced by Derjaguin, Landau, Verwey and Overbeek the resulting potential energy U between two equally charged particles is described as the sum of the potential of attractive vdW forces U_A and the potential of electrostatic repulsive forces U_R :

$$U(L) = U_A(L) + U_R(L)$$

EQUATION 3.0-1 Potential energy between two charged nanoparticles.

Attractive interactions are usually caused by van der Waals forces. These forces appear due to electromagnetic fluctuations, which create positive and negative charges within atoms, molecules or bulk materials. The originated dipoles interact, whereas the magnitude of such interactions can be sufficiently high to cause undesired aggregation. Van der Waals interactions are divided into three kinds of interactions first Keesom interactions (dipole-dipole interactions), second Debye interactions (dipole-induced dipole interactions) and third the London interactions (induced dipole-induced dipole interactions) of polarizable materials^[102]. The potential energy of the attractive forces U_A between two spheres can be expressed as:

$$U_{vdw} = \frac{Ar}{12d}$$

A – Hamaker constant

r – particle radius

d – interparticle distance

EQUATION 3.0-2 Potential of attractive forces appearing between two colloidal spheres.

The Hamaker coefficient A appears according to the Hamaker integral approximation. It depends on the material of colloidal particles as well as on their surrounding medium and is described as:

$$A = \frac{C_{vdw}\pi^2}{v_1v_2}$$

C_{vdw} – constant characterizing the interacting species in surrounding medium

v_i – molar volume of the material i

EQUATION 3.0-3 The Hamaker coefficient depends on intrinsic characteristics of the material and their surrounding medium.

Electrostatic interactions between charged particles can be either repulsive or attractive. Like charged particles will show repulsive behavior whereas oppositely charged particles will attract each other. The surface charge of colloidal particles is mostly procured by the ionization of functional groups on the particle surface. The functionalization with chemical functions such as quaternary ammonium groups, amine groups and carboxylate groups leads to charged nanoparticles, which are prevented from coagulation by electrostatic repulsion. However, in order to achieve electrostatic stabilization of functionalized colloids in a solvent, the pH sensitivity of the charges provided by amine or carboxylate groups needs to be considered as well as the density of the charges present on the particles surface and the dielectric constant of the solvent: all these factors may cause particle coagulation.

Furthermore charges which stabilize the particles may be screened by counterions surrounding the nanoparticle surface. The counterions adsorbing on a charged surface significantly influence its electrostatic potential ψ . The screening strength of the particle surrounding counterions depends on their size, valence and concentration in the medium.

The surrounding of nanoparticles by counterions has been described by the concept of an electric double layer of counterions on a charged surface (see **FIGURE 3.0-2**). Stern describes the presence of an inner ion layer, fixed on the charged surface as proclaimed by Helmholtz, which is called the Stern plane and a diffuse outer layer in which the concentration of the counterions diminishes with increasing distance to the colloidal surface as described by Gouy and Chapman^[103]. The plane between the first adsorbed and the second diffuse layer is called the shear plane, the electric potential ψ_{shear} at this plane is denominated as the ζ potential. It is experimentally determinable and can approximately be taken as the electric potential on the particle surfaces^[104].

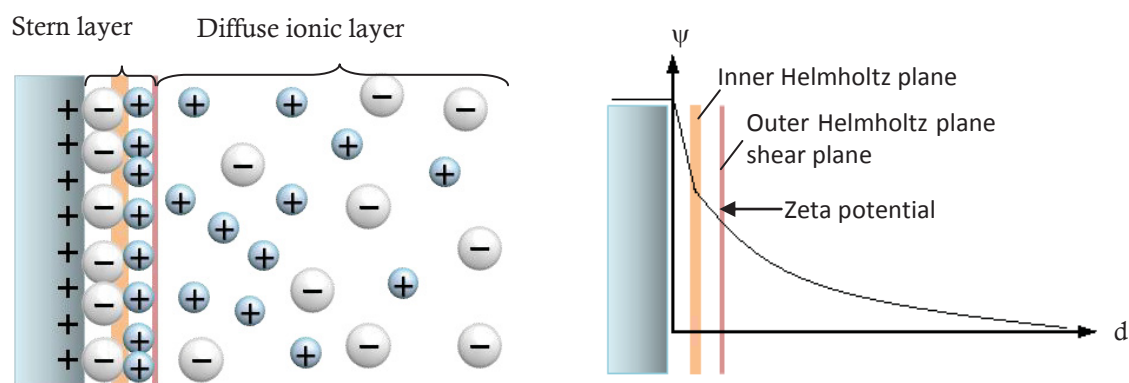


FIGURE 3.0-2 The Stern model of the ionic double layer and the corresponding surface potential.

b) Colloidal stability induced by steric repulsion

In the context of nanoscaled colloidal self-assembly attractive vdWs forces no longer act when the separation between the particle surfaces exceeds 10 nm^[104]. This fact renders the colloidal stabilization by steric repulsion possible. By coating nanoparticles with long molecules, which separate them over a longer distance, their coagulation due to van der Waals forces is prevented. The advantage of steric stabilization of nanoparticles is the fact that it is insensitive to pH and salt concentration in a medium.

However, intending to functionalize a nanoparticle with a macromolecule to achieve its stabilization by steric repulsion, we may choose a macromolecule in relation to the solvent in which the nanoparticles are to be dispersed to stabilize them. To achieve the steric stabilization of coated nanoparticles in nonprotic apolar solvents hydrophobic coating agents need to be employed. To achieve dispersion of macromolecule coated nanoparticles in aqueous media hydrophilic macromolecules such as dextran or polyethylene glycol are first-choice coating agents^[8]. The grafting of such polymers actually enhances the lifetime of the nanocompounds in a physiological environment by protecting them from recognition and elimination by biologic clearance mechanisms. The grafting of the polysaccharide dextran^[105] can already be seen as a first level of biofunctionalization and has been effected by an amination reduction reaction (see **FIGURE 3.0-3**) on the surface of various amino-modified nanoparticles.

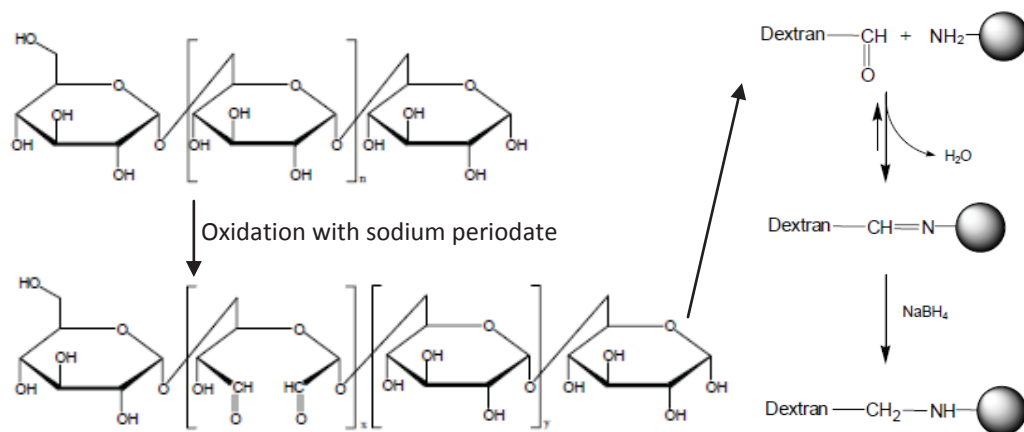


FIGURE 3.0-3 Grafting of dextran pre-oxidized with NaIO₄ to an amine function via reduction with NaBH₄^[105].

Electrodynamic, electrostatic and steric interactions play a key role in providing controlled self-assembly processes between colloids and in governing their interactions with biomolecules^[106]. In the next paragraph we will show some ways to functionalize nanoparticles designed to interact with biomolecules.

3.1 The chemical functionalization of nanoparticle surfaces

The surface chemistry of different nanoparticles depends on the properties of the material present on the surface of a multifunctional nanoobject. The applied modification strategies subsequently vary for different nanoparticles. We will discuss the possibilities to chemically modify the surfaces of metal oxide and metal nanoparticles to give an overview about the chemical modification reactions, which may be executed on the surface of multimodal nanoparticles.

a) Functionalization of metal oxide nanoparticles by silanization

There is a wide range of metal oxide nanoparticles, which have been synthesized in the past as Al₂O₃, TiO₂, SiO₂, Fe₃O₄, γ-Fe₂O₃ or ZnO nanoparticles. Metal oxide surfaces carry free hydroxyl groups, which end their crystal lattice at the solid liquid interface. The hydroxyl groups are present due to the chemisorptions of water on the metal oxide surface. By the formation of hydrogen bonds further water molecules physisorb to the hydroxylated surface and organize themselves into several layers around the nanoparticle^[105]. Properties such as polarity and the charge density of the metal oxide surface determine the thickness of the hydration layer.

Through the hydroxyl groups on their surface metal oxides can react with various reagents such as carboxylic, sulfonic and phosphonic acid as well as silane coupling agents and provide a good platform for various modifications^[8]. However, the surface reactivity of a metal oxide nanoparticle depends on the reaction environment as well as on the reactivity of the metal cation, its degree of oxidation and its coordination number. The modification of metal oxide nanoparticle surfaces with silane coupling agents as organo-functionalized trialkoxysilanes has been widely applied. These organo-functional silane coupling agents consist of three organic groups R bonded to the oxygen

atoms of a tetrahedral orthosilicate ion, whereas the fourth oxygen atom of the originated orthosilicate ion has been replaced by a carbon which connects an organic entity R' to the Si atom^[90].

Silanization reactions are surface modifications, which can be achieved under aqueous reaction conditions as well as in organic solvents. The modification is obtained by a hydrolysis/condensation reaction between the OH groups present on the surface of the modified nanoparticles and the alkoxy groups of a chosen silane coupling agent. A wide range of silane coupling agents is commercially available. The large choice of functional groups (see **FIGURE 3.1-1**)^[50] facilitates the further modification by chemical reactions as well as the conjugation to biomolecules.

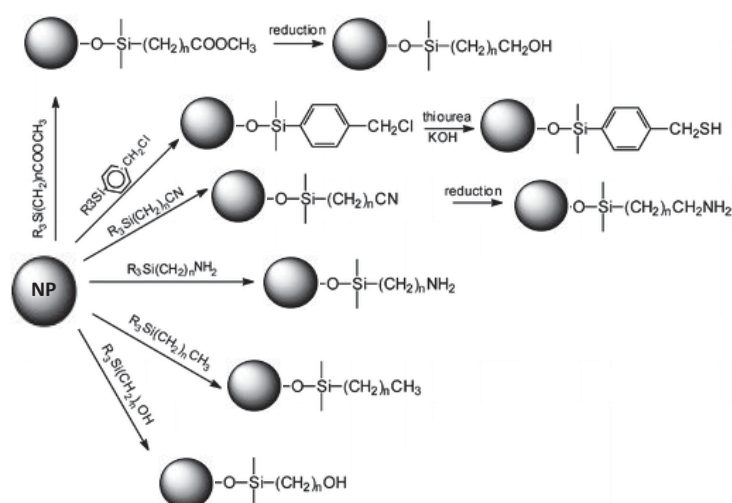


FIGURE 3.1-1 Silanization permits the implementation of various functional groups on hydroxylated surfaces: overview of organofunctional silane coupling agents (R – alkoxy group) with different organic residues^[50].

The mechanism of the silanization of hydroxylated metal oxide nanoparticles is well known and is illustrated for the chemical modification of a silica surface in **FIGURE 3.1-2**^[107]. In the presence of water first the silane monomers will undergo the hydrolysis of their three alkoxy functions, alcohol is freed and three silanol groups arise. Secondly an intermolecular condensation process takes place. In an equilibrium reaction the hydrolyzed monomers will condense to form oligomer chains.

The third step is the adsorption of such a chain to the nanoparticle surface. While they are dispersed in a medium containing silanic oligomer chains, the chains encounter the hydroxyl group bearing nanoparticle surfaces. Between the silanol groups of the silane oligomers and the nanoparticle surface hydrogen bonds form, after which the oligomer chains are adsorbed to the metal oxide surface.

The last step of the modification is composed of the formation of covalent bonds between the hydrogen-bonded silane and the metal oxide substrate. Under the supply of heat further condensation reactions take place leading to the formation of covalent M-O-Si bonds between the former hydroxylated nanoparticle surface and the silane chains^[107].

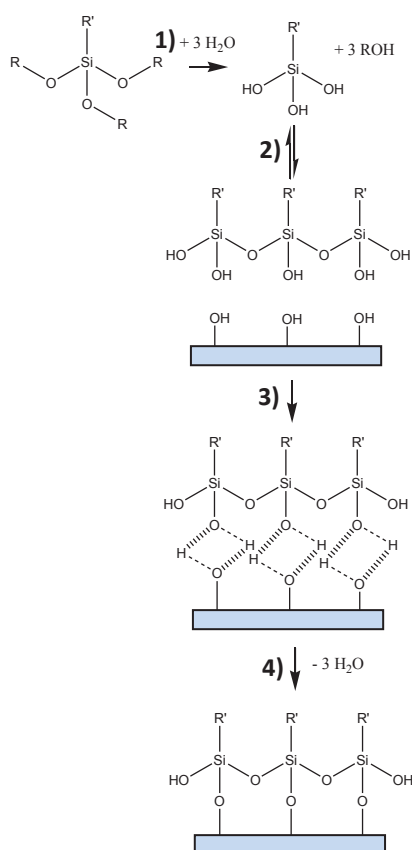


FIGURE 3.1-2 Mechanism of the modification of hydroxylized silica surfaces with organo trialkoxysilanes under aqueous conditions: **1)** Hydrolysis of the three alkoxy groups: alcohol is freed, silanol groups arise **2)** Intermolecular condensation reaction **3)** Adsorption of condensed oligomers to a metal oxide surface by the formation of hydrogen-bonds **4)** A condensation reaction leads to the formation of covalent bonds between the silane coupling agent and the metal oxide surface.

The mechanism occurring in an aqueous medium differs significantly from the hydrolysis/condensation sequence, which has been observed in organic solvents^[108]. Whereas in an aqueous medium the formation of chains, which adsorb to the metal oxide surface has been observed, in an organic reaction environment no formation of silane oligomers takes place, due to the fact that the silane monomers can't hydrolyze in the solvent, but only on the surface of the dispersed particles, where traces of physi- and chemisorbed water are present^[105]. Thus in an organic solvent the cycle of hydrolysis and condensation occur exclusively on the surface of the modified particles.

Depending on the organic function of the silane chosen for the modification a catalyst may or may not be needed. Aminosilanes are self-catalyzing due to their ability to act as a base. The choice of the silane coupling agent also determines the hydrophilic/hydrophobic balance and the surface charge of the modified nanoparticles.

b) Functionalization of metal nanoparticles by self-assembled monolayers (SAMs)

Metal nanoparticles display different chemical and physical properties than individual metal atoms, complexes or bulk metals. They owe their chemical and physical properties to their size, which causes them to have a high quantity of low coordinated metal atoms at their surface compared to the number of fully coordinated atoms in the interior of the particle. In comparison to their properties in the bulk state their chemical reactivity can be significantly enhanced, in that the low coordinated surface atoms undergo redox reactions rather than bulk atoms. Due to their size quantum confinement significantly influences their physical properties, leading to electronic structures different from bulk metals, which permit the occurrence of phenomena such as localized surface plasmons or the photoluminescence of semiconductor quantum dots^[8,109].

Metallic nanoparticles like gold, silver and copper nanoparticles as well as QDs are platforms for reactions with functional thio alkanes, which permit the formation of dense, consistent monolayers (see FIGURE 3.1-3)^[110] on the particle surfaces. The supramolecular assemblies are generally held together by the formation of metal-S bonds and the increase of entropy obtained by the self-organization of the hydrophobic chains of the used thiol ligands. Thiol groups are believed to show high binding affinity towards noble metal surfaces. On gold the formation of a nearly covalent Au-S bond with a binding energy of 200 kJ/mol^[111] occurs via the reaction



EQUATION 3.1-1 Reaction equation of the adsorption of thioalkanes on a gold surface^[112]. R – long alkyl chain.

The freed electrons remain on the gold surfaces rendering it negatively charged during the adsorption of further thioalkanes^[112]. Despite many investigations the knowledge of the chemistry of the alkanethiolate-Au bond is still incomplete^[113], even though it is the most investigated bond underlying the formation of self-assembled monolayers (SAMs).

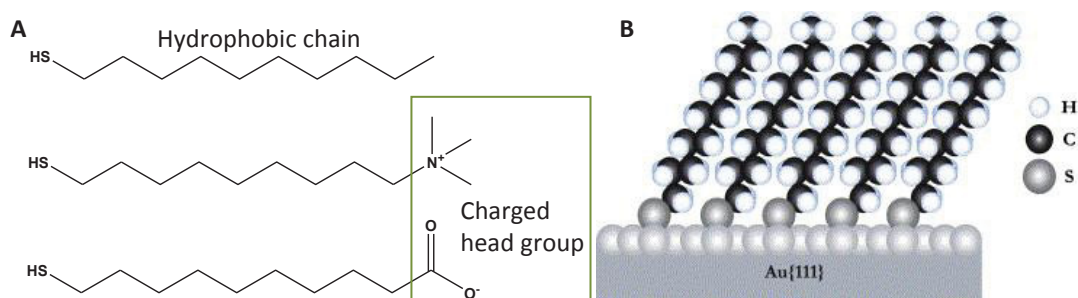


FIGURE 3.1-3 Functionalized ligands form self-assembled monolayers on metallic surfaces: **A** Thiol ligands possessing a hydrophobic chain, which can be unfunctionalized and completely hydrophobic as well as bifunctional bearing terminal functional groups of cationic or anionic nature. **B** Schematic illustration of an n-dodecanethiolate monolayer self-assembled on an atomically flat gold substrate^[110].

Using compounds with electron-rich head groups containing e.g. oxygen or nitrogen atoms attached to an n-alkyl tail^[110] supramolecular self-assembly processes occur, leading to the formation of M-OR or M-NR bonds on the metallic nanosurfaces. Depending on the affinity between the used compound and metal the formation of polar covalent or ionic bonds can be observed. The different affinities between adjacent molecules and the surface can lead to competition between different ligands permitting a ligand exchange^[114]. Murray and co-workers^[115] have shown that ligand exchange reactions are place-exchange reactions, which aim at the establishment of an equilibrium between different ligands on the particle surfaces and in solution. The ligand exchange process reaches its equilibrium at long reaction times. If the ligands are similarly structured the equilibrium constant is close to 1^[114]. The mechanism of ligand exchange is quite complex and difficult to predict and can be achieved by the exchange of bound ligands with a large excess of free ligands in solution as well as by exchange with ligands bound on other nanoparticles.

The formation of a well-organized SAM on a nanoparticle surface is difficult to achieve. Even if the SAM is illustrated as perfectly ordered in most schematics, this image is far from reality^[110]. The

molecular shape and the nature of its terminal head group influence the molecular orientation of a functional thioalkane on a metal surface. Different binding affinities to terraces, edges or vertexes of the nanocrystals decrease the SAM ordering. The radius of curvature^[115] of metallic nanoparticles can also lead to decreased ligand packing densities. The supramolecular assembly of thiol ligands opens a wide range of potential applications in that the modified surfaces may work as protein selective biosensors^[116,117] or bacteria repellent surfaces^[118]. The ligand forming a SAM on nanoparticles is responsible for the stabilization of the modified particle in a corresponding solvent. Hydrophobic chains stabilize the nanoparticles in non-protic apolar solvents. Charged nanoparticles can be dispersed in polar solvents such as water.

3.2 Biofunctionalization of colloidal surfaces

When the surface of nanoparticles is brought in contact with biomolecules, they bind on or interact with the functional groups present on the particle. On the colloidal surface, acting as a frontier between inorganic, organic and biological materials, different types of interactions or binding^[106] can take place (see **FIGURE 3.2-1**). The labeling of biomolecules can be implemented by the creation of noncovalent interactions between the nanoparticle and its target as well as by a covalent attachment of biomolecules to colloidal surfaces. Covalent binding of a biomolecule can be achieved by the use of a bifunctional linker. This type of linkage can be applied to bind many different kinds of biomolecules as DNA or proteins. Non-covalent binding of biomolecules by physicochemical interactions such as electrostatic and van der Waals interactions is equally efficient. Van der Waals interactions take place on a short distance of several nanometers. They are less strong than electrostatic interactions, which can take place at a distance of about 100 nm^[106]. Nature combines these physicochemical interactions as well as steric requirements of proteins to create non-covalently interacting systems like antibody/antigen or enzyme/substrate couples like the streptavidin/biotin couple. The interaction of these compounds follows the so-called “key/lock principle”^[72]. It is highly specific and very affine due to avidity between the key and its lock.

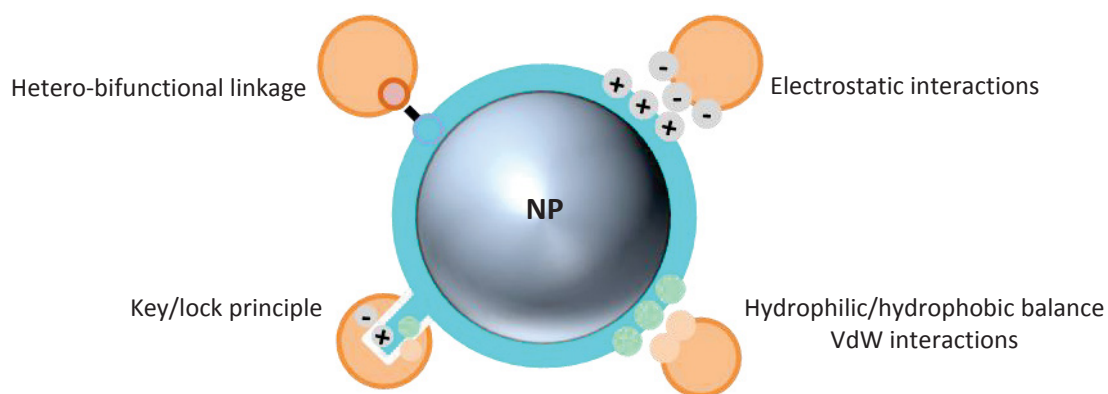


FIGURE 3.2-1 Schematic illustration of the possibilities for attaching a biomolecule to an inorganic surface: a biomolecule can be covalently attached by hetero-bifunctional linkage. The attachment can also occur by non-covalent binding via electrostatic, hydrophilic or hydrophobic interactions and via a key/lock principle.

a) Covalent linkage of biomolecules to nanoparticles

Biofunctionalization of a nanoparticle by the covalent attachment of a bioactive molecule is often achieved by the use of a bifunctional linker (see **FIGURE 3.2-2**). A distinction can be made between a homo-bifunctional and hetero-bifunctional linker molecules. Pardo-Yissar et al.^[119] used glutaric dialdehyde as homo-bifunctional linker to conjugate the enzyme acetylcholine esterase (AcChE) to CdS nanoparticles, which have been previously aminated with cysteamine. They employed the AcChE/CdS nanoparticle as a photoelectrochemical sensing system of enzyme inhibitors. Pierrat et al.^[120] used homo-bifunctional PEG-bis-thiol to conjugate the functionalized biotin N-[6-(Biotinamido)hexyl]-3'-(2'-pyridyldithio)propionamide to gold nanorods, permitting the immobilization of streptavidin labeled colloids on their surface. They claim that the biotinylated gold nanorods are well suited for the self-assembly of nanostructures and single-molecule labeling. In a two-step reaction Das et al.^[121] conjugate folic acid to iron oxide nanoparticles. First they conjugate folic acid to the linker 2,2-(ethylenedioxy)ethylenediamine in anhydrous DMSO with pyridine and dicyclohexyl carbodiimide and subsequently link the functionalized folic acid to a carboxylated nanoparticle with the use of 1-ethyl-3-(3-dimethylamino)-propyl)carbodiimide (EDC) and *N*-hydroxy succinimide (NHS). The functionalization of a nanoparticle with a folate group permits the binding of these particles to cancerous cells^[122], which are over-expressing folate receptors situated in their cellular membranes.

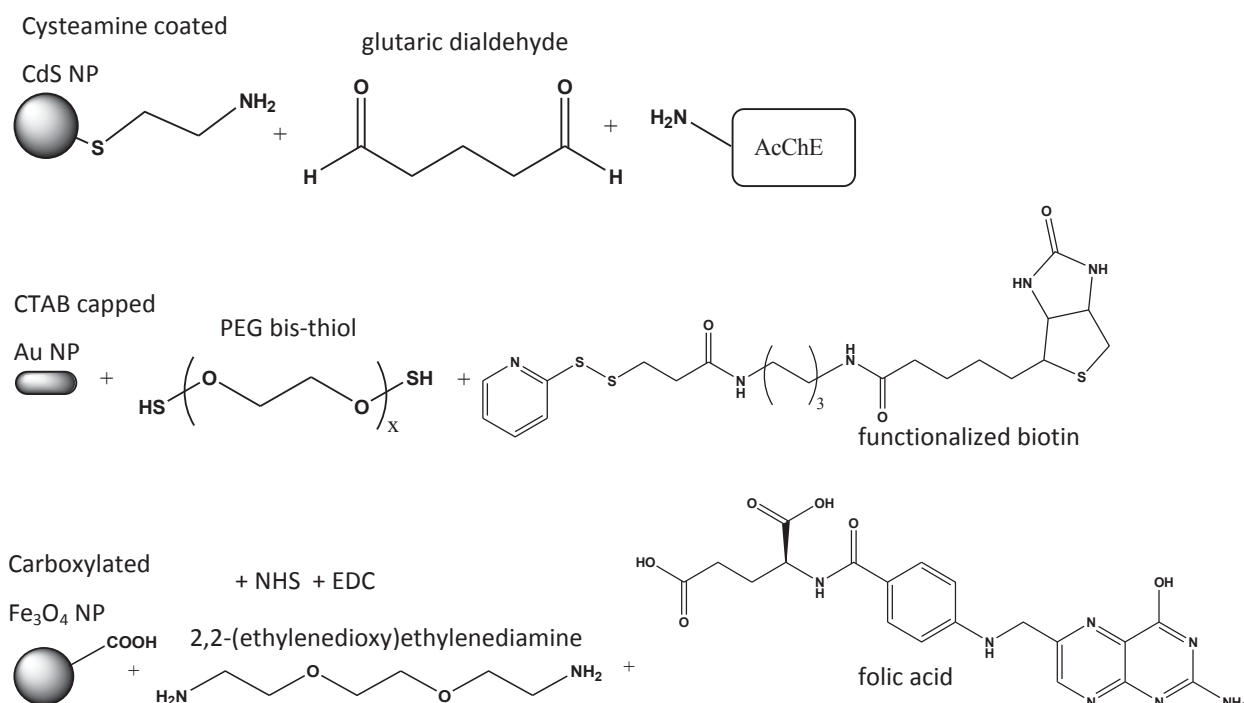


FIGURE 3.2-2 Bioactive molecules are conjugated to different nanoparticles by the use of homo-bifunctional linkers.

The possibility of covalent linking of a biomolecule to an inorganic surface by the use of a hetero-bifunctional linker is particularly attractive due to the fact that a hetero-bifunctional linker may be

reacted chemoselectively with amines on the first molecule and then conjugated to a thiol containing second molecule in a highly controlled manner. It was first executed by Chan et al.^[123], who linked a protein to a ZnS-coated QD by the use of mercaptoacetic acid as hetero-bifunctional linker. The grafting of folic acid on a nanoparticle via the reaction of its succinic anhydride N-hydroxysuccinimid folate with an amine function on the surface of a magnetite nanoparticle using 2-aminoethyl phosphonic acid as a linker is a further example. The phosphonic acid group reacts on the iron oxide surface, whereas the amine function conjugates to the folate NHS ester^[121]. However, with regard to conjugating antibodies on nanoparticle surfaces Bieniarz et al.^[124] showed that the use of long linking molecules as the 30-atom long linker 4-[(2,5-Dihydro-2,5-dioxo-1H-pyrrol-1-yl) methyl]-N-[6-[[[6-[(2,5-dioxo-1-pyrrolidinyl) oxy]-6-oxohexyl] amino]-6-oxohexyl] amino]-6-oxohexyl] cyclohexane carboxamide leads to an increased activity of conjugated antibodies in comparison to antibodies covalently bound to a microparticle by the use of a short linker (9 atoms) (see FIGURE 3.2-3).

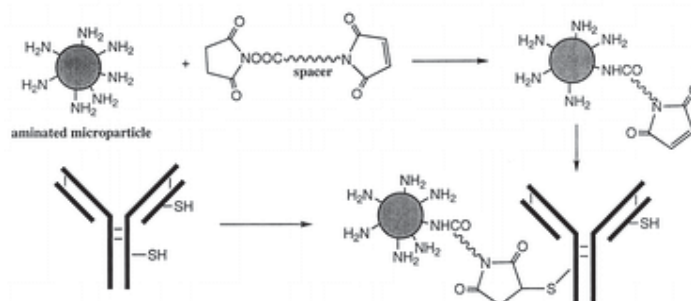


FIGURE 3.2-3 Nanoparticles were conjugated to a IgG antibody with an hetero-bifunctional linker for binding through active ester carbonyl-amine and maleimide-thiol bonds. Depending on the spacer the linker can vary in its length from 9 to 30 atoms^[124].

Mirkin et al.^[125] functionalized gold nanoparticles with thiolated single stranded DNA permitting them to assemble the gold nanoparticles via their functionalizing DNA strands using complementary oligonucleotide sequences, which hybridize to the DNA strands and serve as linkers (see FIGURE 3.2-4). This technique permits them to obtain crystalline 3D assemblies of the modified gold nanoparticles.

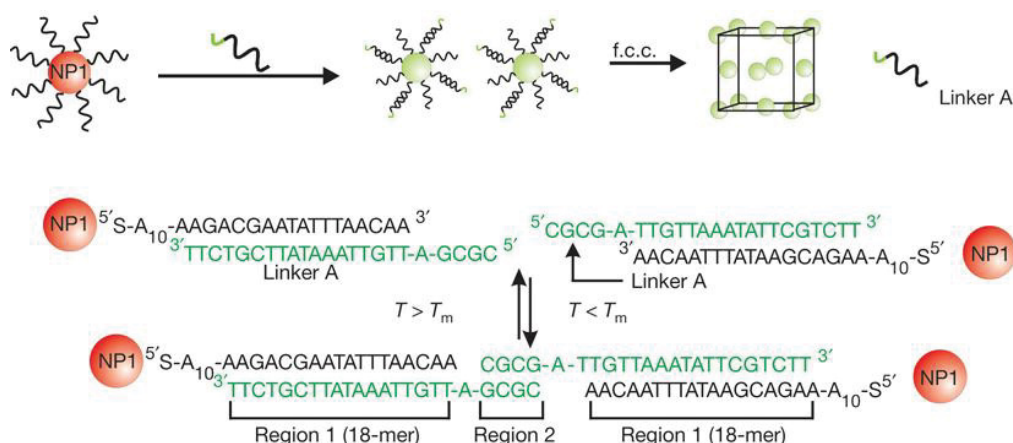


FIGURE 3.2-4 DNA strands function as a linker hybridizing with single strand DNA, which is covalently bound to nanoparticles^[126].

b) Adsorption of biomolecules by physicochemical interactions

Proteins, peptides and other biomolecules can adhere on colloidal surfaces due to physicochemical interactions. Electrostatic interactions, hydrophilic/hydrophobic balance effects as well as van der Waals forces and the formation of hydrogen bonds can attach a biomolecule to a nanoparticle surface. The interactions taking place depend on the physicochemical properties of the nanoparticle surface as well as on the composition of the biomolecule. Puddu et al.^[127] showed that at pH 7 three peptide sequences adsorb to silica surfaces due to the action of different forces (see FIGURE 3.2-5). The positively charged sequence P1 adsorbs due to electrostatic forces on negatively charged silica surfaces. The adsorption is entropically driven by the release of Na⁺ counterions and water molecules from the silica surface. Sequence P2 (AFILPTG) has a pI of 6 and is mainly constituted by nonpolar amino acids resulting in an overall hydrophobic character. Its adsorption is due to vdW interactions, pH independent and driven by the dehydration of hydrophobic areas on the silica, which interact with the hydrophobic peptide sites. Adsorption of the negatively charged peptide 3 must originate from hydrophobic interactions and hydrogen bonding. These non electrostatic forces need to overcome electrostatic repulsion, which has been observed at high peptide concentrations. Peptide P1 binding to silica via electrostatic interactions is released at pH 2.1, while the silica binders P2 and P3 interacting via non-electrostatic interactions stay on the surface.

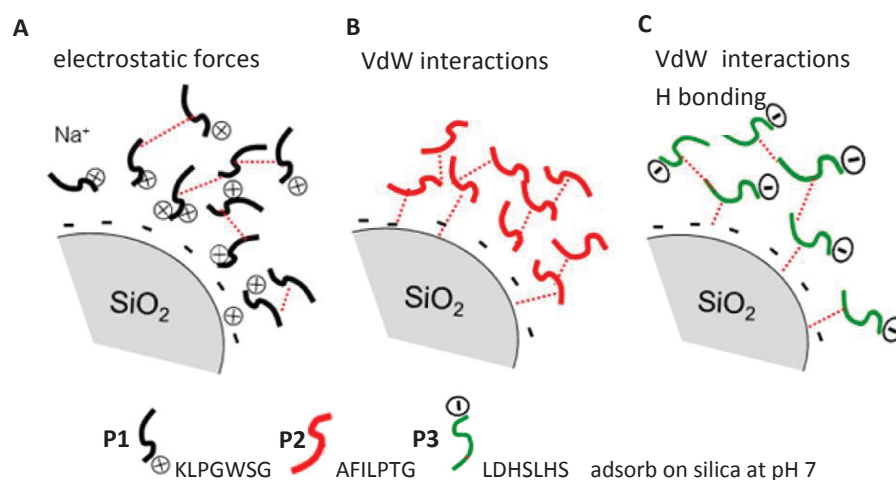


FIGURE 3.2-5 The adsorption of peptides with different sequences and properties to a same silica surface is due to different physicochemical interactions^[127].

Electrostatic interactions also govern the adsorption of polyelectrolyte multilayers (PEMs) on a substrate as well as the formation of supported lipidic bilayers on such polymer cushions. Mulligan et al.^[128] elaborated PEM films of alternating layers of chitosan (CHI) and hyaluronic acid (HA) on a silicon substrate. Subsequently they formed a supported lipidic bilayer of the lipids 1,2-dioleoyl-sn-glycero-3-phosphocholine (DOPC), egg sphingomyelin, cholesterol and 1,2-dipalmitoyl-sn-glycero-3-phosphoethanolamine-N-[methoxy(polyethylene glycol)-2000] (PEGDPPE) via non electrostatic VdW interactions in the presence of high salt concentration on the polyelectrolyte multilayers (see FIGURE 3.2-6).

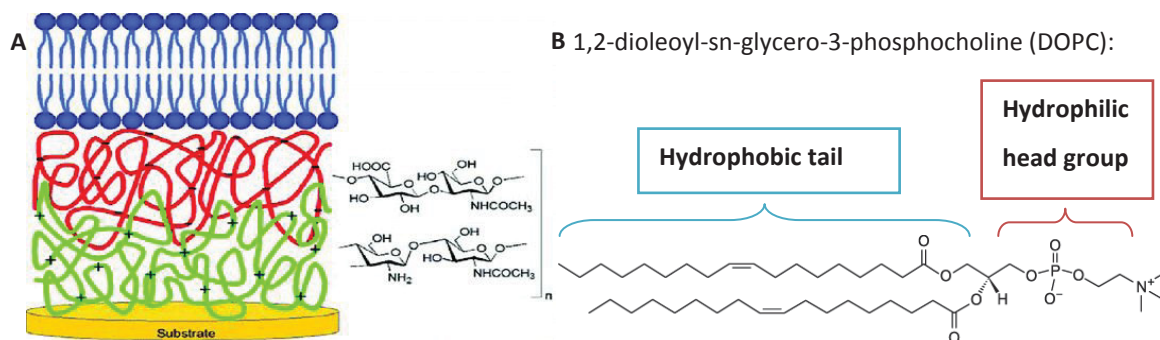


FIGURE 3.2-6 **A** Schematic illustration of a supported lipid bilayer formed on a multilayer of polyelectrolytes. **B** Structural example of an amphiphilic phospholipid; it can be divided into a hydrophilic head and a hydrophobic tail group.

Lipid bilayers are made of two layers of amphiphilic phospholipids, in which the hydrophobic parts are oriented inwards^[98]. Such SLBs therefore form solely on hydrophilic surfaces^[129]. Depending on their lipidic composition artificial SLBs can mimic different membrane compartments and act as a platform for the incorporation of membrane proteins^[130] or further modifications of the surface. In addition, the assembly of a SLB on a multimodal nanoparticle not only makes it possible to render a biomaterial biocompatible but also the labeling and tracking of lipophilic bioentities. A nanoparticle-supported lipid bilayer is usually formed by the interaction of small unilamellar vesicles (SUV) with nanoparticles of interest^[131] (see **FIGURE 3.2-7**).

The assembly process takes place in aqueous conditions. The mechanism of the SLB formation occurring has been described by Richter and co-workers^[132]. It has been shown that, due to electrostatic interactions, the rupture of cationic SUV consisting of 1,2-dioleoyl-3-trimethylammonium-propane (DOTAP) occurs spontaneously, when they come in contact with a hydrophilic, negatively charged silica surface^[132]. It has been shown that under conditions which promote van der Waals forces the vesicles adsorb first on the silica surface and that the rupture leading to the formation of a solid supported lipid bilayer occurs only if critical coverage of the silica surface by adsorbed vesicles is obtained^[129].

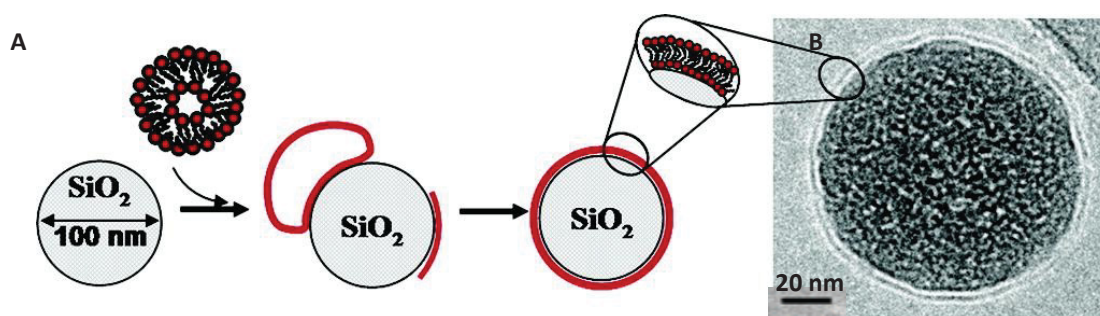


FIGURE 3.2-7 Supported lipid bilayers form on hydrophilic surfaces as silica surfaces. **A**: Schematic illustration of the formation of a supported lipid bilayer on a silica nanoparticle. **B** Cryo-TEM picture of a supported lipid bilayer on a silica nanoparticle^[98].

Handley et al.^[133] used physicochemical interactions to adsorb low density lipoproteins (LDL) on gold nanoparticles. Around a 19 nm sized gold sphere they observed the adsorption of approximately eight

LDL proteins. They used the colloidal gold-LDL conjugate as a probe to investigate lipoprotein receptor dynamics. Furthermore it was observed that in physiological media such as serum or other body fluids material surfaces are generally covered by proteins of the physiological environment, which form a protein corona around the particle and influence their further interactions with cell material^[134]. It has been shown that the adsorption of bovine serum albumin (BSA), myoglobin (Mb) and cytochrome c (CytC) on gold nanoparticles leads to the formation of protein adsorption layers consisting of an irreversibly adsorbed fraction and a reversibly adsorbed fraction depending on the equilibrium binding constants of the proteins to the surface^[134]. The exchange between proteins in physiological media and proteins adsorbed to a nanoparticle depends on a complex function of the protein affinity for the surface, curvature effects from the surface and changes in the surrounding medium.

c) Specific non-covalent binding of biomolecules following the key lock principle

To achieve a more specific interaction between a nanoparticle and a biomolecule Ling et al.^[135,136] used the formation of complex bonds, which are stronger than ionic bonds resulting from electrostatic interactions, between ferrocene or adamant and β -cyclodextrin to precisely assemble a supramolecular 3D nanostructure. Abad et al.^[137] functionalized gold nanoparticles to bear a amino-nitrilotriacetic-Co(II) complex (ANTA-Co²⁺) on their surface which specifically interacts with the histidine tag, which is often used to tag a protein of interest. The strong interaction between His tag fused proteins and nanoparticles modified with Ni²⁺-NTA (nitrilotriacetic acid) can be used to achieve self-assembled protein nanoparticle structures as observed by Hu and co-workers^[138], who assembled His tag fused Ad12 knob proteins around gold nanoparticles of different sizes (see **FIGURE 3.2-8**).

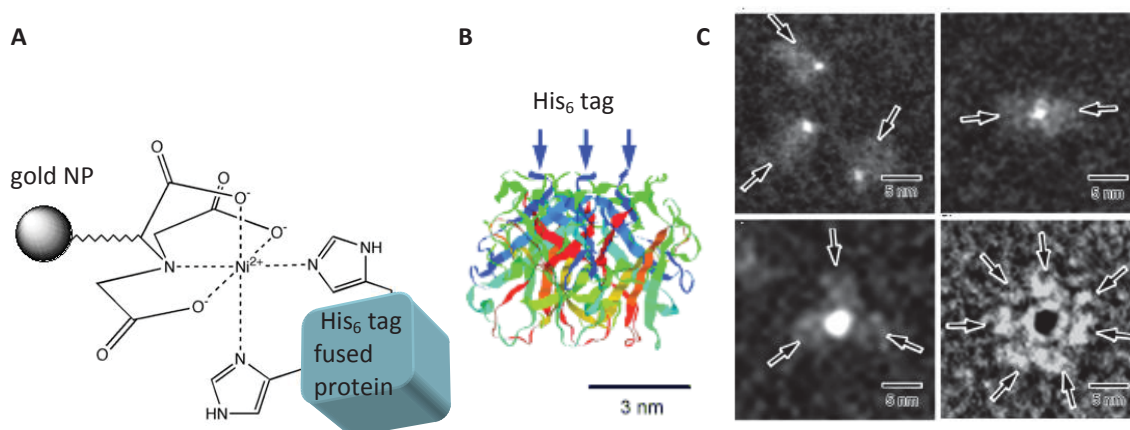


FIGURE 3.2-8 Nanoparticle protein assemblies held by Ni²⁺-NTA-histidine complexes. **A:** The Ni²⁺-NTA-histidine complex links a gold nanoparticle to a His₆ tag labeled protein. **B:** Protein structure of the His₆ tag labeled Ad12knob protein **C:** The His₆ tag labeled Ad12knob protein is assembled around Ni-NTA complexes bearing gold nanoparticles. Depending on the nanoparticle size a different number of proteins assemble around the gold spheres^[138].

A surface-bound protein can continue to interact. Such binding is non-covalent and obtained by electrostatic, van der Waals interactions and hydrogen bonding of different protein domains.

Protein-protein interactions such as antibody-antigen interactions are also used for directed self-assembly of labeled nanoparticles. Antibody-antigen interactions have the advantage of being highly specific and guaranteeing a strong binding as they possess binding constants from 10^8 to 10^{11} M^{-1} . Chen et al. show that directed self-assembly can be used to fabricate molecular junctions in which an antibody molecule (Ig G) binds to two gold nanoparticles^[139].

Proteins may interact with a substrate, which specifically binds to a binding pocket of a nanoparticle attached protein. Protein domains are organized in a tertiary native structure due to hydrogen bonding and van der Waals interactions between their composing amino acids leading to the formation of hydrophilic or hydrophobic regions in the domain. The tertiary protein structure influences the way of interaction with another molecule by the addition of a steric factor. An enzyme domain might form a binding pocket for a substrate for which it shows specificity not only due to electrostatic and electrodynamic interactions but also due to its conformation which promotes interactions only with a substrate molecule which fits perfectly into the offered binding pocket. The non-covalent binding of biotin to the 60 kDa protein streptavidin is the strongest non-covalent interaction known in nature with a dissociation constant K_d of 10^{14} to 10^{15} M^{-1} ^[140].

The protein streptavidin is sub-divided into four equal domains, which are each able to bind a biotine molecule. It may be used to create a specific interaction between a nanoparticle and its target by the attachment of streptavidin to the particle and biotin to the target (see FIGURE 3.2-9). This system has been applied to bind CdSe QDs on a DNA origami scaffold^[141], to assemble biotinylated gold nanorods with avidin coupled gold spheres^[120], or to bind streptavidinylated alkaline phosphatase on biotinylated magnetoliposomes^[142].

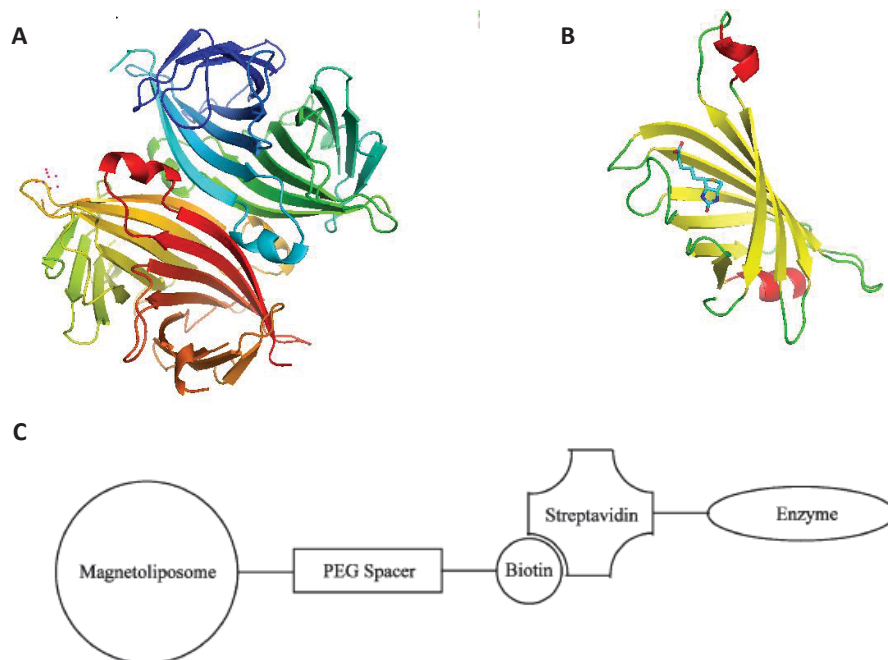


FIGURE 3.2-9 Structure and use of the streptavidin biotin couple. **A:** Protein structure of the native streptavidin tetramer^[143] **B** Protein structure of the streptavidin monomer interacting with a biotin molecule^[140]. **C:** Scheme of magnetoliposomes functionalized with biotin, which interact with an enzyme fused streptavidin domain^[142].

A further protein couple which interacts with high avidity consists of the two proteins barnase (12 kD) and barstar (10 kD) from *Bacillus amyloliquefaciens*. They interact strongly and specifically, possess a binding constant of 10^{14} M^{-1} and are, in contrast to the biotin/streptavidin couple, not naturally present in the blood and tissue of mammals. Their small sizes are equally advantageous for use as fusion proteins as done by Nikitin and co-workers^[144], who fused antibody 4D5scFv fragments to the N- and C-terminus of barnase by gene engineering methods. The labeling of magnetic nanoparticles with barnase and Qdot® 605 quantum dots with barstar permitted them to create protein-directed assemblies of the labeled nanoparticles and biofunctionalizing scFv antibody fragments (see FIGURE 3.2-10), which are useful as targeting moieties in selective delivery applications.

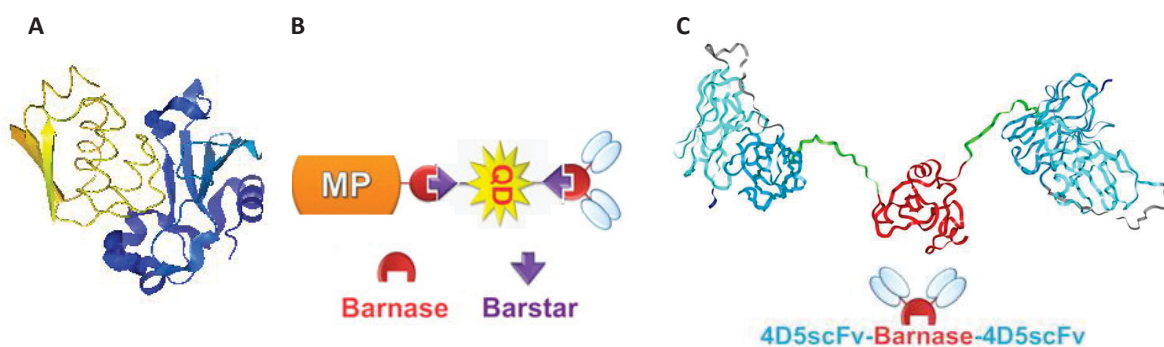


FIGURE 3.2-10 The proteins barnase and barstar can be used to assemble fused proteins and protein labeled nanoparticles. **A:** Protein structure of the interacting barnase (yellow)/barstar (blue) couple^[145] **B:** Schematic of barnase labeled antibody short chains and magnetic nanoparticles (MNP) which assemble on barstar-labeled quantum dots (QD) **C:** Protein structure of the barnase (red) fused 4D5scFv antibody fragments (blue)^[144].

Mazzucchelli et al.^[146] used a similar strategy to preserve the activity of an IgG antibody presented on a nanoparticle surface. They covalently bound the protein A possessing a binding specificity for IgG antibodies to a nanoparticle surface via the trifunctional linker synthesized out of N-phosphonomethyl iminodiacetic acid phosphonate (PMIDA), the bifunctional diaminolinker 2,2-(ethylenedioxy)bis(ethylamine) (EDBE) and N-succinimidyl-3-[2-pyridyldithio]-propionate (SPDP) via N-hydroxysuccinimidyl ester (NHS) activation. The antibody then bound via its Fc fragment to the thiol-engineered recombinant protein A variant spaBC3 (see FIGURE 3.2-11).

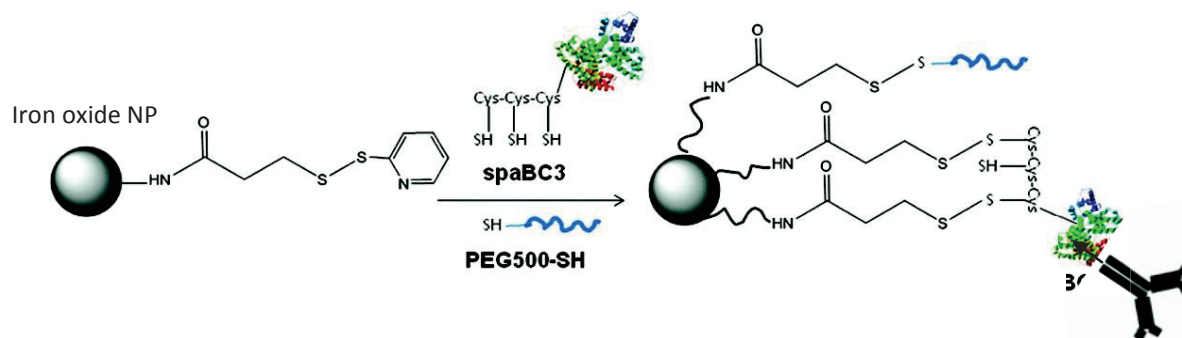


FIGURE 3.2-11 A trifunctional linker is used to synthesize pegylated iron oxide NPs, which bear a protein A variant destined to bind IgG antibodies^[146].

Depending on the natures of a particle and of its biological target various actions can be implemented to yield the biofunctionalization of an inorganic colloid. Different particles, surface modifications and interactions can be chosen and applied to create biofunctional nanosystems.

3.3 The biological fate of nanoparticles destined for theragnostic applications

A nanoparticle introduced to a living biologic system such as cells, tissue or whole organisms needs to be biocompatible and biostable. Biocompatibility means that the nanoparticle interacts with the biological system without showing harmful behavior such as causing oxidative stress and various toxicities including cardiac and hepatic toxicity. The intrinsic toxicity of a nanoparticle is determined by multiple factors such as its size, surface coatings, administered particle dose and the toxicity of its biodegradation metabolites. In consideration of its future application it needs to be determined for each nanoparticle system^[147]. Nanoparticles can be administered by different ways as oral administration, injection to tissues or to the blood circuit. They need to be protected from biological clearing mechanisms.

Nanoparticles injected into the blood circuit are eliminated by the mononuclear phagocyte system, equally known as the reticuloendothelial system, which is destined to eliminate foreign bodies from circulation. To enhance their lifetime in the blood compartment a nanoparticle should hide from recognition by the different types of phagocytes as monocytes circulating in the blood, the Kupfer cells located in the liver and macrophages located in spleen or lung alveoli. These cells particularly capture objects adsorbed to opsonin proteins recognizing them via receptors on their surface^[8].

Opsonins preferably adsorb to hydrophobic surfaces with low curvature. The adsorption of an opsonin to a nanoparticle and the resulting facilitation of its uptake to phagocytes is called opsonization and can be prevented by the chemical modification of the particle surface^[147]. Several surface coatings have been implemented to obtain particles possessing a so-called “stealth shielding”, which means that the compound grafted to the colloidal surface protects the nanoparticles from opsonin adsorption and subsequent fast recognition by a biosystem to enhance their lifetime. Surface modification with polysaccharides, poly(acrylamide), poly(vinyl alcohol) and with PEG or PEG co-polymers show this usefulness^[8,148,149]. These polymers form dense, hydrophilic clouds of long flexible chains on the surface of colloidal particles and prevent the adsorption of opsonins on the particle surfaces (see **FIGURE 3.3-1**) and subsequently their uptake by monocytes or macrophages^[148].

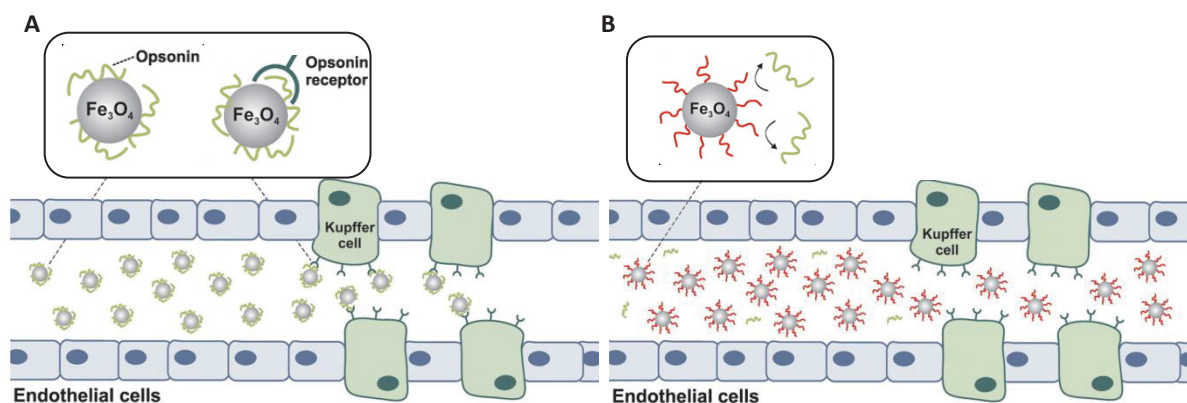


FIGURE 3.3-1 PEGylated nanoparticles are protected from biorecognition and digestion. **A:** Nanoparticles are adsorbed to opsonin proteins, hence recognized and captured by macrophages for transit to the liver. **B:** Nanoparticles coated with PEG coating are prevented from opsonization, resulting in decreased macrophage uptake and following accumulation in the liver. The coating increased the availability of the NP for imaging or therapy^[148].

A second strategy for obtaining biocompatible surfaces is the modification of their surface, following the aim to render it similar to naturally existing biosurfaces. The design of the colloidal surface imitating natural surfaces is called biomimetic^[150]. To render a surface similar to a biologic system it is possible to achieve the coverage of a biomaterial with biomolecules. It can be obtained by the formation of solid supported lipid bilayers (SLB)^[131] composed of phospholipids, which are one constituent of natural membranes.

4. THE CONTEXT OF THE STUDY

As we have already mentioned in the previous sections, there are many possibilities for employing multifunctional nanoparticles to localize and follow biomolecules such as e.g. proteins, lipids or DNA *in vivo* and *in vitro*. In the following we will discuss one problem, which is interesting to investigate by multimodal imaging – the following of the internalization of therapeutic DNA into living cells.

4.1 The exploration of the transfection of therapeutic DNA into living cells

The internalization of therapeutic DNA to living cells can lead to therapies for cancer, cardiovascular or monogenic inherited diseases^[151]. A first challenge is the incorporation of high amounts of DNA into the cell nucleus. This is considered to be necessary, because the delivered DNA can be lost or damaged during the transfection process. The increase of the transfected DNA amount is intended to enhance the chance that intact DNA is internalized to the cell nucleus, where it can be translated, transcribed and gene products expressed. Too little expression of the transcribed genes can be responsible for the non efficiency of a gene therapy. The transfection efficiency depends on the transfecting agent serving as a vector for the therapeutic DNA construct and on the mechanism of the internalization and transfection process^[100]. To visualize and understand these mechanisms multimodal bioimaging tools can be applied.

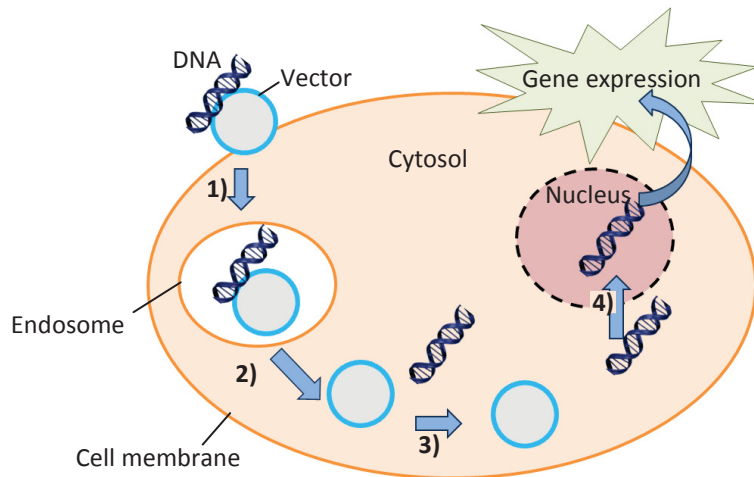


FIGURE 4.1-1 Schematic pathway of DNA-transfection by endocytosis: **1)** Endosomal uptake of vector bound DNA; **2)** Endosomal escape of vector and DNA; **3)** Migration through the cytosol, DNA release from the vector; **4)** Nuclear uptake of DNA and gene expression inside the nucleus.

The cellular uptake of transfected DNA is commonly accomplished by endocytosis (see **FIGURE 4.1-1**). Carriers are internalized to cationic lipid vesicles, which are formed out of the lipidic cell membrane. They are called endosomes and transport the foreign vectors through the cell until the end of their life cycle, when they fuse with lysosomes^[152]. Lysosomes are vesicles produced in the golgi apparatus, they have a lower acidic pH in their interior and are mainly responsible for the digestion and degradation of no longer required compounds. For this purpose carrier systems need to escape the endosome before its fusion with a lysosome to avoid degradation. Several strategies have been developed to induce the rupture of endosomes. The introduction of vector materials causing a so-called proton-sponge effect, which induces that a vesicle rupture occurs due to an osmotic pressure caused by buffering carrier materials such as PEI, is one example^[153]. Released to the cytosol a vector system needs to approach the cell nucleus, which is the destination of the therapeutic gene. The viscosity of the cytoplasm is so high that diffusion through the cytosol is effected four times slower than the diffusion of water. Crossing the cytosol the vector system should be prevented from aggregation with proteins.

One of the most critical and least understood steps of a successful transfection of therapeutic DNA is the last one – the internalization of the DNA into the nucleus. Different ways of internalization seem to be possible depending on the type and size of the vector system^[154]. First molecules or particles smaller than 9 nm may diffuse through pores in the nucleus. Secondly systems up to 25 nm may be internalized by the formation of nuclear pore complexes. Thirdly DNA transported by bigger vector systems may be enclosed in the nucleus during the period of cell division.

The uptake of DNA is a complex and complicated process: all steps have to be successful to guarantee the transcription of the DNA and the final expression of a therapeutic gene product. We suppose that the more DNA is introduced, the more likely it is that the expression of genes and subsequently the gene therapy of a patient will succeed. To advance the transfection efficiency of non-viral vector systems we need to understand at which step the DNA transfection by a vector fails. We need a total understanding of the transfection pathway and the occurring internalization mechanisms of DNA to

the cell and to the nucleus to improve the vector's capacity to pass them. As a matter of course the internalization mechanism is highly dependent on the vector composition.

4.2 Condensation of DNA to functionalized nanoparticles

DNA is a semi-rigid, negatively charged macromolecule. It is a stiff strand which is built up by a negatively charged deoxyribose-phosphate backbone. The nucleobases adenine, thymine, guanine and cytosine are attached to the backbone via the deoxyribose entities. They form hydrogen-bonded base pairs which keep two DNA strands together in a helical conformation. One helical turn contains 10 base pairs and turns over a pitch of 3.4 nm^[155]. The charged phosphate groups in the DNA-backbone are 0.17 nm distant from each other and repulse themselves. This electrostatic repulsion contributes significantly to the stiffness of a DNA-double-helix. Equalizing the charges makes it possible to render a DNA strand more elastic, so that it can be stored in a compact form^[156] (see **FIGURE 4.2-1**). The compact charge neutralized form of DNA is referred to as “condensed” DNA^[157]. The condensation of DNA induced by small cationic ligands is called Manning Condensation with reference to Gerald Manning, who described the physicochemical characteristics of ion clouds surrounding charged cylindrical structures^[158].

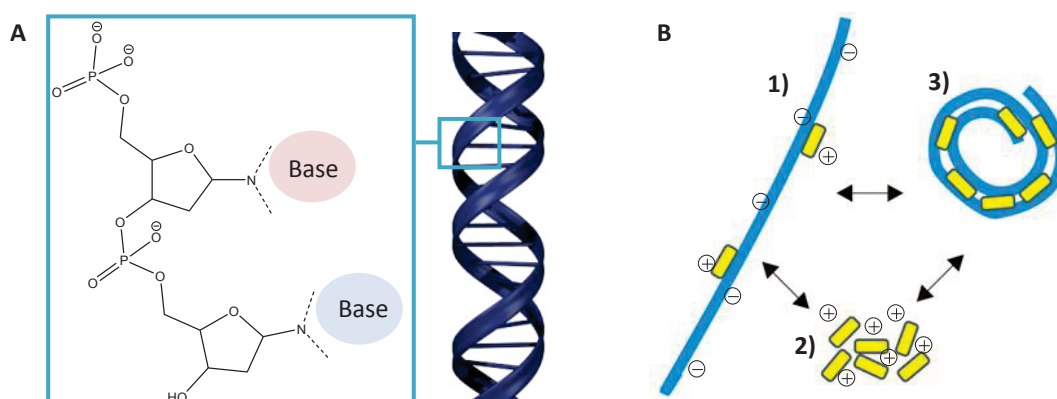


FIGURE 4.2-1 The scheme illustrates the condensation of DNA by small cationic molecules. **A:** Structural element of the deoxyribose phosphate backbone illustrating the presence of negative charges in the DNA backbone, which render the DNA macromolecule stiff and keep it in a linear form. **B:** The negatively charged DNA strand (1) is stretched due to repulsive charges. Small cationic ligands (2) may induce DNA condensation (3) *in vitro*. This process is used to model DNA compaction^[157].

Ghosh and co-workers^[159] assembled DNA and monolayer-protected gold nanoparticles bearing positively charged head groups to form DNA nanoparticle complexes with sizes smaller than 100 nm. The naturally occurring polyamines spermine and spermidine are often employed to artificially condense DNA^[157]. In the presence of such condensation agents double-stranded DNA plasmids condense in sophisticated structures like rods or toroids^[160] (see **FIGURE 4.2-2**). Cationic phospholipids also condense DNA to such small particles. Cationic lipids like 1,2-dioleoyl-3-trimethylammonium-propane (DOTAP) are used to complex DNA by the formation of lipoplexes. These structures are formed via the self-assembly of DNA and cationic liposomes^[161]. Their size varies from 200 nm to 1 μm . The structure of these complexes has been described as a higher-ordered multilamellar lipidic

structure with rod-shaped DNA sandwiched between cationic lipid bilayers. The cationic lipids forming these DNA-lipid complexes act as transfection agents for therapeutic DNA^[152].

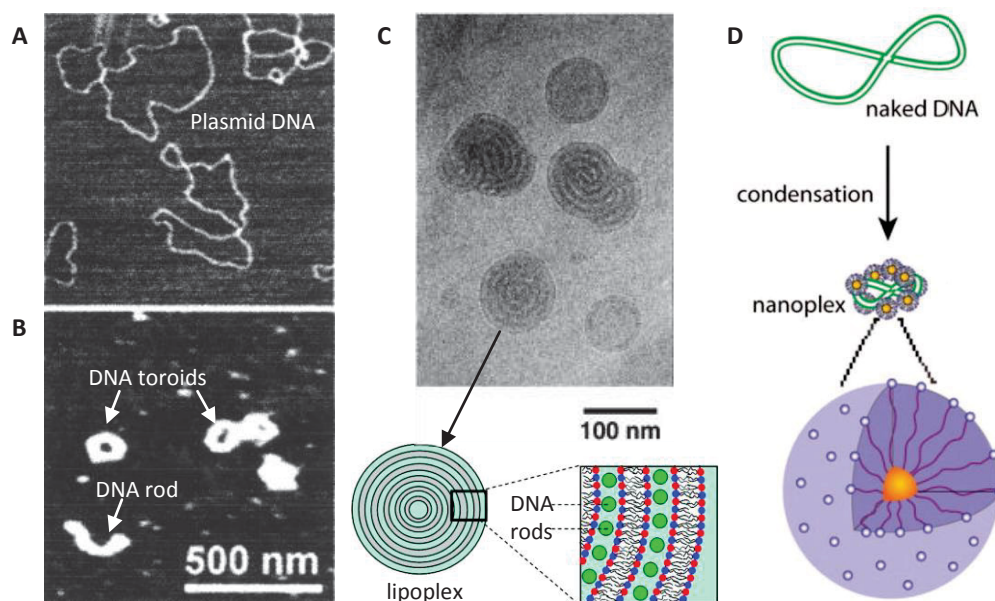


FIGURE 4.2-2 DNA can be condensed by different condensation agents and shows various morphologies. **A:** AFM picture of uncondensed plasmid DNA^[160]. **B:** AFM picture of plasmid DNA condensed to rods or toroids by the use of a polylysine^[160]. **C:** DNA condensed to lipoplexes by cationic lipids - the DNA is condensed to rods with intercalate between lipid sheets^[162,163]. **D:** DNA condenses around positively charged gold nanoparticles to form nanoplexes of about 100 nm size^[159].

The DNA transfection efficiency of a lipoplex is strongly dependent of its lipidic composition, which influences its formation and structuring of the lipoplex and equally the mechanism of cell entry. The endocytosis pathway taking place during the internalization of lipoplexes depends mainly on their shape, lipidic formulation and the cell type^[163]. The release of lipoplexes from endosomes also depends on the composition of the lipoplex. The mechanisms of DNA transfection by cationic lipids are still indistinct. Particularly the transition of lipoplexes through the cytosol and the nuclear uptake of DNA are not fully described.

A study carried out by the collaborating group of O. Lambert employed amine groups bearing nanoparticles synthesized in our group to follow the intracellular path of DNA to the nucleus. They observed a dissociation of the DNA from the nanoparticles in the cytosol, probably due to the competition with polyanions and polycations in the cytosol concerning electrostatic interactions and a subsequent internalization of the DNA to the nucleus^[164].

4.3 Strategies to functionalize nanoparticles destined for DNA labeling

The labeling of DNA by a nanoparticle needs to be done by a non-covalent DNA binding, which allows the release and the expression of DNA in the nucleus. To modify the surface of a nanoparticle to make it attractive to DNA the choice of a functionalization reagent, which once grafted renders the particle surface positively charged, is necessary. To follow all the steps of the DNA transfection to the

cell nucleus it is necessary to modify the surfaces of multimodal nanoparticles in a way which allows the strong binding of DNA to the labeling colloids. Only strongly bound DNA can be followed to the nucleus without desorption from the labeling nanoparticles in the cytosol.

For modifying nanoparticles to attract DNA, the challenge to fix as many positive charges as necessary for the condensation of DNA on a particle surface has been addressed by several strategies. The functionalization reagents, which are chosen most often, are implementing amines, polyamines or quaternary ammonium groups on the particle surfaces. An alternative to these compounds are phosphonium groups containing macromolecules^[165].

Amine-modified particles interact with DNA. Their efficiency as DNA delivery agents has been tested^[166] and it has been shown that the adsorption of the DNA on the nanoparticles prevents it from enzymatic cleavage *in vitro* and in cellular environment^[167,168]. Magnetic aminosilane modified particles have been used for DNA purification assays^[169]. The amine functionalized particles can be further modified, e.g. through methylation of the amine groups^[170]. Covalent conjugation of single DNA strands has been done by del Campo et al.^[171], who used such modified Fe₃O₄@SiO₂ particles for separation assays. Fluorophore-doped silica NPs have been modified with aminosilanes to follow DNA-transfection and release by a FRET effect between the fluorescent nanoparticles and a dye intercalated into the adsorbed DNA^[172]. Using aminated nanoparticles to follow the DNA transfection in living cells, it has been shown that the DNA cannot be marked until it migrates to the inside of the nucleus and that it is probably released in the cytosol, where the nanoparticles have been located^[36].

Considering that compounds with high density of cationic charges are beneficial to future applications as a gene transfection agent, several groups have started to use polyelectrolytes or dendrimers for DNA condensation. Imitating the composition of histone proteins, which naturally condense DNA in the nucleus, arginine grafted polymers are popular agents for nanoparticle functionalization. Poly(L-lysine) or poly(D-arginine) derivatives have been tested as efficient coatings for nanoparticles aiming at DNA condensation on their surface. Arginine has been grafted on poly(amidoamines), poly(propylene imines) or poly(disulfideamines)^[173,174], cholesteryl-oligo-D-arginine and arginine modified chitosan have been synthesized and all these compounds show an enhanced affinity to DNA due to guanidinium groups possessing a pK_a of 12.1^[175]. Their positive charges make it possible to adsorb DNA efficiently under physiological conditions^[174]. Amine-terminated PEG-enrobed γ -Fe₂O₃ nanoparticles have been grafted with poly(Lysine), poly(Arginine) or poly(ethylene-imine) to interact with RNA or DNA^[175] (see FIGURE 4.3-1).

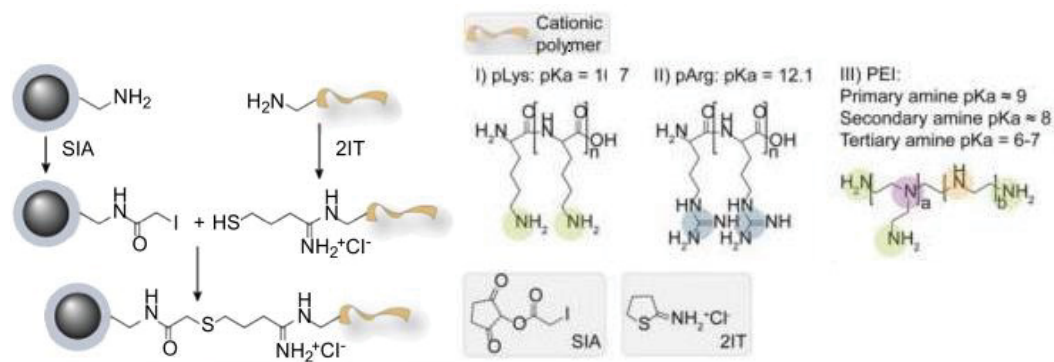


FIGURE 4.3-1 Schematic illustration of the modification of aminated nanoparticles with polyamines as pLys, pArg or PEI^[175]. The modified nanoparticles will interact with DNA after protonation.

Polymeric compounds like e.g. chitosan and trimethyl-chitosan carrying poly(ϵ -caprolactones) have been designed with the aim of building polymers accumulating a high number of positive charges. The lipophilicity of such polymeric compounds is welcome, because it facilitates the cellular internalization process^[176]. Several groups employ polyamidoamine dendrons (PAMAM) to bind DNA or RNA. Their capacity to bind DNA depends on the dendron generation and grows with an increasing arborization of the dendrimers, due to the multiplication of amine or ammonium groups containing residues^[177]. One of the most used polymeric compounds to bind DNA electrostatically is the cationic polyethyleneimine (PEI). It is advantageous because of its capacity to form DNA-polymer-complexes which even offer the possibility of achieving further modifications. Unfortunately an ascending cytotoxicity with increasing length of its polymer chain from a weight of 10 to 25 kDa needs to be controlled to achieve a beneficial outcome^[178].

To obtain cationic gold nanoparticles capable of interacting with DNA strands, a common strategy is their modification with thiol ligands bearing a trialkylammonium group by a ligand exchange reaction. Particles modified with a mixture of octanethiol and trialkylammonium-undecanethiol (see **FIGURE 4.3-2**)^[179] have been shown to be eight times as effective for transporting DNA as poly(ethyleneimine). In contrast to amine functions positive charges obtained from quaternary ammonium groups are pH independent.

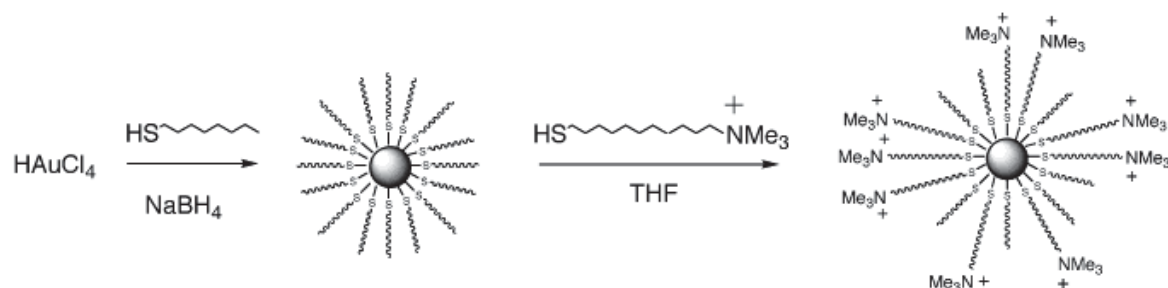


FIGURE 4.3-2 Gold nanoparticles bearing SAMs with quaternary ammonium functions designed to bind DNA: Fabrication and functionalization of gold nanoparticles has been achieved via the Brust and Murray reactions^[179].

Goodman et al.^[180] have shown that the length of the alkyl substituents of the trialkylammonium ions on the surface is important for their interacting with DNA. A comparative study of trialkylammonium ions substituted with methyl-, butyl- or hexyl-chains showed that the DNA adherence to these different compounds varies. Long chains like hexyl-chains seem to be too large to intercalate into the DNA-strands, whereas small residues such as the methyl-chains appear to be too short to benefit from hydrophobic interactions. It has been shown that combinations of long and short chains such as Me₂Hex or MeBu₂ interact the most with DNA strands^[180]. The ratio between hydrophobic and charged entities as well as their organization on the modified surfaces is decisive for the efficiency of the cell internalization and transfection^[181,182].

If they are sufficiently small particles modified with quaternary ammonium groups can intercalate in the DNA grooves to form an assembly resembling pearls on a string^[183] (see FIGURE 4.3-3). The formation of less linearly organized DNA-gold nanoparticle complexes is also possible^[159].

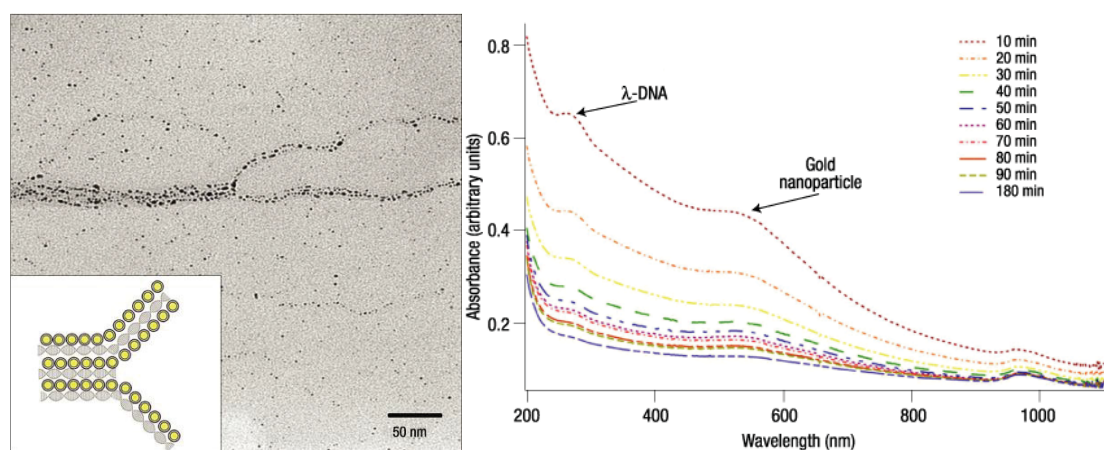


FIGURE 4.3-3 Supramolecular self-assembly of DNA and small gold nanoparticles modified with quaternary ammonium groups: **A** TEM micrograph of a branching portion of a nanoparticle/DNA assembly. It shows a representative example of a branched assembly; the nanoparticles assemble like pearls on a string. **B** A series of ultraviolet-visible spectra collected to monitor the interaction between the functionalized gold nanoparticles and the λ -DNA. The nanoparticles and λ -DNA cross-link to form a dark precipitate which accounts for the decrease in the absorbances of the two species. Spectra were collected every 10 min on a sample with a relative concentration of 7:1 nanoparticle:DNA^[183].

DNA binding on nanoparticles modified with quaternary ammonium groups has been described as sufficiently strong to inhibit the transcription of the complexed DNA^[179]. Goodman et al. have shown that quaternary ammonium groups provide not only a possibility to bind DNA via electrostatic interactions but as well hydrophobic interactions due to the intercalation of alkyl groups into DNA strands. Furthermore quaternary ammonium groups have the advantage that their charge isn't depending on the pH as it is the case for amine groups which need to be protonated to be positively charged. This fact might improve the adherence of DNA on nanoparticle surfaces in the cytosol, where the labeled DNA is exposed to a milieu containing various proteins and a relatively high salt concentration at pH 7.4. In such an environment the charges provided by aminated nanoparticles may be almost totally screened by present anions leading to the release of DNA in the cytosol. Subsequently the following of DNA until the nucleus is impeded. On the contrary nanoparticles

bearing quaternary ammonium groups which possess pH independent charged may be higher charged at pH 7.4 and therefore keep more positive charges on their surface even in a salty environment such as the cytosol. The generation of quaternary ammonium groups on a multifunctional nanoparticle might therefore solve the problem that lipoplex transfected DNA actually couldn't be labeled until its internalization into the cell nucleus^[164]. Ideally a labeled lipoplex would contain DNA adsorbed to a multimodal nanoparticle and secondly marked by small groove intercalating quaternary ammonium group bearing gold nanoparticles (see **FIGURE 4.3-4**).

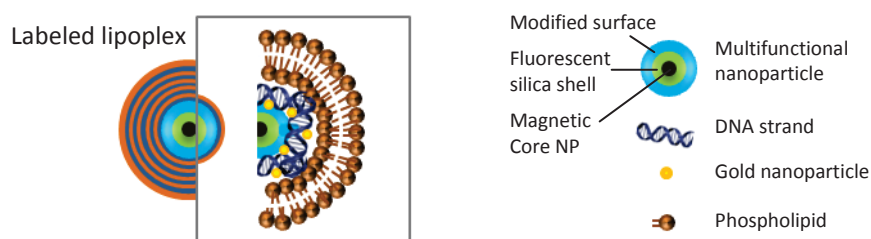


FIGURE 4.3-4 The schematic illustration shows an ideally labeled lipoplex. DNA should be in interaction with quaternary ammonium group bearing multifunctional nanoparticles and equally functionalized gold nanoparticles to assure that it can be followed until its transfection into the cell nucleus.

The labeling nanoparticles should be sufficiently small to enter the nucleus. Furthermore the simultaneously labeling of DNA with multifunctional silica nanoparticles and gold nanoparticles permit to detect DNA as well in the case that it might dissociate of one of the labeling agents. Our goal is in the following to develop a chemical surface modification which permits the syntheses of multimodal silica nanoparticles bearing quaternary ammonium groups on their surface for labeling DNA in lipoplexes more efficiently. The disposition of a surface modification process permitting to implement quaternary ammonium groups on silica will enable us to create a multifunctional nanoparticle allowing the visualization of the transfection of DNA by complementary imaging modalities on different scales.

REFERENCES

- [1] A. G. Rockall, S. A. Sohaib, M. G. Harisinghani, S. A. Babar, N. Singh, A. R. Jeyarajah, D. H. Oram, I. J. Jacobs, J. H. Shepherd, R. H. Reznick, *JCO* **2005**, *23*, 2813–2821.
- [2] S. A. Anderson, J. Shukaliak-Quandt, E. K. Jordan, A. S. Arbab, R. Martin, H. McFarland, J. A. Frank, *Ann. Neurol.* **2004**, *55*, 654–659.
- [3] A. Wunder, R. H. Straub, S. Gay, J. Funk, U. Müller-Ladner, *Rheumatology* **2005**, *44*, 1341–1349.
- [4] F. A. Jaffer, P. Libby, R. Weissleder, *Circulation* **2007**, *116*, 1052–1061.
- [5] D.-E. Lee, H. Koo, I.-C. Sun, J. H. Ryu, K. Kim, I. C. Kwon, *Chem. Soc. Rev.* **2012**, *41*, 2656–2672.
- [6] J. L. Vivero-Escoto, R. C. Huxford-Phillips, W. Lin, *Chem. Soc. Rev.* **2012**, *41*, 2673.
- [7] P. A. Bandettini, in *Neural Correlates of Thinking* (Eds.: E. Kraft, B. Gulyás, E. Pöppel), Springer Berlin Heidelberg, Berlin, Heidelberg, **2009**, pp. 15–38.
- [8] E. Duguet, M. Treguer-Delapierre, M.-H. Delville, in *Nanoscience* (Eds.: P. Boisseau, P. Houdy, M. Lahmani), Springer Berlin Heidelberg, **2009**, pp. 129–170.
- [9] P. Sharma, S. Brown, G. Walter, S. Santra, B. Moudgil, *Adv. Colloid and Interface Sci.* **2006**, *123–126*, 471–485.
- [10] U. I. Tromsdorf, O. T. Bruns, S. C. Salmen, U. Beisiegel, H. Weller, *Nano Lett.* **2009**, *9*, 4434–4440.
- [11] C. Rümennapp, B. Gleich, A. Haase, *Pharm. Res.* **2012**, *29*, 1165–1179.
- [12] G. Ratzinger, P. Agrawal, W. Körner, J. Lonkai, H. M. H. F. Sanders, E. Terreno, M. Wirth, G. J. Strijkers, K. Nicolay, F. Gabor, *Biomaterials* **2010**, *31*, 8716–8723.
- [13] P. Caravan, J. J. Ellison, T. J. McMurry, R. B. Lauffer, *Chem. Rev.* **1999**, *99*, 2293–2352.
- [14] F. Wallis, F. J. Gilbert, *J. R. Coll. Surg. Edinb.* **1999**, *44*, 117–125.
- [15] J.-K. Hsiao, C.-P. Tsai, T.-H. Chung, Y. Hung, M. Yao, H.-M. Liu, C.-Y. Mou, C.-S. Yang, Y.-C. Chen, D.-M. Huang, *Small* **2008**, *4*, 1445–1452.
- [16] J. M. Ollinger, J. A. Fessler, *IEEE Signal Proc. Mag.* **1997**, *14*, 43–55.
- [17] M. M. Brody AL, *Arch. Gen. Psychiatry* **2006**, *63*, 907–914.
- [18] G. Muehlechner, J. S. Karp, *Phys. Med. Biol.* **2006**, *51*, R117–R137.
- [19] M. D. Normandin, K. F. Petersen, Y.-S. Ding, S.-F. Lin, S. Naik, K. Fowles, D. M. Skovronsky, K. C. Herold, T. J. McCarthy, R. A. Calle, et al., *J. Nucl. Med.* **2012**, *53*, 908–916.
- [20] A. Burns, H. Ow, U. Wiesner, *Chem. Soc. Rev.* **2006**, *35*, 1028–1042.
- [21] D. Knopp, D. Tang, R. Niessner, *Anal. Chim. Acta* **2009**, *647*, 14–30.
- [22] T. Kubota, S. Ikeda, H. Yanagisawa, M. Yuki, A. Okamoto, *PLoS ONE* **2010**, *5*, e13003.
- [23] S. Kummer, A. Knoll, E. Socher, L. Bethge, A. Herrmann, O. Seitz, *Angew. Chem. Int. Ed.* **2011**, *50*, 1931–1934.
- [24] K. Brejc, T. K. Sixma, P. A. Kitts, S. R. Kain, R. Y. Tsien, M. Ormö, S. J. Remington, *Proc. Natl. Acad. Sci. U S A* **1997**, *94*, 2306–2311.
- [25] A. J. Lam, F. St-Pierre, Y. Gong, J. D. Marshall, P. J. Cranfill, M. A. Baird, M. R. McKeown, J. Wiedenmann, M. W. Davidson, M. J. Schnitzer, et al., *Nat. Methods* **2012**, *9*, 1005–1012.
- [26] O. M. Subach, P. J. Cranfill, M. W. Davidson, V. V. Verkhusha, *PLoS ONE* **2011**, *6*, e28674.
- [27] D. Shcherbo, I. I. Shemiakina, A. V. Ryabova, K. E. Luker, B. T. Schmidt, E. A. Souslova, T. V. Gorodnicheva, L. Strukova, K. M. Shidlovskiy, O. V. Britanova, et al., *Nat. Methods* **2010**, *7*, 827–829.
- [28] M. Fosbrink, N.-N. Aye-Han, R. Cheong, A. Levchenko, J. Zhang, *PNAS* **2010**, *107*, 5459–5464.
- [29] A. N. Lad, Y. K. Agrawal, *Talanta* **2012**, *97*, 218–221.
- [30] L. Lee, A. P. R. Johnston, F. Caruso, *Langmuir* **2012**, DOI 10.1021/la302587t.
- [31] S. Padilla-Parra, M. Tramier, *Bioessays* **2012**, *34*, 369–376.
- [32] H. H. Rose, *Sci. Tech. Adv. Mater.* **2008**, *9*, 014107.
- [33] A. G. Ekspog, *Nobel Lectures. 1981/90(1993)*, World Scientific, **1993**.
- [34] D. B. Williams, C. B. Carter, D. B. Williams, C. B. Carter, in *Transmission Electron Microscopy*, Springer US, **2009**, pp. 3–22.
- [35] D. E. Bradley, *J. Gen. Microbiol.* **1962**, *29*, 503–516.
- [36] O. Le Bihan, P. Bonnafous, L. Marak, T. Bickel, S. Trépout, S. Mornet, F. De Haas, H. Talbot, J.-C. Taveau, O. Lambert, *J. Struct. Biol.* **2009**, *168*, 419–425.

- [37] D. Danino, Y. Talmon, in *Molecular Gels* (Eds.: R.G. Weiss, P. Terech), Springer Netherlands, **2006**, pp. 253–274.
- [38] W.-S. Cho, M. Cho, J. Jeong, M. Choi, H.-Y. Cho, B. S. Han, S. H. Kim, H. O. Kim, Y. T. Lim, B. H. Chung, et al., *Toxicol. Appl. Pharmacol.* **2009**, *236*, 16–24.
- [39] R. Torres Martin de Rosales, R. Tavaré, R. L. Paul, M. Jauregui-Osoro, A. Protti, A. Glaria, G. Varma, I. Szanda, P. J. Blower, *Angew. Chem. Int. Ed. Engl.* **2011**, *50*, 5509–5513.
- [40] G. Zhang, J. Feng, L. Lu, B. Zhang, L. Cao, *J. Colloid Interface Sci.* **2010**, *351*, 128–133.
- [41] T.-J. Yoon, H. Lee, H. Shao, S. A. Hilderbrand, R. Weissleder, *Adv. Mater.* **2011**, *23*, 4793–4797.
- [42] J. Zhang, Y. Fu, F. Mahdavi, *J. Phys. Chem. C* **2012**, *116*, 24224–24232.
- [43] M. Ma, H. Chen, Y. Chen, X. Wang, F. Chen, X. Cui, J. Shi, *Biomaterials* **2012**, *33*, 989–998.
- [44] C. Plank, O. Zelphati, O. Mykhaylyk, *Adv. Drug Delivery Rev.* **2011**, *63*, 1300–1331.
- [45] M. Ma, H. Chen, Y. Chen, X. Wang, F. Chen, X. Cui, J. Shi, *Biomaterials* **2012**, *33*, 989–998.
- [46] S. Berensmeier, *Appl. Microbiol. Biotechnol.* **2006**, *73*, 495–504.
- [47] R. L. Z. Samantha Cristina de Pinho, *Colloids Surf., B* **2008**, *63*, 249–53.
- [48] S. Laurent, S. Dutz, U. O. Häfeli, M. Mahmoudi, *Adv. Colloid Interface Sci.* **2011**, *166*, 8–23.
- [49] S. Mornet, J. Portier, E. Duguet, *J. Magn. Magn. Mater.* **2005**, *293*, 127–134.
- [50] S. Laurent, D. Forge, M. Port, A. Roch, C. Robic, L. Vander Elst, R. N. Muller, *Chem. Rev.* **2008**, *108*, 2064–2110.
- [51] H. Weller, *Nano Lett.* **2009**, *9*, 4434–4440.
- [52] R. Massart, *IEEE Trans. Magn.* **1981**, *17*, 1247 – 1248.
- [53] M. Allen, D. Willits, J. Mosolf, M. Young, T. Douglas, *Adv. Mater.* **2002**, *14*, 1562–1565.
- [54] P. A. Dresco, V. S. Zaitsev, R. J. Gambino, B. Chu, *Langmuir* **1999**, *15*, 1945–1951.
- [55] T. Hyeon, S. S. Lee, J. Park, Y. Chung, H. B. Na, *J. Am. Chem. Soc.* **2001**, *123*, 12798–12801.
- [56] S. Takami, T. Sato, T. Mousavand, S. Ohara, M. Umetsu, T. Adschiri, *Mater. Lett.* **2007**, *61*, 4769–4772.
- [57] W. Cai, J. Wan, *J. Colloid Interface Sci.* **2007**, *305*, 366–370.
- [58] F. Sonvico, S. Mornet, S. Vasseur, C. Dubernet, D. Jaillard, J. Degrouard, J. Hoebeke, E. Duguet, P. Colombo, P. Couvreur, *Bioconjugate Chem.* **2005**, *16*, 1181–1188.
- [59] R. Hong, M. J. Cima, R. Weissleder, L. Josephson, *Magn. Reson. Med.* **2008**, *59*, 515–520.
- [60] K. A. Willets, R. P. Van Duyne, *Annu. Rev. Phys. Chem.* **2007**, *58*, 267–297.
- [61] W. Deng, E. M. Goldys, *Langmuir* **2012**, *28*, 10152–10163.
- [62] Z. Zhang, R. D. Ross, R. K. Roeder, *Nanoscale* **2010**, *2*, 582–586.
- [63] L. Qian, D. Bera, T.-K. Tseng, P. H. Holloway, *Appl. Phys. Lett.* **2009**, *94*, 073112–073112–3.
- [64] J. Perez-Juste, I. Pastoriza-Santos, L. M. Liz-Marzán, P. Mulvaney, *Coord. Chem. Rev.* **2005**, *249*, 1870–1901.
- [65] B. Nikoobakht, M. A. El-Sayed, *Chem. Mater.* **2003**, *15*, 1957–1962.
- [66] N. R. Jana, L. Gearheart, C. J. Murphy, *Adv. Mater.* **2001**, *13*, 1389–1393.
- [67] T. K. Sau, C. J. Murphy, *Langmuir* **2004**, *20*, 6414–6420.
- [68] M. Grzelczak, J. Pérez-Juste, P. Mulvaney, L. M. Liz-Marzán, *Chem. Soc. Rev.* **2008**, *37*, 1783–1791.
- [69] A. Imhof, M. Megens, J. J. Engelberts, D. T. N. de Lang, R. Sprik, W. L. Vos, *J. Phys. Chem. B* **1999**, *103*, 1408–1415.
- [70] I. L. Medintz, H. T. Uyeda, E. R. Goldman, H. Mattoussi, *Nat. Mater.* **2005**, *4*, 435–446.
- [71] M. Green, *J. Mater. Chem.* **2010**, *20*, 5797.
- [72] T. Pellegrino, S. Kudera, T. Liedl, A. Muñoz Javier, L. Manna, W. J. Parak, *Small* **2005**, *1*, 48–63.
- [73] L. Manna, E. C. Scher, A. P. Alivisatos, *J. Am. Chem. Soc.* **2000**, *122*, 12700–12706.
- [74] A. P. Alivisatos, *Science* **1996**, *271*, 933–937.
- [75] Y. Ghasemi, P. Peymani, S. Afifi, *Acta. Biomed.* **2009**, *80*, 156–165.
- [76] J. E. Fuller, G. T. Zugates, L. S. Ferreira, H. S. Ow, N. N. Nguyen, U. B. Wiesner, R. S. Langer, *Biomaterials* **2008**, *29*, 1526–1532.
- [77] F. Gao, L. Wang, L. Tang, C. Zhu, *Microchim. Acta* **2005**, *152*, 131–135.
- [78] T. Doussineau, M. Smaïhi, G. J. Mohr, *Adv. Funct. Mater.* **2009**, *19*, 117–122.
- [79] L. Xue, B. Li, Q. Fei, G. Feng, Y. Huan, Z. Shi, *Nanotechnology* **2010**, *21*, 215502.
- [80] E. J. McLaurin, A. B. Greytak, M. G. Bawendi, D. G. Nocera, *J. Am. Chem. Soc.* **2009**, *131*, 12994–13001.
- [81] B. Ou, M. Hampsch-Woodill, R. L. Prior, *J. Agric. Food Chem.* **2001**, *49*, 4619–4626.

- [82] T. Doussineau, A. Schulz, A. Lapresta-Fernandez, A. Moro, S. Körsten, S. Trupp, G. J. Mohr, *Chemistry* **2010**, *16*, 10290–10299.
- [83] H.-S. Peng, S.-H. Huang, O. Wolfbeis, *J. Nanopart. Res.* **2010**, *12*, 2729–2733.
- [84] D. Ross, M. Gaitan, L. E. Locascio, *Anal. Chem.* **2001**, *73*, 4117–4123.
- [85] A. Van Blaaderen, A. Vrij, *Langmuir* **1992**, *8*, 2921–2931.
- [86] L. D. R. O. W. Hooisweng, V. H. D, H. A. A, W. Ulrich, W. W. W, *Chem. Mat.* **2008**, *20*, 2677–2684.
- [87] Key Laboratory of Surface and Interface Chemistry of Jilin Province, College of Chemistry, Jilin University, CHN, Z. LU, J. XU, Y. HAN, Z. SONG, J. LI, Y. Wensheng, *Colloids Surf., A* **2007**, *303*, 207–210.
- [88] Hybrid Silica Technologies,, Department of Materials Science and Engineering, Cornell University,, H. Erik, O. Hooisweng, B. Daniel, B. Andrew, W. Ulrich, *J. Mater. Chem.* **2009**, *19*, 6341–6347.
- [89] W. Stöber, A. Fink, E. Bohn, *J. Colloid Interface Sci.* **1968**, *26*, 62–69.
- [90] D. Rother, T. Sen, D. East, I. J. Bruce, *Nanomedicine* **2011**, *6*, 281–300.
- [91] A. Van Blaaderen, J. Van Geest, A. Vrij, *J. Colloid Interface Sci.* **1992**, *154*, 481–501.
- [92] J. Samuel, O. Raccurt, O. Poncelet, A. Auger, W.-L. Ling, P. Cherns, D. Grunwald, O. Tillement, *J. Nanopart. Res.* **2010**, *12*, 2255–2265.
- [93] R. P. Bagwe, L. R. Hilliard, W. Tan, *Langmuir* **2006**, *22*, 4357–4362.
- [94] R. P. Bagwe, C. Yang, L. R. Hilliard, W. Tan, *Langmuir* **2004**, *20*, 8336–8342.
- [95] J. M. Rosenholm, C. Sahlgren, M. Lindén, *Nanoscale* **2010**, *2*, 1870–1883.
- [96] I. I. Slowing, J. L. Vivero-Escoto, C.-W. Wu, V. S.-Y. Lin, *Adv. Drug Deliv. Rev.* **2008**, *60*, 1278–1288.
- [97] T. Suteewong, H. Sai, R. Cohen, S. Wang, M. Bradbury, B. Baird, S. M. Gruner, U. Wiesner, *J. Am. Chem. Soc.* **2011**, *133*, 172–175.
- [98] S. Mornet, O. Lambert, E. Duguet, A. Brisson, *Nano Lett.* **2005**, *5*, 281–285.
- [99] L. Song, E. J. Hennink, I. T. Young, H. J. Tanke, *Biophys. J.* **1995**, *68*, 2588–2600.
- [100] L. Y. T. Chou, K. Ming, W. C. W. Chan, *Chem. Soc. Rev.* **2011**, *40*, 233–245.
- [101] X. Xue, F. Wang, X. Liu, *J. Mater. Chem.* **2011**, *21*, 13107–13127.
- [102] P. W. Atkins, J. D. Paula, *Physikalische Chemie*, Wiley-VCH, **2006**.
- [103] G. Wedler, *Lehrbuch der Physikalischen Chemie*, Wiley-VCH, **2004**.
- [104] K. J. M. Bishop, C. E. Wilmer, S. Soh, B. A. Grzybowski, *Small* **2009**, *5*, 1600–1630.
- [105] S. Mornet, *Synthèse et Modification Chimique de La Surface de Nanoparticules de Maghémite à Des Fins D'applications Biomédicales*, **2002**.
- [106] A. E. Nel, L. Mädler, D. Velegol, T. Xia, E. M. V. Hoek, P. Somasundaran, F. Klaessig, V. Castranova, M. Thompson, *Nat. Mater.* **2009**, *8*, 543–557.
- [107] K. L. Mittal, *Silanes and Other Coupling Agents*, BRILL, **2009**.
- [108] N. Tsubokawa, A. Kogure, *J. Polym. Sci. A: Polym. Chem.* **1991**, *29*, 697–702.
- [109] S. Eustis, M. A. El-Sayed, *Chem. Soc. Rev.* **2006**, *35*, 209–217.
- [110] R. K. Smith, P. A. Lewis, P. S. Weiss, *Prog. Surf. Sci.* **2004**, *75*, 1–68.
- [111] R. A. Sperling, W. J. Parak, *Phil. Trans. R. Soc. A* **2010**, *368*, 1333–1383.
- [112] T. Arakawa, D. Hobara, M. Yamamoto, T. Kakiuchi, *Electrochem. Commun.* **2005**, *7*, 848–852.
- [113] C. Vericat, M. E. Vela, G. Benitez, P. Carro, R. C. Salvarezza, *Chem. Soc. Rev.* **2010**, *39*, 1805.
- [114] A. Caragheorghopol, V. Chechik, *Phys. Chem. Chem. Phys.* **2008**, *10*, 5029–5041.
- [115] M. J. Hostetler, A. C. Templeton, R. W. Murray, *Langmuir* **1999**, *15*, 3782–3789.
- [116] D. F. Moyano, V. M. Rotello, *Langmuir* **2011**, *27*, 10376–10385.
- [117] C. Subramani, A. Bajaj, O. R. Miranda, V. M. Rotello, *Adv. Mater.* **2010**, *22*, 5420–5423.
- [118] B. Fang, S. Gon, M. Park, K.-N. Kumar, V. M. Rotello, K. Nusslein, M. M. Santore, *Colloids Surf. B Biointerfaces* **2011**, *87*, 109–115.
- [119] V. Pardo-Yissar, E. Katz, J. Wasserman, I. Willner, *J. Am. Chem. Soc.* **2003**, *125*, 622–623.
- [120] S. Pierrat, I. Zins, A. Breivogel, C. Sönnichsen, *Nano Lett.* **2007**, *7*, 259–263.
- [121] M. Das, D. Mishra, T. K. Maiti, A. Basak, P. Pramanik, *Nanotechnology* **2008**, *19*, 415101.
- [122] B. Stella, S. Arpicco, M. T. Peracchia, D. Desmaële, J. Hoebeke, M. Renoir, J. D'Angelo, L. Cattel, P. Couvreur, *J. Pharm. Sci.* **2000**, *89*, 1452–1464.
- [123] W. C. W. Chan, S. Nie, *Science* **1998**, *281*, 2016–2018.
- [124] C. Bieniarz, M. Husain, G. Barnes, C. A. King, C. J. Welch, *Bioconjugate Chem.* **1996**, *7*, 88–95.
- [125] C. A. Mirkin, *Inorg. Chem.* **2000**, *39*, 2258–2272.

- [126] S. Y. Park, A. K. R. Lytton-Jean, B. Lee, S. Weigand, G. C. Schatz, C. A. Mirkin, *Nature* **2008**, *451*, 553–556.
- [127] V. Puddu, C. C. Perry, *ACS Nano* **2012**, *6*, 6356–6363.
- [128] K. Mulligan, Z. J. Jakubek, L. J. Johnston, *Langmuir* **2011**, *27*, 14352–14359.
- [129] R. Richter, A. Mukhopadhyay, A. Brisson, *Biophys. J.* **2003**, *85*, 3035–3047.
- [130] E. Reimhult, K. Kumar, *Trends Biotechnol.* **2008**, *26*, 82–89.
- [131] A.-L. Troutier, C. Ladavière, *Adv. Colloid Interface Sci.* **2007**, *133*, 1–21.
- [132] R. P. Richter, R. Bérat, A. R. Brisson, *Langmuir* **2006**, *22*, 3497–3505.
- [133] D. A. Handley, C. M. Arbeeny, L. D. Witte, S. Chien, *Proc. Natl. Acad. Sci. U S A* **1981**, *78*, 368–371.
- [134] I. Lynch, K. A. Dawson, *Nano Today* **2008**, *3*, 40–47.
- [135] X. Y. Ling, D. N. Reinhoudt, J. Huskens, *Langmuir* **2006**, *22*, 8777–8783.
- [136] X. Y. Ling, I. Y. Phang, W. Maijenburg, H. Schönherr, D. N. Reinhoudt, G. J. Vancso, J. Huskens, *Angew. Chem.* **2009**, *121*, 1001–1005.
- [137] J. M. Abad, S. F. L. Mertens, M. Pita, V. M. Fernández, D. J. Schiffrin, *J. Am. Chem. Soc.* **2005**, *127*, 5689–5694.
- [138] M. Hu, L. Qian, R. P. Briñas, E. S. Lymar, J. F. Hainfeld, *Angew. Chem. Int. Ed.* **2007**, *46*, 5111–5114.
- [139] Y.-S. Chen, M.-Y. Hong, G. S. Huang, *Nat. Nano* **2012**, *7*, 197–203.
- [140] M. L. B. Magalhães, C. M. Czekster, R. Guan, V. N. Malashkevich, S. C. Almo, M. Levy, *Protein Sci.* **2011**, *20*, 1145–1154.
- [141] R. Wang, C. Nuckolls, S. J. Wind, *Angew. Chem. Int. Ed.* **2012**, *51*, 11325–11327.
- [142] M. Hødenius, M. De Cuyper, L. Desender, M. D. Iler-Schulte, A. Steigel, H. Lueken, *Chem. Phys. Lipids* **2002**, *120*, 75–85.
- [143] R. E. Stenkamp, I. L. Trong, L. Klumb, P. S. Stayton, S. Freitag, *Protein Sci.* **1997**, *6*, 1157–1166.
- [144] M. P. Nikitin, T. A. Zdobnova, S. V. Lukash, O. A. Stremovskiy, S. M. Deyev, *PNAS* **2010**, *107*, 5827–5832.
- [145] A. M. Buckle, G. Schreiber, A. R. Fersht, *Biochemistry* **1994**, *33*, 8878–8889.
- [146] S. Mazzucchelli, M. Colombo, C. De Palma, A. Salvadè, P. Verderio, M. D. Coghi, E. Clementi, P. Tortora, F. Corsi, D. Prospero, *ACS Nano* **2010**, *4*, 5693–5702.
- [147] L. H. Reddy, J. L. Arias, J. Nicolas, P. Couvreur, *Chem. Rev.* **2012**, *112*, 5818–5878.
- [148] J. V. Jokerst, T. Lobovkina, R. N. Zare, S. S. Gambhir, *Nanomedicine* **2011**, *6*, 715–728.
- [149] D. E. Owens III, N. A. Peppas, *Int. J. Pharm.* **2006**, *307*, 93–102.
- [150] S. Chemburu, K. Fenton, G. P. Lopez, R. Zeineldin, *Molecules* **2010**, *15*, 1932–1957.
- [151] M. L. Edelstein, M. R. Abedi, J. Wixon, R. M. Edelstein, *J. Gene Med.* **2004**, *6*, 597–602.
- [152] V. Vijayanathan, T. Thomas, T. J. Thomas, *Biochemistry* **2002**, *41*, 14085–14094.
- [153] M. Günther, J. Lipka, A. Malek, D. Gutsch, W. Kreyling, A. Aigner, *Eur. J. Pharm. Biopharm.* **2011**, *77*, 438–449.
- [154] C. Liu, N. Zhang, *Prog. Mol. Biol. Transl. Sci.* **2011**, *104*, 509–562.
- [155] D. Voet, J. G. Voet, C. W. Pratt, A. Beck-Sickinger, *Lehrbuch der Biochemie*, Wiley VCH Verlag GmbH, **2010**.
- [156] L. D. Williams, L. J. Maher 3rd, *Annu. Rev. Biophys. Biomol. Struct.* **2000**, *29*, 497–521.
- [157] V. B. Teif, K. Bohinc, *Prog. Biophys. Mol. Biol.* **2011**, *105*, 208–222.
- [158] G. S. Manning, *J. Chem. Phys.* **1969**, *51*, 924–933.
- [159] P. S. Ghosh, C.-K. Kim, G. Han, N. S. Forbes, V. M. Rotello, *ACS Nano* **2008**, *2*, 2213–2218.
- [160] S. Golan, Y. Talmon, *Langmuir* **2012**, *28*, 1668–1672.
- [161] C. Madeira, L. M. S. Loura, M. R. Aires-Barros, M. Prieto, *Biochim. Biophys. Acta* **2011**, *1808*, 2694–2705.
- [162] A. R. Thierry, V. Norris, F. Molina, M. Schmutz, *Biochim. Biophys. Acta* **2009**, *1790*, 385–394.
- [163] C. Marchini, D. Pozzi, M. Montani, C. Alfonsi, A. Amici, H. Amenitsch, S. Candeloro De Sanctis, G. Caracciolo, *Langmuir* **2010**, *26*, 13867–13873.
- [164] O. Le Bihan, R. Chèvre, S. Mornet, B. Garnier, B. Pitard, O. Lambert, *Nucleic Acids Res.* **2011**, *39*, 1595–1609.
- [165] S. T. Hemp, M. H. Allen, M. D. Green, T. E. Long, *Biomacromolecules* **2011**, *13*, 231–238.
- [166] C. Kneuer, M. Sameti, U. Bakowsky, T. Schiestel, H. Schirra, H. Schmidt, C. M. Lehr, *Bioconjug. Chem.* **2000**, *11*, 926–932.

- [167] C. Kneuer, M. Sameti, E. G. Haltner, T. Schiestel, H. Schirra, H. Schmidt, C. M. Lehr, *Int. J. Pharm.* **2000**, *196*, 257–261.
- [168] X. He, K. Wang, W. Tan, B. Liu, X. Lin, C. He, D. Li, S. Huang, J. Li, *J. Am. Chem. Soc.* **2003**, *125*, 7168–7169.
- [169] M. E. Park, J. H. Chang, *Mater. Sci. Eng. C.* **2007**, *27*, 1232–1235.
- [170] S. Cerneaux, S. M. Zakeeruddin, J. M. Pringle, Y.-B. Cheng, M. Grätzel, L. Spiccia, *Adv. Funct. Mater.* **2007**, *17*, 3200–3206.
- [171] A. del Campo, T. Sen, J.-P. Lellouche, I. J. Bruce, *J. Magn. Magn. Mater.* **2005**, *293*, 33–40.
- [172] I. Roy, T. Y. Ohulchanskyy, D. J. Bharali, H. E. Pudavar, R. A. Mistretta, N. Kaur, P. N. Prasad, *Proc. Natl. Acad. Sci. U.S.A.* **2005**, *102*, 279–284.
- [173] J. Beloor, C. S. Choi, H. Y. Nam, M. Park, S. H. Kim, A. Jackson, K. Y. Lee, S. W. Kim, P. Kumar, S.-K. Lee, *Biomaterials* **2012**, *33*, 1640–1650.
- [174] T. Kim, M. Ou, M. Lee, S. W. Kim, *Biomaterials* **2009**, *30*, 658–664.
- [175] O. Veiseh, F. M. Kievit, H. Mok, J. Ayesh, C. Clark, C. Fang, M. Leung, H. Arami, J. O. Park, M. Zhang, *Biomaterials* **2011**, *32*, 5717–5725.
- [176] J. Haas, M. N. V. Ravi Kumar, G. Borchard, U. Bakowsky, C.-M. Lehr, *AAPS Pharm. Sci. Tech.* **2005**, *6*, E22–30.
- [177] M. A. Herrero, F. M. Toma, K. T. Al-Jamal, K. Kostarelos, A. Bianco, T. Da Ros, F. Bano, L. Casalis, G. Scoles, M. Prato, *J. Am. Chem. Soc.* **2009**, *131*, 9843–9848.
- [178] T. Xia, M. Kovoichich, M. Liong, H. Meng, S. Kabehie, S. George, J. I. Zink, A. E. Nel, *ACS Nano* **2009**, *3*, 3273–3286.
- [179] C. M. McIntosh, E. A. Esposito 3rd, A. K. Boal, J. M. Simard, C. T. Martin, V. M. Rotello, *J. Am. Chem. Soc.* **2001**, *123*, 7626–7629.
- [180] C. M. Goodman, N. S. Chari, G. Han, R. Hong, P. Ghosh, V. M. Rotello, *Chem. Biol. Drug. Des.* **2006**, *67*, 297–304.
- [181] K. K. Sandhu, C. M. McIntosh, J. M. Simard, S. W. Smith, V. M. Rotello, *Bioconjugate Chem.* **2002**, *13*, 3–6.
- [182] A. Verma, O. Uzun, Y. Hu, Y. Hu, H.-S. Han, N. Watson, S. Chen, D. J. Irvine, F. Stellacci, *Nat. Mater.* **2008**, *7*, 588–595.
- [183] M. G. Warner, J. E. Hutchison, *Nat. Mater.* **2003**, *2*, 272–277.

CHAPTER II – SYNTHESIS OF SILICA NANOPARTICLES BEARING QUATERNARY AMMONIUM GROUPS ON THEIR SURFACE

For the purpose of synthesizing multifunctional nanoparticles to label DNA we aim to modify the surface of multimodal silica nanoparticles with quaternary ammonium ions. We have chosen this functional group because of the strong affinity of quaternary ammonium ions to the negatively charged phosphate entities in the DNA backbone and the pH independence of their positive charge. The purpose is to optimize the chemical surface modification of silica nanoparticles to obtain surfaces with high zeta potentials under physiological conditions and an isoelectric point at a basic pH. We will effectuate the chemical surface modifications tested in our study on basic silica nanoparticles taking into consideration the fact that silica is an excellent material for the buildup of different multimodal nanoparticles serving as bioimaging tools, which, in spite of the different materials they may include, possess the same silica surface serving as a platform for chemical surface modifications.

1. SYNTHESIS AND CHARACTERIZATION OF EXEMPLARY SILICA NANOPARTICLES SERVING AS BODY MATERIAL FOR CHEMICAL MODIFICATIONS

To develop a reliable protocol of chemical surface modification of silica nanoparticles with the objective of affixing quaternary ammonium groups on their surface, we synthesize silica nanoparticles serving us as body material during the study. The establishment of a chemical surface modification protocol relies on the presence of stocks of reproducible, basic silica nanoparticles on which different chemical surface modifications can be conducted. The particles need to be sufficiently big and heavy to facilitate the observation of their colloidal stability as well as their handling during the washing and centrifuging stages of the modification protocols. On the other hand they need to be sufficiently small to possess a high surface/weight ratio to facilitate the characterization of the modified surfaces. They also need to be small enough to permit the testing of their incorporation to lipoplexes and determine their potential for bioimaging applications. We therefore choose to synthesize silica nanoparticles with a diameter of 50 nm on which we carry out different chemical surface modifications during our study. Their size in the range of tenth of nanometers permits easy handling during the testing of chemical surface modifications, furnishes a surface area sufficiently large to permit the characterization of the modified surfaces and allows the investigation of their interactions with DNA in lipoplexes.

The synthesis of silica nanoparticles is accomplished in a hydro-alcoholic reaction medium under alkaline catalysis of ammonia, which originates from the synthesis protocol studied by Stöber, Fink and Bohn in 1968^[1]. By this method we synthesize small silica nanoparticles, which serve us as seeds for further particle growth up to the desired nanoparticle diameter of 50 nm.

The mechanism of nucleation of silica particles is still controversial. Whereas some authors have proposed a nucleation based on the idea of a monomer addition model^[2], where monomers react on the surface of silica nuclei, which arise in supersaturated solutions of silicic acid provided from the hydrolysis of tetraethylorthosilicate (TEOS), in contrast Bogush and Zukovski^[3] developed an

aggregative growth model in which the formation of nanoparticles is attributed to the coagulation of silica clusters.

Both the growth of the particles and their final size is influenced by multiple parameters such as solvents, temperature and the ionic strength of the reaction media. Van Helden et al. used the so-called “Stöber process” to synthesize uniform, monodisperse silica nanoparticles, which they stabilized in organic media^[4]. Whereas Tan et al.^[5] studied temperature effects, others like van Blaaderen et al.^[6] investigated the influence of the ionic strength of the reaction medium on the particle synthesis. They determined the production of the hydrolyzed monomer silicic acid as rate limiting during the growth process. They showed that concentrations of ammonia and water determine the ionic strength of the reaction medium and the ratio of hydrolysis and condensation processes taking place at the same time. The nucleating silica clusters coagulate to nanoparticles until their colloidal stability is reached. The number of positively charged ammonium ions in the reaction medium determines the particle size at which the colloidal stability of the negatively charged silica spheres is obtained. Low concentrations of ammonia lead to a fast colloidal stabilization of small particles. High concentrations of ammonia result in the growth of nanoparticles which achieve their colloidal stability at higher diameters. Based on the Stöber synthesis a reaction protocol has been optimized in our group to obtain small silica nanoparticles, which we use as seeds for further growth.

PROTOCOL 1.0-1 Condition for the synthesis of small silica nanoparticles

Silica seeds were synthesized by a Stöber process^[1]. 2.85 mL H₂O (18.2 MΩ) and 28.95 mL NH₄OH (28-30% w/v) were added to 270 mL EtOH. Under continuous stirring 6 mL TEOS in 270 mL of ethanol were rapidly added. The reaction was completed after two hours of stirring at room temperature. Silica nanoparticles with diameters of about 11.4 nm were obtained and used as seeds to synthesize silica nanoparticles of controlled size. The final reaction volume needed to be composed of the ingredients following the partition (% v/v): 93.46% EtOH, 0.49% H₂O, 5.01% NH₄OH, and 1.04% TEOS (equivalent to a final concentration of 0.047 mol/L). The size of the seeds was determined by TEM for each preparation to permit an exact calculation of the volume of TEOS needed for subsequent particle growth. The concentration of silica NPs/L was determined by inductively coupled plasma (ICP) (see Annex 1).

The silica particles synthesized by **PROTOCOL 1.0-1** have a mean diameter of 11.4 ± 2.8 nm, which is determined by transmission electron microscopy (see **FIGURE 1.0-1**). The transmission electron micrographs are analyzed with the help of the program imageJ. The computation of histograms of the particle size distribution is based on the sizes counted of over 2000 nanoparticles. We implemented dynamic light scattering (DLS) measurements to determine the hydrodynamic mean diameter at and also the polydispersity index (PDI) using the cumulants method. According to the cumulants method the polydispersity index is a measure for the broadness of the size distribution. Particles with a PDI < 0.05 are regarded as highly monodisperse, while particles with a PDI between 0.1 and 0.2 possess a narrow distribution and are still considered as monodisperse, whereas nanoparticles possessing a PDI from 0.2 to 0.5 show intermediate distribution broadness. With a PDI > 0.5 we consider the

synthesized nanoparticles as polydisperse; if they have a $PDI > 1$ we judge them as highly polydisperse. For silica seeds a hydrodynamic diameter of 22.33 nm and a polydispersity index of 0.235 is determined by DLS measurements. This hydrodynamic diameter shown by a size distribution by intensity is determined as double-sized compared to the diameter measured by TEM. This is due to the fact that the scattering intensities of larger nanoparticles are higher than the scattering intensities of smaller nanoparticles, leading to an overestimation of the population of the larger nanoparticles. To solve this problem the size of the particles can be determined by showing the size distribution by volume, which determines a hydrodynamic diameter of 11.43 nm for the same DLS measurement (see **FIGURE 1.0-1**). Equally it is possible to correct the overestimation of population of larger nanoparticles by the application of the Mie theory, which allows the calculation of the size of spherical particles in dilute solutions if their refractive index in the surrounding medium is known.

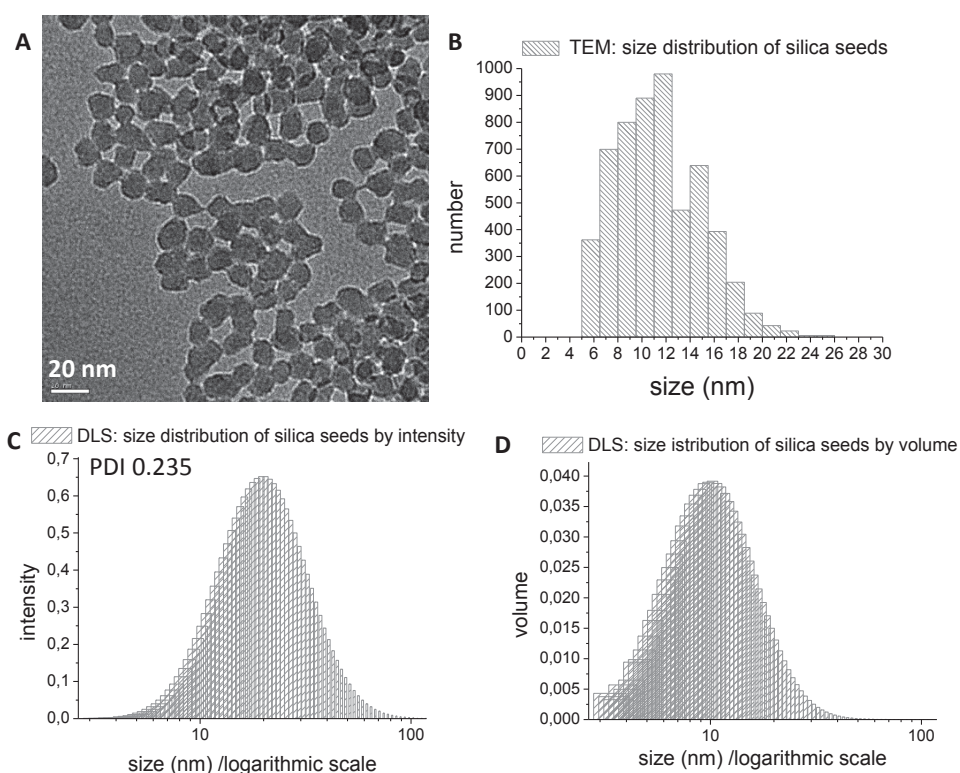


FIGURE 1.0-1 **A:** TEM picture of synthesized silica-seeds obtained in a Stöber reaction environment. **B:** Size distribution of the diameter of silica seeds determined by TEM measurements. **C:** Size distribution by intensity determined by DLS shows the hydrodynamic diameters of the synthesized seeds. **D:** Size distribution by volume determined by DLS.

We use these small silica particles, synthesized in a Stöber reaction medium, as seeds, which under growth supporting reaction conditions are grown to spherical particles of a chosen size. The ratio of ethanol, water and ammonia, chosen to avoid nucleation and to promote the growth of a steady number of silica-particles, is determined in a way that the growth of the silica seeds depends solely on the quantity of TEOS which is added in the reaction medium. This approach is valid because the quantity of TEOS, slowly added to the chosen growth-supporting reaction medium, hydrolyses and condenses completely on the provided silica-seeds, without occurrence of secondary nucleation. The volume of TEOS needed to undergo particle growth from particles with the diameter d up to a desired

particle size with the diameter D can easily be calculated. First we calculate the mass of silica which we add to the spherical particles during the growth process:

$$m_{SiO_2\text{added}} = \rho_{SiO_2} \times V_{SiO_2\text{added}} \times N_{NP} = \rho_{SiO_2} \times (V_{NP\text{final}} - V_{NP0}) \times N_{NP}$$

$$= 2.0 \frac{g}{cm^3} \times \frac{1}{6} \pi (D^3 - d^3) \times N_{NP}$$

ρ – density

N_{NP} – number of nanoparticles

EQUATION 1.0-1 Calculation of the mass of TEOS needed to grow a silica shell with a predetermined thickness.

Due to the fact that the amount of TEOS used is equal to the amount of SiO₂ formed, the volume of TEOS to add is then calculated by the following formula:

$$V_{TEOS} = \frac{M_{TEOS}}{\rho_{TEOS}} \times \frac{m_{SiO_2\text{added}}}{M_{SiO_2}}$$

M – molar mass

EQUATION 1.0-2 Calculation of the volume of TEOS needed to grow a silica shell with a predetermined thickness.

The particles formed by this process are relatively monodisperse spheres. They consist of a porous, amorphous silica matrix and have a rough, silanol group bearing surface. Their point of zero charge is achieved at pH 2.5, while at lower pHs the silica-particles are positively charged and with increasing pH their surface potential becomes more negative and attains values of about -50 mV to -60 mV above pH 6 (see **FIGURE 1.0-3**).

PROTOCOL 1.0-2 Condition for the growth of silica nanoparticles

200 mL of the freshly prepared seed containing solution were introduced to a reaction environment consisting of 729 mL EtOH, 279 mL H₂O (18.2 MΩ) and 13.5 mL NH₄OH (28-30 % w/v). The final partitions (% v/v) of EtOH, H₂O and NH₄OH need to be 75.2 % EtOH, 22.9 % H₂O and 1.9% NH₄OH. A volume of TEOS, depending on the final particle size chosen (Equation), was added constantly during 4 hours under continuous stirring at room temperature. The reaction finished after 2 hours of stirring at room temperature and led to monodisperse spherical silica nanoparticles of the desired size. After the synthesis, ammonia and ethanol were removed from the medium by evaporation at 40°C. The size of the grown nanoparticles was determined by TEM, the concentration of silica NPs/L by ICP.

In the following silica nanoparticles of 50 nm diameter are shown (see **FIGURE 1.0-2**). Their polydispersity index is determined by DLS. We obtain a polydispersity index of 0.329 for the NPs grown to a target diameter of 50 nm. The spherical form of nanoparticles becomes more even as they become larger. The mean size of silica nanoparticles evaluated by statistical analysis of transmission electron micrographs is 51.8 nm.

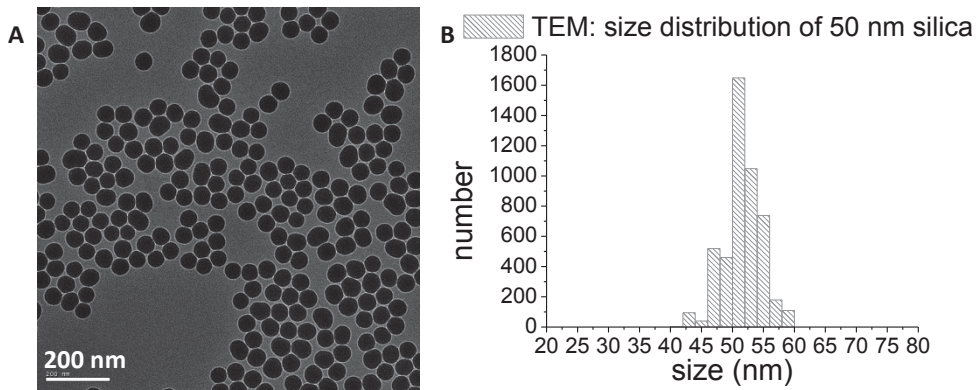


FIGURE 1.0-2 Silica nanoparticles of different sizes (50 nm) obtained by growth of the seeds. **A:** TEM picture nanoparticles grown to 50 nm **B:** Size distribution of the synthesized nanoparticles determined by statistics based on the evaluation of TEM pictures.

The synthesized silica nanoparticles consist of an amorphous, porous silica matrix. The density of colloidal silica synthesized by the Stöber method has been determined in literature as between 1.8 and 2.2 g/m^{2[6-8]} depending on their size and the synthesis method. According to van Blaaderen and coworkers^[6] we suppose our 50 nm sized silica particles to possess a density of 2.0 g/m². Subsequently the mass of one particle m_{NP} is calculated as 1.3089·10⁻¹⁶ g via the equation:

$$m_{NP} = \frac{4}{3}\pi r^3 * \rho_{SiO_2}$$

r – nanoparticle radius (cm)

ρ – density (g/cm³)

EQUATION 1.0-3 Calculation of the mass of one silica nanoparticle.

Considering the particles as dense, perfect spheres the developed surface area S_D of one silica nanoparticle is determined as 7.854·10⁻¹⁵ m² by the following equation:

$$S_D = 4\pi r^2$$

EQUATION 1.0-4 Calculation of the surface area area of one silica nanoparticle.

Based on the two equations the surface per gram of 50 nm sized nanoparticles is calculated as 60 m²/g. The surface of silica nanoparticles of the same size synthesized by the “Stöber” method has been determined as 102 m²/g by BET measurements^[8] and the high difference of these two values has been explained by the natural porosity of the amorphous silica nanoparticles.

Silica nanoparticles are covered with non condensed silanol groups, which transform to silanolate groups above pH 2.5. This behavior influences their zeta potential. Silica nanoparticles dispersed in an aqueous solution at pHs above pH 2.5 possess progressively deprotonated silanolate groups on their surface and show an decreasing negative zeta potential. Below pH 2.5 the silanol groups are increasingly protonated and the zeta potential of the silica nanoparticles becomes positive. At pH 2.5, where solely silanol groups are present on the particle surface it is supposed to be zero. This point is known as the point of zero charge of silica nanoparticles. It is determined by the measurement of the zeta potential in relation to the pH (see **FIGURE 1.0-3**). In reality it corresponds more to what is known

to be an isoelectric point, because of the fact that the point where solely uncharged silanol groups cover the surfaces can't be determined and the zeta potential is also monitored as zero, when the charges of protonated and deprotonated silanol groups equilibrate each other. Considering that silica nanoparticles are stabilized by electrostatic repulsion we note that the pH and their zeta potential determine their colloidal stability. The silica colloids start to coagulate below pH 4 at pHs near to their isoelectric point.

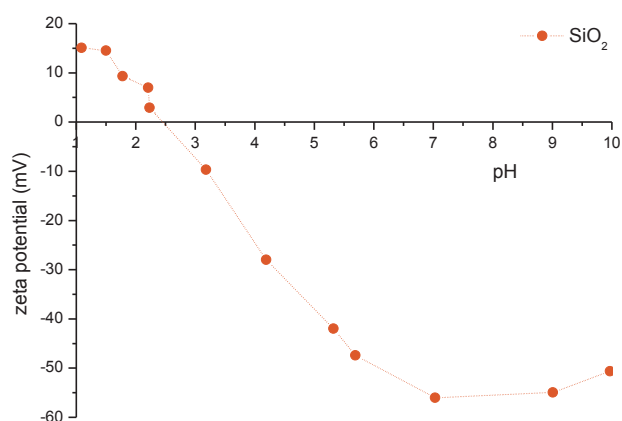


FIGURE 1.0-3 The surface potential of colloidal silica is depending on the pH. A potential of zero charge is observable at pH 2.5 reliant on the pKa of 3.54 of the silanol groups on the particle surface. The circles show the effect that the use of a catalyst has on the zeta potential of the particles to be modified.

It has been shown^[9-12] that the surface of amorphous silica synthesized by a Stöber process bears four to six silanol groups per nm². By thermogravimetric analysis (TGA) measurements we can follow the mass loss of silica nanoparticles depending on the temperature (see **FIGURE 1.0-4 A**).

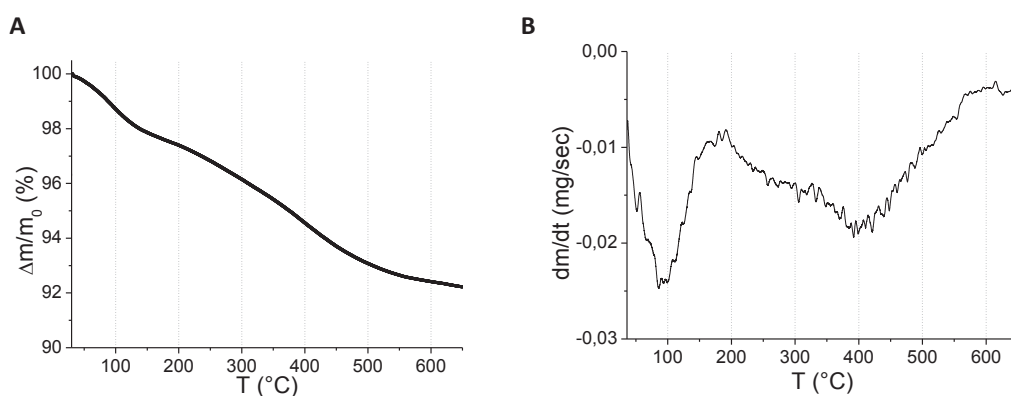


FIGURE 1.0-4 A: TGA diagrams of 50 nm sized silica nanoparticles **B:** Differentiated TGA diagram of silica nanoparticles synthesized by the “Stöber” method.

We can clearly distinguish the loss of physisorbed and chemisorbed compounds by the visualization of the differentiation of the thermogravimetric diagram (see **FIGURE 1.0-4 B**). A first intense mass loss observed at about 100 °C can be attributed to the loss of water molecules physically adsorbed to the

silica surface. A second mass loss can be observed between 160 °C and 600 °C. It can be attributed to the loss of chemically adsorbed molecules. Regarding the aspect of this mass loss we can differentiate a plateau at a temperature of about 300 °C and at a peak about 400 °C. This observation can be explained by the fact that molecules chemically adsorbed to the surface of the nanoparticles leave the particles at lower temperatures than molecules chemically adsorbed in the inside of the porous silica matrix^[13]. The second mass loss is partly due to the condensation of uncondensed silanol groups and the loss of chemisorbed water. Perro and co-workers^[8] have shown that the mass loss observed between 160 °C and 600 °C is too important to be attributed solely to the loss of water. It is equally caused by the departure of C₂H₅ fragments remaining in the silica matrix due to an incomplete hydrolyzation of the TEOS precursor during the synthesis of the amorphous colloidal silica.

We analyzed the silica nanoparticles by diffuse reflectance infrared fourier transform spectroscopy (DRIFT). The infrared spectrum of colloidal silica is well known and has already been published in literature^[14-17]. **FIGURE 1.0-5** shows the DRIFT spectrum of colloidal silica. In the spectrum we distinguish the vibration bands from 400-1200 cm⁻¹ characterized as Si-O-Si vibration, the bands between 1600-2000 cm⁻¹, the two bands in the range of 2900 to 3000 cm⁻¹ attributed to vibrations of alkyl chains of unreacted TEOS and the broad band at in the range from 3400 to 3700 cm⁻¹ due to the H and OH vibrations.

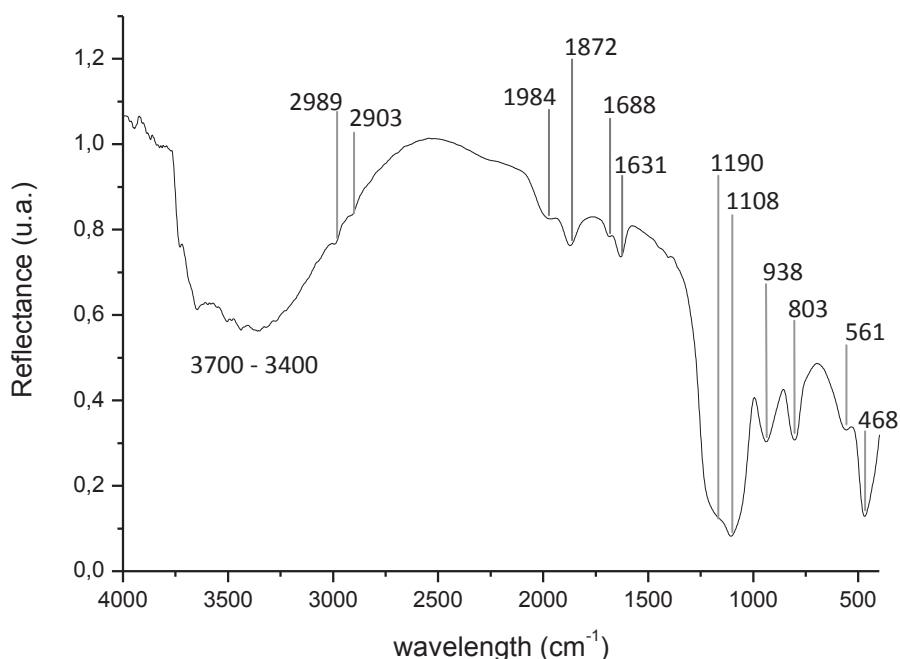


FIGURE 1.0-5 Infrared spectrum of colloidal silica synthesized by a Stöber reaction process recorded by DRIFT spectrometry (see Annex 1).

More precisely the broad and intense band at 3700 - 3400 cm⁻¹ has to be attributed to the stretching vibrations of hydrogen bonds and Si-OH groups covering the surface of the colloidal silica, H-bonded

H₂O and H-bonded OH vibrations of alcohol. According to Martinez et al.^[17] the broadness of this band may indicate different local environments for hydroxyl groups located in the silica matrix. The weak band at 2989 cm⁻¹ is attributed to asymmetric stretching vibrations of C-H bonds and the second weak band at 2903 cm⁻¹ to their symmetric stretching vibrations. The C-H bonds detected belong to alkyl chains of only partially hydrolyzed TEOS, which are incorporated to the silica matrix. The bands in the range of 1600 to 2000 cm⁻¹ have also been observed^[15]. The band at 1872 cm⁻¹ can be identified as a typical silica overtone band^[18,19]. It has been supposed that the band at 1630 cm⁻¹ is due to H₂O molecules^[17] incorporated in the matrix and has been identified as scissor-bending vibration of matrix intercalated molecular water^[16]. Bands appearing in the region of 1600 to 1700 cm⁻¹ could also pertain to stretching vibrations of ammoniac incorporated in the matrix, which is present during the sol-gel synthesis of the silica colloids. In contrast the vibration bands in the range of 400-1200 cm⁻¹ are fully attributed to Si-O-Si vibrations. The band at 1108 cm⁻¹ belongs to antisymmetric stretching vibrations, possessing a shoulder at 1190 cm⁻¹. This shoulder appears due to a splitting of longitudinal optical and transverse optical stretching motions. The band at 938 cm⁻¹ has been attributed to Si-O-Si stretching vibrations, the band at 803 cm⁻¹ to Si-O-Si bending and the band at 468 cm⁻¹ to Si-O-Si rocking vibrations. The weaker band at 561 cm⁻¹ arises due to cyclic structures in the silica network^[14,16]. The analyzed vibrations are resumed in Annex 2 TABLE 0-1. The detailed analysis of infrared spectra of Stöber silica is important, because we will characterize modified silica colloids by DRIFT and analyze bands appearing due to organic residues on the silica surfaces.

We have now introduced the synthesis of the 50 nm sized silica nanoparticles, which we accomplished via a sol-gel process introduced by Stöber and coworkers. This paragraph served to analyze the morphological and physico-chemical characteristics of these nanoparticles. We were able to show that we can synthesize homogeneously sized spherical silica nanoparticles. We calculated their mass and their surface area. We commented on their amorphous character, their surface potential and the density of silanol groups present on their surface. We were able to prove that synthesized silica nanoparticles possess a natural porosity and contain high amounts of chemisorbed water and ethoxy residues in their matrix. The fact that colloidal silica synthesized by the Stöber method possesses well-known physico-chemical properties is advantageous for their use as a platform for chemical surface modifications. In what follows these nanoparticles will serve as body material for the study of chemical surface modifications suitable to affix quaternary ammonium groups on silica surfaces.

2. SYNTHESIS OF QUATERNARY AMMONIUM GROUP BEARING SILICA SURFACES BY CHEMICAL SURFACE MODIFICATION WITH AN ORGANOFUNCTIONAL SILANE COUPLING AGENT

Silica surfaces are - like the surfaces of other metal oxides - an ideal platform for chemical modification with organofunctional silane coupling agents (see **CHAPTER I, PASSAGE 3.1**). The silanization of the synthesized silica nanoparticles with an organofunctional silane coupling agent wearing an organic graft, which contains a quaternary ammonium group, is one strategy to implement these functional groups on a metal oxide surface.

2.1 General information about the silanization process and the choice of a quaternary ammonium group bearing silane coupling agent

It will be remembered that organofunctional silane coupling agents are built up of three alkoxy groups bonded to a central Si atom, whereas an organic entity R' is equally connected to the Si atom. We previously explained that the chemical modification of a metal oxide surface is obtained by a hydrolysis/condensation reaction between the OH groups present on the surface of the metal oxide nanoparticles and the alkoxy groups of a chosen silane coupling agent. The silane monomers undergo the hydrolysis of their three alkoxy functions and an intermolecular condensation process takes place. In an equilibrium reaction the hydrolyzed monomers will condense to form oligomer chains, which adsorb to the metal oxide surfaces. Subsequently covalent M-O-Si bonds form via a condensation reaction.

Hydrolysis and condensation reactions can be catalyzed under alkaline or acidic reaction conditions. In both cases the catalyzed hydrolysis follows an S_N2 mechanism. An S_N2 reaction is a nucleophilic substitution reaction taking place via one transition state as shown in **CHAPTER I, FIGURE 2.2-9** for the hydrolysis of tetraethylorthosilicate (TEOS). It is a reaction of the second order; therefore its reaction rate is defined by the **EQUATION 2.1-1**:

$$\frac{d[Nu - R]}{dt} = k[Nu:^\ominus][R - X]$$

Nu – nucleophil

X – leaving group

k – rate constant

EQUATION 2.1-1 Equation determining the reaction rate of a S_N2 substitution reaction^[20].

Because of the fact that alkoxy groups need to be activated before being able to act as a leaving group^[20] the hydrolysis of organofunctional silane coupling agents solely takes place if it is catalyzed as shown by Leyden and coworkers for trimethoxymethylsilane, trimethoxyethylsilane and monomethoxytrimethylsilane^[21]. Weak Brønsted bases are known to be good leaving groups, therefore the reaction rates depends on the length of the alkylgroup of the alkoxy leaving group.

Subsequently tetramethoxysilanes have been shown to hydrolyse twenty times faster than tetraethoxysilanes^[22]. The reaction rates of condensation reactions depend mainly on the quantity of hydrolyzed silane present in the reaction environment^[21], the length of the organic graft and the mode of catalysis. Under acidic catalysis it becomes the rate determining step of the silanization reaction due to the fact that under these conditions hydrolysis takes place much faster^[23].

Whereas aminofunctionalized silane coupling agents are able to autocatalyze hydrolysis and condensation due to the basicity of amine groups and are often used in the presence of a base, most silane coupling agents are grafted during acid catalyzed silanization processes. The choice of the catalysis mode depends subsequently on the applied silane coupling agent. We decided to operate with a common quaternary ammonium bearing silane coupling agent during our study *N*-trimethoxysilylpropyl-*N,N,N*-trimethylammonium chloride (TMAPS) (see FIGURE 2.1-1). It has already been utilized to synthesize silica nanomaterials containing quaternary ammonium groups under acidic or alkaline catalysis.

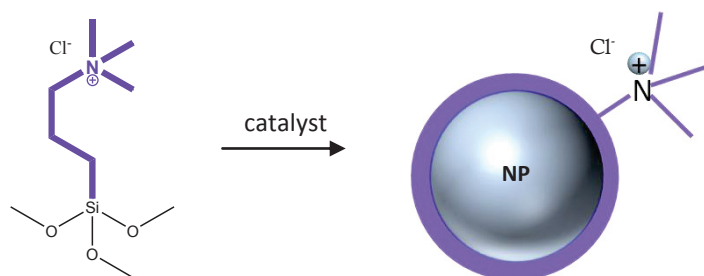


FIGURE 2.1-1 Structure of *N*-Trimethoxysilylpropyl-*N,N,N*-trimethylammonium chloride (TMAPS), which is used to modify silica and iron oxide nanoparticles. The modified nanoparticles bear quaternary ammonium groups on their surface.

TMAPS was first employed for the synthesis of hybrid organo-silica spheres. By cocondensing TMAPS and TEOS the synthesis of positively charged silica nanoparticles was achieved in 2000, when Markowitz et al.^[24] added quaternary ammonium functionalized silane to a reversed microemulsion before adding TEOS to form silica colloids. The hybrid nanoparticles obtained showed a higher mesoporosity than particles synthesized by co-condensation with the organofunctional silane coupling agent (3-Aminopropyl)trimethoxysilane (APS)^[24]. Hence this strategy was used to synthesize mesoporous silica nanoparticles functionalized with quaternary ammonium groups in the presence of surfactants^[25-27]. After a thermal treatment at 50 °C for 25 hours the prepared hybrid nanoparticles show positive zeta potentials of about 35 mV at acidic pH 5, but an isoelectric point which is situated at pH 6.73.

Also the chemical surface modification of silica-materials with TMAPS has been undergone. Some groups added TMAPS directly to the Stöber medium used for the synthesis of colloidal silica without the employment of a thermal treatment^[28-30] leading to particles with maximal zeta potentials of about 30 mV. Atchison et al.^[31] developed two different modification strategies. They modified silica particles once under basic reaction conditions with Lysine as the base, a second time under acidic conditions with HCl as the catalyst. After the hydrolysis of TMAPS thermal treatment at 60 °C was

applied for both during 24 hours to improve the condensation process. The obtained silica particles are positively charged and possess a maximal zeta potential of 40 mV at pH 4, but the modified particles showed an isoelectric point at about pH 7 for lysine catalyzed synthesis and pH 8 for acid catalyzed modification^[31]. Chang et al. modified silica particles with TMAPS in EtOH using a basic catalysis for 6 hours. They obtained particles still positively charged at pH 7.35^[32]. By applying thermal treatment of 70 °C for 12 hours Chen et al. obtained positively charged particles with an isoelectric point at pH 8.4^[33].

Considering that modifying metal oxide nanoparticles with APS or EDPS already leads to particles possessing a point of zero charge at about pH 10^[23], it is quite surprising that silica nanoparticles modified with quaternary ammonium groups, whose charge is pH independent, up to now showed points of zero charge between pH 6 and pH 8. Instead gold nanoparticles bearing quaternary ammonium functions on their surface show zeta potentials about 34 mV at pH 7.4^[34]. Modification of Fe₃O₄ nanoparticles with TMAPS led to particles with an isoelectric point at nearly pH 11^[35-37]. These results show the enormous potential of the improvement of the chemical surface modification of silica nanoparticles with TMAPS. To use quaternary ammonium functionalized nanoparticles to label DNA, we need to achieve modified particles, which possess an isoelectric point at highly basic pH to guarantee their colloidal stability under physiological conditions at pH 7.4.

Nevertheless there are limitations to the chemical surface modification of silica with TMAPS. Apart from the fact that when we modify colloids chemically we need to guarantee their stability in the surrounding medium during the modification process, we should consider that quaternary ammonium groups are sensitive to degradation under the supply of temperature at basic pH. Hofmann elimination reactions^[38] can occur at basic pH and degrade the quaternary ammonium functions (see **FIGURE 2.1-2 A**).

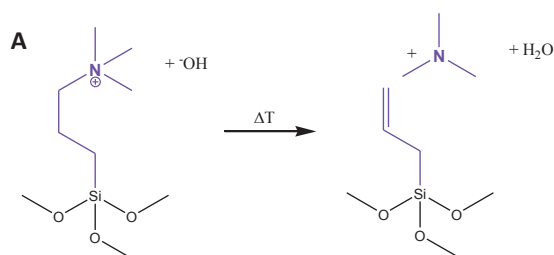


FIGURE 2.1-2 The use of TMAPS as a silane coupling agent is limited by several phenomena. **A:** Hofmann elimination reaction may take place under basic conditions under the supply of heat and leads to the elimination of a tertiary amine group under the formation of a C-C double bond.

We have now noted the reactions taking place during the silanization of a metal oxide surface and discussed the potential and limitations of a chemical modification of an silica surface with the quaternary ammonium bearing silane coupling agent TMAPS. The next passage shows the reactions undergone to chemically modify a silica surface with TMAPS.

2.2 Exemplary reaction protocols to undergo chemical surface modification of silica nanoparticles with the silane coupling agent TMAPS

For the chemical surface modification of silica nanoparticles with TMAPS we established two standard surface modification protocols, on which our study is based. At the beginning of this chapter exemplary modification protocols used to conduct the chemical surface modification of silica nanoparticles with TMAPS will be introduced together with the standard characterizations used to verify that successful silanization has taken place.

PROTOCOL 2.2-1 Modification of silica nanoparticles with TMAPS under basic catalysis

To 25 mL of 50 nm sized silica nanoparticles possessing a surface area of 6.4 m², kept in a Stöber reaction environment at pH 11.9, 0.36 mL of TMAPS (50% w/v in methanol) was added. The reaction mixture was stirred under room temperature for 12 hours before 15 mL of glycerol was added. The particles were transferred to the wetting agent glycerol by evaporation of EtOH, NH₄OH and H₂O. Thermal treatment was undergone for two hours at 100°C under vacuum. The modified particles were washed four times in absolute ethanol by centrifuging them at 13000 g for 25 minutes and finally dispersed in 10 mL H₂O (18.2 MΩ). After the redispersion in water, ethanol residues were removed from the medium by evaporation at 40°C.

PROTOCOL 2.2-2 Modification of silica nanoparticles with TMAPS under acidic catalysis

From 50 nm sized silica nanoparticles, synthesized in a Stöber reaction environment, EtOH and NH₄OH are evaporated using a rotary evaporator and 10 mL of the particles was transferred to 20 mL of a mixture of EtOH/H₂O (1:1). The particle concentration of the sol was determined by ICP. Different acids such as acetic acid (glacial), HCl (37 % w/v), HNO₃ (69 % w/v) or H₃PO₄ (85 % w/v) were used to adjust the pH of the sol; the pH was adjusted to 4.5 using acetic acid, pH 2 with H₃PO₄ and to pH 1 using HCl or HNO₃. To a sol containing nanoparticles with a surface area of 19.5 m² 1.09 mL of TMAPS (50% w/v in methanol) was added. The reaction mixture was stirred at room temperature during 12 hours. Subsequently 15 mL of glycerol was added. The particles were transferred to the wetting agent by evaporation of EtOH and H₂O. Thermal treatment was undergone for two hours at 100°C under vacuum. The modified particles are washed four times in absolute ethanol by centrifuging them at 13000 g during 25 minutes and finally dispersed in 10 mL H₂O (18.2 MΩ). After the redispersion in water ethanol residues were removed from the medium by rotative evaporation at 40°C.

After each modification process diffuse reflectance infrared fourier transform (DRIFT) spectroscopy has been used to identify the organic residues attached to the silica nanoparticles after the modification. In **FIGURE 2.2-1** we show an exemplary spectrum of TMAPS modified silica.

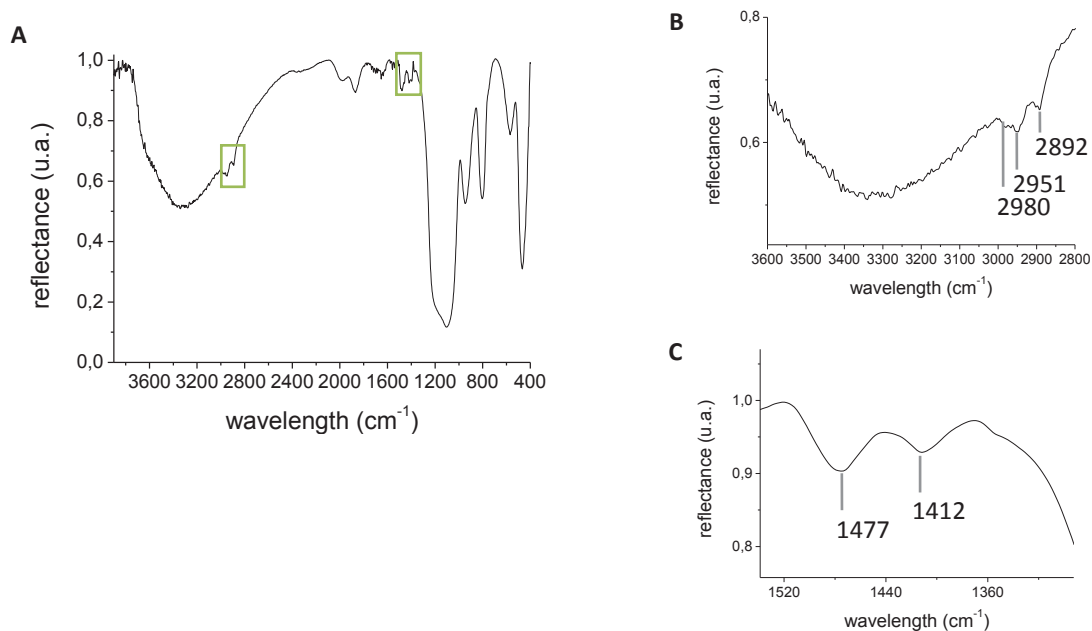


FIGURE 2.2-1 A: Infrared spectra of colloidal silica bearing quaternary ammonium groups after chemical surface modification of silica nanoparticles with TMAPS (condition 006, see Annex 2, **TABLE 0-3**). The green boxes indicate regions containing supplementary vibrations detectable after the modification with TMAPS. **B:** Enlargement of the section containing O-H and C-H vibrations. **C:** Enlargement of the spectrum showing C-N and N-H vibrations, making it possible to distinguish quaternary ammonium groups.

Compared to the spectrum of bare silica shown in **FIGURE 1.0-5** we can see an additional band at 2951 cm^{-1} in the spectrum, which can be attributed to C-H stretching vibrations of the methyl groups attached to a nitrogen atom. In the range from 1500 to 1390 cm^{-1} we can distinguish two vibration bands, which arise after TMAPS modification. The band at 1412 cm^{-1} is attributed to scissoring C-N deformation vibrations. The band of C-H scissoring vibrations arises at a value of 1477 cm^{-1} in the presence of quaternary ammonium groups^[39,40]. The analyzed vibrations are resumed in Annex 2 **TABLE 0-1**.

Further proof of successful surface modification of the nanoparticle surfaces can be given by mass spectrometry. We will discuss the mass spectrum shown in **FIGURE 2.2-2**, which we obtained by detecting the mass fragments leaving from TMAPS modified nanoparticle surfaces with increasing temperature recorded during the thermogravimetric analysis of TMAPS modified nanoparticles. In the temperature range from $160\text{ }^{\circ}\text{C}$ to $650\text{ }^{\circ}\text{C}$ solely fragments of the organic part TMAP (TMAP = $\text{C}_5\text{H}_{15}\text{N}$) of the TMAPS coupling agent are detectable due to its degradation. The inorganic part of the silica particles remains stable. The loss of grafted organic fragments starts when heating up the samples above $160\text{ }^{\circ}\text{C}$. Mass losses obtained below this temperature are caused by desorption of physically adsorbed water. Later loss of water leads to the volatilization of water molecules, which are chemically adsorbed or enclosed to the silica matrix.

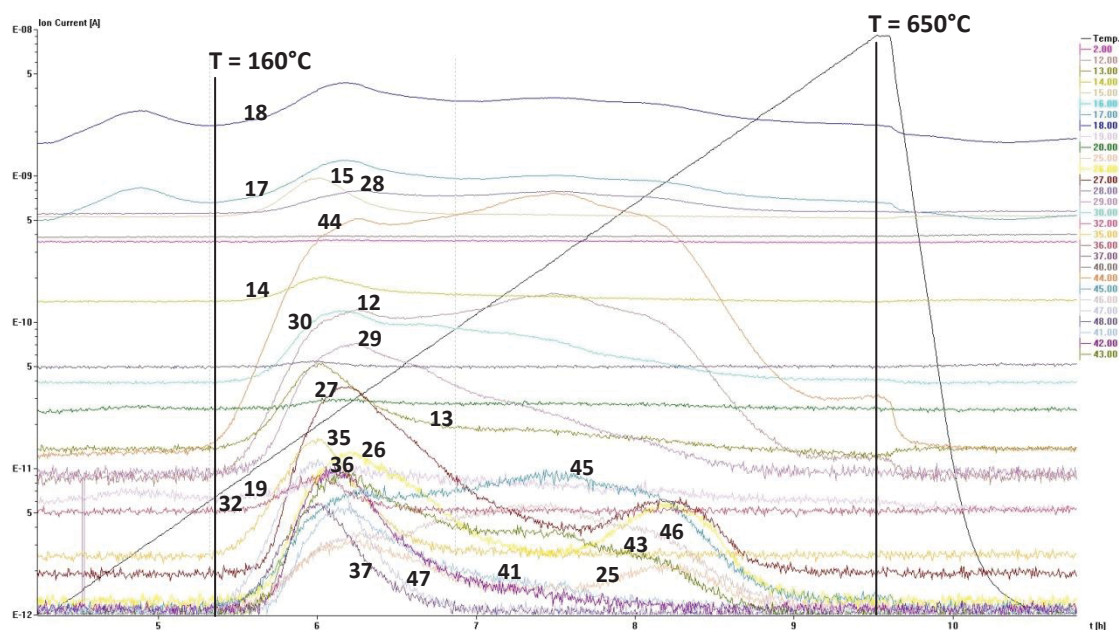


FIGURE 2.2-2 Mass spectrum of TMAPS modified silica nanoparticles (condition 006, see Annex 2, **TABLE 0-3**) recorded with a TG coupled mass spectrometer (see Annex 1).

Regarding the mass spectrum of TMAPS we detect a spectral line of m/z 18, which can be attributed to water and CH_4^+ , m/z 19 can be attributed to H_3O^+ and m/z 17 to OH^+ fragments provided from water. Contributing to the mass spectrum there may also be fragments such as CO^+ and N_2^+ ($m/z = 28$), NO^+ ($m/z = 30$), O_2 ($m/z = 32$) and NO_2^+ ($m/z = 46$). The fragments at m/z 35 and 37 are provided by Cl^+ isotopes, fragment m/z 36 probably from HCl^+ fragments.

The most intense spectral line is that of m/z 44; it can be assigned to different compounds such as CO_2^+ , but also C_3H_8^+ fragments emerging out of the propyl chain of the graft and $\text{C}_2\text{H}_6\text{N}^+$ fragments, which originate from the quaternary ammonium functions. Related nitrogen-containing fragments which we observe are $\text{C}_2\text{H}_7\text{N}^+$ fragments ($m/z = 45$), $\text{C}_2\text{H}_5\text{N}^+$ fragments ($m/z = 43$), $\text{C}_2\text{H}_3\text{N}^+$ ($m/z = 41$) and CH_4N^+ ($m/z = 30$). Further decomposition of the propyl chain leads to the fragments C_3H_7^+ ($m/z = 43$), C_2H_6^+ ($m/z = 30$), C_2H_5^+ ($m/z = 29$), C_2H_4^+ ($m/z = 28$), C_2H_3^+ ($m/z = 27$) and C_2H_2^+ ($m/z = 26$).

The spectral lines at 15, 14 and 12 m/z correspond to CH_3^+ , CH_2^+ and C^+ fragments. It is noticeable that the spectral line corresponding to m/z 26 shows a second peak, which does not appear at the line of m/z 27, which indicates that in addition to the alkyl fragment C_2H_2 a second species contributes to this mass repartition, which can be identified as $\text{CH}_3\text{Cl}^{2+}$ and $\text{CH}_2\text{Cl}^{2+}$ (^{37}Cl). Adjacently the related fragments of $\text{CH}_3\text{Cl}^{2+}$ and $\text{CH}_2\text{Cl}^{2+}$ (^{35}Cl) appear which are both detectable at m/z 25. These fragments are characteristic fragments deriving from quaternary methyl ammonium chlorides^[41]. All the fragments observed in the presented mass spectrum are shown in Annex 2 **TABLE 0-2**, which allows an overview of the detected fragments.

PROTOCOL 2.2-1 and **PROTOCOL 2.2-2** are suitable for the chemical surface modification of silica nanoparticles with TMAPS. The analysis of chemically modified nanoparticles by DRIFT and mass spectrometry shows that the surface modification of the silica nanoparticles with TMAPS takes place. Considering the fact that quaternary ammonium silanes don't autocatalyze the hydrolysis/condensation process occurring during this type of modification, we needed to choose a catalyst. Therefore we have implemented the chemical surface modification of silica nanoparticles with TMAPS using different catalysts at basic and acidic pHs. The formation of silanic layers formed by condensation depends in general on the conditions of the modification reaction as the quantity of TMAPS added per m² of silica surface available for silanization or the duration time and temperature of the thermal treatment^[42].

By implementing a chemical surface modification we can vary these different parameters to influence the silanization process. In what follows we will investigate the influence of the above named parameters on the success of the surface modification of colloidal silica with TMAPS. Furthermore we will explore the physico-chemical characteristics of the nanoparticles modified under different conditions. The conditions used to conduct these experiments are resumed in Annex 2, **TABLE 0-3**.

2.3 Influence of the amount of TMAPS during the chemical surface modification of silica nanoparticles on the final TMAP coverage

The amount of silane coupling agent added during the chemical surface modification to modify a fixed surface of silica generally impacts the surface density of the organic grafts TMAP present on the modified silica nanoparticle after the silanization process. Thermogravimetric analysis of the modified nanoparticles gives information about the density of the grafts on the particles surface. Observing the TG coupled mass spectrum of TMAPS modified nanoparticles we have seen that organic residues attached to the silica NPs are detected in the temperature range from 160 to 650°C and that mass losses below 160 °C result from the loss of physically adsorbed water. The surface density *d* of an organic graft is therefore calculated by the following equation:

$$d_{(graft)} = \frac{\Delta m_{160-650^{\circ}\text{C}}}{S \times m_{0(160^{\circ}\text{C})} \times M_{(graft)}}$$

d(*graft*) – surface density of an organic residue leaving between 160 and 650°C

$\Delta m_{160-650^{\circ}\text{C}}$ – mass loss measured between 160 and 650°C

$m_{0(160^{\circ}\text{C})}$ – mass of modified silica after the loss of physisorbed water

$M_{(graft)}$ – molar mass of the organic graft

(for TMAPS graft = TMAP⁺ +Cl⁻, C₅H₁₅NCl = 136.45 g/mol)

S_{spec} – specific surface area of the modified NP

EQUATION 2.3-1 Surface density of organic residues on the modified silica surface.

The specific surface *S* of silica colloids depends on their volume and surface area. It has been calculated by the following formula:

$$S = \frac{N_{NP} \times S_d}{m_T} = \frac{S_d}{\rho_{SiO_2} \times V_{NP}}$$

N_{NP} – number of nanoparticles (m_T/m_{NP})

S_d – surface area of one nanoparticle

m_T – total mass of nanoparticles in the sample

ρ_{SiO_2} – density of amorphous silica (g/cm^3)

V_{NP} – volume of one silica nanoparticle (cm^3)

EQUATION 2.3-2 Calculation of the specific surface of silica nanoparticles.

For nanoparticles of 50 nm diameter a specific surface of $60 \text{ m}^2/\text{g}$ is calculated. By determining the surface density of the attached organic residues we receive information about the amount of TMAPS needed to achieve saturation of the silica surface with the silanes used after the chemical modification process. The surface modification of silica with TMAPS has been effected as described in **PROTOCOL 2.2-2** with varying concentrations of TMAPS added (conditions 001-008, see Annex 2, **TABLE 0-3**) and the measured TGA diagrams are shown in **FIGURE 2.3-1 A**. For weak concentrations of TMAPS ($2.5 \mu\text{mol}/\text{m}^2$, $5 \mu\text{mol}/\text{m}^2$) the calculated surface densities (see **FIGURE 2.3-1 B**) may be overestimated due to the fact that the coating obtained under these conditions is not supposed to be homogenous and the contribution of chemically adsorbed water also leaving in the temperature range between $160 \text{ }^\circ\text{C}$ and $650 \text{ }^\circ\text{C}$ may be more important than for homogeneously coated surfaces. In general we try to avoid the falsification of the calculated surface densities due to the loss of water and ethoxy groups chemically adsorbed to the silica matrix of nanoparticle by the subtraction of the mass loss measured for the unmodified silica in the temperature range from $160 \text{ }^\circ\text{C}$ to $650 \text{ }^\circ\text{C}$.

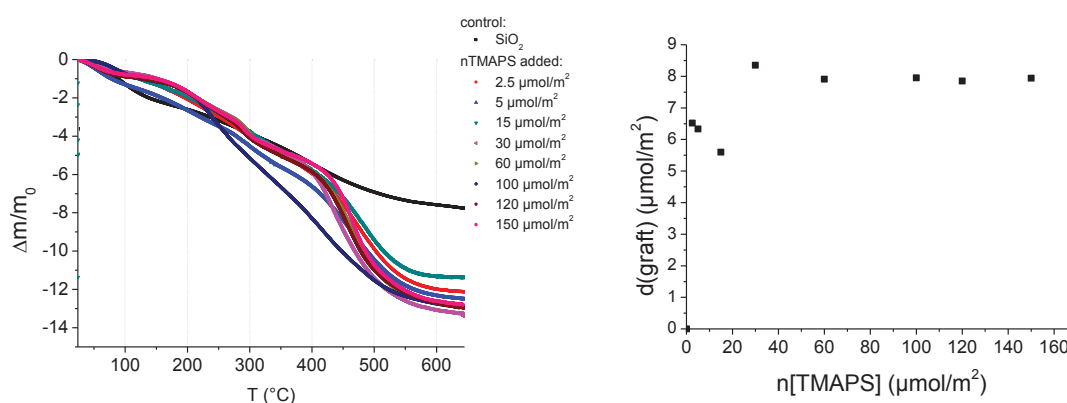


FIGURE 2.3-1 The two plots show the influence of the concentration of TMAPS added per m^2 of silica surface on the surface density obtained after TMAPS grafting. **A:** TGA diagrams of 50 nm sized silica nanoparticles chemically modified in the presence of different amounts of TMAPS. **B:** The calculated surface density of TMAP grafts on the modified silica colloids is presented in function of the amount of TMAPS added during the modification process.

Regarding the evolution of the surface densities of the modified nanoparticle as a function of the amount of TMAPS ($n\text{TMAPS}$) during the modification process, we can see that upon the addition of $60 \mu\text{mol}$ of TMAPS per m^2 of silica surface the surface densities of the graft stay constant (see **FIGURE 2.3-1**). The surface density of TMAP grafts on the modified silica colloids presented in function of the amount of TMAPS added during the modification process show a plateau due to the fact that even by

adding higher amounts of TMAPS the surface density of the modified nanoparticles batches stays around $7.91 \pm 0.04 \mu\text{mol}$ of TMAP grafts per m^2 on the modified silica. The finding that with increasing concentration of an organofunctional silane coupling agent the surface density of the organic grafts increases as well corresponds to similar observations in literature. A similar increase of surface density in relation to the silane concentration present during the surface modification measured by TGA mass loss has also been observed for the modification with aminosilanes as APTES^[23]. Aiming to achieve a maximal coverage of silica nanoparticles with TMAPS we will implement the chemical surface modifications using an amount of $100 \mu\text{mol}$ TMAPS per m^2 of silica surface which we wish to modify.

The observation that the amount of grafted silane on a nanoparticle can be enhanced by the increase of nTMAPS during the chemical surface modification has been indirectly confirmed by the analysis of the zeta potential of nanoparticles modified with increasing amounts of TMAPS. An increase in the surface density of TMAP grafts should also lead to an increase in the positive charges present on the nanoparticle surface and subsequent an increase of the zeta potential of the modified nanoparticle. For low amounts of nTMAPS it has been shown that the zeta potential of TMAPS modified particles increases with the increase of the initial concentration of TMAPS added to the reaction environment^[32,43]. It proved possible to increase the zeta potential of TMAPS modified nanoparticles from 7.9 mV at pH 7.35 using $0.296 \mu\text{mol}/\text{m}^2$ TMAPS to a potential of 19.0 mV at the same pH by the use of $2.18 \mu\text{mol}/\text{m}^2$ TMAPS^[32]. The relation of the increase in surface density and the increase in the zeta potential as a function of nTMAPS added to the modification reaction may be shown by the fact that the increase of surface density as well the increase of the zeta potential in function to the added silane amount follow the form of a Langmuir-type isotherm expression^[23,43].

In summing up all the relevant information this paragraph has enabled us to see that the surface density of a TMAPS modified nanoparticle increases with the amount of TMAPS added to the chemical surface modification. We saw that the values of surface density reach a plateau as soon as nTMAPS exceeds $60 \mu\text{mol}$ per m^2 of silica surface available for modification. Further addition of TMAPS apparently can't increase the grafting density further, because the silica surface becomes saturated.

2.4 Investigation of the surface density of TMAPS-coated silica nanoparticles obtained by chemical surface modification at different pHs

Intending that the pH on which the chemical surface modification is conducted may influence hydrolysis and condensation taking place (see PARAGRAPH 2.1) as well as the adsorption behavior of formed polysiloxane chains on the silica nanoparticles, we decided to implement the chemical surface modification of silica nanoparticles with TMAPS following PROTOCOL 2.2-1 and PROTOCOL 2.2-2 at different pHs (conditions 006,009-011, see Annex 2, TABLE 0-3). Comparing the TGA diagrams of

TMAPS-coated silica (see FIGURE 2.4-1), we can see that the observed mass losses differ from each other depending on the pH used during the modification process.

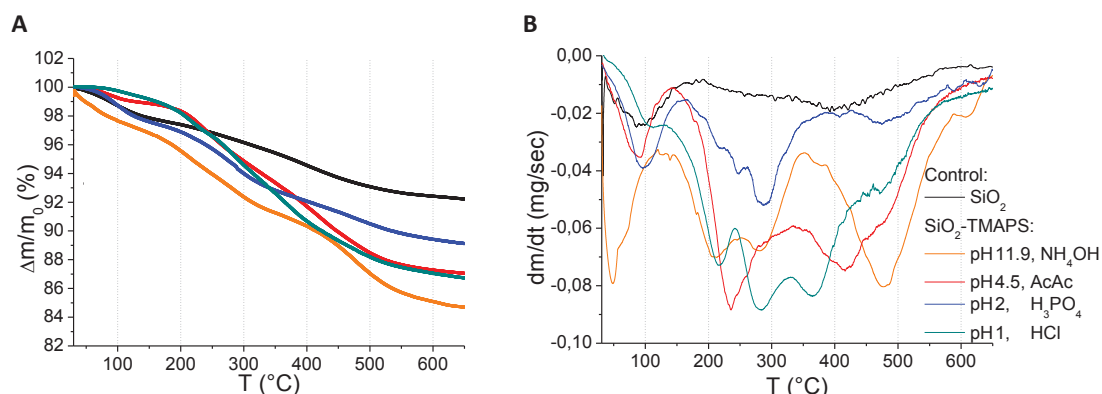


FIGURE 2.4-1 A: TGA diagrams of TMAPS-coated nanoparticles resulting from modifications with different catalysts. **B:** Differentiated TGA diagrams of TMAPS-coated nanoparticles resulting from modifications with different catalysts.

Desorption and degradation of differently adsorbed silane layers can be followed by thermogravimetric analysis (TGA). During the heating process for modified nanoparticles physically adsorbed compounds such as water molecules stabilized on the modified surface by hydrogen bonds, will leave first in the temperature range from 30 °C to 160 °C. The mass spectrum of TMAPS (see FIGURE 2.2-2) enabled us to see that organic fragments of the graft leave above temperatures of 160 °C and that they are completely removed when the maximum temperature of 650 °C is reached. Regarding the differentiated TGA diagrams (see FIGURE 2.4-1 B) we can see that at 160 °C a further mass loss takes place. The intensities of the observed mass losses increase first in the range from 160 °C to 360 °C and a second time in the temperature range from 360 °C to 600 °C.

The mass losses in the temperature range from 160 °C to 360 °C increase due to the departure of ionically adsorbed compounds like Cl⁻ ions as observed in the mass spectrum shown in FIGURE 2.2-2. The mass losses subsequently decrease when all ionically adsorbed compounds leave the surface at about 360 °C. It has been shown that a covalently bound monolayer of an organofunctional silane coupling agent on silica starts its decomposition at about 460°C^[44,45]. Therefore we presume that in the temperature range from 160 °C to 360 °C we detect the departure of organic fragments provided by the decomposition of the organic grafts of the outer layer of disordered silane multi layers condensed to the particle surface. The second increase of the mass losses observed in the TG diagrams in the temperature range from 360 °C to 650 °C may result from the loss of lower covalently bound silane layers of the cross-linked silane multilayers.

Regarding the total mass loss in the range from 160 °C to 650 °C we observe the highest mass loss for nanoparticles modified with TMAPS under basic conditions. The modifications implemented at pH 1 (HCl) and pH 4.5 (acetic acid) show a similar mass loss, whereas nanoparticles modified at pH 2 (phosphoric acid) show the smallest mass loss. From the mass losses Δm (mg) observed in the temperature range from 160 to 650 °C we subtract the mass loss Δm (mg) observed on the silica control particles in the same temperature range, which permits us to exclude the desorption of

chemically adsorbed water out of the calculations implemented to determine the surface density of TMAPS. An exemplary calculation is presented in EQUATION 0-1 (see Annex 3) and the calculated surface densities are reproduced in TABLE 2.4-1.

TABLE 2.4-1 Surface density of TMAPS-modified silica nanoparticles obtained by conducting the surface modifications at different pHs

Catalyst	pH	$\Delta m_{160-650^\circ\text{C}}$	d_{TMAPS} ($\mu\text{mol}/\text{m}^2$)	Graft/ nm^2
NH_4OH	11.9	- 11.93	8.08	4.8
Acetic acid	4.5	- 11.75	7.69	4.6
H_3PO_4	2.0	- 8.34	0.80	0.5
HCl	1.0	- 12.3	8.38	5.0

These values as well as the surface densities shown in FIGURE 2.3-1 B are high compared to maximum grafting densities of the structurally similar but sterically less big silane coupling agent APS. On metal oxide surfaces a maximum grafting density of $7.5 \mu\text{mol}/\text{m}^2$ has been determined^[23]. If we implement a modification with TMAPS which bears a sterically large trimethylammonium group we expect a grafting density inferior to the maximal grafting density of APS, but similar to the density that is observed for the modification of iron oxide with EDPS of $4.9 \mu\text{mol}/\text{m}^2$ ^[23]. However, for the modifications effectuated with NH_4OH , acetic acid or HCl we can determine grafting densities of about 7.69 to $8.38 \mu\text{mol}/\text{m}^2$. Only the TMAPS film obtained by catalysis with phosphoric acid possess a surface density of $0.8 \mu\text{mol}/\text{m}^2$, which might indicate the presence of about 0.5 TMAP grafts on one nm^2 of the modified silica surface.

It is known that with the increase of the initial concentration of the silane used for the surface modification the percentage of doubly and triply bridged silane units increases as well^[42]. The formation of silane multilayers has been observed for different silanes on different materials^[44,46-49]. A monolayer of (3-aminopropyl)ethoxy-dimethylsilane possesses a surface density of two amine functions per nm^2 ^[50]. Aminosilanes as APTES have been shown to form multilayers, which consist of 4 to 6 layers deposited on a modified surface^[51]. The grafting of disordered silane multilayers might be the origin of these unexpectedly high surface densities. Moreover the surface densities calculated are overestimated due to the fact that in the temperature range from 160-650 °C the TMAPS modified silica nanoparticles lose at the same time as water and ethoxy residues, which have been chemically adsorbed to the silica matrix. The subtraction of the mass loss measured for the unmodified silica from the Δm values obtained out of the TGA diagrams of modified nanoparticles permits us to avoid this falsification as much as possible. Anyhow we can't fully exclude the possibility that the departure of chemically adsorbed water in the silica matrix and ethoxy molecules contribute to the calculated surface density.

In this paragraph we have discussed the surface densities of TMAP grafts on silica nanoparticles, which have been modified at different pHs. We noted that the calculated surface densities may be overestimated due to a continuous loss of matrix adsorbed water and ethoxy residues of the silica nanoparticles. The differences between the surface densities of surface coatings of TMAPS on silica

observed between particles modified at unequal pHs may result from a differing “organization” of the silane layer conjugated to the colloidal silica. The pH may influence the hydrolysis/condensation rates and surface modifications at different pH may follow different adsorption processes of the silane oligomers on the metal oxide surface before the condensation of the silane film to the surface leading to silane coatings of different morphologies.

2.5 Investigation of the zeta potential of TMAPS-coated silica nanoparticles obtained by chemical surface modification at different pHs

The assumption that the pH of the reaction environment influences the chemical surface modification of silica with TMAPS can be maintained, considering the fact that the silica surface which is modified possesses a differing zeta potential depending on the pH at which the modification has been conducted (see FIGURE 1.0-3). Under basic reaction conditions silica has a negatively charged surface. When conducting the surface modification of silica with TMAPS in the presence of NH_4OH as a base (cond. 009, Annex 2, TABLE 0-3), the pH of 11.9 of the reaction setting determines a zeta potential of the particles of about -55 mV. Using a weak acidic catalyst such as acetic acid (AcAc) with a pKa of 4.75 we implemented the surface modification on silica particles possessing a zeta potential of about -30 mV. Using strong acids like H_3PO_4 (cond. 010), HCl (cond. 011) or HNO_3 (cond. 012) as a catalyst we adjusted the pH of the reaction at pH 2 to 1 permitting us to conduct the silanization of silica with TMAPS on a surface, which possesses positive zeta potential of about 10 mV. These differences may have a significant impact on the adsorption behavior of TMAPS on the silica surfaces during the silanization process.

Regarding the zeta potential (see FIGURE 2.5-1) of TMAPS-coated particles obtained by the differently catalyzed modification processes (conditions 006,009-012, Annex 2, TABLE 0-3) we see that nanoparticles modified at different pHs possess a different isoelectric point.

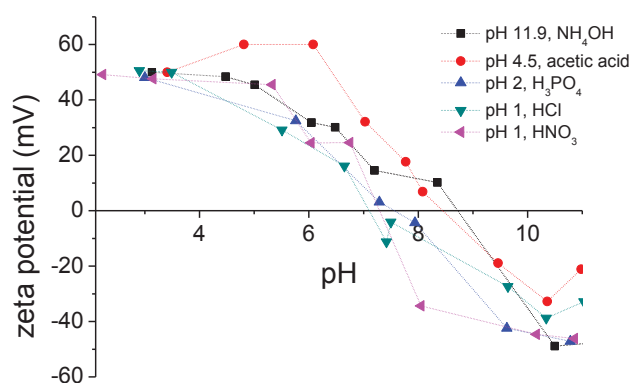


FIGURE 2.5-1 Zeta potential of TMAPS-coated silica nanoparticles chemically modified at different pHs.

Catalysis with H_3PO_4 at pH 2 shows an isoelectric point at pH 7.56, whereas the TMAPS-coated particles by modifications implemented at pH 1 with the acids HCl and HNO_3 show isoelectric points at pH 7.1 and pH 7.3. The nanoparticles modified in the presence of acetic acid as a catalyst show an intermediate isoelectric point at about pH 8.44, similar to the particles modified under basic conditions possessing an isoelectric point at pH 8.7. Even if the isoelectric point of nanoparticles modified under basic conditions is higher than the isoelectric point of nanoparticles modified at pH 4.5, the particles modified in the presence of acetic acid show a much faster increase in the zeta potential at pHs below 8.4. However, the modified nanoparticles start to coagulate in a potential range from 20 mV to -20 mV. Subsequently even for the TMAPS modified nanoparticles with the highest obtained isoelectric point (cond. 006, 009) we observe a reduced colloidal stability in the pH range from pH 6.5 up to pH 10, where the optical density of the samples increases due to higher light scattering of coagulated particle clusters. The problem of the colloidal stability of the modified nanoparticles is even more critical under physiological conditions, because of supplemental salts present in physiological media, which screen the positive charges of the modified surface decreasing their repulsion to each other.

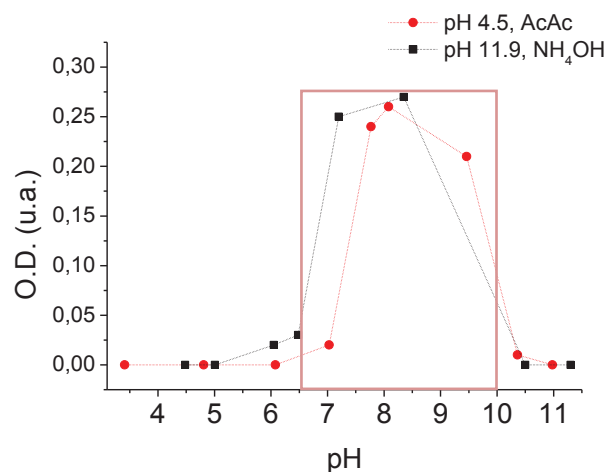


FIGURE 2.5-2 A: Optical density of nanoparticles modified with TMAPS resulting from modifications underwent with NH_4OH an acetic acid as catalysts is shown in dependence of the pH. It has been measured by UV-VIS spectrometry at 800 nm. The zone of flocculation is surrounded by a light red box.

The isoelectric points observed stay in the pH range where isoelectric points of TMAPS modified silica nanoparticles have been observed in the literature. Atchison et al.^[31] effectuated the modification silica nanoparticles with TMAPS at pH 8.9 catalyzed by lysine underwent and obtained TMAPS modified silica particles with an isoelectric point at pH 6.8, but they showed that the modification of silica colloids with TMAPS in an acidic environment at pH 1.2 leads to TMAPS modified silica NPs, which possess an isoelectric point at pH 8.1 and a zeta potential of about 10 mV at pH 7.4. Xiao et al.^[43] were able to obtain modified TMAPS particles possessing zeta potentials of about 22 mV at pH 6 and an isoelectric point at pH 8.3 by the use of HCl as a catalyst undergoing the modification at pH 4, whereas Chen et al.^[33] obtained positively charged particles with an isoelectric point at pH 8.4.

The inability to increase the isoelectric point of TMAPS-coated silica nanoparticles may be explained by the presence of uncondensed silanolate groups remaining on the modified surfaces. The TMAPS silanes may be grafted in disordered structures, permitting its positively charged organic head groups to interact with free silanolate groups on the silica surface (see **FIGURE 2.5-3**).

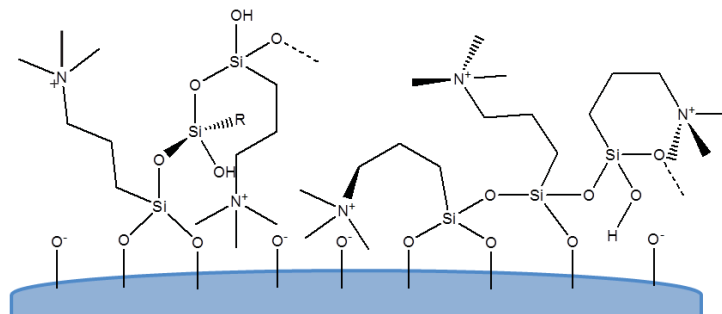


FIGURE 2.5-3 Scheme of possible orientations of TMAPS oligomer chains on negatively charged silica surfaces.

To know if the slow addition of TMAPS might lead to the adsorption and formation of a less disordered TMAPS coating we effectuated an experiment during which we added the amount of TMAPS drop-wise for five hours to the silica nanoparticles dispersed in a sol which has been adjusted to pH 4.5 with acetic acid. But even the slow addition of the silane TMAPS for five hours (condition 013, Annex 2, **TABLE 0-3**) did not seem to improve the outcome of the coating of silica nanoparticles with TMAPS (see **FIGURE 2.5-4**).

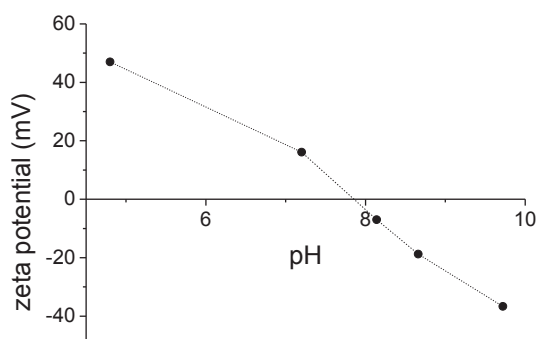


FIGURE 2.5-4 Zeta potential of nanoparticles modified with TMAPS under slow addition of the silane (condition 013).

The striving of TMAPS to organize itself with its positively charged quaternary ammonium group oriented to a negatively charged surface as shown in **FIGURE 2.5-3 A** has been demonstrated by Jin et al.^[52], who exploited this effect to synthesize porous silica matrixes around negatively charged, polyphosphate macromolecules. They used electrostatic interactions to assemble TMAPS molecules around DNA strands and then condensed silanolate groups at the exterior of this supramolecular assembly with TEOS to obtain two dimensional porous silica frameworks. Zheng et al.^[25] used the self organization of TMAPs around droplets of anionic surfactants such as N-myristoyl-l-glutamic acid to synthesize silica materials possessing quaternary ammonium functions bearing pores. Taking advantage of the electrostatic interactions of quaternary ammonium headgroups of TMAPS on

negatively charged surfactant, they use TMAPS functions as a co-structure-directing agent. Similar materials have been obtained by the co-condensation of TMAPS and TEOS around CTAB micelles, which permit the organization of TEOS and a subsequent formation of mesoporous silica on their quaternary ammonium bearing micelles surface^[26,27]. Chen et al.^[33] even suppose that during the use of such micelles TMAPS might even exchange with CTAB molecules of the micelles, which underlines their urge to orient their positive charge towards negatively charged compounds such as hydrolyzed TEOS. The tendency of quaternary ammonium bearing silanes to form disorderd networks of multilayers on modified surface with the quaternary ammonium headgroups plunged in the interior of the silane layer has, as we suggest, been indirectly demonstrated by Marchini et al.^[53]. They showed that surfaces modified with quaternary ammonium-bearing silanes by spin-coating processes can, after previous removal of quaternary ammonium functions on the surface, regenerate their antibacterial functions during treatment at 80 °C for 24 hours. They explain this observation by the movement to the surface of quaternary ammonium moieties, which had originally been located in the inner of the hybrid silane network.

Nevertheless we would have expected that when modifying silica nanoparticles with TMAPS under acidic conditions, we would decrease this behavior due to the fact that the surface of the silica nanoparticles, which we wish to modify, is positively charged and therefore electrostatically repulses the positively charged quaternary ammonium groups. Although we expected more even silane layers on silica surfaces for modifications implemented with strong acids, the nanoparticles obtained under these conditions finally show the lowest isoelectric points at about pH 7.

We might explain these results due to an observation we made on samples modified at pH 2. Measuring the zeta potential of silica nanoparticles modified with TMAPS at pH 2 in phosphoric acid immediately after the modification process we observed them to possess an isoelectric point at pH 9.8. After dialyzing the sample in ultrapure water (18.2 MΩ) for one day the zeta potential of the same particles was decreased and the isoelectric point shifted to pH 7.56 (see FIGURE 2.5-5).

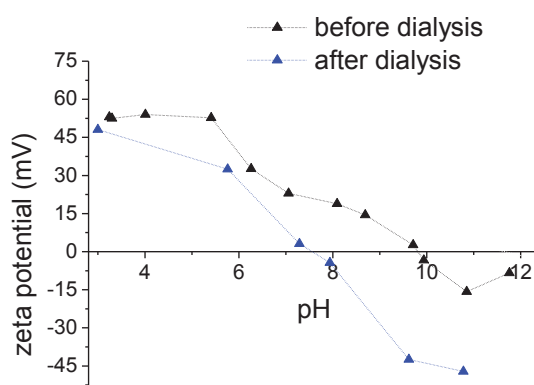


FIGURE 2.5-5 Zeta potential of NPs modified with TMAPS in the presence of phosphoric acid as a catalyst before and after dialysis.

Imagine that in the beginning of the silanization reaction the positively charged silica surface is surrounded by negatively charged phosphate ions, to which formed polysiloxane oligomers adsorb to the surface in a more or less disordered way and are then grafted on the silica surface. We assume that at first the remaining silanolate groups are screened by phosphate ions, which stay adsorbed to the modified silica surface, so that the quaternary ammonium groups of the coating stay at the surface of the silane layer and contribute to the overall charge of the nanoparticle surface (see FIGURE 2.5-6). In the following we measure an isoelectric point at pH 9.8.

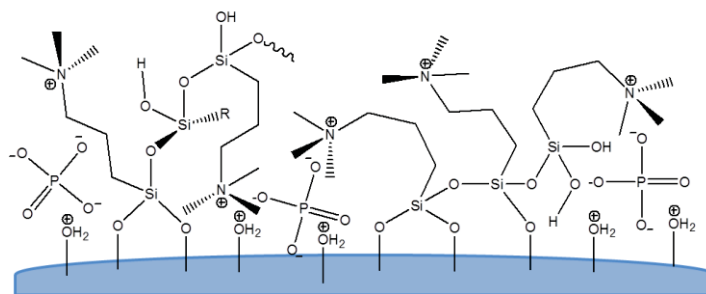


FIGURE 2.5-6 Scheme representing the surface of nanoparticles modified with TMAPS at pH 2 immediately after the silanization process.

Dialysis of these nanoparticles in ultrapure water will lead to a progressive release of the phosphate ions, which were electrostatically attracted to the silica surface, which has been positively charged during the execution of the chemical surface modification but becomes negatively charged in water. When we measured the pH of a sol containing TMAPS-coated nanoparticles modified at pH 2 in the presence of phosphoric acid immediately after the first dispersion of the newly modified nanoparticles in ultrapure water (18.2 M Ω , pH 5.8) we detected that the pH of the sol is pH 4, which is an observation that might be evidence of the release of phosphate ions taking place.

After the release of all phosphate ions originally adsorbed to the particle surface during dialysis negatively charged silanolate groups emerge on the surface of the modified nanoparticles. Subsequently the quaternary ammonium groups will interact with the appearing silanolate groups, so that the isoelectric point of the TMAPS-coated nanoparticles shifts to pH 7.56. The fact that the isoelectric point shifts to even a pH lower than the pHs observed for nanoparticles coated with TMAPS at pH 4.5 and pH 11.9 might be explained by the fact that the initial adsorption of phosphate ions to the positively charged silica surface at pH 2 prevented the surface from interaction with the TMAPS molecules and hindered the accomplishment of the chemical surface modification.

To ameliorate the modification process further modification conditions have been tested (conditions 014-016, Annex 2, TABLE 2.4-1). To find out whether during thermal treatment a change of catalyst and pH before the condensation of the silane layers to the surfaces may affect the quality of the coated silane films, the use of different acidic and basic catalysts during the hydrolysis, oligomerization and supramolecular assembly of silane oligomers on the silica colloids and during the condensation process has been tested. The experiments did not lead to improved results (see FIGURE

2.5-7 A, B, C), which shows that once they are adsorbed to the silica surface, polysiloxane films are not able to easily reorganize before their condensation to the particle surface.

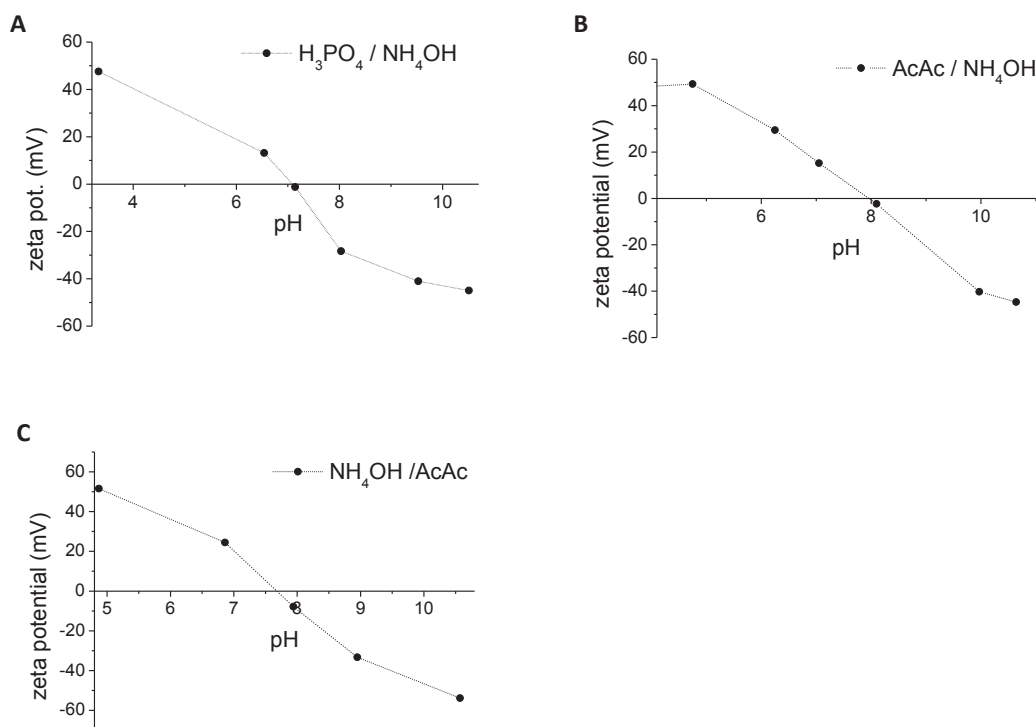


FIGURE 2.5-7 Zeta potential of NPs modified in the presence of different acidic and basic catalysts during the hydrolysis in an aqueous medium and during the condensation process in glycerol (**A**: condition 014, **B**: condition 015, **C**: condition 016).

The results presented up to now show the influence of pH on the development of a silanization reaction with TMAPS and made it possible to outline a major problem related to the coating of silica nanoparticles with the a permanently positively charged head group possessing silane coupling agent TMAPS, which is its tendency to interact electrostatically with negatively charged silanolate groups on the silica surfaces. This behavior leads to the formation of a disordered silane coating in which the quaternary ammonium groups plunge towards silanolate groups remaining on the surface after the silanization. If we compare the different conditions tested, the chemical surface modification of silica nanoparticles with TMAPS seems to work best at pH 4.5 adjusted with acetic acid. For this condition we obtain nanoparticles with an isoelectric point at pH 8.4, but almost more important a zeta potential rapidly increasing below pH 8.4 so that they possess a zeta potential of about 25 mV at pH 7.4 (see **FIGURE 2.5-1**). Nevertheless the zeta potential at this pH is too low to guarantee the colloidal stability of these TMAPS-coated nanoparticles under physiological conditions. In the following we will try to improve these results by varying the temperature and the duration time of the thermal treatment.

2.6 Influence of temperature and duration time of the thermal treatment on the condensation of TMAPS oligomers on silica NPs

The importance of thermal treatment to the success of the modification of metal oxide nanoparticles with organofunctional silane coupling agents is well known^[21,23,33,49]. By refluxing mesoporous silica nanoparticles in ethanol at 70 °C in the presence of TMAPS for 12 hours and subsequent heating at 60 °C for 24 hours of the nanoparticles in acidic ethanol, well-modified nanoparticles possessing an isoelectric point at pH 8.4 have been obtained^[33]. Xiao et al.^[43] showed that an increase in the temperature applied during the modification of silica with TEOS from 20 °C to 70 °C makes it possible to increase the zeta potential at pH 4.5 of about 4 mV. Furthermore it is known that moderate heating liberates amine functions which are deficiently turned towards and captivated in the grafted silane layers^[49]. This can be explained by the fact that heating under vacuum as accomplished during thermal treatment leads to the breaking of the hydrogen bond formed between silanolate groups of the silica nanoparticles and the amine groups of the silane^[23]. Similar behavior has been shown on surfaces modified with quaternary ammonium group bearing silanes by Marchini and co-workers^[53], who showed that heating at 80 °C for 24 hours permits the regeneration of antibacterial activity of surfaces coated with TMAPS. Therefore we would like to investigate if higher temperature or a longer duration time of the thermal treatment, which we effectuate to promote the condensation of TMAPS on silica nanoparticles, has a beneficial effect on the zeta potential of TMAPS-coated nanoparticles. The increase in temperature or duration time of the thermal treatment might help to break the ionic bond forming between quaternary ammonium groups and the silanolate groups of silica nanoparticles, and lead to an improved grafting.

Subsequently we effectuated the thermal treatments of the differently catalyzed modifications at temperatures of 130 °C and at 150 °C (conditions 017-025, see Annex 2, TABLE 0-3) Thermal treatments have been undergone in glycerol serving as a wetting agent at high temperatures for modification reactions at pH 1, pH 2, pH 4.5 and pH 11.9, and the zeta potentials were measured afterwards. The results are presented in comparison with the zeta potential of nanoparticles modified by thermal treatment at 100 °C (see FIGURE 2.6-1).

Regarding the zeta potentials measured we noted that thermal treatment at high temperature did not lead to TMAPS-modified nanoparticles with higher zeta potential nor isoelectric point. The modifications implemented with NH₄OH or acetic acid led to lower zeta potentials and lower isoelectric points of TMAPS-coated particles, which may be caused by an intermolecular condensation of silane oligomers and less condensation of silane molecules to the nanoparticle surface. Equally nanoparticles obtained from modifications undergone at high temperature at pH 1 in the presence of nitric acid do not show an improved zeta potential. We observed that the isoelectric points of modified nanoparticles modified at high temperatures in the presence of phosphoric acid increase a little, but after dialysis of the samples we noted that their isoelectric points decrease significantly as shown before (see FIGURE 2.5-5).

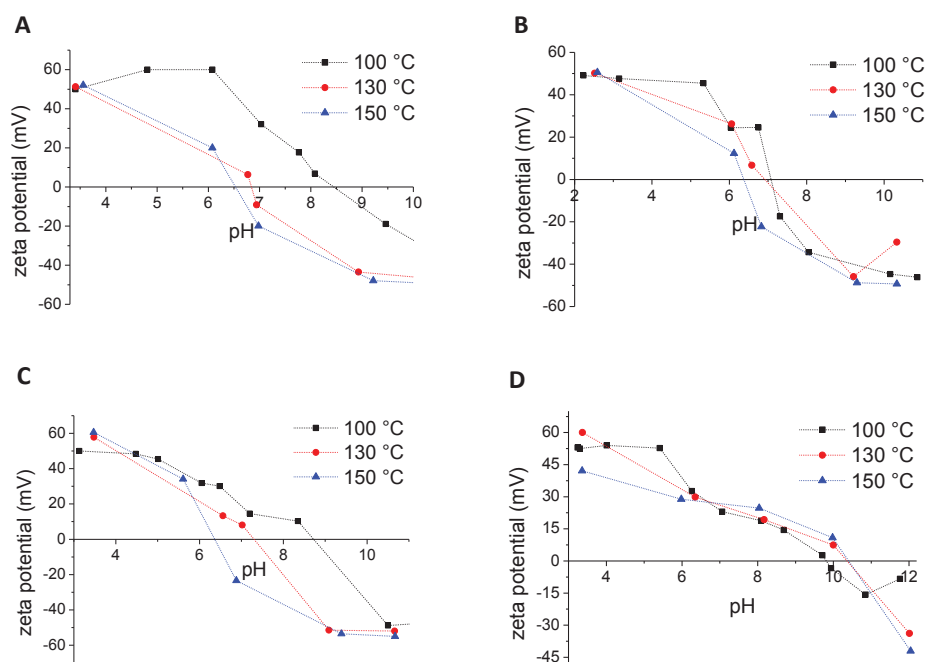


FIGURE 2.6-1 Zeta potentials of NPs modified with TMAPS after thermal treatments at different temperatures in the presence of **A:** Acetic acid (cond. 006, 017, 018), **B:** HNO₃ (cond. 012, 019, 020), **C:** NH₄OH (cond. 009, 021, 022) and **D:** H₃PO₄ (cond. 010, 024, 025) as a catalyst.

The observation that the isoelectric points of nanoparticles modified with TMAPS at high temperatures shift to more acidic pHs may be explained by the fact that physically adsorbed silane oligomers may detach from silica surfaces more rapidly under the influence of heat, so that they can leave the particle surface without being condensed to the grafted layer. At alkaline pHs heat induces degradation processes of the quaternary ammonium groups via Hofmann elimination reactions^[54], which might be a further reason for the low isoelectric points observed for nanoparticles modified at high temperature in the presence of a base. To be sure to avoid such chemical degradations we decided to accomplish a surface modification of silica nanoparticles at lower temperature (50 °C) and in the presence of acetic acid. At this temperature (50 °C) modifications of iron oxide nanoparticles with TMAPS led to isoelectric points at pH 11^[35-37]. However in our case the effectuation of thermal treatment at 50 °C for two hours as well as the effectuation of a thermal treatment for twelve hours (conditions 026, 027, Annex 2, **TABLE 0-3**) didn't improve the condensation of TMAPS at the nanoparticle surface (see zeta potentials in **FIGURE 2.6-2 A** and **B**). The high isoelectric points observed for iron oxide nanoparticles, which have been modified with TMAPS are probably due to the characteristic surface properties of unmodified iron oxide nanoparticles already possessing an isoelectric point at pH 7.

To investigate the influence of a prolongation of the duration time of the thermal treatment further, thermal treatment has been accomplished at 100 °C for twelve hours for the modification of silica nanoparticles with TMAPS in the presence of acetic acid or NH₄OH (conditions 028, 029,

Annex 2, TABLE 0-3). The zeta potentials of the nanoparticles obtained under these conditions are presented in FIGURE 2.6-2 C and D.

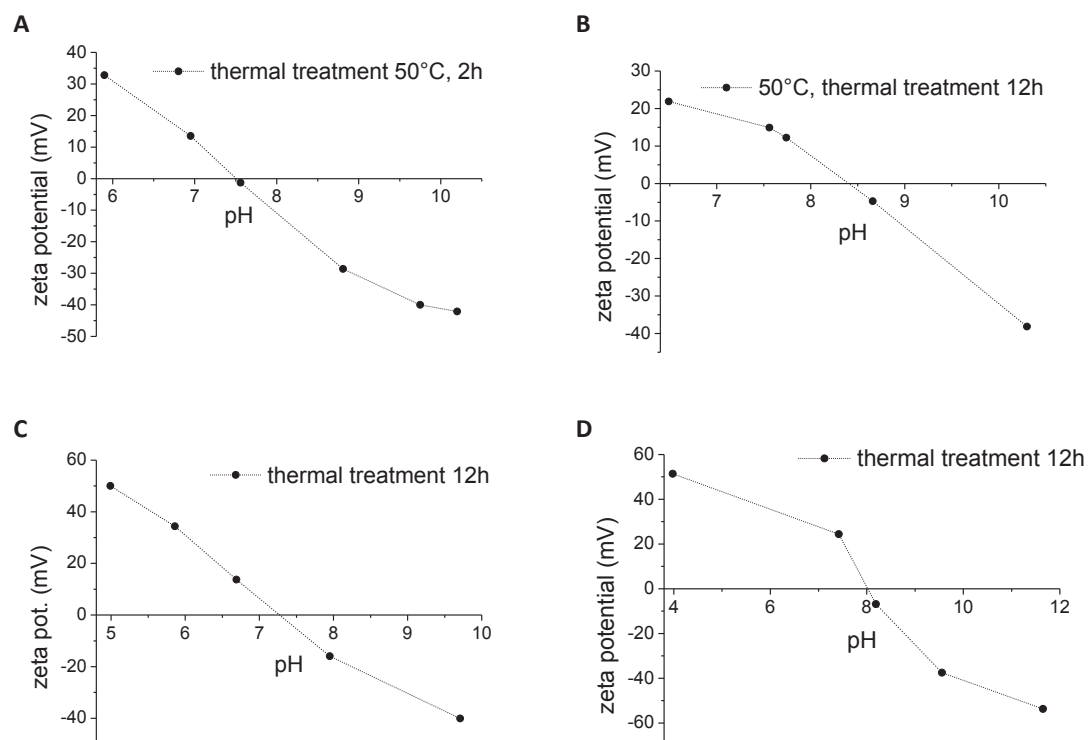


FIGURE 2.6-2 Zeta potentials of silica nanoparticles modified with TMAPS while applying a thermal treatment at **A:** A temperature 50 °C for two hours in the presence of acetic acid (cond. 026). **B:** A temperature of 50 °C for twelve hours in the presence of acetic acid (cond. 027). **C:** A temperature of 100 °C for twelve hours in the presence of acetic acid (cond. 028). **D:** A temperature of 100 °C for twelve hours in the presence of NH₄OH.

In recapitulating we can say that the results shown in this paragraph demonstrate that conducting of thermal treatment of chemical surface modification process with TMAPS at high temperatures or extended duration time is not suitable for improving the TMAPS coating on silica nanoparticles. This is probably due to the fact that the application of heat under vacuum is enough to break relatively weak physical bonds due to van der Waals interactions and hydrogen bonding but not to abrogate ionic bonds forming between quaternary ammonium groups and silanolate groups. Therefore polysiloxane chains only physically adsorbed to the silica nanoparticle may, under the influence of heat, leave the surface of the modified nanoparticles before being condensed on it, whereas a positive effect on the grafting as expected, if the abrogation of ionic bonds would have been successful, was not observed. The prolongation of the duration time for ten further hours to twelve hours solely showed a beneficial effect for nanoparticles modified by a thermal treatment at 50 °C, which can be explained by the fact, that at lower temperatures less condensation reactions per hour take place. A longer duration time is needed to condense TMAPS molecules to the silica surface until its saturation. Apart from the fact that the isoelectric point of such modified particles did not shift to a higher pH than pH 8.4 shows that Hofmann degradation reactions can virtually be excluded as an explanation for the continuous obtainment of TMAPS nanoparticles with isoelectric points at about pH 8.4.

2.7 The execution of end-capping reactions on TMAPS modified nanoparticles

The remaining silanol groups on the silica surface may transform into silanolate groups above pH 2.5 and therefore decrease the overall zeta potential of the TMAPS modified particles at alkaline pHs. To prevent the zeta potentials of the modified nanoparticles being affected by uncondensed silanol groups remaining on the surface after silanization, the modified nanoparticles (cond. 006, see Annex 2, TABLE 0-3) were further allowed to react with chlorotrimethylsilane ClSiMe₃ or glycidol. We expect that the end-capping of silanolate groups with ClSiMe₃ or glycidol might shift the isoelectric point of TMAPS modified nanoparticles to higher pHs.

Silylating end capping reactions of silanol groups with ClSiMe₃ can be effectuated in dry solvents at room temperature in the presence of a base and are often used to render silica surface hydrophobic^[55,56]. Deschner et al.^[57] showed that the silylation of silica NPs with chlorosilanes and NEt₃ as a base in mixtures of hexane and toluene or hexane and THF can achieve 90 % yield. The reaction was effectuated under different conditions to ensure the elimination of free silanolate groups and the zeta potential of the prepared nanoparticles (cond. 006, Annex 2, TABLE 0-3) was measured to determine the influence of remaining uncondensed silanolate groups on the isoelectric point of the modified samples.

PROTOCOL 2.7-1 Modification of TMAPS modified silica nanoparticles with chlorotrimethylsilane

To a dispersion of TMAPS modified silica nanoparticles with a surface area of 8.236 m² in 10 mL of absolute EtOH 700 μL of triethylamine and 1 mL chlorotrimethylsilane were added under magnetic stirring at room temperature. Instantaneous crystallization of triethylamine chloride was observed and the reaction mixture became dense, hindering further stirring. After 15 minutes of incubation the particles were sonicated in a sonication bath for 2 minutes, leading to redissolution of the crystals and the redispersion of the treated particles. 1 mL of chlorotrimethylsilane was added leading to the same effect of crystallization. Again the reaction mixture was sonicated for 2 minutes. The redispersed particles are centrifuged at 13000 g during 15 min. and washed four times with 20 mL of H₂O (18.2 MΩ).

The same reaction has been implemented in anhydrous toluene, anhydrous hexane and THF to which the particles had been transferred by rotary evaporation of EtOH at 40°C. The macroscopic observations and proceedings were similar to these described for the reaction in absolute EtOH.

The ring opening of glycidol by reaction with OH or COOH groups is often effectuated in toluene under refluxing for several hours^[58]. Ring opening can also be effected by the reaction of glycidol with amine groups of aminosilanes^[59]. The reaction has been employed to cap remaining silanol groups on the silica surface by the reaction of glycidol^[60], leading to a ring opening of the molecule and the development of two alcoholic OH groups instead of one silanol group. It is advantageous to replace

silanolate groups by trimethylsilyl or by alcohol groups. Alcohol groups possess a high pKa of 16, which will hinder their deprotonation in the pH range of interest.

PROTOCOL 2.7-2 Modification of TMAPS modified silica nanoparticles with glycidol

2 mL of a sol of silica nanoparticles modified with TMAPS dispersed in absolute EtOH was added to 20 mL of DMF. Ethanol was eliminated out of the reaction mixture by rotary evaporation at 40 °C. To the solution containing modified nanoparticles with 3.73 m² of surface area 933 μL of glycidol was added. Under magnetic stirring the particles were refluxed at 75°C for 5 hours. Subsequently the particles were centrifuged at 13000 g for 15 min and washed four times with H₂O (18.2 MΩ). The modified nanoparticles were then redispersed in 10 mL H₂O (18.2 MΩ). Also the reaction has been done using dry toluene as a solvent; but undesired particle coagulation occurred then.

FIGURE 2.7-1 shows the zeta potentials of TMAPS modified nanoparticles, which have been end-capped with chlorotrimethylsilane or glycidol under different reaction conditions. We observe that the modifications of TMAPS-modified nanoparticles implemented with ClSiMe₃ and glycidol do not induce a shift of the isoelectric point to more basic pHs.

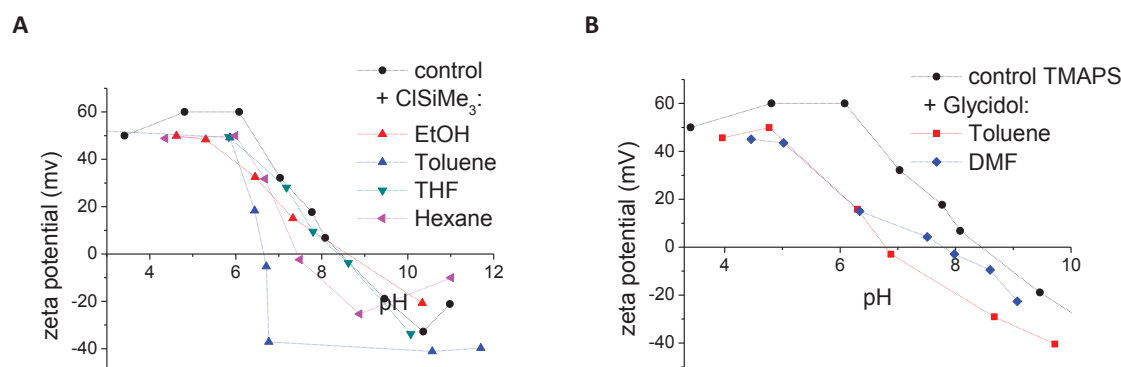


FIGURE 2.7-1 **A**: Zeta potential data of TMAPS modified silica nanoparticles after subsequent modification of the NPs with ClSiMe₃ in different solvents. **B**: Zeta potential data of TMAPS modified silica nanoparticles after subsequent modification of the NPs with glycidol in different solvents.

It seems that the silanolate groups, which we would like to react with ClSiMe₃ or glycidol are not accessible to these two molecules because of the fact that while they interacting with quaternary ammonium groups they are sterically protected from further reaction. Control reactions accomplished on unmodified silica nanoparticles led to the generation of hydrophobic silica nanoparticles, which after reaction with end-capping reagents could not be dispersed in ultrapure water (18.2 MΩ) anymore.

2.8 Steric effects on the organization of TMAPS oligomers on silica

It is generally known that the dimension of the organic part of an organofunctional silane coupling agent influences its grafting. Markowitz et al. showed the influence of alkyl chainlength of various trimethoxysilylpropyl- trialkylammonium chlorides on the formation of silica xerogels^[35]. The length of the carbon chains significantly influenced the polycondensation degree of co-condensed TEOS-silane networks, leading to variations of both the density and the homogeneity of the material porosity. We imagined that the inverse orientation of quaternary ammonium groups bearing silane coupling agents on negatively charged silica surfaces may be prevented by steric hindrance. To test this hypothesis we carried out surface modifications of silica using *N*-Trimethoxysilylpropyl-*N,N,N*-tributylammonium chloride (TBAPS), which possesses three sterically large butyl chains around the quaternized ammonium group, which might keep apart the positively charged nitrogen from negatively charged silanolate groups. TBAPS modifications have been effectuated in the same manner as the modification with TMAPS described above in **PROTOCOL 2.2-1** and **PROTOCOL 2.2-2**, the reaction conditions are detailed in **TABLE 0-4** (see Annex 2). Instead of TMAPS the silane coupling agent TBAPS is added into the silica nanoparticle suspension.

FIGURE 2.8-1 shows the TG-coupled mass spectrum of TBAPS modified nanoparticles using 100 μmol of TBAPS/ m^2 , acetic acid as a catalyst and thermal treatment of two hours at 100°C (see cond. 031, Annex 2, **TABLE 0-4**). We observe mainly the same fragments as for TMAPS modified silica, but note that for better visibility the mass fragments (m/z 35, 37) are not shown and that a spectral line at m/z 22 appears. Its form resembles to the spectral line observed at m/z 44 and may indicate a higher content of species as CO_2^+ and C_3H_8^+ fragments.

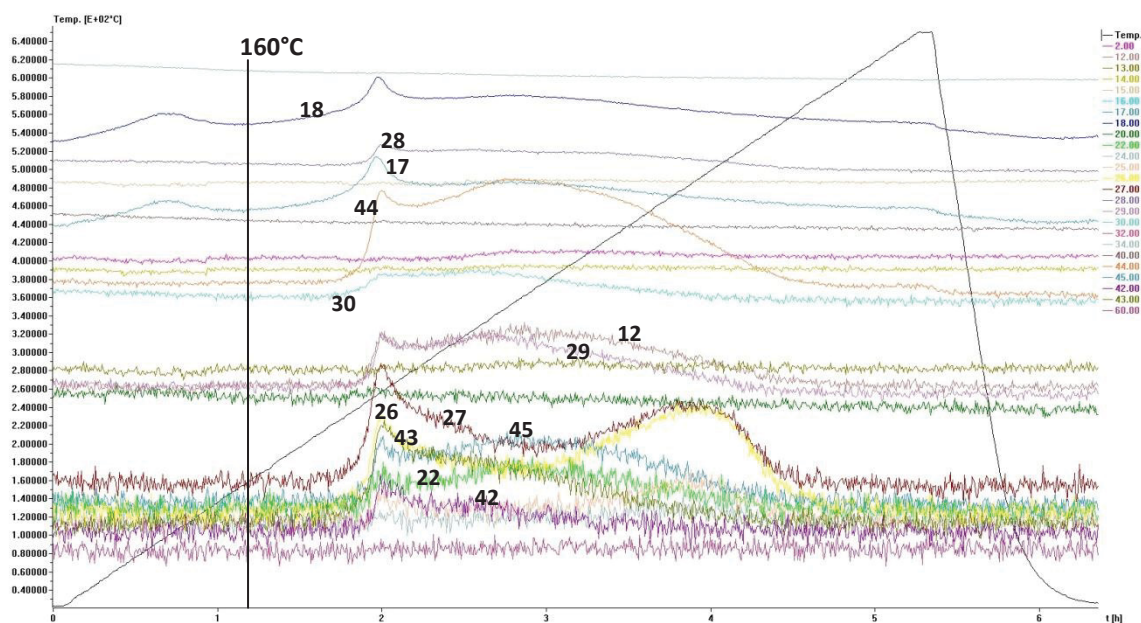


FIGURE 2.8-1 Mass spectrum of TBAPS modified silica nanoparticles recorded with a TG coupled mass spectrometer.

The results shown in **FIGURE 2.8-2** resemble to the observations we have already made modifying the silica colloids with TMAPS. Particle modifications catalyzed with strong acids such as HNO_3 and H_3PO_4 (cond. 032-033, Annex 2, **TABLE 0-4**) lead to samples showing an isoelectric point about pH 7, whereas the modifications catalyzed with NH_4OH and acetic acid (cond. 030-031, Annex 2, **TABLE 0-4**) show higher isoelectric points at about pH 8.7. The coagulation of nanoparticles of these batches has been observed to start from about pH 7.5 to pH 10. As seen above an increase in the temperature (cond. 034-035, Annex 2, **TABLE 0-4**) with the aim of improving the condensation process does not change the surface potential of modified nanoparticles significantly.

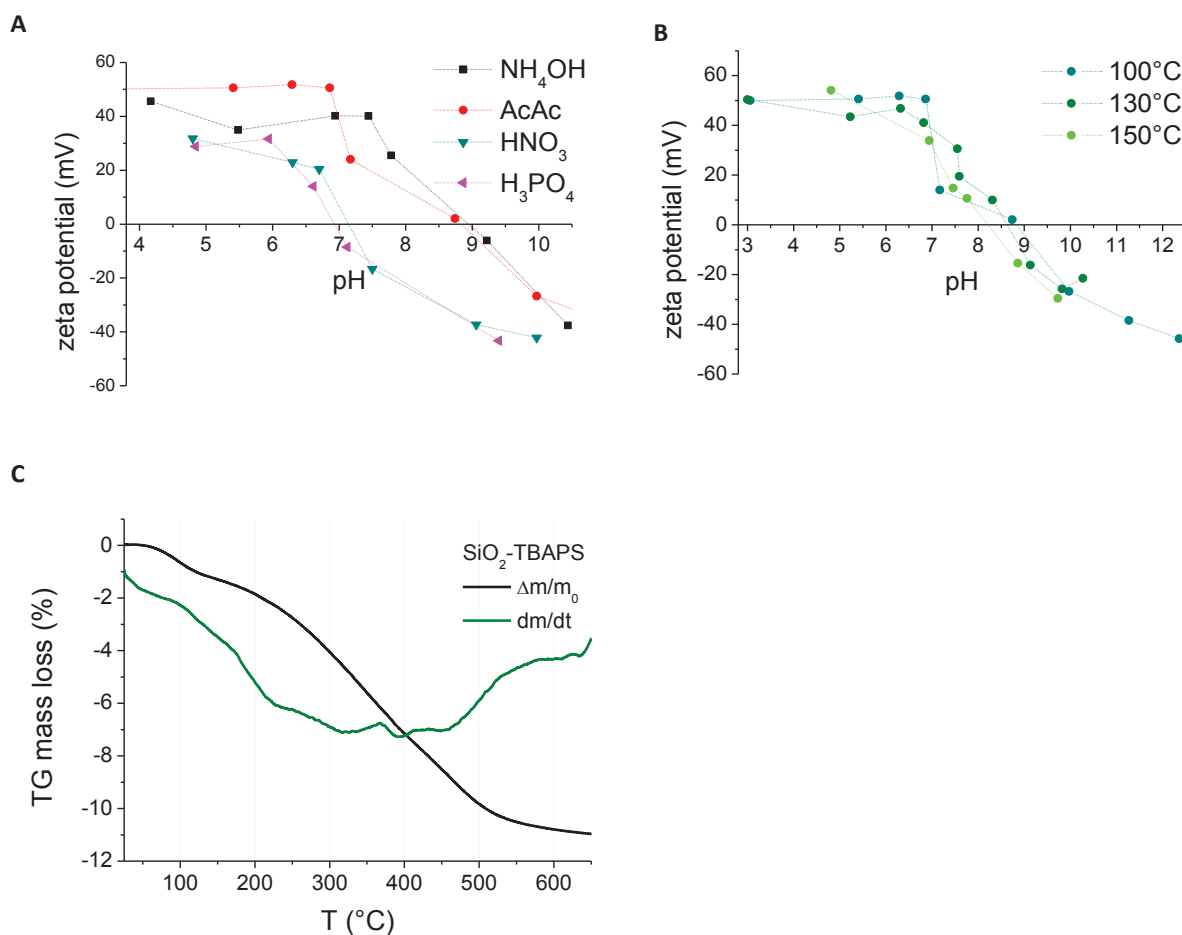


FIGURE 2.8-2 **A:** Zeta potential data of TBAPS modified silica nanoparticles resulting from differently catalyzed modifications. **B:** Zeta potential data of TBAPS modified nanoparticles resulting from modifications catalyzed by acetic acid and implemented with varying temperatures in the thermal treatment. **C:** TGA diagram and its differentiation of silica nanoparticles modified with TBAPS (condition: 100 μmol , acetic acid, 100°C).

By exploiting the TGA of TBAPS-modified nanoparticles (cond. 031, Annex 2, **TABLE 0-4**) we can determine a surface density of 3.9 $\mu\text{mol}/\text{m}^2$ of TBAPS corresponding to 2.4 grafts/ nm^2 on the silica surface. This is half of the surface density which we observed for TMAPS-coated nanoparticles (cond. 006, Annex 2, **TABLE 0-3**). This may be due to the fact that the TBAPS chains are sterically large and cannot be grafted as densely as TMAPS grafts. This observation correlates with studies carried out by Markowitz et al.^[35], who showed that the longer the alkylchains attached to the

ammonium groups are, the lower the yield of the condensation of trialkylammonium-propyltrimethoxysilanes to TEOS becomes.

The fact that we obtain similar zeta potentials as those observed for TMAPS-coated nanoparticles may indicate that the organization of the TBAPS monolayer might be more homogenous than the organization of TMAPS films on silica. At the same time the differentiated TG measurement does not show two distinct peaks as observed above for TMAPS modified particles, which may indicate the formation of a more even TBAPS layer. Nevertheless the fact that nanoparticles modified in the presence of phosphoric or nitric acid still show isoelectric points of about pH 7 and particles modified in the presence of acetic acid or NH_4OH show isoelectric points below pH 9 demonstrates that the presence of longer butyl chains attached to the quaternized nitrogen does not improve the coating sufficiently. Even the TBAPS-modified nanoparticles possessing isoelectric points at pH 8.7 start to coagulate in the range from pH 7.5 to pH 10. Hence they are not sufficiently charged to keep their stability under physiological conditions at pH 7.4.

2.9 Conclusions

In this second part of Chapter II we explored the direct surface modification of silica nanoparticles by silanization with silane coupling agents bearing quaternary ammonium groups such as TMAPS and TBAPS. We have seen that the surface density of a TMAPS-modified nanoparticle increases with the amount of TMAPS added to the chemical surface modification as it has also been observed for aminosilanes in the literature^[23]. As soon as nTMAPS exceeds $60 \mu\text{mol per m}^2$ of silica surface available for modification the surface densities reached a plateau varying around $7.91 \mu\text{mol/m}^2$, which is due to the saturation of the modified silica surfaces with TMAPS. This observation enabled us to fix the amount of silane used during the successive modification processes at $100 \mu\text{mol/m}^2$. Chemical surface modification of silica nanoparticles with TMAPS seemed to work best at pH 4.5 adjusted with acetic acid leading to the obtainment of modified nanoparticles which possess an isoelectric point at pH 8.4 and a zeta potential rapidly increasing below this pH. Although they possess a zeta potential of about 25 mV at pH 7.4, the zeta potential at this pH is too low to guarantee the colloidal stability of these TMAPS-coated nanoparticles under physiological conditions.

We could reveal a major problem related to the coating process of silica nanoparticles with the silane coupling agent TMAPS, which is the predisposition of its quaternary ammonium group to form an ionic bond by interacting electrostatically with negatively charged silanolate groups on silica surfaces. The formation of a disordered silane coating in which the quaternary ammonium groups plunge towards silanolate groups remaining on the surface after the silanization has been detected. Less dense disorganized silane layers facilitate the electrostatic interactions of quaternary ammonium groups and silanolate groups. Attempts to improve the condensation of TMAPS on silica colloids by varying of temperature and duration time of the thermal treatment did not improve the TMAPS coating on silica nanoparticles. This has been explained by the fact that the application of heat under vacuum is sufficient to break relatively weak physical bonds due to van der Waals interactions and hydrogen bonding but not to abrogate ionic bonds forming between quaternary ammonium groups and

silanolate groups. This reasoning enables us to understand why thermal treatment under vacuum is an appropriate method for improving the grafting of aminosilanes on metal oxide surface, but is not effective when we try to improve the condensation of TMAPS layers on colloidal silica.

Efforts to decrease the number of ionic bonds formed between quaternary ammonium groups and silanolate groups by the end-capping of silanolate groups with ClSiMe_3 or glycidol were not successful, because of the fact that while they interact with quaternary ammonium groups they are sterically protected from further reaction. In addition the application of TBAPS which possesses longer alkylchains keeping quaternary ammonium groups and silanolate groups at a longer distance than methyl groups was not sufficient to keep the modified nanoparticles electrostatically stabilized under physiological conditions at pH 7.4. We therefore decided to change our strategy to circumvent the formation of highly disordered silane coatings due to the quaternary ammonium groups striving to interact electrostatically with silanolate groups on silica as will be shown in the next part of this chapter.

3. QUATERNIZATION OF SURFACE-AMINATED SILICA NANOPARTICLES

To obtain modified surfaces with a high number of quaternary ammonium functions on the silica surfaces and an isoelectric point at highly basic pHs we changed the modification strategy. Instead of the direct grafting of a silane coupling agent which is already functionalized with a quaternary ammonium group such as TMAPS or TBAPS on silica colloids we explored a two-step procedure. We first modified the silica surfaces with an aminosilane and secondly alkylated the amine groups to obtain quaternary ammonium groups on the modified silica particles.

Aminosilanes have been widely used to functionalize metal oxide nanoparticles by silanization^[23,61-64]. The use of aminosilanes for the chemical surface modification of silica nanoparticles has several advantages. Their organic parts do not possess quaternary ammonium groups, which orient themselves on the negatively charged silica surface forming an ionic bond, but solely primary or secondary amine groups. These amine groups also interact with negatively charged silica surfaces but develop only van der Waals bonds, which can be abrogated by thermal treatment under vacuum during the silanization process. The condensation of aminosilanes on metal oxide nanoparticles leads to the obtainment of aminated nanoparticles, which possess isoelectric points in the scope of pH 9 to pH 11^[23]. By modifying the colloidal silica surface with *N*-[3-(Trimethoxysilyl)propyl]ethylenediamine (EDPS) and by an alkylation of its amine groups with iodomethane, we tried to implement a high number of quaternary ammonium groups on the silica colloids. EDPS possesses a relatively long graft containing one secondary and one primary amine group and therefore permits us to synthesize two quaternary ammonium groups per organic graft. The modification of silica nanoparticles with EDPS was implemented by the **PROTOCOL 3.0-1**, which has been optimized in our group for the silanization of iron oxide nanoparticles and which can also be applied on silica surfaces^[23,62,65].

PROTOCOL 3.01 Modification of colloidal silica with aminosilanes

Under continuous stirring a volume of 3.87 mL of N-[3-(Trimethoxysilyl)propyl]ethylenediamine (EDPS) was added to 200 mL EtOH/H₂O 1:1 containing silica nanoparticles with a surface area of 119 m². The mixture was stirred for 12h at room temperature. Subsequently 200 mL of glycerol are added, then ethanol and water are evaporated to transfer the particles in the wetting agent. Under vacuum thermal treatment at 100°C is accomplished for two hours. The modified particles were washed four times in absolute ethanol by centrifuging them at 13000 g for 25 minutes, finally they were dispersed in 100 mL of absolute ethanol or peptized in the presence of HCl in 100 mL H₂O (18.2 MΩ), depending on their subsequent application.

We alkylated the amine groups present on colloidal silica surfaces previously modified with EDPS using the well known Mentschutkin reaction^[54]. The alkylation of amines with alkyl halides for the synthesis of quaternary ammonium compounds is a common reaction in organic chemistry and has been extensively studied by Sommer et al., who tested the reaction outcome of alkylating various molecules, which contain amine groups under the use of different solvents and bases^[66]. The

Mentschutkin reaction has already been applied to quaternize ungrafted trialkoxysilanes bearing tertiary amine groups with a yield of almost 100 %^[67]. It has been used to quaternize amines, chitosan, polyethyleneimine or polysaccharide bearing nanoparticles^[68-72] and equally to quaternize silica nanoparticles bearing tertiary amines on their surface^[73].

3.1 Implementation of a reaction protocol to obtain quaternization of aminated silica nanoparticles and verification of its achievement

The alkylation reaction of amine groups with iodomethane can take place in different solvents and can be accomplished with different bases^[66]. In modifying colloids we can choose not only optimal conditions for carrying out the organic reaction but also reaction conditions which allow the dispersion of the nanoparticles during the synthesis stages. For this purpose we tested different reaction conditions (036-041), which are resumed in **TABLE 0-5** (see Annex 2). The alkylation of silica nanoparticles bearing amine groups has already been effected in the literature using acetonitrile as a solvent and K_2CO_3 as a base^[72], but we observed that EDPS-modified nanoparticles couldn't be dispersed in acetonitrile. Due to this observation we performed the quaternization reaction in EtOH/acetonitrile 1:3 (cond. 038,039) and absolute ethanol (cond. 040, 041). The ratio of EtOH and acetonitrile has been chosen to permit the dispersion of EDPS-modified nanoparticles at the beginning of the reaction due to the presence of ethanol. The dielectric constant of acetonitrile is 37.5 and is higher than the dielectric constant of ethanol of 24.3 which means that we might stabilize quaternized particles better in a mixture of EtOH and acetonitrile than in absolute alcohol. We also compared the use of K_2CO_3 (cond. 036, 038, 040) and NEt_3 (cond. 037, 039, 041) as a base, after which we noted that the addition of NEt_3 to dispersed SiO_2 -EDPS nanoparticles led to a slight destabilization of the nanoparticles.

To explore the quality of stabilization of quaternized nanoparticles in water after the alkylation reactions have been implemented under different conditions, we as an exception chose to implement the modification processes on nanoparticles with a diameter of 120 nm to determine the quality of their dispersion after modification because their coagulation was expected to lead to a distinct change of the size distribution measured by DLS. For each condition modified nanoparticles were observed to coagulate in the end of the reaction, due to the fact that quaternary ammonium groups do not support solvation interactions with EtOH molecules. In general quaternized nanoparticles were immediately dispersed when they were brought into contact with water without the need of the presence of an acid to peptize the particles, as is necessary for nanoparticles with aminated surfaces. This behavior can be seen as an indirect proof of the quaternization, because the continuous presence of the pH-independent charges of quaternary ammonium groups permits the immediate dispersion and stabilization of the modified nanoparticles in ultrapure water. Zeta potential measurements of particles modified in the presence of NEt_3 in EtOH or EtOH/acetonitrile (1:3) show a similar profile (see **FIGURE 3.1-1 A**). The isoelectric point of the modified nanoparticles is the same for nanoparticles modified in both solvents; for nanoparticles modified in the EtOH/acetonitrile mixture as well as for nanoparticles modified in absolute EtOH it has been observed at pH 9.5. DRIFT measurements

showed that both conditions can be used to alkylate the amine groups of the SiO₂-EDPS nanoparticles. DLS measurements show that SiO₂-EDPS nanoparticles quaternized in the presence of NEt₃ in both absolute EtOH and EtOH/acetonitrile (1:3) are better dispersed in H₂O (18.2 MΩ) than nanoparticles quaternized in reaction mixtures containing K₂CO₃, which stay coagulated. Concerning the two reactions undergone EtOH/NEt₃ and EtOH/acetonitrile/NEt₃ DLS measurements do not show a major difference: both curves show the same maximum but the size distribution is larger in the case of samples quaternized in the presence of acetonitrile (see FIGURE 3.1-1 B). The larger size distribution indicates that these nanoparticles are dispersed less well in water than the nanoparticles quaternized in absolute EtOH.

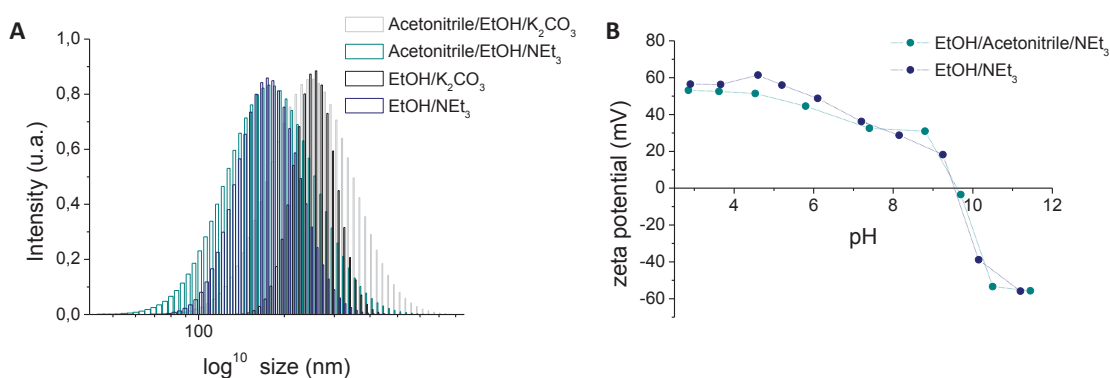


FIGURE 3.1-1 A: DLS graphs show the size distribution of silica particles quaternized under different conditions (cond. 038-041, see TABLE 0-5, Annex 2) dispersed in H₂O (18.2 MΩ). **B:** Zeta potential of nanoparticles quaternized in EtOH or Acetonitrile/EtOH (cond. 039, 041, see TABLE 0-5, Annex 2).

In the following we chose to effectuate the quaternization reactions in absolute ethanol. The amount of MeI needed to alkylate the amine groups on the nanoparticles was calculated from the grafting density of EDPS estimated to be of about 5 μmol/m² on silica according to literature^[23,62]. The alkylation reactions are undergone following PROTOCOL 3.1-1.

PROTOCOL 3.1-1 Alkylation of the primary and secondary amines present on silica particles previously modified with EDPS by the use of iodomethane

To a sol of SiO₂-EDPS with a surface area 26.4 m² dispersed in 10 mL absolute EtOH 220 μL of NEt₃ was added under continuous stirring and subsequent 410 μL of iodomethane was added dropwise. The reaction mixture was stirred for 12 hours at room temperature and for 30 min. at 70 °C in a water bath. The particles were then washed twice with absolute EtOH, once with EtOH (50% v/v) and subsequent two times with H₂O (18.2 MΩ) by centrifugation during 25 min at 13000 g. Iodide ions remaining in the solution were either precipitated by the addition of AgNO₃ or removed by ionic exchange in a solution of 1 M NaCl. After recovery of the modified particles two additional washing steps are effected in H₂O (18.2 MΩ) by centrifuging 25 min at 13000 g.

The modified silica nanoparticles are analyzed by DRIFT. FIGURE 3.1-2 shows the spectra of EDPS-modified silica nanoparticles (SiO₂-EDPS) before and after the alkylation with iodomethane (SiO₂-EDPS-Me).

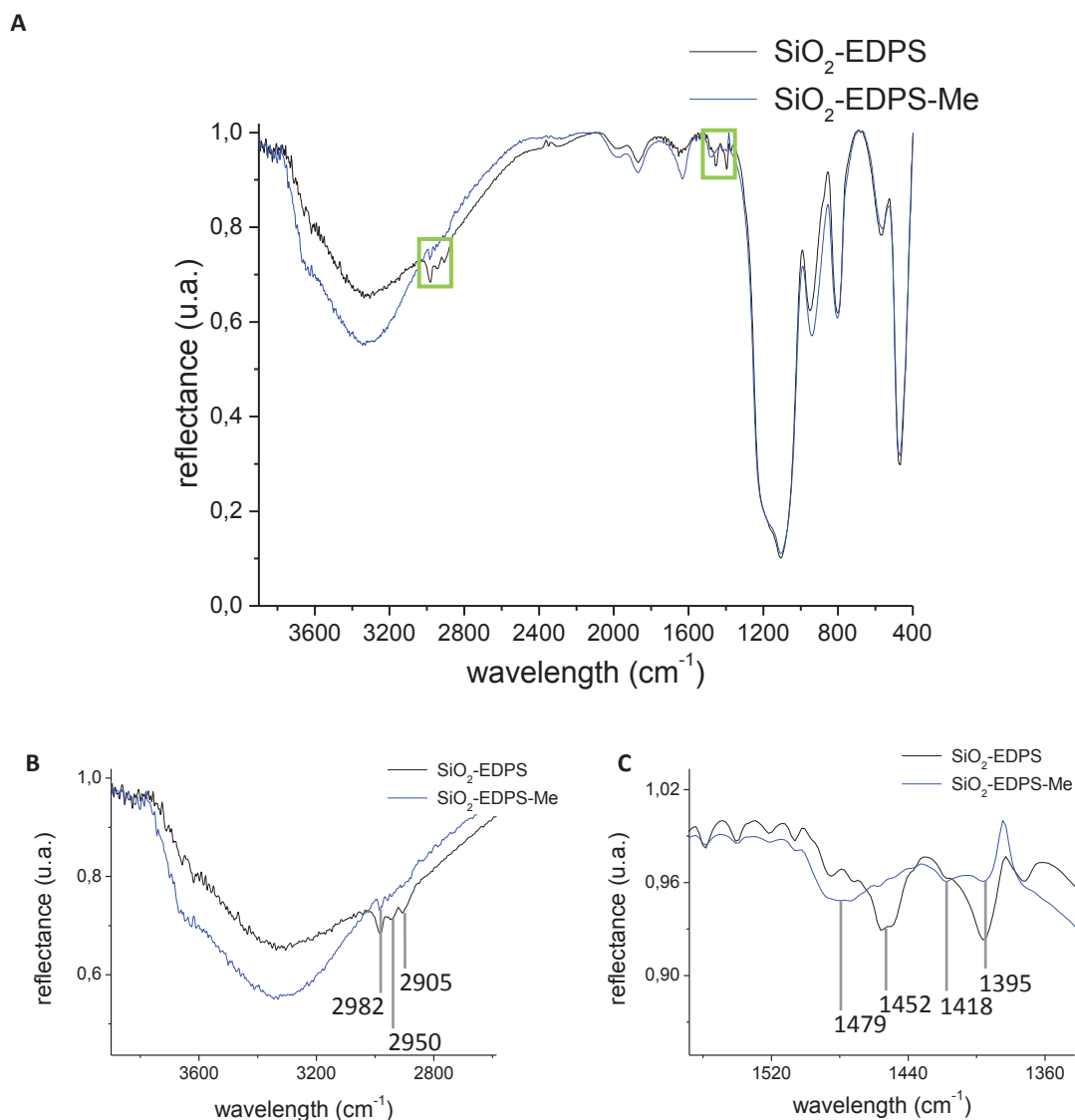


FIGURE 3.1-2 A: Infrared spectra of colloidal modified with EDPS before (black line) and after quaternization (blue line). The green boxes indicate regions containing supplementary vibrations detectable after the chemical surface modification of silica. **B:** Enlargement of the section containing O-H and C-H vibrations. **C:** Enlargement of the spectrum showing C-N and N-H vibrations, permitting unalkylated and alkylated quaternary amines to be distinguished.

Compared to the spectrum of colloidal silica we can see an additional band at 2950 cm^{-1} in the spectrum of alkylated nanoparticles, which can be attributed to C-H stretching vibrations of the methyl groups attached to a nitrogen atom. In the range from 1500 to 1390 cm^{-1} we can distinguish four vibration bands. The bands at 1395 cm^{-1} and 1418 cm^{-1} are attributed to C-N deformation vibrations; the band at 1395 cm^{-1} shifts to higher wavelengths in the presence of quaternary ammonium ions. In the same manner the band of C-H deformation vibrations shifts from a value of 1452 cm^{-1} if the carbon chain is attached to a primary or a secondary amine group, to a value of 1479 cm^{-1} in the presence of quaternary ammonium groups^[39,40].

We also recorded the mass spectra of EDPS and methylated EDPS-modified nanoparticles. The mass spectrum of EDPS-modified silica nanoparticles is shown in **FIGURE 3.1-3**. We detected a spectral line of m/z 18, which can be attributed to water and CH_4^+ and m/z 17 to OH^+ fragments provided from

water. The spectral line of m/z 44 assigned to CO_2^+ , C_3H_8^+ and $\text{C}_2\text{H}_6\text{N}^+$ fragments was also observed. The only related nitrogen-containing fragments that can be observed may be the $\text{C}_2\text{H}_7\text{N}^+$ fragment ($m/z = 45$), and CH_4N^+ ($m/z = 30$).

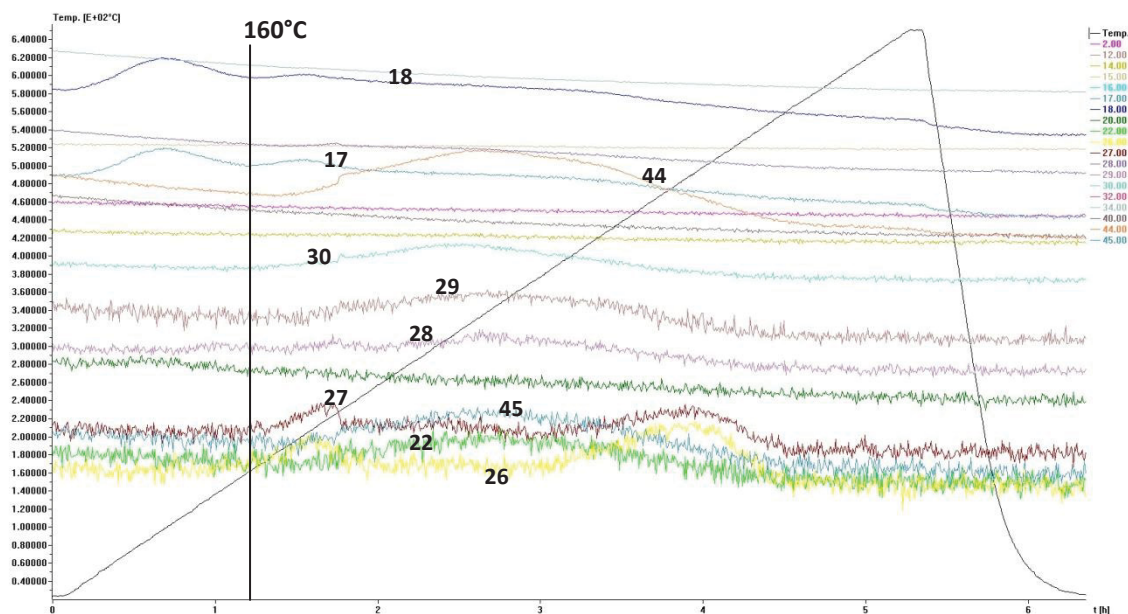


FIGURE 3.1-3 Mass spectrum of EDPS-modified silica nanoparticles recorded with a TG coupled mass spectrometer.

Mass spectra of 3-(2-aminoethylamino)propyltrimethoxysilane, isopropylethylenediamine and ethylenediamine usually show a mass fragment with m/z 58, which can be attributed to the fragment $\text{C}_2\text{H}_6\text{N}_2^+$ (source: Spectral Database for Organic Compounds, SDBS) but cannot be observed in our spectrum. Again decomposition of the propyl chain leads to the fragments C_2H_6 ($m/z = 30$), C_2H_5 ($m/z = 29$), C_2H_4^+ ($m/z = 28$), C_2H_3^+ ($m/z = 27$) and C_2H_2 ($m/z = 26$). Smaller carbon fragments as seen in the spectra of TMAPS-modified nanoparticles as CH_4^+ , CH_3^+ , CH_2^+ or C^+ are not detected.

After methylation of EDPS-modified nanoparticles with iodomethane, which have been washed in EtOH and H_2O the spectrum recorded during their decomposition (see **FIGURE 3.1-4**) shows additional spectral lines, which are not present in the spectrum of unalkylated particles. We can see the spectral line corresponding to remaining I^+ ions at m/z 127, which serves as counterion for the synthesized and positively charged methylammonium groups. The spectral line of CH_3^+ at m/z 15, which was present in the spectrum of TMAPS-modified nanoparticles, reappears. We observe the presence of a fragment at m/z 47, which might be attributed to CH_3I^{3+} fragments that can evolve out of quaternary methyl ammonium iodides. The mass fragment detected at m/z 33 is generally attributed to CH_5O^+ , which is produced from the reaction of H_2O^+ and CH_3^+ ^[41]. As well as for TMAPS-modified nanoparticles $\text{C}_2\text{H}_7\text{N}^+$ fragments ($m/z = 45$), $\text{C}_2\text{H}_5\text{N}^+$ fragments ($m/z = 43$), $\text{C}_2\text{H}_3\text{N}^+$ ($m/z = 41$) and CH_4N^+ ($m/z = 30$) can be detected.

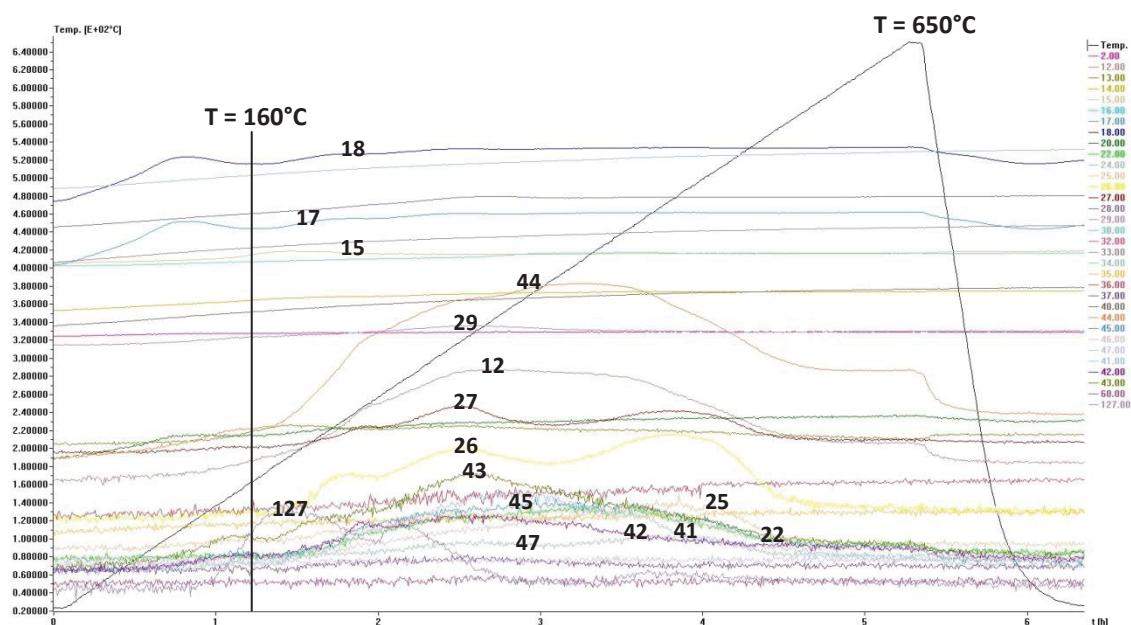


FIGURE 3.1-4 Mass spectrum of methylated EDPS-modified silica nanoparticles after washing steps with ethanol and H₂O (18.2 MΩ) recorded with a TG-coupled mass spectrometer.

All the fragments observed in the presented mass spectra are shown in TABLE 0-2 (see Annex 2), which allows an overview of the detected fragments per spectrum. The mass spectra showed that the surface modifications aimed at have taken place on the silica nanoparticles. We identified the same characteristic fragments of quaternary ammonium groups in the spectra of TMAPS, TBAPS and EDPS-Me. We can also identify fragments of the alkyl chains as well as the iodide ions, which are located close to the quaternary ammonium groups serving them as counterions.

To analyze the success of the alkylation of EDPS-modified particles we recorded ¹H-NMR spectra of colloidal silica (SiO₂), EDPS-modified (SiO₂-EDPS) and alkylated EDPS-modified nanoparticles (SiO₂-EDPS-Me). The spectra have been recorded in D₂O with a Bruker NMR spectroscope working at 9.4 Teslas (400 MHz). In analyzing the spectrum of colloidal silica (see FIGURE 3.1-5) we can identify three resulting peaks of the solvent and ethanol which may be incorporated to the silica matrix as well as ethoxy groups of uncondensed TEOS molecules.

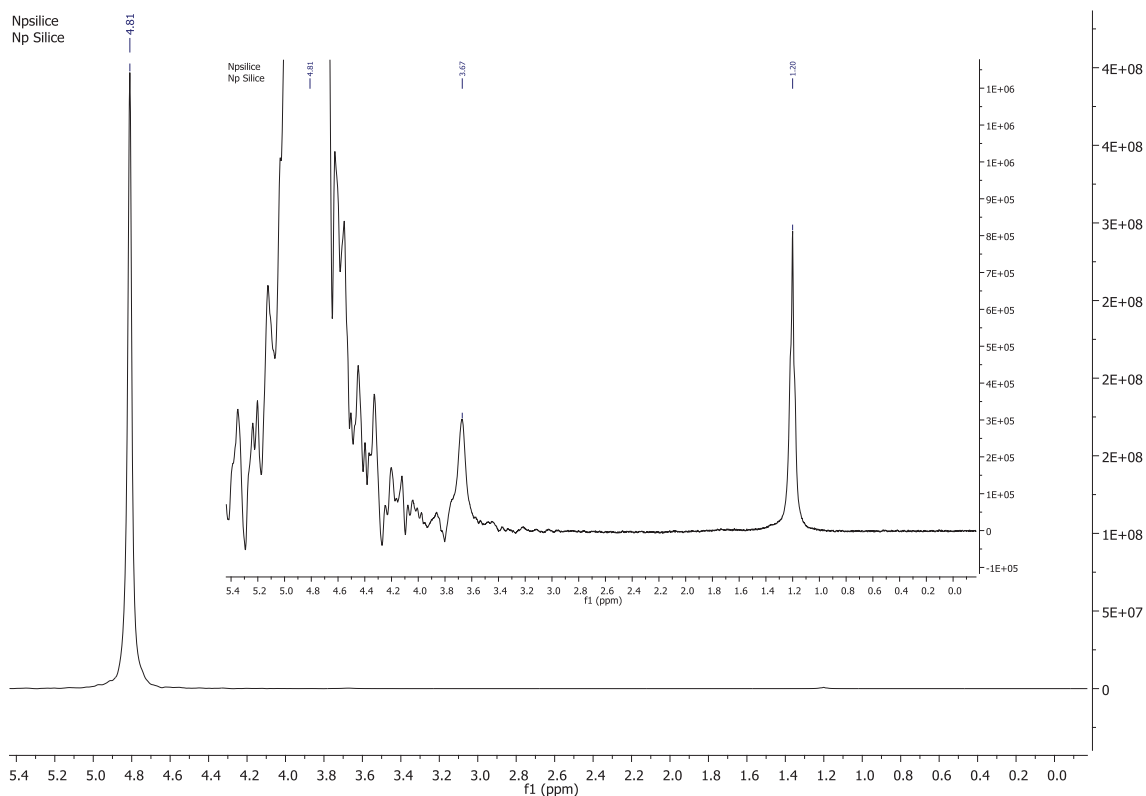
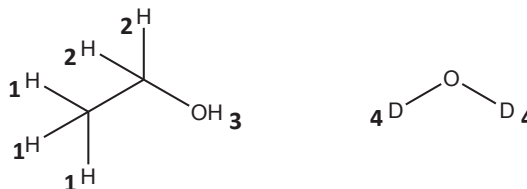


FIGURE 3.1-5 ¹H-NMR spectrum of colloidal silica.

Analytical data ¹H-NMR, D₂O, 400 MHz, δ(ppm):

δ = 1.200 (s, 3H, H₁), δ = 3.676 (s, 2H, H₂),
 δ = 4.810 (s, 2D, D₄)



The identified signals are characteristic for ethanol or ethoxy groups and D₂O as reported in many NMR spectra and spectroscopy databases such as the spectral database for organic compounds (sdb). The fact that we can't identify a peak belonging to H₃ of ethanol, which we would expect at 2.6 ppm, is explained by the fast exchange of OH protons with deuterium of the solvent D₂O. The observation that the H₁ and H₂ signals do not split up into a triplet and a quadruplet as we expect indicates that the detected signals may be the result of ethoxy groups of molecules enclosed in the silica matrix.

In the ¹H-NMR spectrum of EDPS-modified silica (not shown) the characteristic peak of D₂O at 4.810 ppm and the two peaks at 3.67 ppm and 1.2 ppm resulting from the ethoxy group of ethanol and uncondensed TEOS can be seen. FIGURE 3.1-6 shows a zoom in the spectrum between 0.3 ppm and 4.2 ppm revealing the characteristic peaks of the 3-(2-aminoethylamino)propyl group which are present on the modified silica surface:

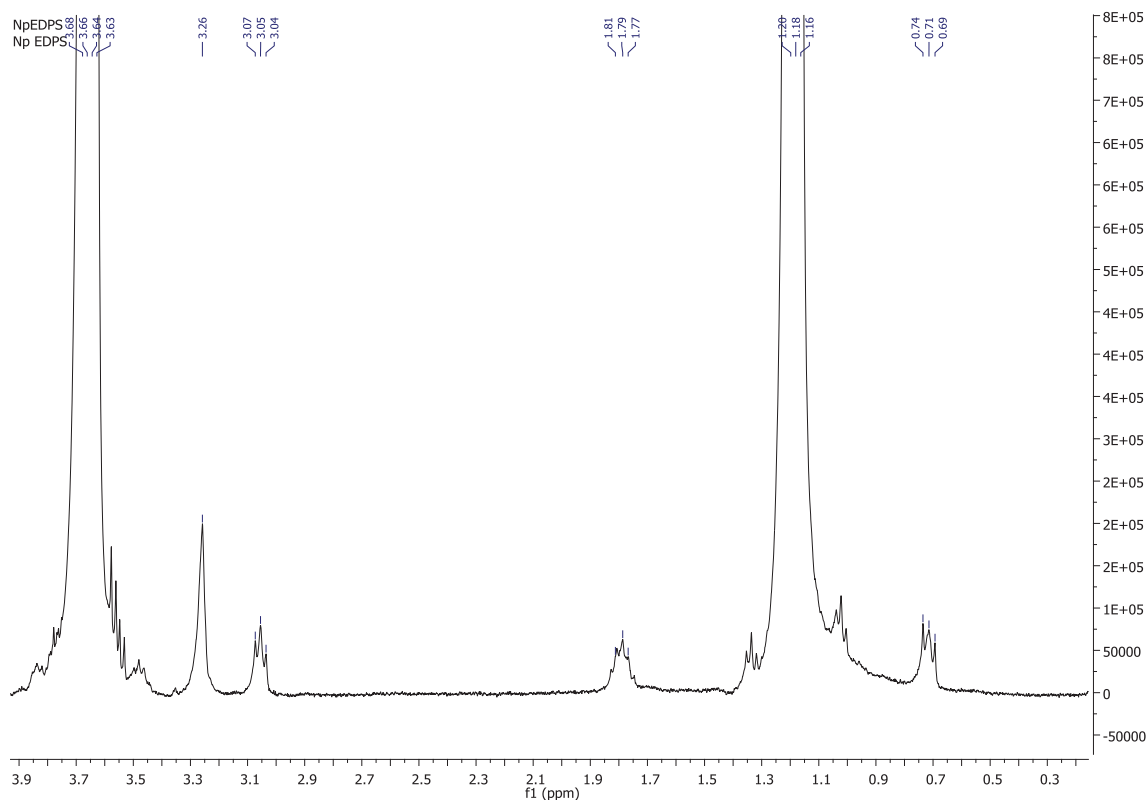
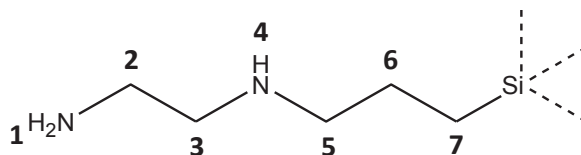


FIGURE 3.1-6 $^1\text{H-NMR}$ spectrum of EDPS-modified silica. Zoom in the range of 0.3 to 4.2 ppm showing the peaks attributed to the grafted 3-(2-aminoethylamino)propyl chain.

Analytical data $^1\text{H-NMR}$, D_2O , 400 MHz, $\delta(\text{ppm})$:

$\delta = 0.722$ (t, 2H, $J = 8.4$ Hz, H_7), $\delta = 1.189$ (t, 3H, $J = 6.8$ Hz, $\text{H}_{1\text{ethanol}}$), $\delta = 1.787$ (m, 2H, $J = 6.8$ Hz, H_6), $\delta = 3.039$ (m, 2H, H_5), $\delta = 3.225$ (s, 4H, H_2 , H_3), $\delta = 3.669$ (q, 2H, $J = 6.8$ Hz, $\text{H}_{2\text{ethanol}}$)



The triplet at 0.722 ppm can be attributed to H_7 . The signal at 1.787 ppm corresponds to H_6 . It seems to be a triplet but due to the fact that the H atoms are coupled with four other H atoms located at different C atoms it is assumed to be a less resolved multiplet. The signal at 3.039 ppm is attributed to H_5 : as a signal we would expect the doublet of a triplet, but observe a not well resolved multiplet. The chemically and magnetically equivalent protons of H_2 and H_3 produce a singlet signal at 3.225 ppm.

The spectrum of alkylated EDPS-modified particles has been recorded on nanoparticles of the same batch as those used to record the spectrum shown in **FIGURE 3.1-6**, but after their alkylation with iodomethane described in **PROTOCOL 3.1-1**. As previously we identified the peak of D_2O at 4.810 ppm and the two peaks at 3.670 ppm and 1.200 ppm resulting from ethoxy groups (not shown). **FIGURE 3.1-7** shows a part of the spectrum zoomed in the range between 0.0 and 4.2 ppm to show the characteristic peaks of the 3-(2-trimethylammonium-ethyl)dimethylammonium)propyl group present on the modified silica surface:

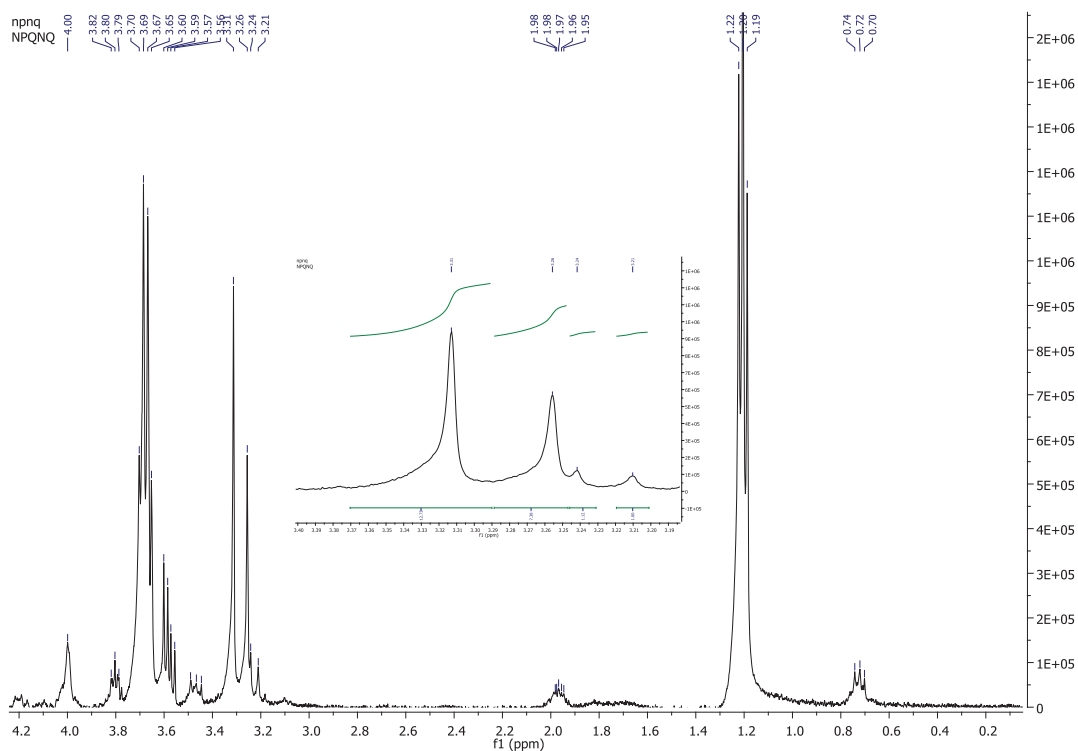


FIGURE 3.1-7 $^1\text{H-NMR}$ spectrum of alkylated EDPS-modified nanoparticles ($\text{SiO}_2\text{-EDPS-Me}$).

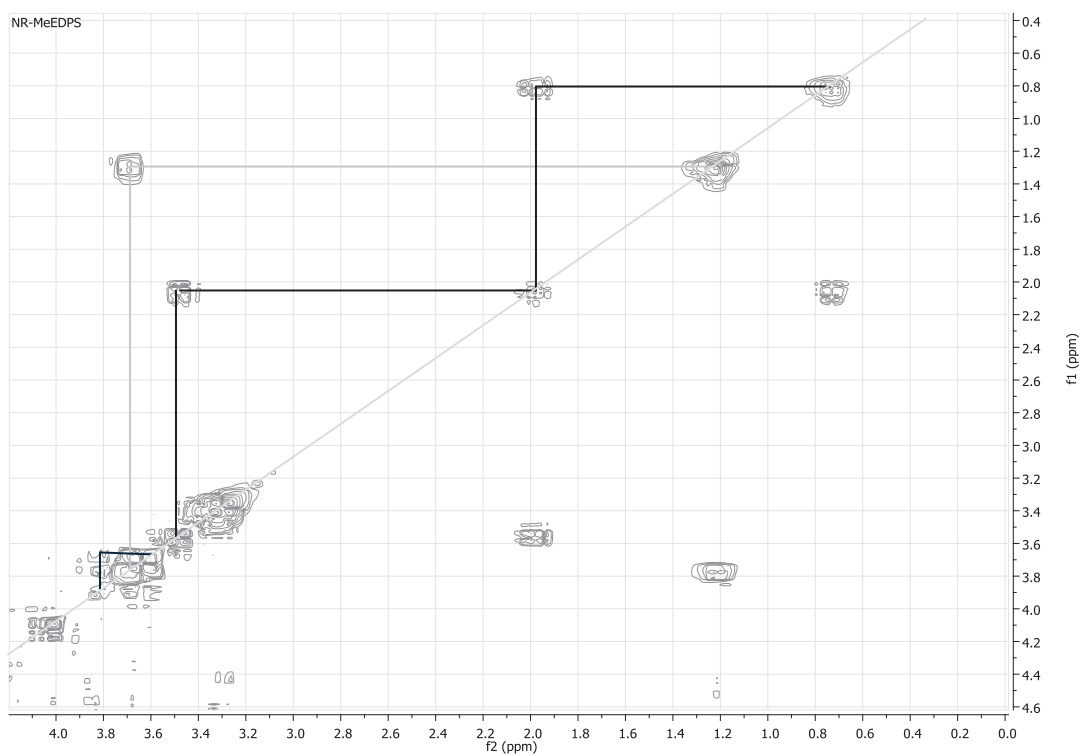
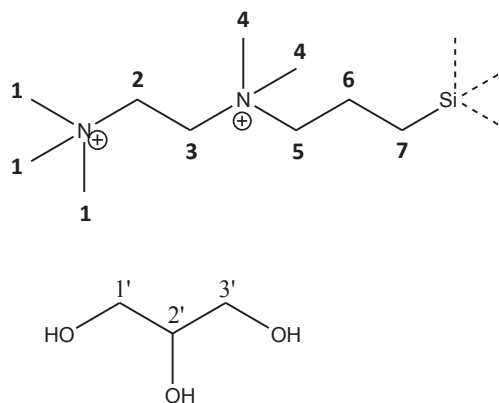


FIGURE 3.1-8 COSY NMR spectrum of alkylated EDPS-modified nanoparticles ($\text{SiO}_2\text{-EDPS-Me}$). **Black lines:** Couplings within the organic graft. **Grey lines:** Coupling within ethoxy groups. **Dark blue lines:** coupling within remaining glycerol residues.

Analytical data $^1\text{H-NMR}$, D_2O , 400 MHz, δ (ppm):

$\delta = 0.722$ (t, 2H, $J = 8$ Hz, H_7), $\delta = 1.205$ (t, 3H, $J = 7.4$ Hz, $\text{H}_{1\text{ethanol}}$), $\delta = 1.969$ (m, 2H, H_6), $\delta = 3.211$ (s, 3H, H_4), $\delta = 3.243$ (s, 6H, H_1), $\delta = 3.257$ (s, 9H, H_1), $\delta = 3.314$ (s, 6H, H_4), $\delta = 3.471$ (m, 2H, H_5), $\delta = 3.573$ (dd, 4H, $J_{1'2',3'2'} = 12$ Hz, $J_{1'ab,3'ab} = 6.4$ Hz, H_2, H_3), $\delta = 3.668$ (q, 2H, $J = 6.8$ Hz, $\text{H}_{2\text{ethanol}}$), $\delta = 3.804$ (m, 1H, H_2), d = 4.0 (s, 4H, H_2, H_3)



The first signal at 0.722 ppm belongs to the H_7 next to the Si atom, which is coupled with the two protons of H_6 . The signal at 1.969 ppm can be attributed to H_6 protons, which are coupled with H_5 and H_7 in a multiplet structure. The two singlets at 3.211 ppm and 3.243 ppm are attributed to protons H_4 and H_1 of CH_3 groups attached to tertiary amines, which have not been completely alkylated. This observation is in accordance with the results of Sieval et al.^[74], who have observed the appearance of tertiary side products during quaternization reactions. The singlets appearing at 3.257 and 3.314 ppm have been attributed to protons H_4 and H_1 from CH_3 groups attached to positively charged quaternary ammonium groups, which are extremely electron withdrawing. The multiplet at 3.471 ppm has been attributed to H_5 . The singlet at 4.0 ppm is due to four protons of H_2 and H_3 which are both situated next to a quaternary ammonium group. The doublet of a doublet with $J_{1'2',3'2'}$ of 12 Hz and $J_{1'ab,3'ab}$ of 6.4 Hz is attributed to protons of $\text{H}_{1'}$ or $\text{H}_{3'}$ of remaining glycerol residues. The splitting of the signal is explained by the fact that the two protons at $\text{H}_{1'}$ and $\text{H}_{3'}$ are non equivalent; they are diastereotopic and couple with each other. The multiplet at 3.804 ppm is attributed to $\text{H}_{2'}$ of remaining glycerol residues.

In the COSY 2D spectrum shown in FIGURE 3.1-8 we can see that the signals at 0.72 ppm and 3.47 ppm are both coupled with the signal 1.97 ppm, which confirms their attribution to the protons belonging to the propyl chain of the organic graft. The proton signals of $\text{H}_{1',3'}$ and $\text{H}_{2'}$ at 3.5 ppm and 3.8 ppm couple with each other which indicates that the measured signals are provided from protons located in chains of the same molecule which has been identified as glycerol.

In the $^1\text{H-NMR}$ spectrum shown in FIGURE 3.1-7 the intensity of the two signals attributed to H_1 and H_4 atoms next to quaternary ammonium groups is about nine times higher than the intensity of the signals of H_1 and H_4 atoms next to tertiary amine groups, which indicates that the quaternization of amine groups is nearly complete. Integration of the four singlets shows an integral of 12.73 and 7.33 for the quaternary proton peaks in contrast to integrals of 1.12 and 1.0, which is a repartition of 92 % of quaternized ammonium groups to 8 % of tertiary amine groups at position 1 and 88 % of quaternized ammonium groups to 12 % of tertiary amine groups at position 4. We do not observe the NH peak of H_1 and H_4 , which we would expect at 2.5 ppm, which is also explained by the fast exchange of NH protons with deuterium of the solvent D_2O . Therefore it is not possible to determine

the yield of alkylation of the propyl-ethylenediamine grafts, but the results show that about 90 % of alkylated amine groups have been quaternized.

3.2 Attempts to estimate the surface density of quaternary ammonium groups on quaternized silica nanoparticles

The presence of quaternary ammonium groups on alkylated EDPS-modified nanoparticles has been proven by DRIFT and NMR spectroscopy. Supposing that each quaternary ammonium group is accompanied by one iodide ion serving as a counterion, we tried to estimate the number of quaternary ammonium groups indirectly by a conductometric dosage of iodide ions present in the sol of quaternized nanoparticles by the addition of AgNO_3 solution (0.1 M) and the precipitation of AgI ($K_s 8.52 \cdot 10^{-17}$). When the total amount of iodide reacted, no more precipitation of AgI takes place and, by that time, the added Ag^+ ions start to contribute to the increase in the conductivity of the dispersion. In the same way the amount of EDPS grafts on EDPS-modified silica nanoparticles peptized with hydrochloric acid has been dosed by the precipitation of AgCl ($K_s 1.77 \cdot 10^{-10}$) after two washing steps with ultrapure water to eliminate the excess of chloride ions. A detailed protocol of the conductometric titrations is described in Annex 1.

To 2 mL of a sol containing EDPS-modified nanoparticles (36.4 g/L) 295 μL AgNO_3 (0.1 M) was added to reach the turning point. This corresponds to the presence of 6.8 μmol of chloride ions per m^2 of nanoparticle surface area. Assuming that each EDPS graft is accompanied by one or two Cl^- ions according to the pH, we can deduce that there are 6.8 μmol of EDPS per m^2 of silica (see **FIGURE 3.2-1**).

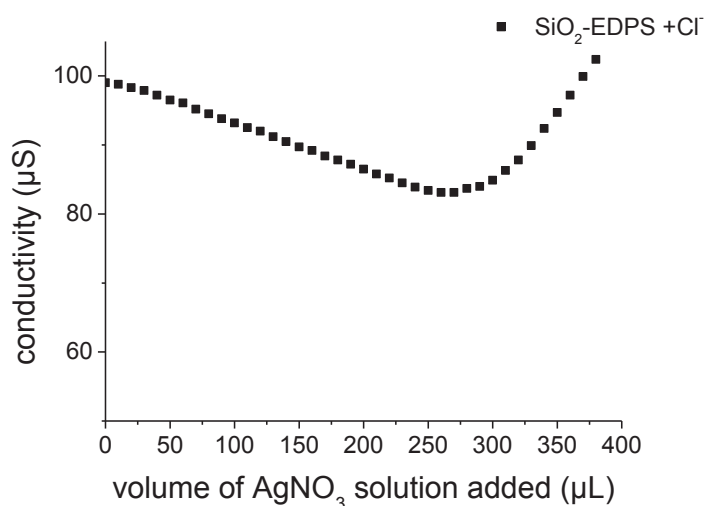


FIGURE 3.2-1 Conductometric titration of chloride ions precipitated as AgCl by the addition of AgNO_3 solution.

After estimating of the amount of iodide ions contained in 2 mL of a sol of quaternized nanoparticles (47.9 g/L), we firstly observed a slight decrease of the conductivity until a volume of 50 μL of AgNO_3 (0.1 M) was added. Then a marginal increase until the addition of 140 μL of AgNO_3 was observed (see **FIGURE 3.2-2**). This observation may be explained by the fact that first weakly adsorbed iodide ions

located on the outer part of the ionic double layer are accessible for precipitation and second iodide ions adsorbed to the modified surface are precipitated. Above the volume of 140 μL added AgNO_3 corresponding to $1.40 \cdot 10^{-5}$ mol AgNO_3 , the conductivity measured increases significantly, inducing the consumption of all iodide ions present in the sol of quaternized nanoparticles. Subsequently we calculated that 5.2 μmol of iodide ions are present per m^2 of modified silica, indicating the attendance of 5.2 μmol of positively charged amine and quaternary ammonium groups per m^2 .

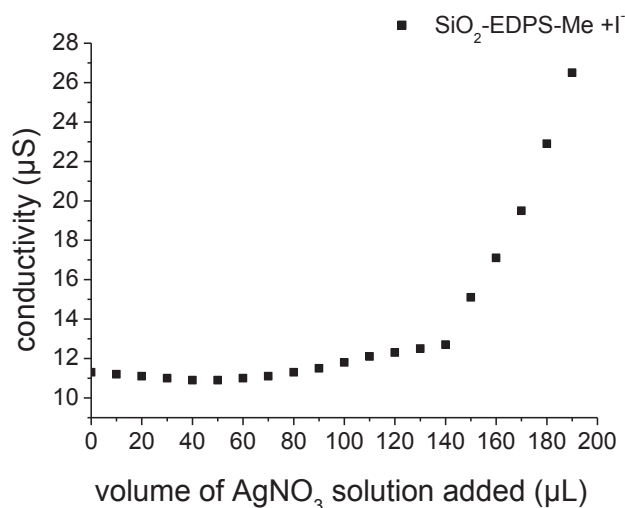


FIGURE 3.2-2 Conductometric titration of iodide ions precipitated as AgI by the addition of AgNO_3 solution.

The determined values of 6.8 μmol EDPS grafts per m^2 of modified silica and of 5.2 μmol of quaternary ammonium groups present per m^2 on the EDPS grafts may be slightly overestimated considering that surface densities of maximal 4.9 μmol EDPS/ m^2 have been observed to be grafted on metal oxide colloids^[23]. The number of washing steps in water may influence the amount of iodide ions dosed by conductometry, nevertheless the determined amounts of iodide ions per m^2 stay in a realistic order of magnitude. In determining the presence of quaternary ammonium groups by a dosage of iodide counterions we follow the presumption that iodide ions, which do not interact electrostatically with charges on the surface of modified nanoparticles have been seized by $^+\text{NEt}_3$ present during the reaction at a large excess and removed during washing in EtOH and two further washing steps in ultrapure water. It is possible that as observed for TMAPS-modified silica colloids quaternary ammonium groups interact with silanolate groups remaining on the surface and that hence iodide ions are released and removed during washing steps, which might lead to an inexact estimation of the surface density of quaternary ammonium groups. For this reason conductometric titration of iodide serving as counterions of quaternary ammonium groups on modified silica has been accomplished for quaternized particles, which after washing in absolute EtOH have been redispersed and washed twice in ultrapure water adjusted to pH 3 with HNO_3 . At pH 3 quaternary ammonium groups are prevented from interactions with silanolate groups, due to the fact that their pKa silanol groups are solely present on the surface of the quaternized silica nanoparticles. To 2 mL of quaternized NPs (60.9 g/L) 150 μL of AgNO_3 solution (0,1 M) was added until the conductivity

measured increased significantly, signaling the consumption of all iodide ions present (see FIGURE 3.2-3).

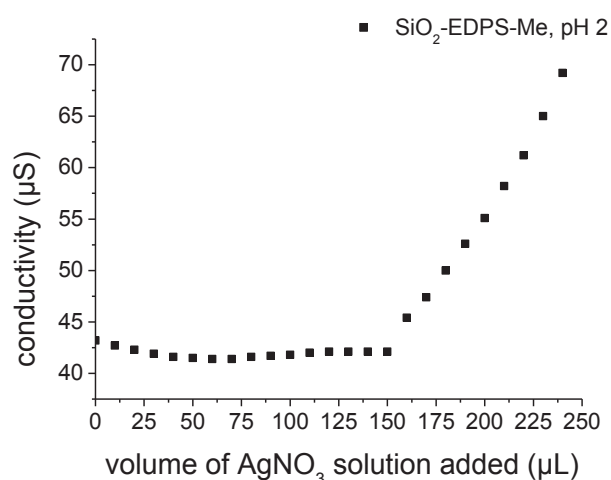


FIGURE 3.2-3 Conductometric titration of iodide ions precipitated as AgI by the addition of AgNO₃ solution.

The amount of AgNO₃ added until the conductivity increased made it possible to determine the presence of 4.3 µmol of iodide ions and correspondingly 4.3 µmol of quaternary ammonium groups per m² surface area of the modified silica colloids. The surface density of iodide counterions of 4.3 µmol/m² determined for quaternized nanoparticles dispersed and washed at pH 3 is a less high than the 5.2 µmol/m² determined for a sol of quaternized nanoparticles, which have been dispersed and washed in ultrapure water at pH 6.8.

To estimate the amount of quaternary ammonium groups per m² surface area of the modified nanoparticles we employed further methods. To determine the surface density of EDPS grafts per m² of modified silica we carried out the thermogravimetric analysis of EDPS-modified nanoparticles before and after the alkylation with iodomethane.

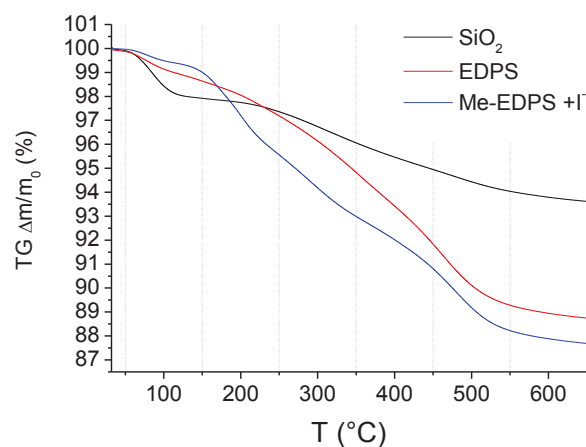


FIGURE 3.2-4 Percentual mass loss of silica nanoparticles after different steps of functionalization to obtain SiO₂-EDPS-Me nanoparticles. **Black line:** Unmodified colloidal silica **Red line:** SiO₂-EDPS nanoparticles, **Blue line:** SiO₂-EDPS-Me nanoparticles after four washing steps with EtOH.

When we look at the TGA diagrams of EDPS-modified and alkylated EDPS-modified nanoparticles after washing with EtOH and H₂O (see FIGURE 3.2-4) we can see that there is a significant difference between the mass loss of quaternized nanoparticles and unalkylated EDPS-modified nanoparticles. The difference between the mass loss of quaternized nanoparticles and unalkylated EDPS-modified nanoparticles shows a maximum in the temperature range from 160 °C to 360 °C due to the presence of ionically adsorbed species such as I⁻ detected in the coupled mass spectrum (see FIGURE 3.1-4). The surface densities calculated for EDPS-modified silica nanoparticles before and after alkylation are shown in TABLE 3.2-1. Assuming that the surface density of the EDPS grafts on the surface did not change we can suppose that the difference in mass loss is due to the methyl groups added during alkylation. We subtract the mass loss between 160 °C and 650 °C of EDPS-modified nanoparticles from the mass loss of alkylated nanoparticles to calculate the number of fully methylated grafts assuming the presence of one iodide counterion per quaternized nitrogen (see exemplary calculation in Annex 3, EQUATION 0-2).

TABLE 3.2-1 Surface density of EDPS-modified silica nanoparticles and quaternized EDPS chains after methylation with iodomethane

Graft	M	$\Delta m_{160-650^{\circ}\text{C}}$ (%)	D_{GRAFT} ($\mu\text{mol}/\text{m}^2$)	Graft/ nm^2
EDPS	101	- 9.78	9.19	5.5
2.5 Me + [⊖] -1.5H ⁺	162.9	- 11.056	2.61	1.57

In the light of these results we presume a full methylation for one EDPS branch per nm^2 , which corresponds to the creation of one quaternary ammonium group on 28 % of the EDPS grafts. We determined that the surface density of EDPS is about 2-6 times higher than observed elsewhere. According to the literature the surface coverage of EDPS is nominally $55 \text{ \AA}^2/\text{molecule}^{[75]}$, on silica surfaces grafting densities of $1.5 \mu\text{mol}/\text{m}^2$ to $3 \mu\text{mol}/\text{m}^2$ have been determined^[76,77]. The surface density of EDPS of $4.9 \mu\text{mol}/\text{m}^2$ was achieved on iron oxide nanoparticles^[23]. The presence of $2.6 \mu\text{mol}$ of quaternary ammonium groups per m^2 of modified silica would fit in the range to the surface densities observed before. The quaternization degree of about 28 % might be explained by the fact that the surface density of grafted EDPS films is overestimated due to the loss of water, ammoniac, ethoxy residues or glycerol molecules which may be included in the grafted silane layer. Furthermore the EDPS film probably does not consist of a well-ordered monolayer, but of polymerized silane networks condensed on the silica surface^[78], which renders a part of the grafted amine groups inaccessible for modification as has been observed for various aminosilanes^[23,79,80].

To calculate a more exact degree of effective methylation we removed iodide ions by a washing step in one molar NaCl solution to induce an ionic exchange of iodide and chloride ions. In the TG-coupled mass spectrum shown in FIGURE 3.2-5 we can see that an ionic exchange between iodide and chloride ions takes place.

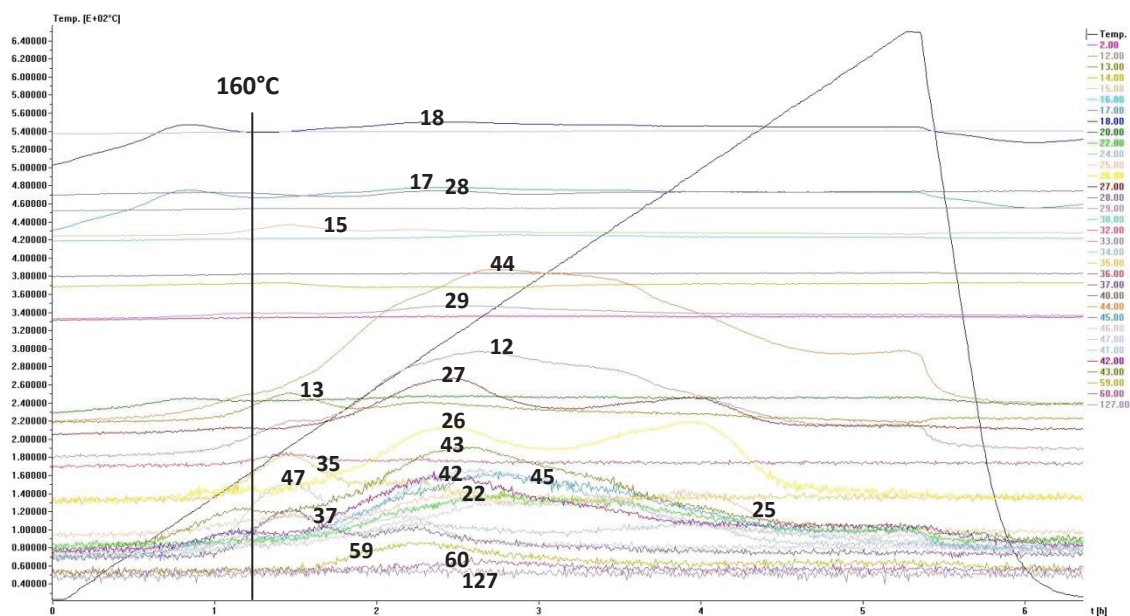


FIGURE 3.2-5 Mass spectrum of methylated EDPS-modified silica nanoparticles after washing steps with ethanol, H₂O (18.2 MΩ) and NaCl (1M) recorded with a TG coupled mass spectrometer.

After the washing step of the methylated EDPS-modified nanoparticles with NaCl, we were unable to detect the release of I⁺ ions m/z 127 anymore, but two peaks at m/z 35 and 37 belonging to Cl⁺ isotopes reappeared. As proof of a successful methylation reaction we observed the presence of the fragments of a tertiary amine group C₃H₉N⁺ (m/z = 59) and C₃H₁₀N⁺ (m/z = 60). Furthermore we observed mass fragments already identified in previously shown mass spectra (see **FIGURE 3.1-3** and **FIGURE 3.1-4**).

In comparing the TG diagrams of EDPS-modified and alkylated EDPS-modified nanoparticles before (EDPS-Me +I) and after NaCl washing (EDPS-Me +Cl) we can observe that the mass loss of washed nanoparticles is significantly smaller than the mass losses obtained for EDPS-modified and methylated EDPS-modified particles before NaCl washing (see **FIGURE 3.2-6**). When we look at the differentiated TG diagrams for EDPS modified nanoparticles we observe a continuous increase in the mass loss with a clear peak in the temperature range from 360 °C to 650 °C. After alkylation with iodomethane we observe a first peak at 200 °C which is attributed to the loss of iodide ions, but also a peak in the temperature range from 360 °C to 650 °C. These two peaks nearly disappear in the differentiated diagram of salt-washed nanoparticles. The silane layer of the surface modification seems to disappear partly during the washing step.

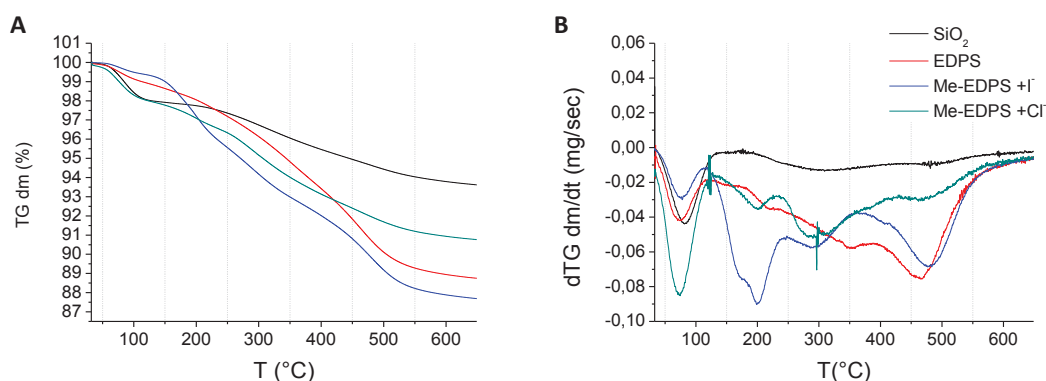
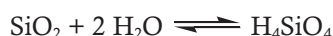


FIGURE 3.2-6 A: TGA diagrams of silica nanoparticles after different steps of functionalization to obtain SiO₂-EDPS-Me nanoparticles. **B:** Differentiated TGA diagrams of silica nanoparticles after different functionalization steps to obtain EDPS-Me modified silica particles. **Black line:** Unmodified colloidal silica, **Red line:** Silica modified with EDPS, **Blue line:** SiO₂-EDPS nanoparticles methylated with MeI after four washing steps in EtOH, **Green line:** SiO₂-EDPS-Me nanoparticles after complete washing in EtOH, NaCl (1M) and H₂O (18.2 MΩ).

Similar effects of washing steps have been observed by Marini et al.^[67], who washed polyethylene samples coated with quaternary ammonium silanes in physiological media and observed a reduced antibacterial activity by the modified polymer surfaces after several washing cycles. The dissolution of silica nanoparticles synthesized by the Stöber method in biological media has also been described^[81,82]. Mahon et al.^[82] were able to show that colloidal silica produced by the Stöber process is easily dissolvable compared to colloidal silica produced by the arginine method implemented by Hartlen^[83] and co-workers, because of the lower density of Stöber silica, the porosity of which facilitates nucleophilic attacks on the silica matrix. One reason for the loss of silanes on the modified surfaces due to washing with electrolyte solutions may be the dissolution of silica in salt solutions. In general silica polymorphs implement dissolution by the reaction:



EQUATION 3.2-1 Reaction of the dissolution of silica in aqueous near neutral media.

in near-neutral media^[84], where molecular water acts as a weak nucleophile. In acidic or basic solvents H⁺ or OH⁻ ions attack the silica surface more aggressively. But this dissolution can equally be accelerated by the increase in temperature or the addition of dilute solutions of cations to the silica surrounding media^[85-87]. Dove et al.^[86] showed that weak concentrations of 0.001 M Na⁺ ions already increase the dissolution rate of silica and that the increase in the dissolution follows the form of a Langmuir-type isotherm expression. Positively charged cations such as Na⁺ adsorb to the silica surfaces as described by the reaction:



EQUATION 3.2-2 Reaction of the adsorption of sodium cations to silica surfaces.

As a consequence of the dissolution process NaCl, NaOH, NaSiO(OH)₃ and H₄SiO₄ are formed in solution^[85]. Further sodium orthosilicate complexes can be detected by fast atom bombardment mass

spectrometry^[88]. The dissolution rate increases sharply up to the Na^+ concentration needed to cover the silica surface completely, the presence of supplementary Na^+ ions having no influence on the dissolution rate of silica. The dissolution rate in a 0.05 M solution of NaCl is 21 times larger^[89] than that in deionized water. Comparing different cations Dove et al.^[86] demonstrated that the dissolution rate is highly dependent on the adsorption strength of a cation, showing that the addition of weaker adsorbing ions such as Mg^{2+} or Ca^{2+} can even decrease the dissolution rate of silica in a solution of different cations.

In looking for an alternative method to eliminate iodide ions and determine the exact methylation degree of the alkylated nanoparticles we precipitated the iodide ions remaining in solution by adding 200 μL of an AgNO_3 solution (0.1M). The resulting extremely fine AgI precipitate was separated from the nanoparticles by centrifuging six times at 1000 g for 10 min. The solution obtained shows a yellow-brownish color, due to AgI precipitate which cannot be completely separated from the silica nanoparticles because of their small size (see FIGURE 3.2-7). This fact renders the determination of methylgroups added during quaternization by TGA error-prone.

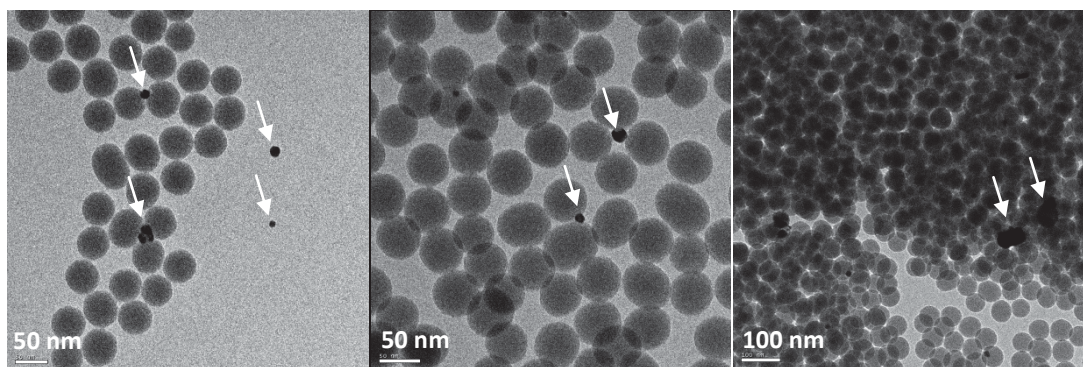


FIGURE 3.2-7 TEM pictures of methylated EDPS-modified silica nanoparticles after removal of iodide ions with AgNO_3 . AgI precipitate of inhomogeneous size remains in the centrifuged solutions and can be observed on all three TEM pictures as indicated by the white arrows.

To permit a further estimation of iodide ions, serving as counterions for quaternary ammonium groups per m^2 present on modified silica nanoparticles, the collected AgI precipitate was weighed. For a sol containing nanoparticles with a surface area of 25.8 m^2 it was possible to precipitate 0.02739 g of AgI precipitate corresponding to $1.167 \cdot 10^{-4} \text{ mol}$ AgI and subsequently to the presence of $4.5 \mu\text{mol}$ iodide ions per m^2 . This value resembles the surface density of quaternary ammonium groups determined by conductometry and seems to be more realistic considering the fact that the surface density of EDPS on silica is – according to the literature^[23,76,77] – expected to be between about $1.5 \mu\text{mol}$ and $4.9 \mu\text{mol}$ EDPS per m^2 of modified metal oxide surface. Nevertheless it may be overestimated, due to the fact that sporadically silica particles retained in the precipitate could contribute to the weighed mass of the precipitate.

The methods we used to determine the amount of quaternary ammonium groups should be regarded as complementary. In recapitulating we assume a presence of $2.6 \mu\text{mol}$ to $4.5 \mu\text{mol}$ of quaternary ammonium groups per m^2 surface area of the modified nanoparticles. The value of $4.5 \mu\text{mol}$ of

quaternary ammonium groups per m^2 of the modified colloids determined by weighing AgI precipitate may be slightly overestimated, due to the fact that silica particles might be retained in the precipitate and contribute to the weighed mass. The values of $5.2 \mu\text{mol}$ and $4.3 \mu\text{mol}$ of quaternary ammonium groups per m^2 of quaternized particles determined by conductometric titration of iodide ions remaining in a sol of modified nanoparticles stay in the same order of magnitude. Nevertheless, surface densities determined by conductometry are sensitive to the washing process, because of a possible ionic interaction between quaternary ammonium groups and silanolate groups present on the particle surfaces causing a release of iodide counterions which we dose. The value of $2.6 \mu\text{mol}$ of quaternary ammonium groups per m^2 determined by TGA needs to be treated with care due to the fact that the decomposition of EDPS grafts and chemisorbed water, ethoxy residues or ammoniac enclosed in the porous silica nanoparticles contribute to the mass loss measured in the temperature range from $160 \text{ }^\circ\text{C}$ to $650 \text{ }^\circ\text{C}$. Furthermore we have seen that the modified nanoparticles need to be prevented from exposure to high salt concentrations to prevent the outer silane layer from dissolution. In this respect we should notice that depending on their electronegativity cations possess a different adsorption strength and dissolution potential. The smaller the cation is, the higher is its electronegativity and its potential to adsorb to silica and to initiate dissolution by the polarization of the Si-O-Si network.

3.3 Surface potential and colloidal stability of EDPS modified and quaternized EDPS modified silica nanoparticles

The surface potential of quaternized nanoparticles is amongst other factors depending on the quality of the EDPS modification of the nanoparticles. If it is well accomplished the EDPS-modified nanoparticles can reach a zeta potential of about 33 mV at $\text{pH } 7.4$ and possess an isoelectric point at $\text{pH } 9.0$. Zeta potential measurement of the same particles after methylation shows that the quaternization of the EDPS-modified nanoparticles leads to a shift of the isoelectric point to $\text{pH } 10.5$ and that the particles show a zeta potential of about 36 mV at $\text{pH } 7.4$ (see **FIGURE 3.3-1 A**).

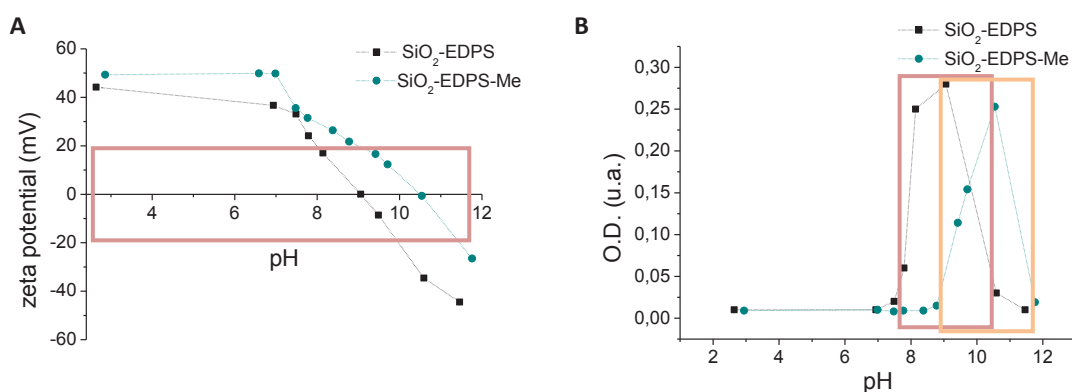


FIGURE 3.3-1 A: Comparison of the zeta potential of alkylated EDPS-modified and simple EDPS-modified nanoparticles. The red zone marks the zone of particle coagulation. **B:** Optical density depending on the pH of samples of alkylated EDPS-modified and simple EDPS-modified nanoparticles at various pH. The red line marks the zone of the coagulation of EDPS-modified nanoparticles; the orange line marks the zone nanoparticle coagulation of SiO₂-EDPS-Me.

In contrast to EDPS-modified nanoparticles, which coagulate in the pH range from pH 7.5 to pH 10.5, the zone of coagulation is shifted to the pH range from about pH 8.9 to pH 11.6 for quaternized particles (see FIGURE 3.3-1 B). This effect can be explained by the pH independence of quaternary ammonium groups, which diminishes the compensation of the charges by the addition of a base in comparison to charges of protonated amine groups, which are sensitive to deprotonation and are revoked in the presence of a base. However, the quaternized nanoparticles show coagulation around pH 10, which can be explained by the dissolution of silica and the subsequently appearance of silanolate groups at basic pH via the reaction:



EQUATION 3.3-1 Reaction equation of the dissolution of silica at basic pHs.

The shift of the zone of coagulation for EDPS-Me modified nanoparticles permits us finally to dispose of silica nanoparticles bearing quaternary ammonium groups possessing a sufficient colloidal stability at physiological pH to be exploited as labeling agents in physiological media, as is shown by the high zeta potential we were able to measure of such quaternized nanoparticles in the presence of salt (see FIGURE 3.3-2).

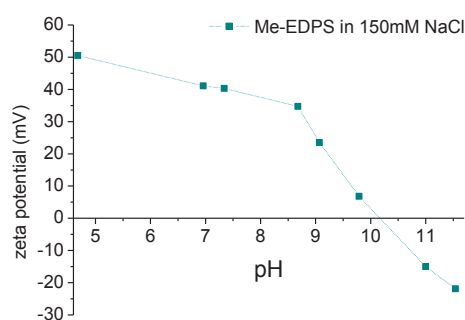


FIGURE 3.3-2 Zeta potential of quaternized EDPS-modified nanoparticles in the presence of 150 mM NaCl.

It is interesting that during the preparation of the samples for zetametric measurements a shift in the initially adjusted pH of the samples is observed over time (see FIGURE 3.3-3). The observed shifts of the pH seem to be most important at basic pHs and might be explained by the fact that due to the addition of a base such as NaOH silanolate groups appear continuously on the surface of the modified nanoparticles due to the fact that not every silanol group present on the surface of silica has been condensed to an EDPS molecule. In what follows the emergence of negatively charged silanolate groups causes the attraction of positively charged quaternary ammonium groups. The organic chain of the grafted EDPS molecules turns inside the coating silane layer and an ionic bond forms between quaternary ammonium groups and surfaced silanolates. At the same time iodide ions previously serving as counterions of the quaternary ammonium groups are released as well as the protons of the original silanol groups – causing the decrease of the pH over time before the surface stabilizes, forming HI. This phenomenon is limited by the number of quaternary ammonium groups on the particle surface area and by the pKa of silanol groups determining the availability of silanolate groups. It has

also been observed for nanoparticles modified with TMAPS and EDPS (data not shown) in which case we notice much larger pH shifts for TMAPS-modified nanoparticles than for quaternized nanoparticles probably as a result of the presence of more silanolate groups due to a more irregular silane layer on the surface of TMAPS-coated silica colloids.

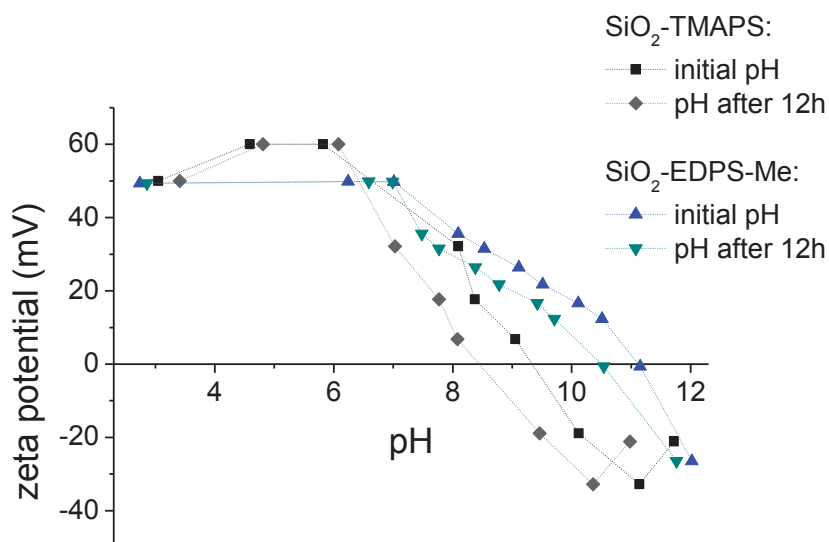
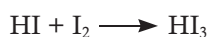


FIGURE 3.3-3 Illustration of the shifts of the pH of samples prepared for zetametric measurements for 12 hours.

By redispersing freshly quaternized nanoparticles (SiO₂-EDPS-Me) with a surface area of 14.04 m² in 20 mL water at pH 6.61 we can measure an instantaneous shift of the pH to pH 4.64 corresponding to the release of 4.52·10⁻⁷ mol of H₃O⁺ ions. Supposing that the release of protons is not induced by the addition of a base but solely due to the creation of an ionic bond between quaternary ammonium groups and silanolate groups we assume that the release of HI is exclusively responsible for the decrease in the pH. Subsequently the decrease in the pH gives an idea of the concentration of protons released and consequently of the amount of quaternary ammonium groups immersing into the silane layer to form ionic bonds with silanolate groups on the surface, which we calculated to be of 0.03 μmol per m² surface area of the modified nanoparticles. In contact with air HI will over time undergo oxidation according to the following reaction equations:



EQUATION 3.3-2 Due to the oxidation of hydrogen iodide with oxygen the formation of HI₃ becomes possible due to the redox potentials of the couples O₂/H₂O = 1,23, I₂/I⁻ = 0,621 et I₃⁻/I⁻ = 0,54.

This process leads to a decrease in the pH, which we observed for the sample described and which increased to pH 5 after 30 minutes and to pH 6.5 after 5 days, while the sample took on a brownish color due to the formation of HI₃.

3.4 Conclusions

In the third part of this second chapter we showed the development of a protocol for the chemical surface modification of silica nanoparticles, which permits the fabrication of highly cationic charged nanoparticles bearing quaternary ammonium functions on their surface. We set up a reaction protocol permitting us to conduct the Mentschutkin alkylation reaction on EDPS-modified silica nanoparticles preserving their colloidal stability during the reaction process. We were able to estimate the amount of quaternary ammonium groups present on one m^2 surface area of a modified nanoparticle as between $4.3 \mu\text{mol}$ and $5.2 \mu\text{mol}$. Quaternized nanoparticles have been shown to immediately disperse in ultrapure water after washing in EtOH, while shifting the initial pH of the sol to lower pHs due to the release of HI occurring when quaternary ammonium groups interact with silanol and silanolate groups remaining on the surface of the modified nanoparticles. Shifts of the pH have also been observed during the preparation of samples at basic pHs for zetametric measurements, which can be explained by the fact that silanol groups are deprotonated when the pH of a sol is raised and subsequently quaternary ammonium ions immerse to the silane layer to interact with the occurring silanolate groups. Hence the immersion of organic grafts to the coated silane layer may be reversible. It is driven by the formation of ionic bonds between the positively charged organic grafts and silanolate groups on the surface of the modified nanoparticles which may be abrogated by the addition of a counterion competing for the interaction with the negatively charged silanolate. This should result in a ionic exchange causing the liberation of quaternary ammonium groups. Nevertheless, we observed that the modified nanoparticles do not resist accelerated dissolution at high salt concentrations and need to be handled with care. The major gain of the modification strategy to first accomplish the surface modification of silica nanoparticles with the aminosilane EDPS and to quaternize the amine groups via a second chemical modification step is the achievement of nanoparticles bearing quaternary ammonium groups on their surface and possessing an isoelectric point at pH 10.5. The nanoparticles obtained are still positively charged and well dispersed under physiological conditions in the presence of 150 mM NaCl at pH 7.4. They are suitable for application in biologic environments and for use as DNA labeling tool.

In what follows we will explore the ability of the quaternized nanoparticles to interact with DNA and cationic lipids, which are the major constituents of lipoplexes. The high selectivity of quaternary ammonium groups for phosphate-containing compounds has been multiply demonstrated by different studies. It has been shown that silica materials bearing quaternary ammonium groups selectively adsorb different phosphonates such as the neurotransmitter pinacoyl methylphosphonate^[22], but that the adsorption of bulkier phosphonates^[34] is of lower efficiency. To ensure that the quaternized nanoparticles, which we synthesized, are suitable for use as a DNA labeling agents we examined the interactions between quaternized nanoparticles and DNA as well as phospholipids, as we will show in the next chapter.

REFERENCES

- [1] W. Stöber, A. Fink, E. Bohn, *J. Colloid Interface Sci.* **1968**, *26*, 62–69.
- [2] T. Matsoukas, E. Gulari, *J. Colloid Interface Sci.* **1989**, *132*, 13–21.
- [3] G. . Bogush, C. . Zukoski IV, *J. Colloid Interface Sci.* **1991**, *142*, 19–34.
- [4] A. K. Van Helden, J. W. Jansen, A. Vrij, *J. Colloid Interface Sci.* **1981**, *81*, 354–368.
- [5] C. G. Tan, B. D. Bowen, N. Epstein, *J. Colloid Interface Sci.* **1987**, *118*, 290–293.
- [6] A. Van Blaaderen, J. Van Geest, A. Vrij, *J. Colloid Interface Sci.* **1992**, *154*, 481–501.
- [7] D. Green, J. Lin, Y.-F. Lam, M. Z.-C. Hu, D. W. Schaefer, M. . Harris, *J. Colloid Interface Sci.* **2003**, *266*, 346–358.
- [8] A. Perro, *Synthèse Et Valorisation de Particules Colloïdales de Morphologie Et de Fonctionnalité de Surface Contrôlées*, Université Bordeaux 1, **2006**.
- [9] L. T. Zhuravlev, *Langmuir* **1987**, *3*, 316–318.
- [10] L. T. Zhuravlev, *Colloids Surf., A* **2000**, *173*, 1–38.
- [11] R. Mueller, H. K. Kammler, K. Wegner, S. E. Pratsinis, *Langmuir* **2002**, *19*, 160–165.
- [12] P. K. Jal, S. Patel, B. K. Mishra, *Talanta* **2004**, *62*, 1005–1028.
- [13] S. Ek, A. Root, M. Peussa, L. Niinistö, *Thermochim. Acta* **2001**, *379*, 201–212.
- [14] T. A. Guiton, C. G. Pantano, *Colloids Surf. A* **1993**, *74*, 33–46.
- [15] S. Cousinié, M. Gressier, C. Reber, J. Dexpert-Ghys, M.-J. Menu, *Langmuir* **2008**, *24*, 6208–6214.
- [16] P. Innocenzi, *J. Non-Cryst. Solids* **2003**, *316*, 309–319.
- [17] J. R. Martínez, F. Ruiz, Y. V. Vorobiev, F. Pérez-Robles, J. González-Hernández, *J. Chem. Phys.* **1998**, *109*, 7511–7514.
- [18] L. T. Arenas, J. C. P. Vaghetti, C. C. Moro, E. C. Lima, E. V. Benvenuti, T. M. H. Costa, *Materials Letters* **2004**, *58*, 895–898.
- [19] F. A. Pavan, T. M. H. Costa, E. V. Benvenuti, *Colloids Surf., A* **2003**, *226*, 95–100.
- [20] R. Brückner, *Reaktionsmechanismen: Organische Reaktionen, Stereochemie, Moderne Synthesemethoden*, Spektrum Akademischer Verlag, **2009**.
- [21] K. L. Mittal, *Silanes and Other Coupling Agents*, BRILL, **2009**.
- [22] H. K. Schmidt, A. Kaiser, **2009**.
- [23] S. Mornet, *Synthèse Et Modification Chimique de La Surface de Nanoparticules de Maghémite à Des Fins D'applications Biomédicales*, **2002**.
- [24] M. A. Markowitz, G. Deng, B. P. Gaber, *Langmuir* **2000**, *16*, 6148–6155.
- [25] H. Zheng, C. Gao, S. Che, *Microporous Mesoporous Mater.* **2008**, *116*, 299–307.
- [26] C.-H. Lee, L.-W. Lo, C.-Y. Mou, C.-S. Yang, *Adv. Funct. Mater.* **2008**, *18*, 3283–3292.
- [27] C. Lee, S. Cheng, Y. Wang, Y. Chen, N. Chen, J. Souris, C. Chen, C. Mou, C. Yang, L. Lo, *Adv. Funct. Mater.* **2009**, *19*, 215–222.
- [28] I. Dekany, J. Nemeth, M. Szekeres, R. Schoonheydt, *Colloid Polym. Sci.* **2003**, *282*, 1–6.
- [29] O. Weichold, B. Tigges, M. Bertmer, M. Möller, *J. Colloid Interface Sci.* **2008**, *324*, 105–109.
- [30] S.-W. Ha, C. E. Camalier, G. R. Beck Jr., J.-K. Lee, *Chem. Commun.* **2009**, 2881.
- [31] N. Atchison, W. Fan, D. D. Brewer, M. A. Arunagirinathan, B. J. Hering, S. Kumar, K. K. Papas, E. Kokkoli, M. Tsapatsis, *Angew. Chem. Int. Ed.* **2011**, *50*, 1617–1621.
- [32] T.-H. Chung, S.-H. Wu, M. Yao, C.-W. Lu, Y.-S. Lin, Y. Hung, C.-Y. Mou, Y.-C. Chen, D.-M. Huang, *Biomaterials* **2007**, *28*, 2959–2966.
- [33] Y.-P. Chen, H.-A. Chen, Y. Hung, F.-C. Chien, P. Chen, C.-Y. Mou, *RSC Advances* **2012**, *2*, 968.
- [34] P. S. Ghosh, C.-K. Kim, G. Han, N. S. Forbes, V. M. Rotello, *ACS Nano* **2008**, *2*, 2213–2218.
- [35] M. A. Markowitz, G. Deng, M. C. Burleigh, E. M. Wong, B. P. Gaber, *Langmuir* **2001**, *17*, 7085–7092.
- [36] D. Nagao, M. Yokoyama, N. Yamauchi, H. Matsumoto, Y. Kobayashi, M. Konno, *Langmuir* **2008**, *24*, 9804–9808.
- [37] D. N. Hideki Matsumoto, *Langmuir* **2009**, DOI 10.1021/la903266e.
- [38] J. Clayden, N. Greeves, S. Warren, P. Wothers, *Organic Chemistry*, OUP Oxford, **2001**.
- [39] F. Zheng, D. N. Tran, B. J. Busche, G. E. Fryxell, R. S. Addleman, T. S. Zemanian, C. L. Aardahl, *Ind. Eng. Chem. Res.* **2005**, *44*, 3099–3105.
- [40] E. Pigorsch, *Starch - Stärke* **2009**, *61*, 129–138.
- [41] M. Hesse, H. Meier, B. Zeeh, *Spektroskopische Methoden in der organischen Chemie*, Georg Thieme Verlag, **2005**.

- [42] F. Beari, M. Brand, P. Jenkner, R. Lehnert, H. j Metternich, J. Monkiewicz, H. w Siesler, *J. Organomet. Chem.* **2001**, 625, 208–216.
- [43] H. Xiao, N. Cezar, *J. Colloid Interface Sci.* **2003**, 267, 343–351.
- [44] G. J. Kluth, M. M. Sung, R. Maboudian, *Langmuir* **1997**, 13, 3775–3780.
- [45] G. J. Kluth, M. Sander, M. M. Sung, R. Maboudian, in *Papers from the 44th National Symposium of the AVS*, AVS, **1998**, pp. 932–936.
- [46] D. G. Kurth, T. Bein, *Langmuir* **1995**, 11, 3061–3067.
- [47] R. Maoz, J. Sagiv, *Adv. Mater.* **1998**, 10, 580–584.
- [48] M. Hoikkanen, M. Honkanen, M. Vippola, T. Lepistö, J. Vuorinen, *Prog. Org. Coat.* **2011**, 72, 716–723.
- [49] E. P. Plueddemann, *Silane Coupling Agents*, Springer, **1991**.
- [50] J. H. Moon, J. W. Shin, J. W. Park, *Mol. Cryst. Liq. Cryst. Sci. Tech., A.* **1997**, 295, 185–188.
- [51] F. J. Boerio, L. H. Schoenlein, J. E. Greivenkamp, *J. Appl. Polym. Sci.* **1978**, 22, 203–213.
- [52] C. Jin, L. Han, S. Che, *Angew. Chem. Int. Ed.* **2009**, 48, 9268–9272.
- [53] C. Marchini, D. Pozzi, M. Montani, C. Alfonsi, A. Amici, H. Amenitsch, S. Candeloro De Sanctis, G. Caracciolo, *Langmuir* **2010**, 26, 13867–13873.
- [54] J. March, *Advanced Organic Chemistry: Reactions, Mechanisms, and Structure*, Wiley, **1985**.
- [55] K. Hara, S. Akahane, J. W. Wiench, B. R. Burgin, N. Ishito, V. S.-Y. Lin, A. Fukuoka, M. Pruski, *J. Phys. Chem. C* **2012**, 116, 7083–7090.
- [56] C. P. Tripp, M. L. Hair, *Langmuir* **1991**, 7, 923–927.
- [57] T. Deschner, Y. Liang, R. Anwender, *J. Phys. Chem. C* **2010**, 114, 22603–22609.
- [58] S. E. Hankari, B. Motos-Pérez, P. Hesemann, A. Bouhaouss, J. J. E. Moreau, *J. Mater. Chem.* **2011**, 21, 6948–6955.
- [59] H. Mori, A. H. E. Müller, J. E. Klee, *J. Am. Chem. Soc.* **2003**, 125, 3712–3713.
- [60] R. J. Markovich, X. Qiu, D. E. Nichols, C. Pidgeon, B. Invergo, F. M. Alvarez, *Anal. Chem.* **1991**, 63, 1851–1860.
- [61] F. Sonvico, S. Mornet, S. Vasseur, C. Dubernet, D. Jaillard, J. Degrouard, J. Hoebeke, E. Duguet, P. Colombo, P. Couvreur, *Bioconjugate Chem.* **2005**, 16, 1181–1188.
- [62] S. Trépout, S. Mornet, H. Benabdelhak, A. Ducruix, A. R. Brisson, O. Lambert, *Langmuir* **2007**, 23, 2647–2654.
- [63] P. Voisin, E. J. Ribot, S. Miraux, A.-K. Bouzier-Sore, J.-F. Lahitte, V. Bouchaud, S. Mornet, E. Thiaudière, J.-M. Franconi, L. Raison, et al., *Bioconjugate Chem.* **2007**, 18, 1053–1063.
- [64] M. E. Park, J. H. Chang, *Mater. Sci. Eng., C* **2007**, 27, 1232–1235.
- [65] O. Le Bihan, R. Chèvre, S. Mornet, B. Garnier, B. Pitard, O. Lambert, *Nucleic Acids Res.* **2011**, 39, 1595–1609.
- [66] H. Z. Sommer, H. I. Lipp, L. L. Jackson, *J. Org. Chem.* **1971**, 36, 824–828.
- [67] M. Marini, M. Bondi, R. Iseppi, M. Toselli, F. Pilati, *Eur. Polym. J.* **2007**, 43, 3621–3628.
- [68] I. Yudovin-Farber, C. Yanay, T. Azzam, M. Linial, A. J. Domb, *Bioconjugate Chem.* **2005**, 16, 1196–1203.
- [69] R. J. Verheul, S. van der Wal, W. E. Hennink, *Biomacromolecules* **2010**, 11, 1965–1971.
- [70] T. Rojanarata, M. Petchsangai, P. Opanasopit, T. Ngawhirunpat, U. Ruktanonchai, W. Sajomsang, S. Tantayanon, *Eur. J. Pharm. Biopharm.* **2008**, 70, 207–214.
- [71] A. Dehshahri, R. K. Oskuee, W. T. Shier, A. Hatefi, M. Ramezani, *Biomaterials* **2009**, 30, 4187–4194.
- [72] S. Cerneaux, S. M. Zakeeruddin, J. M. Pringle, Y.-B. Cheng, M. Grätzel, L. Spiccia, *Adv. Funct. Mater.* **2007**, 17, 3200–3206.
- [73] J. R. Baran, D. D. Fansler, *US 2008/0069887*
- [74] A. B. Sieval, M. Thanou, A. F. Kotze', J. C. Verhoef, J. Brussee, H. E. Junginger, *Carbohydr. Polym.* **1998**, 36, 157–165.
- [75] S. Mornet, C. Elissalde, O. Bidault, F. Weill, E. Sellier, O. Nguyen, M. Maglione, *Chem. Mater.* **2007**, 19, 987–992.
- [76] R. Corneliussen, *J. Polym. Sci.: Polym. Lett.* **1975**, 13, 184–185.
- [77] H. Ishida, *Polymer Composites* **1984**, 5, 101–123.
- [78] T. Bayer, K.-J. Eichhorn, K. Grundke, H.-J. Jacobasch, *Macromol. Chem. Phys.* **1999**, 200, 852–857.
- [79] E. Briand, V. Humblot, J. Landoulsi, S. Petronis, C.-M. Pradier, B. Kasemo, S. Svedhem, *Langmuir* **2011**, 27, 678–685.
- [80] W. Wang, M. W. Vaughn, *Scanning* **2008**, 30, 65–77.

- [81] F. Roelofs, W. Vogelsberger, *J. Phys. Chem. B* **2004**, *108*, 11308–11316.
- [82] E. Mahon, D. R. Hristov, K. A. Dawson, *Chem. Commun.* **2012**, *48*, 7970–7972.
- [83] K. D. Hartlen, A. P. T. Athanasopoulos, V. Kitaev, *Langmuir* **2008**, *24*, 1714–1720.
- [84] P. M. Dove, N. Han, A. F. Wallace, J. J. De Yoreo, *Proc. Natl. Acad. Sci. U S A* **2008**, *105*, 9903–9908.
- [85] D. J. W. Michael C. Davis, *Geochim. Cosmochim. Acta* **2011**, 401–415.
- [86] P. M. Dove, *Geochim. Cosmochim. Acta* **1999**, *63*, 3715–3727.
- [87] A. R. Felmy, H. Cho, J. R. Rustad, M. J. Mason, *J. Solution Chem.* **2001**, *30*, 509–525.
- [88] M. Tanaka, K. Takahashi, *J. Mass Spectrom.* **2000**, *35*, 853–859.
- [89] J. P. D. Icenhower, *Geochim. Cosmochim. Acta* **2000**.
- [90] T. Ung, L. M. Liz-Marzán, P. Mulvaney, *Langmuir* **1998**, *14*, 3740–3748.

CHAPTER III – STUDY OF THE
INTERACTIONS TAKING PLACE BETWEEN
QUATERNIZED SILICA SURFACES, LIPIDS
AND DNA

We wish to adapt the surface of multimodal silica nanoparticles to strongly interact with DNA transfected through the cell by lipidic transfection agents in the form of lipoplexes. In the last chapter we showed that the modification of silica nanoparticles with the amino functionalized silane N-(3-(trimethoxysilyl) propyl) ethylenediamine (EDPS) (see **FIGURE 0.0-1**) and a subsequent quaternization of the amine groups with iodomethane permitted us to obtain nanoparticles which possess a high colloidal stability under physiological conditions and which show an isoelectric point at pH 10.5. Quaternary ammonium groups are known to possess a high attraction to the adsorption of phosphate groups containing compounds such as phosphonates^[1-3] or DNA^[4,5]. Nanoparticles solely modified with primary and secondary amine groups showed an isoelectric point at pH 9.5 and released labeled DNA in the cytosol^[6]. As a result it

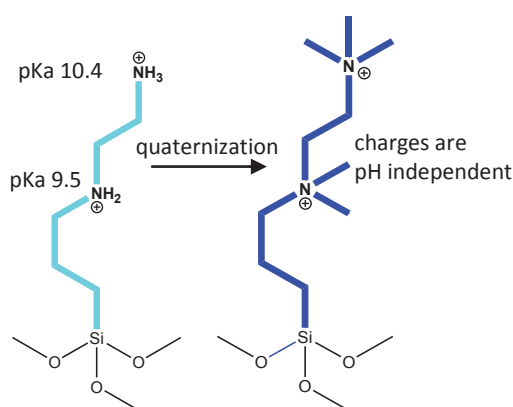


FIGURE 0.0-1 Silane N-(3-(trimethoxysilyl) propyl) ethylenediamine EDPS before (A) and after quaternization (B).

was not possible to display the migration of DNA through the cytosol and its internalization to the nucleus during Cryo-TEM experiments. However, the DNA transfection by cationic lipids could be shown to be successful, due to the detection of expressed gene product. After synthesizing quaternary ammonium group bearing nanoparticles destined for the labeling of DNA which is incorporated into lipoplexes, we have a strong interest in exploring the interactions between the nanoparticles and biomolecules such as lipids and DNA.

The exploration of interactions taking place between quaternized silica surfaces, lipids and DNA will permit us to estimate if our newly modified nanoparticles are appropriate to be tested as DNA labeling tools for the tracing of the migration of lipoplexes *in vivo* or *in vitro*. To analyze if the quaternized SiO₂-EPDS-Me nanoparticles are more appropriate DNA labeling tools than nanoparticles bearing primary and secondary amine groups, we regard the interactions taking place between quaternized silica surfaces and biomolecules with which they come into contact during the transfection process. We will focus on the exploration of interactions between the positively charged quaternized nanoparticles and negatively charged phospholipids as present in cell and endosome membranes^[7] which are crossed by lipoplexes during the transfection process. Subsequently we will investigate the interactions of quaternized nanoparticles with DNA. We will explore the influence of pH and salt concentration on the labelling of DNA with quaternized nanoparticles to investigate if the new surface modification which we have implemented improves the interaction between labeling nanoparticles and DNA in a salt-rich environment such as the cytosol. Finally we will explore the potential of nanoparticles modified with quaternary ammonium groups for labelling DNA in lipoplex structures. The ability of quaternized nanoparticles to be included into lipoplexes while they interact with DNA is crucial in terms of allowing us to visualize the transfection of DNA by cationic lipids.

1. INVESTIGATING THE ADSORPTION OF LIPOSOMES ON BARE, AMINATED OR QUATERNIZED SILICA SURFACES

1.1 The formation of supported lipid bilayers on silica surfaces

To explore the interactions between phospholipids, which are one group of molecular constituents of the cell membrane, and quaternized nanoparticles we will investigate the formation of a supported lipid bilayer (SLB) on silica surfaces. The mechanisms of the formation of supported lipid bilayers on silica nanoparticles are well documented. Supported lipid bilayers can be formed on silica colloids by the interactions of small liposomes with the nanoparticle surface.

Liposomes are spherical vesicles which, due to their amphiphilic properties^[23], organize themselves in a bi- or a multilayer. Possessing charged polar phosphatidyl-headgroups linked to apolar, lipophilic alkylchains they form small lamellar structures within a solvent depending on its polarity. Within water the hydrophilic head groups are on the outside and stay in contact with the solvent while the hydrophobic chains are oriented towards the inside of lipid membranes. Several types of liposomes can appear in water. First there are multilamellar vesicles (MLV). These consist of multiple lipidic layers forming vesicles which are polydisperse in size in the range from 80 nm to 100 μm and in morphology. The second liposome type consists of liposomes called giant unilamellar vesicles (GUV), which possess sizes up to 50 μm ^[24] but consist of a single lipid bilayer. Large unilamellar vesicles (LUV) are also formed by a single lipidic bilayer. Their size varies between 200 nm and 1 μm . Another type of vesicles are small unilamellar vesicles (SUV). They consist of a single lipid bilayer and from vesicles in a size range from 20 to 50 nm. Their size distribution is less polydisperse than for the other LUVs or MLVs.

Liposomes can be prepared by different methods^[25] such as dialysis, extrusion or sonication. To obtain small unilamellar vesicles of the desired lipid composition we used the film hydration method and a subsequent sonication process following **PROTOCOL 1.1-1**:

PROTOCOL 1.1-1 Formation of small unilamellar lipid vesicles

400 μL of a lipid stock solution in chloroform (50 mg/mL) was taken with a glass syringe and added into a 5 mL round bottom glass flask. The chloroform was evaporated at room temperature on a rotary evaporator to form a thin film of lipid layers on the wall of the glass flask. Twice the lipid layer is redissolved in 1 mL of diethyl ether and reformed by evaporation of the solvent. The film of lipid layers on the glass wall was then dried at room temperature in a desiccator which was set under vacuum for 20 minutes. The thin lipid film was then hydrated by the addition of 2 mL of ultrapure water (18.2 M Ω) and vortexed for one minute. Subsequently the mixture was frozen in liquid nitrogen at -72 $^{\circ}\text{C}$ and thawed out in a 37 $^{\circ}\text{C}$ water bath. The freezing-thawing cycle was repeated four times; the liquid was then transferred to a pyrex tube placed in an ice bath and a sonication tip was introduced to the solution. Sonication pulses of two seconds with

20 % amplitude were applied for 30 minutes to form small unilamellar vesicles of the present lipids using a tip sonicator (vibra-cell™ 75042 from Bioblock scientific). The volume was separated by pipetting of 1 mL vesicle dispersion into two separate 1.5 mL Eppendorf tubes. The vesicle dispersion was centrifuged at 13000 rpm to eliminate titanium, which detaches from the sonication tip during the sonication process. The supernatant was taken and 2 mL of a dispersion of small unilamellar lipid vesicles with a lipid concentration of 10 mg/mL was obtained. The concentration of phospholipids can be dosed by a colorimetric dosage of phosphate groups (see Annex 1).

During this preparation a film of lipid layers was hydrated leading to the formation of large multilamellar vesicles of different sizes. The freezing-thawing cycles permit the homogenization of the sizes of these vesicles. Subsequently the sonication process enables the formation of small unilamellar vesicles. The introducing of energy during the sonication process permits the fragmentation of the vesicles and the formation of small unilamellar vesicles after the sonication pulses (see FIGURE 1.1-1).

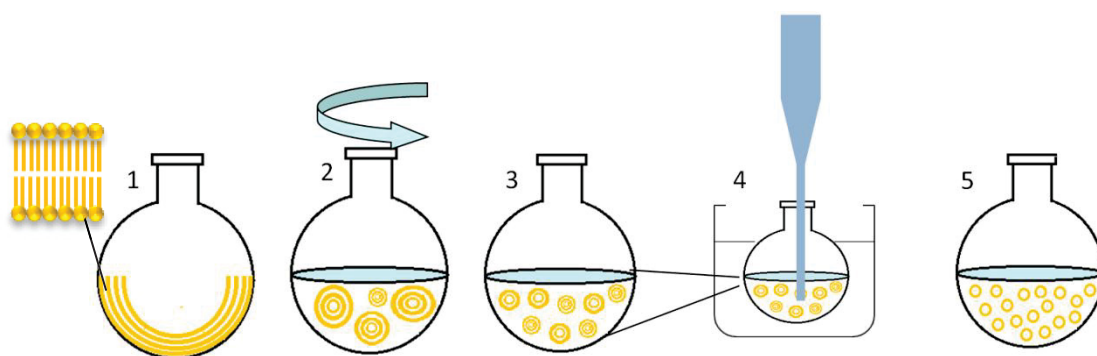


FIGURE 1.1-1 Illustration of the formation of small unilamellar vesicles. **1:** A thin film of lipidic bilayers is formed on the bottom of the glass flask. **2:** The hydration of the film and the vortexing of the sample lead to the formation of large multilamellar vesicles of inhomogeneous size. **3:** Freezing of the sample in liquid nitrogen and subsequent decongelation for several times permit the homogenization of the vesicle sizes. **4:** Pulsing sonication of the dispersion of large multilamellar vesicles leads to the formation of small unilamellar vesicles (5) in water.

When small unilamellar vesicles (SUV) are brought into contact with nanoparticles they can form supported lipid bilayers (SLB) on the nanoparticle surface if an attractive interaction takes place between lipids and nanoparticles. SLBs can be visualized by TEM or Cryo-TEM as shown by Mornet and coworkers^[8] for lipid bilayers of a composition of DOPC/DOPS 4:1 (IUPAC names and structures of all lipids mentioned in this chapter are shown in FIGURE 0-1 in Annex 4) on 100 nm sized silica nanoparticles (see FIGURE 1.1-2).

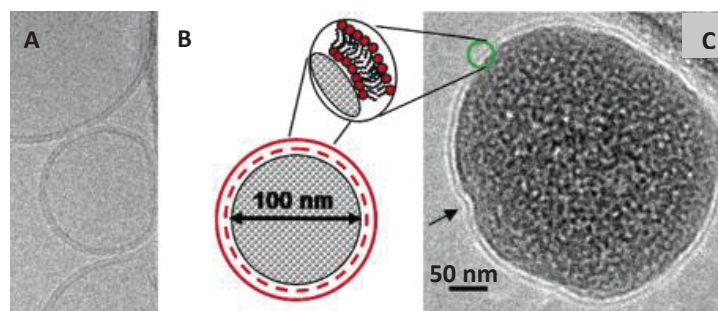


FIGURE 1.1-2 Silica nanoparticles have been brought into contact with DOPC/DOPS 4:1 liposomes resulting in the formation of a supported lipid bilayer in the presence of salt. Both Cryo-TEM pictures are at the same scale. **A:** Cryo-TEM picture of small unilamellar vesicles. **B:** A schematic illustration of the Cryo-TEM picture (**C**) showing the supported lipid bilayer on a silica nanoparticle^[8].

The formation of supported lipid bilayers has been investigated by Cryo-TEM^[8], atomic force microscopy (AFM) or the use of a quartz crystal microbalance with dissipation monitoring (QCM-D)^[9]. Furthermore their characteristics such as thickness and hydration state can be studied by the implementation of complementary optical mass-sensitive techniques such as dual polarization interferometry, ellipsometry, surface plasmon resonance (SPR), optical waveguide lightmode spectroscopy or reflectometry^[10-12]. In the present study we will use QCM-D measurements to monitor the interactions between modified silica surfaces and phospholipids. The principle of a QCM-D measurement is based on the piezoelectric properties of quartz crystals. Sandwiched by two gold electrodes such crystals are excited to mechanical oscillation by the application of an alternating electric field^[13]. After cutting off the electric circuit the decaying oscillation of the crystal can be monitored by measuring the decaying electric field (see **FIGURE 1.1-3 B**).

The decay of the oscillation of the crystal, A , can be fitted over the time t by the **EQUATION 1.1-1**:

$$A(t) = A_0 \exp(-\pi f D t) \sin(2\pi f t + \Phi)$$

f – resonance frequency of the crystal

D – dissipation

A_0 – initial oscillation

Φ – phase shift

EQUATION 1.1-1 Equation fitting the temporal change of the crystal oscillation after cutting off of the driving circuit^[14].

As is known from classic oscillation phenomena the periodic time of one oscillation corresponds to $1/f$. The dissipation energy is measured by means of the amortization of the oscillation of the crystal (see **FIGURE 1.1-3 C**).

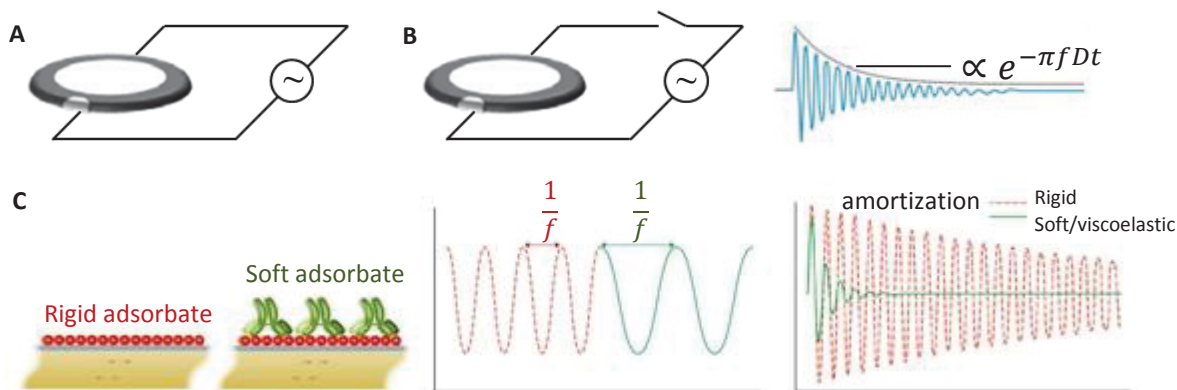


FIGURE 1.1-3 The diagram illustrates the principle of QCM-D measurement. **A:** A quartz crystal is excited to oscillation by application of an alternating current. **B:** When the electric circuit is cut off the free oscillation of the crystal can be measured. The fit of the decaying oscillation is proportional to $\exp(-\pi f D t)$ which permits the extraction of the value of its resonance frequency f and dissipation D ^[14]. **C:** Illustration of the frequency and dissipation shift due to the adsorption of soft matter as a viscoelastic layer^[15].

Once a mass adsorbs to the surface of the quartz crystal a change in its resonance frequency can be observed. The relationship between the difference of adsorbed mass Δm and the shift of the resonance frequency Δf_n has been explained by G. Sauerbrey^[16] and is expressed in the EQUATION 1.1-2:

$$\Delta m = -\frac{v_q \rho_q}{2f_0^2} \frac{2f_n}{n} = -C \frac{\Delta f_n}{n}$$

m – mass of the adsorbed molecules

f_0 – fundamental resonance frequency of the crystal (5 MHz)

f_n – fundamental resonance with the overtone n

v_q – speed of sound intrinsic to quartz (3340 m/s)

ρ_q – density of the quartz crystal (2.65 g/cm³)

EQUATION 1.1-2 The Sauerbrey equation relates the change in the resonance frequency of a quartz crystal to the mass of an adsorbed species on the crystal.

The resonance frequency $\frac{f_n}{n}$ which is measured is normalized to the fundamental resonance frequency of a quartz crystal. After the determination of a Δf it can be introduced to the Sauerbrey equation without the need to be divided by the overtone number n . The fundamental resonance frequency as well as the speed of sound through the crystal and the crystal density are intrinsic values of a quartz sensor and can be merged to the mass sensitivity constant C . For commonly used sensors the constant C has the value of 17.7 ng/cm² Hz^[17]. In determining the mass of a species adsorbed to the sensor surface, we need to consider that the resolution in frequency is about 0.2 Hz, which permits a mass resolution of several ng/cm². The Sauerbrey equation is only valid if the adsorbed mass is smaller than the mass of the crystal and homogeneously adsorbed to the surface. The adsorbed species also needs to be rather rigid and adsorbed to the crystal surface without having the possibility of gliding on the plane^[18]. In addition it must be noted that the adsorbed masses measured by the QCM-D technique include water, which may be coupled to the adsorbed film or enclosed to adsorbed vesicles^[12,19].

While adsorbing a mass to a quartz sensor, as reported by Keller and Kasemo^[20], not only the resonance frequency but equally the dissipation of the crystal shifts. The dissipation D is defined as:

$$D = \frac{E_{lost}}{2\pi E_{stored}}$$

E_{lost} – vibrational energy dissipated during one oscillation cycle

E_{stored} – vibrational energy stored in the oscillator

EQUATION 1.1-3 Dissipation is defined as the loss of vibrational energy divided by the energy stored in the resonating quartz crystal. It causes the amortization of the oscillation curve^[15].

The shift in the dissipation indicates the loss of vibrational energy in the crystal, when a sample adsorbs to its surface. This is explained by the fact that the vibrational energy of the crystal is dissipated through the whole adsorbed sample. If the sample coupled to a sensor surface behaves like a rigid film the dissipation increases only a little. On the contrary, the adsorption of soft matter on the sensor leads to a higher dissipation shift. The dissipation shift gives information about the viscosity, rigidity and compactness of an adsorbed layer. It can be used to detect phase transitions between different adsorption states such as, for example, the rupture of adsorbed lipid vesicles on a fully covered surface leading to the formation of a supported lipid bilayer^[20] or the rigidification of an adsorbed protein layer^[21].

The monitoring of the formation of supported lipid bilayers on silica coated QCM-D crystals gives information about the mechanism of the bilayer formation on a surface^[9,17]. As an example, silica-coated crystals were placed in the sensor modules of the Q-sense E4 QCM-D machine, which were connected to a peristaltic pump which regulated the speed of the flow (see **FIGURE 1.1-4**). The flow rates are in the range of 1 $\mu\text{L}/\text{min}$ to 650 $\mu\text{L}/\text{min}$. Liquid samples were injected over the center of the crystal and left at its periphery, with every sample injection followed by two washing steps. All measurements were accomplished at 25 °C. The tubes included a total volume of 1.5 mL. for a complete exchange of liquid in the sensor cell 500 μL is required, the liquid volume on the sensor is 40 μL . The quartz crystals have a diameter of 14 mm and possess an active surface of 0.2 cm^2 on which the adsorption of injected compounds is monitored.

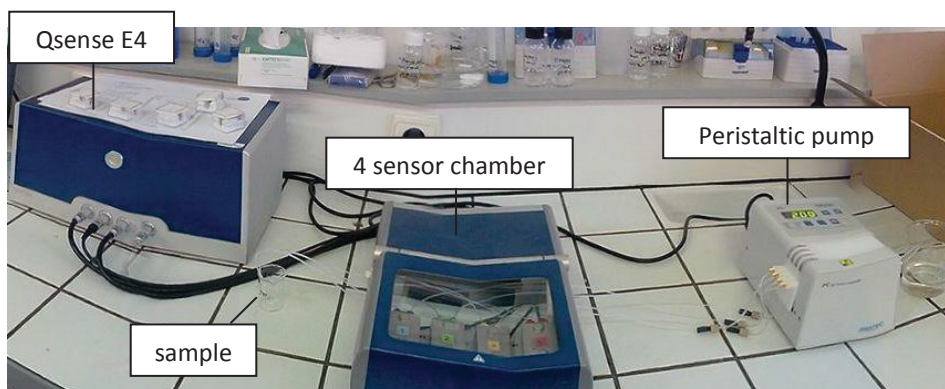


FIGURE 1.1-4 The picture shows the buildup of the Qsense E4 QCM-D used for QCM-D measurements. The liquid sample flows continuously through the cycle. The flow of the liquid is driven by a peristaltic pump and follows the direction indicated by the blue arrows^[14].

The QCM-D measurement is accomplished on overtones 1, 3, 5, 7, 9, 11 and 13. In the following we show the results measured at the seventh overtone f_7 and D_7 . They provide results corresponding to theoretical predictions calculated for a finite circular crystal^[22]. Furthermore resonance frequencies at high overtones between overtone 5 and overtone 13 are less susceptible to external events. The results which we present are already normalized to the fundamental resonance frequency of 5 MHz, therefore the Sauerbrey law can be applied for Δf values measured without the need of dividing by the number of the overtone. By injecting a solution of DOPC SUVs with a lipid concentration of 100 $\mu\text{g}/\text{mL}$ buffered at pH 7.4 with a HEPES buffer (10 mM HEPES, 150 mM NaCl) to an unmodified SiO_2 coated quartz crystal, we could follow the formation of a supported lipid bilayer on the sensor (see FIGURE 1.1-5). In a first time DOPC vesicles adsorb to the SiO_2 surface. They contain large amounts of water and are highly viscoelastic leading to high frequency and dissipation shifts $\Delta f = -55 \text{ Hz}$, $\Delta D = 2.1 \cdot 10^{-6}$. When the surface is saturated with DOPC vesicles and the lipid concentration exceeds a critical level they explode and fuse to form a supported lipid bilayer on the surface. This phenomenon can be followed by the decrease in frequency and dissipation shifts as observed previously in the literature^[9]. Typical frequency and dissipation shifts obtained from a supported lipid bilayer on a silica coated quartz crystal are a Δf of -25 Hz and a ΔD of $0.1 \cdot 10^{-6}$. These values correspond to the adsorption of a rigidly attached mass of 440 ng, which is equivalent not only to the number of DOPC molecules forming the supported lipid bilayer on the silica surface but also to water molecules connected to the lipids^[19]. In FIGURE 1.1-5 we observe a ΔD of $0.1 \cdot 10^{-6}$ Hz and a Δf of -23.5 Hz after twice rinsing the surface with 500 μL buffer solution, corresponding to an adsorbed mass of 416 ng of DOPC bilayer on the silica-coated sensor.

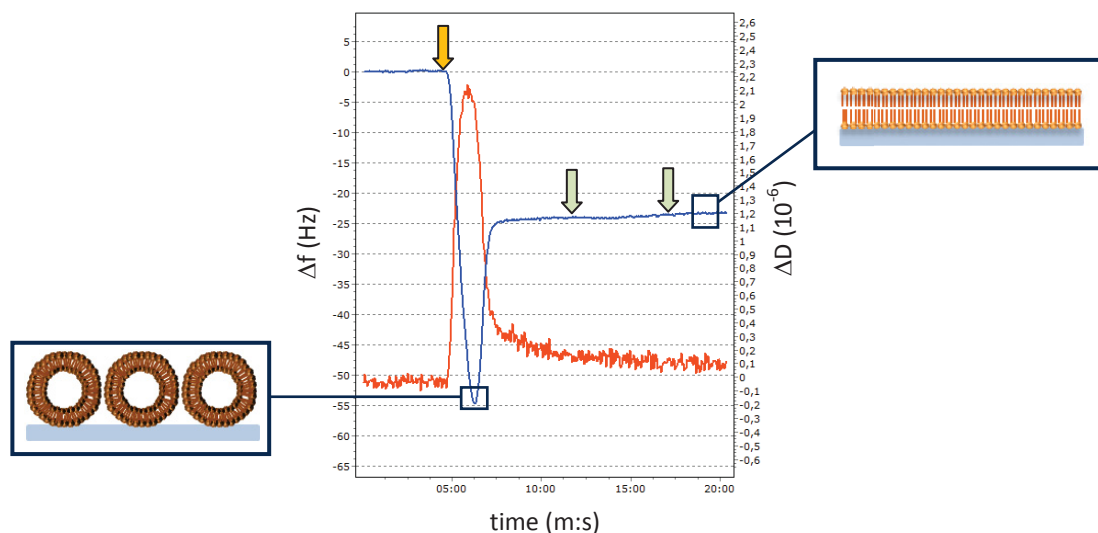


FIGURE 1.1-5 Graph showing the formation of a supported lipid bilayer of DOPC on silica. The evolution of frequency (blue line) and dissipation (orange line) is monitored over time. The measurement was accomplished at pH 7.4 in HEPES buffer (10 mM) in the presence of salt (150 mM NaCl), all injections were implemented at a flow rate of 150 $\mu\text{L}/\text{min}$. The yellow arrow indicates the injection of 950 μL sample containing DOPC SUVs (100 $\mu\text{g}/\text{mL}$); the light green arrows indicate the injection of 500 μL HEPES buffer.

The injection of small unilamellar DOTAP (see IUPAC name and structure in Figure 0-1, Annex 4) vesicles leads to a spontaneous rupture of vesicles reaching the silica surface. When the positively charged DOTAP liposomes come in contact with the negatively charged silica surface, a supported lipid bilayer forms immediately on the bare silica surface (see **FIGURE 1.1-6**).

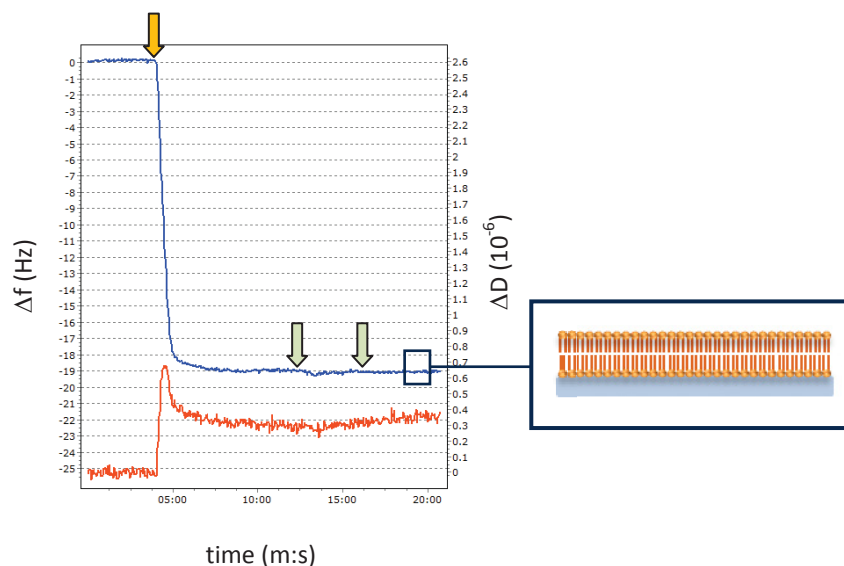


FIGURE 1.1-6 The formation of a supported lipid bilayer of DOTAP on silica is monitored by the evolution of frequency and dissipation over time. The measurement was accomplished at pH 7.4 in HEPES buffer (10 mM), all injections were implemented at a flow rate of 150 $\mu\text{L}/\text{min}$. The yellow arrow indicates the injection of 950 μL sample containing DOTAP SUVs (100 $\mu\text{g}/\text{mL}$); the light green arrows indicate the injection of 500 μL HEPES buffer.

For the adsorption of DOTAP on silica we observe a ΔD of $0.4 \cdot 10^{-6}$ Hz and a Δf of -19.0 Hz after twice rinsing the surface with 500 μL buffer solution, corresponding to an adsorbed mass of 354 ng of DOTAP bilayer on the silica-coated sensor (see **FIGURE 1.1-6**). Although the frequency shift and subsequently the adsorbed mass of DOTAP is less than observed for a SLB of DOPC, it corresponds to the formation of a lipid bilayer because of the fact that the molar mass of the cationic lipids DOTAP is lower than the mass of the phospholipid DOPC.

The mechanistic difference between the monitored formation of a DOPC and a DOTAP bilayer on silica can be explained by taking into account the difference between the zeta potentials of the liposomes used and the silica surface on which the SLB formation takes place (see **FIGURE 1.1-7**). The potential difference between negatively charged silica nanoparticles and positively charged DOTAP vesicles is about 70 mV and is relatively high, which allows the formation of a supported lipid bilayer by strong electrostatic interactions. The strength of these interactions induces a spontaneous rupture of vesicles in contact with the silica surface, and enables the rapid formation of a supported lipid bilayer of DOTAP on the silica surface. In contrast the potential difference between silica nanoparticles and DOPC vesicles is about 10 mV. The formation of a supported lipid bilayer of DOPC on a silica surface therefore can not be explained by a reaction mechanism involving electrostatic interactions. In the presence of salt which decreases the zeta potential of lipids and silica van der Waals forces promote the interaction. The vesicles adsorb to the silica surface where they do not burst spontaneously when

coming in contact with silica, but instead fuse to form an SLB when they are in contact with neighbouring vesicles. This behavior results in the formation of a supported lipid bilayer if the coverage of the silica surfaces with vesicles exceeds a critical concentration^[17,19].

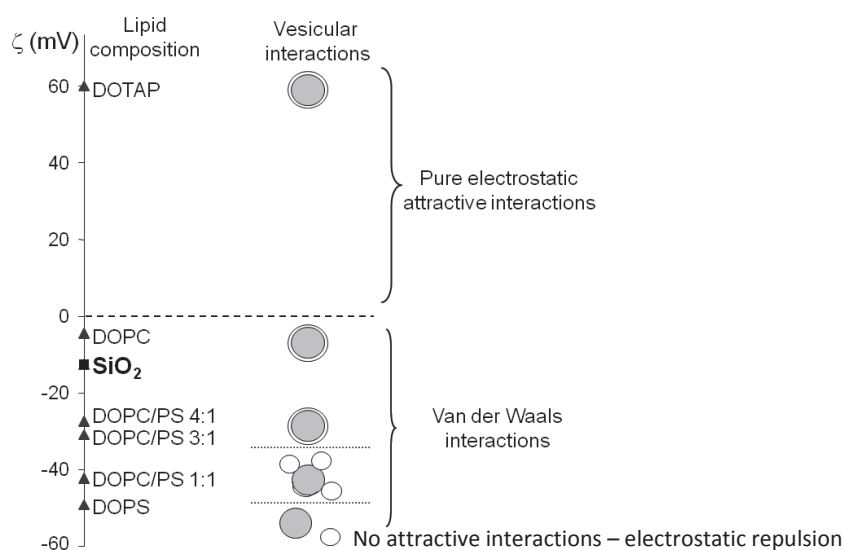


FIGURE 1.1-7 Zeta potentials of small unilamellar vesicles of different composition and silica nanoparticles at pH 7.4 at 150 mM NaCl.

In the presence of 150 mM NaCl even the formation of a supported lipid bilayer of negatively charged phospholipid vesicles of compositions such as DOPC/DOPS 4:1, 3:1 can occur due to van der Waals interactions, because the repulsive electrostatic forces are screened by the salt ions which are present (see IUPAC name and structure of DOPS in **FIGURE 0-1**, Annex 4). However, vesicles containing higher amounts of the negatively charged phospholipid DOPS do not interact with silica surfaces even in the presence of 150 mM NaCl because the repulsive electrostatic forces are not sufficiently screened to allow the prevalence of the weaker van der Waals forces.

1.2 Formation of supported lipid bilayers on silica surfaces bearing primary and secondary amines or quaternary ammonium groups

To study the interactions taking place between negatively charged phospholipids and chemically modified silica nanoparticles, we investigated the formation of supported lipid bilayers of 1,2-dioleoyl-*sn*-glycero-3-phospho-L-serine (DOPS) on EDPS-modified nanoparticles before and after quaternization. The supported lipid bilayers are directly formed by electrostatic interactions. We chose to use negatively charged DOPS liposomes to maximize the zeta potential difference between the modified silica surfaces and vesicles which facilitates the rapid formation of a supported lipid bilayer. To accomplish these experiments we needed to prepare small unilamellar DOPS liposomes.

Supported lipid bilayers form only on hydrophilic surfaces^[14]. To initiate the formation of a supported lipid bilayer on the modified silica nanoparticles, liposomes of 1,2-dioleoyl-*sn*-glycero-3-phospho-L-serine (DOPS) were brought into contact with the modified colloids. The formation of supported lipid

bilayers of negatively charged DOPS molecules on the surface of modified, positively charged silica colloids was implemented in HEPES buffer (10 mM) at pH 7.4 in the absence of salt to facilitate the formation of a supported lipid bilayer via electrostatic interactions. To put the modified nanoparticles in interaction with small unilamellar vesicles a dispersion of nanoparticles was added to a dispersion of small unilamellar lipid vesicles under vortex following **PROTOCOL 1.2-1**. 0.5 mg of DOPS allows the formation of 0.125 m² lipidic bilayer on a surface. The experiments were implemented at different ratios of potentially formed lipid bilayer to the surface of the nanoparticles, which are to be covered with lipid bilayers (LB).

PROTOCOL 1.2-1 Formation of a supported lipid bilayer on the surface of silica colloids by electrostatic interactions

After selecting lipids of an adequate composition we chose the ratio of potentially formed LB surface to the surface area of nanoparticles on which we wished to implement the SLB formation. For a chosen ratio of 4.5 the SLB formation was accomplished as follows: to 110 μL of ultrapure water (18.2 M Ω) 15 μL of HEPES (100 mM, pH = 7.4) was added, as well as 25 μL of SUV (10 mg/mL). 150 μL of 0.25 mg lipids in HEPES (10 mM) buffered solution was obtained; corresponding to a surface of 0.0625 m² lipid bilayer. To 40.2 μL of water 5 μL of HEPES (100 mM, pH 7.4) and 4.8 μL of NPs dispersed in water (46 g/L, diameter 50 nm) were added. The developed surface of the nanoparticles in solution amounted to 0.0139 m². Under vortexing at 1200 rpm the prepared nanoparticle dispersion was added to the dispersion of SUVs. The total volume in which the assembly took place was 200 μL .

The formation of a supported lipid bilayer can also be achieved in the presence of salt. For this purpose in the total volume 30 μL water is replaced by 30 μL of a solution of NaCl (1M) to adjust the final salt concentration at 150 mM NaCl.

The assemblies formed are stable in solution when the lipids are present in excess and the ratio of the surface possibly covered by a lipid bilayer and the surface area of nanoparticles ($S_{\text{LB}}/S_{\text{NP}}$) exceeds 4, whereas they coagulate at surface ratios below 2.5. The supported lipid bilayers, which formed on the surface of modified nanoparticles, could be observed by transmission electronic microscopy. The specimens were stained by the use of stains such as phosphotungsten acetate or uranyl acetate. In **FIGURE 1.2-1** exemplary TEM pictures of quaternized nanoparticles supporting a lipid bilayer of DOPS on their surface are shown.

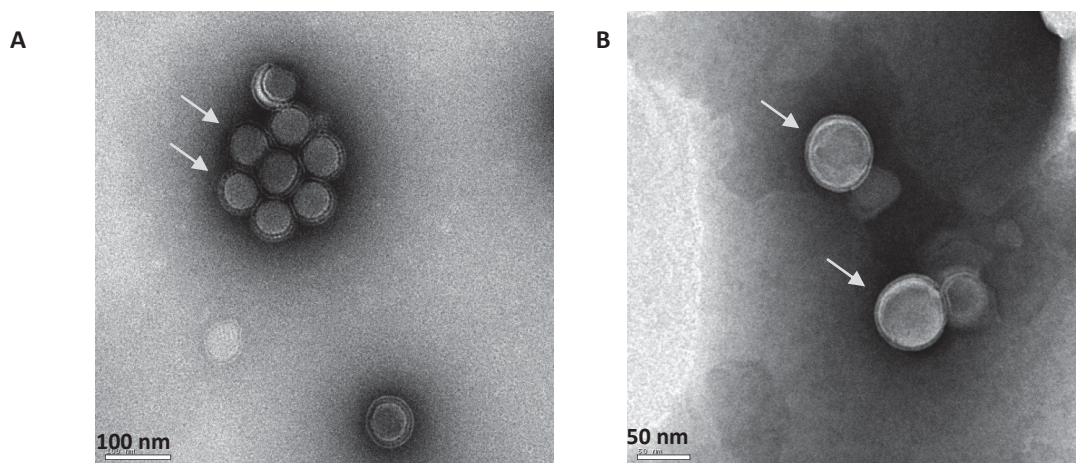


FIGURE 1.2-1 A, B: TEM pictures of quaternized nanoparticles after interaction with DOPS SUVs stained with phosphotungstic acid (2 % w/v) at different magnifications. Supported lipid bilayers are indicated by light grey arrows.

In the present study we displayed the formation of supported lipid bilayers on differently modified silica supports such as quaternized silica supports or silica supports solely modified with EDPS by QCM-D. Due to the fact that the sensing capacity of the QCM-D sensor is based solely on the physical properties of the quartz crystal, but not on the properties of the surface of the crystal, it can be covered with a multitude of materials, which then act as support for adsorbing masses. Crystals coated with thin films of Au, Pt, Al₂O₃, TiO₂ or SiO₂ are commercially available and can be chemically modified without influencing the measurement signal, even when metal foils or mica layers^[26] are deposited on the crystals, whose thickness exceeds 10 μm^[9,27].

During this study we chemically modified SiO₂-coated quartz crystals by the condensation of the silane coupling agent EDPS on the silica coating. Subsequently we implemented a quaternization of the grafted amine groups. The modifications were accomplished as described in **PROTOCOL 1.2-2** and **PROTOCOL 1.2-3**.

PROTOCOL 1.2-2 Surface modification to implement primary and secondary amine groups on silica coated quartz crystals

*The received SiO₂ coated quartz crystals (Qsense QSX 303, 50nm SiO₂) were immersed in a solution of sodium dodecyl sulfate (2 % w/v) for 12 hours, then rinsed with ultrapure water and dried under a nitrogen flux. The dry crystals were then placed on a clean glass support. The electrode-bearing side lay on the glass support, the support was then cleaned by the application of UV radiation on the crystal surface in an UV ozone generator. The clean crystals were immersed in water (18.2 MΩ, pH 8) for 30 seconds and then transferred to a mixture of 9.6 mL ethanol and 400 μL N-(3-(trimethoxysilyl) propyl) ethylenediamine in a 25 mL glass beaker. The crystals stayed submerged in the solution for 12 hours, while the glass beaker containing the crystals was slightly agitated several times (see **FIGURE 1.2-2** step 1, 2). After 12 hours of incubation the crystals were transferred to a 25 mL glass beaker containing 15 mL glycerol and placed in an oven (see **FIGURE 1.2-2** step 3). The oven was set under vacuum and stayed at room temperature for 30 minutes; hence the temperature was augmented to 60 °C for 45 min and subsequently to*

110 °C for two hours. The crystals were placed in 10 mL of absolute alcohol; they were agitated and immersed in EtOH several times to remove glycerol from their surface (see FIGURE 1.2-2 step 4). If the crystals were to be used directly, they were placed in 10 mL of ultrapure water (see FIGURE 1.2-2 step 5).

PROTOCOL 1.2-3 Quaternization of amine groups on previously modified silica coated quartz crystals

To quaternize primary and secondary amine groups present on EDPS modified crystals, instead of immersing them in water they were placed in 9.7 mL of absolute ethanol (see FIGURE 1.2-2 step 4). 100 μ L NEt_3 and 200 μ L MeI were added with a glass syringe (see FIGURE 1.2-2 step 5). The crystals stayed immersed in the reaction mixture for 12 hours, while the glass beaker was slightly agitated several times. The glass beaker was then placed in a water bath at 70 °C for 30 minutes. Subsequently the crystals were washed twice in 10 mL EtOH and were placed in a glass beaker containing 10 mL of ultrapure water (see FIGURE 1.2-2 step 6, 7). Throughout all the modification steps it is important to ensure that the crystal surfaces do not dry out during the transfer from one solution to another. After the modification the crystals were immediately used for QCM-D measurements. They were dried under a gentle nitrogen flux before being placed in the QCM-D sensor cell. Each modified crystal was used for one measurement to achieve reproducible results.

All the steps of the modification process are summarized and illustrated in FIGURE 1.2-2:

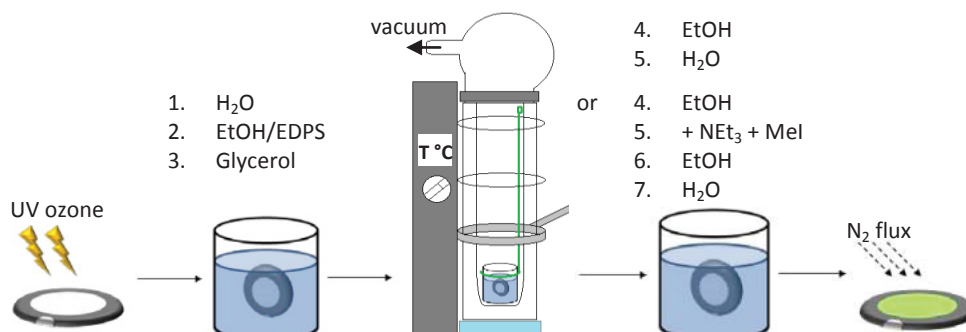


FIGURE 1.2-2 Illustration of the modification process of a SiO_2 -coated quartz crystal with EDPS and subsequent quaternization of the amine groups.

By the injection of sample solutions which contain DOPS (see IUPAC name and structure in FIGURE 0-1, Annex 4) SUVs with a lipid concentration of 100 μ g/mL in HEPES buffer (10 mM) on differently modified crystals we were able to follow the adsorption of DOPS on primary and secondary amines bearing or on quaternized sensors. We implemented these injections at different pHs to compare how the zeta potential of the surfaces influences their interactions with the DOPS vesicles.

Negatively charged DOPS liposomes were injected on silica coated QCM-D crystals previously modified with EDPS which were hydrated with 10 mM buffer solutions, fixing the pHs at pH 7.4 and pH 9 without the presence of further salt. We observed the formation of a supported lipid bilayer of DOPS on EDPS modified surfaces at pH 7.4, which led to a frequency shift of -22 Hz and a

dissipation shift of $0.6 \cdot 10^{-6}$ (FIGURE 1.2-3 A). At pH 7.4 the primary and secondary ammonium group bearing silica surface has a zeta potential of about 30 mV (see FIGURE 3.3-1 A, chapter II). The difference between the zeta potential of negatively charged DOPS vesicles and the positively charged EDPS-modified crystal surface is sufficiently high to allow the formation of a supported lipid bilayer by electrostatic interactions. The observed frequency and dissipation shifts correspond to data observed for the formation of a supported lipid bilayer of 1,2-Dioleoyl-*sn*-glycero-3-phospho-rac-(1-glycerol) (DOPG) on an EDPS modified QCM-D crystal. In this case a frequency shift of -25 Hz and a dissipation shift $0.7 \cdot 10^{-6}$ were measured by QCM-D^[19]. Both supported lipid bilayers formed on EDPS modified crystals show higher dissipation values than observed for supported lipid bilayers on SiO₂ coated quartz crystals, which might be explained by the presence of propyl(ethylenediamine) grafts forming a kind of viscoelastic surface coating. Water molecules may also be intercalated in between the silane layer which can also lead to a higher dissipation shift measured for a bilayer obtained on a modified surface in comparison to the dissipation shift of a supported lipid bilayer formed on bare silica.

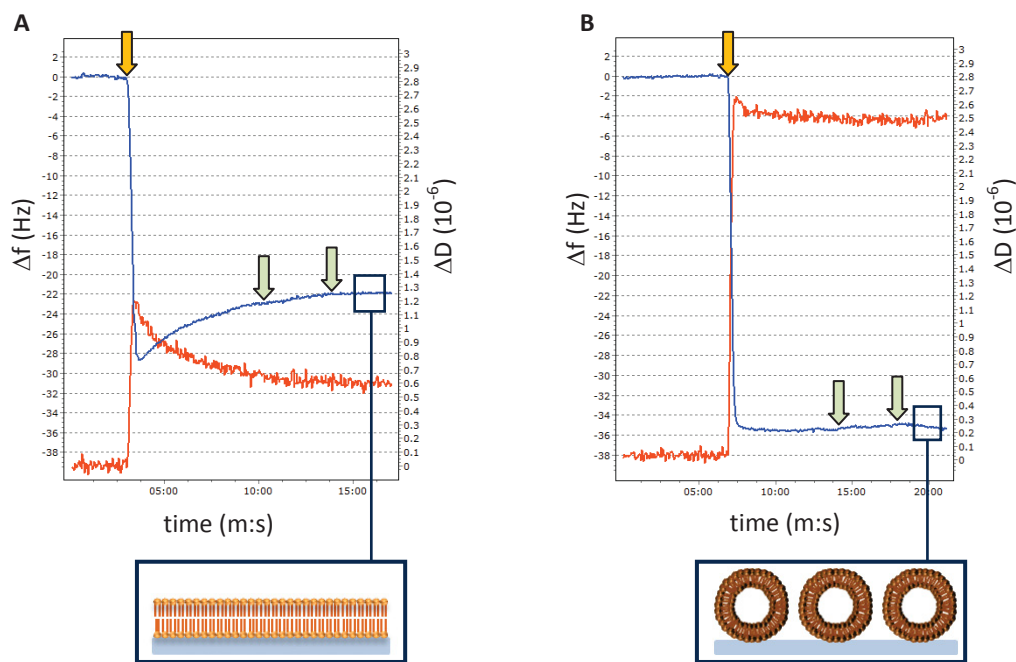


FIGURE 1.2-3 Supported lipid bilayers of DOPS formed on chemically modified QCM-D crystals, the graphs display Δf (blue line) and ΔD (orange line). DOPS was injected on an EDPS modified sensor at pH 7.4 (A) or pH 9 (B). The measurements were implemented in HEPES buffer (10 mM); all injections were effectuated at a flow rate of 150 μ L/min. The yellow arrow indicates the injection of a 950 μ L sample containing DOPS SUVs (100 μ g/mL); the light green arrows indicate the injection of 500 μ L HEPES buffer.

At pH 9 DOPS vesicles were injected on an EDPS-modified surface. We observe a frequency shift of -35.5 Hz and a dissipation shift of $2.5 \cdot 10^{-6}$ (see FIGURE 1.2-3 B). The high dissipation shift indicates the adsorption of a viscoelastic layer of lipidic vesicles. The frequency shift of -33.5 Hz is lower than the frequency shift of -55 Hz, which we observed in FIGURE 1.1-5 for the adsorption of DOPC vesicles on a silica surface. The comparatively low frequency shift of -33.5 Hz indicates that the vesicles which

are adsorbed to the primary and secondary amine-bearing silica surface do not exceed the critical concentration of vesicles needed on the surface to initiate SLB formation. We do not observe a fusion of the adsorbed DOPS vesicles to build a supported lipid bilayer as we observed for DOPC vesicles adsorbed on bare silica. This observation can be explained by several reasons. The zeta potential of an EDPS modified silica surface at pH 9 is nearly zero (see **FIGURE 3.3-1 A**, chapter II) and as a consequence DOPS vesicles are not attracted by electrostatic forces which would permit their spontaneous rupture and the immediate formation of an SLB, but they do adsorb due to van der Waals forces. Furthermore fewer vesicles adsorb to the surface because the injection was implemented in the absence of salt, and as a consequence the negative zeta potential of DOPS vesicles is not screened. The vesicles are still negatively charged and repulse each other. This behavior avoids their fusion and the formation of a supported lipid bilayer.

DOPS vesicles have also been injected on SiO₂-coated crystal surfaces bearing quaternary ammonium groups on their surface after the quaternization of previously present primary and secondary amines with iodomethane. The vesicles have been injected on quaternized surfaces at pH 7.4 and at pH 9 in the absence of salt (see **FIGURE 1.2-4 A, B**). In addition we implemented the injection of DOPS vesicles on a quaternized crystal, which subsequent to the quaternization process was exposed to a solution of 1 M NaCl for 30 seconds (see **FIGURE 1.2-4 C**).

When injecting DOPS small unilamellar vesicles on Me-EDPS-modified surfaces at pH 7.4 we observed a frequency shift of -18 Hz corresponding solely to an adsorbed mass of 319 ng, but a dissipation shift of only $0.3 \cdot 10^{-6}$ (**FIGURE 1.2-4 A**). Whereas the dissipation shift clearly indicated the adsorption of a rigid lipid structure the frequency shift was too low to provide a supported lipid bilayer formed on the quaternized surface. Considering the zeta potential of a quaternized surface of about 36 mV at pH 7.4 we expected that the formation of a supported lipid bilayer would take place immediately due to electrostatic interactions between the positively charged surface and DOPS vesicles. On the contrary we observed the formation of bilayer patches. Nevertheless the formation of supported lipid bilayers of DOPS on quaternized silica nanoparticles has been observed by electron transmission microscopy (see **FIGURE 1.2-1**).

It may be possible that the presence of the quaternizing methyl groups on the quaternized crystal surface renders the sensor less hydrophilic and therefore has a perturbing impact on the formation of a lipid layer on a Me-EDPS modified QCM-D crystal leading to unequally covered surfaces which support bilayer patches. The low frequency shift may be explained by fewer water molecules conjugated in the modifying silane layer. A further explanation of the low frequency shift may be the fact that iodide counterions of the quaternary ammonium groups leave the surface when quaternary ammonium groups start to interact with DOPS lipids. In view of the presence of $4.3 \mu\text{mol}/\text{m}^2$ of iodide on the active surface of 0.2 cm^2 of the modified crystal, the release of iodide ions may lead to a frequency shift of +0.61 Hz and of about +1.18 Hz when we consider the simultaneous departure of water from the iodide salvation layer. The employment of complementary methods such as AFM and SPR needs to be accomplished to verify the mentioned hypotheses.

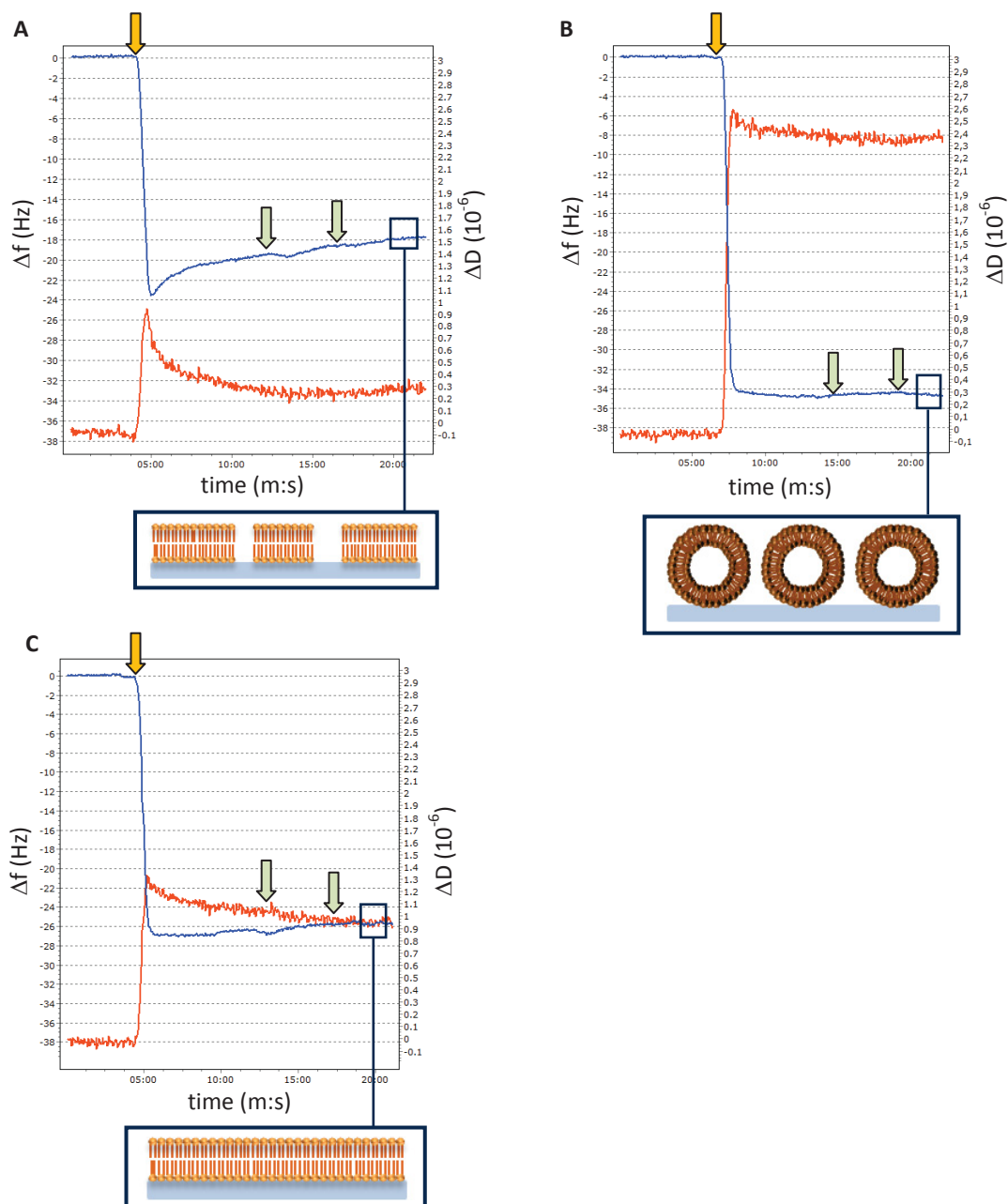


FIGURE 1.2-4 Supported lipid bilayers of DOPS formed on Me-EDPS modified QCM-D crystals, the graphs display Δf shifts (blue line) and ΔD shifts (orange line). The measurements have been implemented in HEPES buffer (10 mM). The yellow arrow indicates the injection of a 950 μL sample containing DOPS SUVs (100 $\mu\text{g}/\text{mL}$); the light green arrows indicate the injection of 500 μL buffer. **A:** DOPS injected to a quaternized sensor at pH 9. **B:** DOPS injected on a quaternized sensor at pH 9. **C:** DOPS injected on a quaternized sensor after washing with NaCl (1 M) at pH 7.4.

When injecting DOPS vesicles on the salt washed quaternized crystal we observed a frequency shift of -25.6 Hz and a dissipation shift of $0.95 \cdot 10^{-6}$, which is about nine times higher than the value of $0.1 \cdot 10^{-6}$ typically observed for a SLB (FIGURE 1.2-4 C). Nevertheless the frequency shift of -25.6 Hz corresponds well to the frequency shift which is generally obtained if a complete supported lipid bilayer has formed on a QCM-D crystal surface. Knowing that the washing step in a 1 molar salt solution degrades the modified surface by acceleration of the dissolution of the modifying silane layer, we might have rendered the surface a less more hydrophilic by the removal of quaternary ammonium

groups which may facilitate the insertion of water molecules to the silane layer and the formation of supported lipid bilayers.

In **FIGURE 1.2-4 B** we show the frequency and dissipation shifts monitored subsequent to the injection of DOPS vesicles on a quaternized silica surface at pH 9. We observe a frequency shift of -34.6 Hz and a dissipation shift of $2.4 \cdot 10^{-6}$. The zeta potential of quaternized silica surfaces at pH 9 is still about 18 mV (see **FIGURE 3.3-1 A**, chapter II) and we would therefore expect that the electrostatic attraction between the quaternized silica surfaces of the QCM-D crystals and DOPS vesicles is sufficiently strong to induce the formation of a supported lipid bilayer. Instead of the formation of a SLB we observe the adsorption of DOPS vesicles on the modified crystal surface. The frequency and dissipation shifts observed are similar to the results obtained on primary and secondary amine-bearing surfaces (see **FIGURE 1.2-3 B**).

1.3 Conclusions

In the last section we explored the formation of supported lipid bilayers of DOPS on EDPS- and Me-EDPS-modified silica. In recapitulating we can say that we have not observed an improvement of interactions between negatively charged DOPS vesicles and quaternized surfaces in comparison to SiO₂ surfaces solely modified with primary and secondary amine groups. Whereas the formation of a supported lipid bilayer of DOPS occurs on SiO₂ surfaces bearing primary and secondary amine groups (see **FIGURE 1.2-3 A**) we cannot observe the formation of an equivalent SLB on a quaternized surface (see **FIGURE 1.2-4 A**) under the same operating conditions. Only after the rinsing of quaternized crystals in 1 M NaCl solution did we achieve the formation of a supported lipid bilayer of DOPS on a quaternized crystal (see **FIGURE 1.2-4 B**). Even for injections of DOPS at the basic pH 9 the implementation of quaternary ammonium groups on the sensor surface did not improve the interaction of the modified surface with the injected vesicles. Apparently the increase of the zeta potential of about 20 mV compared to a surface bearing primary and secondary amine groups is not sufficient to induce the formation of a supported lipid bilayer of DOPS. The implementation of quaternary ammonium groups on silica surfaces does not seem to improve their interactions with negatively charged phospholipids such as DOPS.

Evidently we are aware of the fact that these experiments are not sufficient to predict the interactions between quaternized nanoparticles and negatively charged cell membranes which contain a multitude of different lipids, proteins and further compounds in a physiological environment where they are also exposed to salt concentrations which might be able to facilitate van der Waals interactions. Furthermore when they are labeling DNA in a lipoplex the nanoparticles should be prevented from interactions with the membrane of the cell and as well the membrane of endosomes because they are enclosed into the lipoplex structures. Nevertheless, these results may indicate that quaternized SiO₂-EDPS-Me nanoparticles which label DNA in a lipoplex structure may be less attracted to interact with negatively charged phospholipids present in the cell membranes than EDPS modified nanoparticles. Subsequently quaternized nanoparticles might be more appropriate to keep adsorbed DNA on their surface during the transfection process.

2. INVESTIGATING THE ADSORPTION OF DNA ON AMINATED OR QUATERNIZED SILICA SURFACES

In this section we will investigate the interactions between DNA and modified silica surfaces. Surfaces bearing quaternary ammonium groups have been described as strongly attracting phosphate group containing compounds and especially DNA^[1-3,5]. Due to quaternary ammonium groups quaternized silica nanoparticles possess pH independent charges and higher zeta potentials than aminated silica nanoparticles at pH 7.4 and in the presence of 150 mM NaCl. The presence of quaternary ammonium groups might therefore prevent the release of lipoplex-transfected DNA from a labeling nanoparticle and allow its labeling until its internalization into the cell nucleus^[6]. In what follows we analyse if there are differences between the adsorption of DNA on silica surfaces bearing solely primary and secondary amines, and quaternized surfaces in addition bearing quaternary ammonium groups. We combine cosedimentation experiments and QCM-D measurements to achieve an insight into the interactions occurring between DNA strands and aminated or quaternized silica surfaces.

2.1 The formation of nanoparticle/DNA complexes during cosedimentation assays

For all cosedimentation experiments we used commercially available DNA extracted from herring sperm. The DNA has been purified of proteins and salt residues following **PROTOCOL 2.1-1**:

PROTOCOL 2.1-1 Purification of herring sperm DNA

The purification of DNA was accomplished in a 50 mL falcon tube. First 14 mg of herring sperm DNA was suspended in 7.5 mL H₂O (18.2 M Ω), then 10 mL chloroform was added. The mixture was incubated for 5 minutes under agitation and then centrifuged for 15 minutes at 5000 g. Proteins were denatured, aggregated and formed a white deposit floating on the chloroform phase, whereas DNA stayed in the aqueous supernatant. The aqueous phase of the supernatant was taken and 1.5 mL NaCl (3 M) as well as 40 mL absolute EtOH, which has been previously cooled at -20 °C, were added to precipitate the DNA. The mixture was then centrifuged for 15 minutes at 4 °C and 11000 g. The supernatant was discarded and the DNA pellet resuspended in 20 mL of ethanol (70 % v/v) which had also been cooled down to -20 °C. The DNA suspension was then centrifuged again at 11000 g for 10 minutes at 4 °C. This washing step in ethanol (70 % v/v) was repeated twice. The supernatant was discarded and the DNA pellet dried at room temperature. After that it was resuspended in 10 mL ultrapure water (18.2 M Ω). The DNA concentration was estimated by UV-VIS spectrophotometry at 260 nm. The absorption of the sample was measured at 280 nm as well, in order to determine the DNA/protein ratio of the sample. 1000 μ L of the sample was pipetted to 1.5 mL Eppendorf tubes, which were stored at -20 °C. It has to be noted that the agitation and resuspension of DNA has to be done carefully without vortexing, which damages the DNA strands. Before its utilization in cosedimentation experiments the DNA was sonicated six times for 6 seconds in a sonication bath to homogenize the length of the DNA

strands.

To determine the length of the prepared DNA strands a gel electrophoresis was implemented (see **PROTOCOL 2.1-2**). A DNA ladder, unsonicated and sonicated DNA were pipetted to the chambers of an agarose gel which was covered with a running buffer. After application of a voltage DNA migrated through the agarose gel according to its length. The running buffer serves as an electrolyte and facilitated the migration of DNA during the electrophoresis. The negatively charged DNA migrated to the cathode with small DNA fragments crossing the gel network faster than large ones. A DNA ladder containing differently sized DNA fragments indicates the running length of the different fragments. Generally the DNA is stained with a fluorescent dye such as SYBR® Safe or ethidium bromide, and displayed under blue or ultraviolet light.

PROTOCOL 2.1-2 Agarose gel electrophoresis

To 60 mL of electrophoresis running buffer (TAE buffer: 40 mM Tris, 20 mM acetic acid, 1 mM EDTA) 1% w/v agarose was added. The mixture was heated until the added agarose was fully dissolved. The clear solution was cooled down to 50 °C and 20 µL of the DNA intercalant dye SYBR® Safe was added. The liquid mixture was poured into a gel chamber and a comb was placed in the gel to allow well formation. When the gel had cooled down to room temperature it was covered with running buffer and the comb was retained. To guarantee that the DNA samples sank to the wells they were mixed with a buffer containing Ficoll-400 (15 % w/v). This buffer also contained bromophenol blue (0.25 % w/v) and xylene cyanol (0.25 % w/v) which made it possible to observe the migration of the samples, due to their color. Then 10 µL of DNA samples and Gene ruler™ 1kb DNA ladder (250 – 10000 bp) were pipetted to different wells. A voltage of 130 V was applied until the visible marks resulting from bromophenol blue and xylene cyanol reached the end of the gel. The DNA fragments were displayed under blue light (497 nm), due to the SYBR Safe, which intercalates within DNA strands and then shows a fluorescence signal at 520 nm.

FIGURE 2.1-1 shows a photographed picture of an agarose gel containing a DNA ladder, unsonicated and sonicated herring sperm DNA:

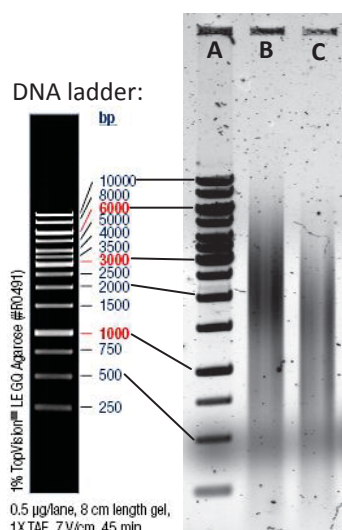


FIGURE 2.1-1 The illustration shows the electrophoretic separation of DNA fragments due to their electrophoretic migration through a 1% agarose gel. On the left the DNA ladder used is shown. On the right we display the photographic image of the agarose gel where we pipetted in the different wells **A**: DNA ladder **B**: Unsonicated herring sperm DNA **C**: DNA strands after sonication.

The picture of the agarose gel monitors the migration of the DNA ladder, unsonicated and sonicated DNA (see **FIGURE 2.1-1**). In the sample of unsonicated DNA (see **FIGURE 2.1-1 B**) we detect the presence of fragments with lengths from 200 bp up to about 4000 bp. In regarding the sample of sonicated DNA fragments (see **FIGURE 2.1-1 C**) we can see that the length of the DNA fragments diminished and that most fragments are smaller than 2000 bp.

To explore interactions between DNA and modified colloids a cosedimentation assay^[6] was implemented (see **FIGURE 2.1-2**). An exact amount of DNA was incubated in the presence of surface-modified nanoparticles. After 15 minutes of incubation the sample was centrifuged to pellet the modified nanoparticles and particle-adsorbed DNA. The concentration of DNA which remained in the supernatant was determined by spectrophotometric analysis.

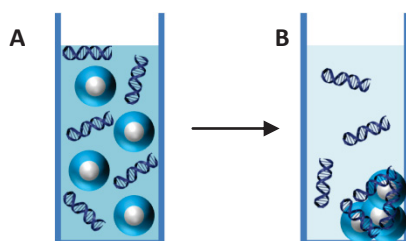


FIGURE 2.1-2 Scheme of the principle of the implemented cosedimentation experiments. **A**: DNA (dark blue strands) and surface modified nanoparticles (blue spheres) are incubated together. **B**: After 15 minutes the particles are centrifuged, nanoparticles and adsorbed DNA form a pellet. The DNA concentration of the supernatant is determined by UV-VIS spectrophotometry.

In the present study we indicate the ratio of nanoparticles and DNA used during cosedimentation experiments by the expression of the disposable surface area of the added nanoparticles (nm^2) per base pair of DNA. This relationship is of interest because the coverage of a surface by one DNA base pair is

situated in the nm range. DNA is a stiff strand^[28] built up by a negatively charged deoxyribosephosphate backbone. The nucleobases adenine, thymine, guanine and cytosine are attached to the backbone via the deoxyribose entities. They form hydrogen-bonded base pairs, which hold two DNA strands together in a helical conformation. One helical turn H contains 10 base pairs and turns over a pitch of 3.4 nm^[29]. The charged phosphate groups in the DNA backbone are 0.17 nm distant from each other and repulse each other. This electrostatic repulsion contributes significantly to the stiffness of a DNA double helix. Equalizing the charges makes it possible to render a DNA-strand more elastic, so that it can be stored in a compact form^[28]. For double-stranded DNA one helix possesses a diameter D of 2 nm.

The surface covered by a base pair in a DNA double strand can be calculated by EQUATION 2.1-1:

$$\frac{D \times H}{n} = \frac{2 \times 3.4}{10} = 0.68 \text{ nm}^2$$

D – diameter of double-stranded DNA helix (nm)

H – length of one helix turn (nm)

n – number of base pairs in one turn

EQUATION 2.1-1 Calculation of the surface occupied by one base pair of double stranded DNA in nm².

The cosedimentation assays were implemented for different ratios of nanoparticle surface area to a number of base pairs. They were carried out in 10 mM buffer solutions at different pHs or salt concentrations. All cosedimentation experiments were implemented in accordance with PROTOCOL 2.1-3:

PROTOCOL 2.1-3 Cosedimentation assay

60 μL of a diluted dispersion of modified nanoparticles was added to 40 μL of a solution containing 5 μg of previously prepared herring sperm DNA. Both solutions were buffered to fix the pH and adjusted to a desired salt concentration. Samples adjusted to pH 3.5 and pHs 6 were buffered in MES buffer (10 mM), samples at pH 7.4 in HEPES buffer (10mM) and samples at pH 8.6 and pH 9 in borate buffer (10 mM). A control sample without the presence of nanoparticles in the same final volume was prepared under the chosen conditions. After 15 minutes incubation time the samples were centrifuged at 21000g for 15 minutes. The DNA concentration in the supernatant was determined by a spectrophotometric measurement at 260 nm (NanoDrop1000 spectrophotometer). The percentage of cosedimented DNA was calculated in accordance with the DNA concentration measured in the control sample.

Cosedimentation of DNA with quaternized nanoparticles led to the formation of nanoparticle/DNA complexes. Transmission electron microscopy permitted us to examine the nanoparticle/DNA complexes by the observation of specimens stained with uranyl acetate. We were able to display the DNA strands remaining in the supernatant next to nanoparticles (see FIGURE 2.1-3 B). Furthermore we noted that the size of the nanoparticle/DNA complexes increases with the increase of the ratio of nanoparticles to DNA (see FIGURE 2.1-3). This observation in agreement with previous observations in

the literature^[6,30,31] showing that the size of agglomerates of aminated nanoparticles and plasmidic DNA increases in relation to the augmentation of the number of nanoparticles per amount of DNA. Furthermore Kneuer^[31] and Kumar^[30] showed that complexes of aminated nanoparticles and DNA possess a higher transfection efficiency than naked DNA, but that the transfection efficiency also depends on the size of the tested agglomerates. Lipoplex size has also been shown to influence their transfection efficiency. Large lipoplexes have been shown to transfect DNA more efficiently than smaller ones^[32]. The choice of the ratio of nanoparticles employed in order to complex DNA is therefore an important parameter when we label DNA which is destined to be transfected by lipoplexes.

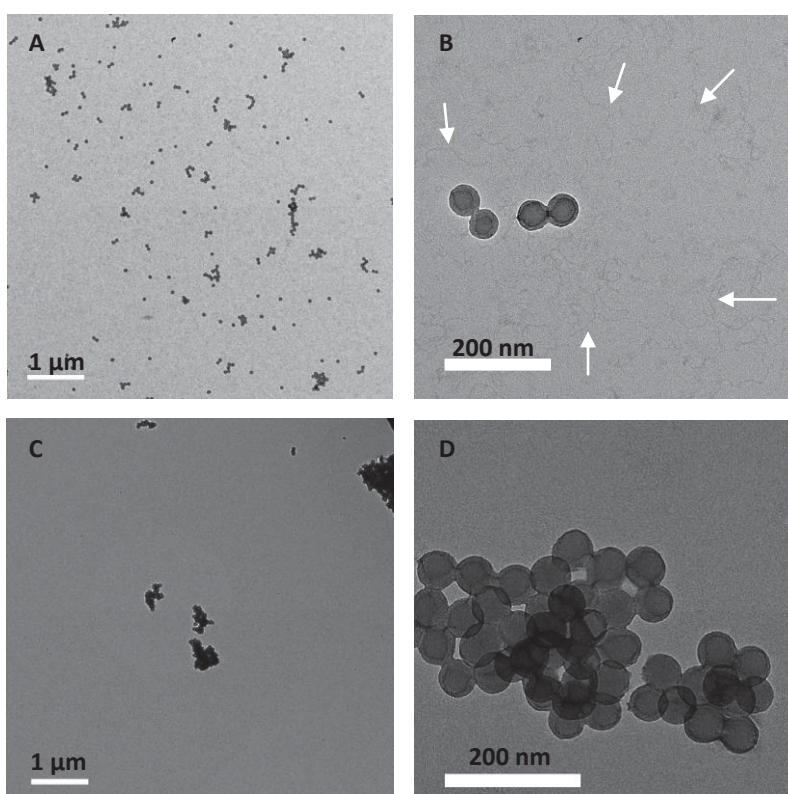


FIGURE 2.1-3 TEM micrographs show nanoparticle DNA complexes formed at different nanoparticle/DNA ratios at pH 7.4 and 150 mM NaCl. The specimens were stained with uranyl acetate solution. **A:** Nanoparticle/DNA complexes assembled at NP/DNA ratio of 0.5 nm²/bp. **B:** Free DNA strands in the supernatant are recognizable next to the assembled nanoparticle DNA complexes (SiO₂-EDPS-Me/DNA ratio 0.5 nm²/bp) and are indicated by white arrows. **C, D:** Nanoparticle-DNA complexes assembled at NP/DNA ratio 3 nm²/bp include a higher amount of nanoparticles.

The complex stability was investigated by a competitive exchange of DNA adsorbed to the nanoparticles and dextran sulfate. It is known that dextran sulfate can be used to extract histone-depleted chromosome DNA^[33,34]. We measured the amount of DNA complexed by quaternized nanoparticles with increasing concentrations of dextran sulfate. With the increase of the concentration of dextran sulphate more DNA was recovered in the supernatant (see FIGURE 2.1-4).

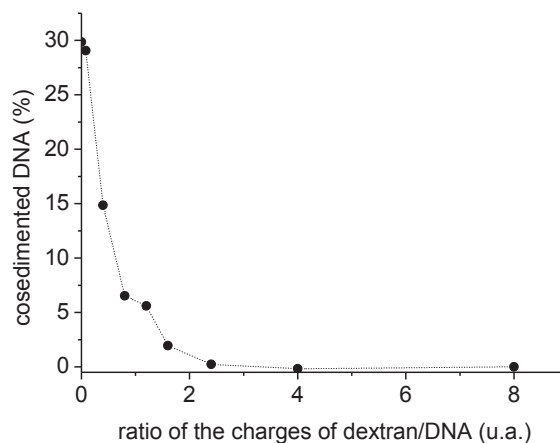


FIGURE 2.1-4 Cosedimentation of DNA by quaternized EDPS-modified silica nanoparticles in relation to an increasing dextran sulfate (average Mw > 500000) concentration at pH 7.4 in the presence of 150 mM NaCl.

The decrease in cosedimented DNA is shown in relation to the ratio of negative charges brought by the dextran sulfate to the charges provided by the present amount of DNA. Without the presence of dextran sulfate 30 % of DNA strands is complexed by the nanoparticles. At a ratio of charges dextran sulfate/DNA of one we would therefore expect cosedimentation of 15 % if the nanoparticles possess no specificity for DNA, or of more than 15 % if the quaternized nanoparticles preferably interact with DNA rather than with the added dextran sulfate. Instead we observed cosedimentation of only 6.5 % of the DNA, which means that the nanoparticles preferably interact with dextran sulfate. The preference of the quaternized nanoparticles to interact with the dextran sulfate polymer may be explained by its higher flexibility compared to the rather rigid DNA strands. This result shows that if quaternized nanoparticles are used the release of DNA from nanoparticles in the presence of a polyelectrolyte as observed in the literature for aminated nanoparticles^[6] is also possible, because a significant part of the interactions between quaternized nanoparticles and DNA is due to electrostatic forces.

2.2 The investigation of the pH dependence of DNA adsorption on differently modified cationic silica surfaces

We investigated the influence of the pH on the ability of modified nanoparticles to complex DNA. With increasing pH the zeta potential of aminated as well as of quaternized nanoparticles decreases, which should have a direct influence on their capacity to interact with DNA. The cosedimentation assays were implemented at an electrolyte concentration comparable to the concentration of salts in the cytosol. This has the advantage that the salt screens a part of the charges of the deoxyribose-phosphate backbone of the DNA, rendering the strands less rigid and more flexible. In measuring the DNA concentrations remaining in the supernatant after the centrifugation of nanoparticle/DNA complexes at different pHs we observed a diminution of the interactions between DNA and quaternized nanoparticles at basic pHs (see **FIGURE 2.2-1**).

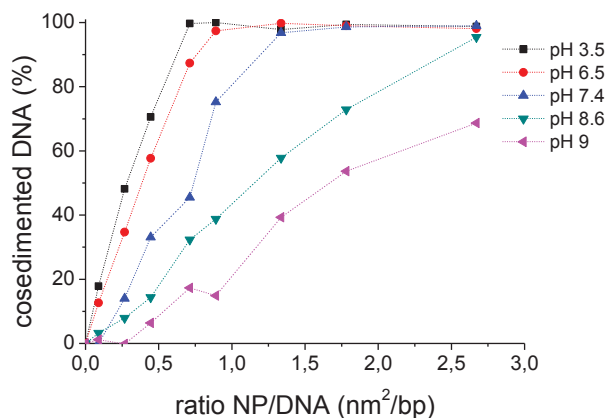


FIGURE 2.2-1 Effect of the pH on the capacity of quaternized nanoparticles to complex DNA strands determined by cosedimentation assays (150 mM NaCl, 10 mM buffers: pH 3.5, pH 6 = MES; pH 7.4 = HEPES; pH 8.6, pH 9 = borate).

As we expected, the increase in pH leads to a diminution of the amount of DNA which can be bound per nm² of the nanoparticle surface area. As a consequence the surface area which is needed to bind 100 % of the disposed DNA increases. At pH 3.5 nanoparticle surface area of 0.7 nm² is needed to complex one DNA base pair, which corresponds to an ideal binding of DNA in view of the fact that one base pair requires 0.68 nm². Whereas at pH 6.5 the cosedimentation of 100 % of DNA is reached at a ratio of 0.9 nm² per base pair, which is near to the ideal case observed at pH 3.5, we observe a diminution on the DNA-binding-capacity of quaternized nanoparticles at the physiological pH 7.4, where 1.3 nm² is needed to complex one DNA base pair. The further augmentation of the pH has an increasing influence of the DNA-binding-capacity of the nanoparticles due to the more rapid decrease of their zeta potential at basic pHs (see **FIGURE 3.3-1 A**, chapter II).

To determine the potential of quaternized and aminated nanoparticles to complex DNA we compared the amount of nanoparticles necessary to complex 50 % of the DNA present in the sample.

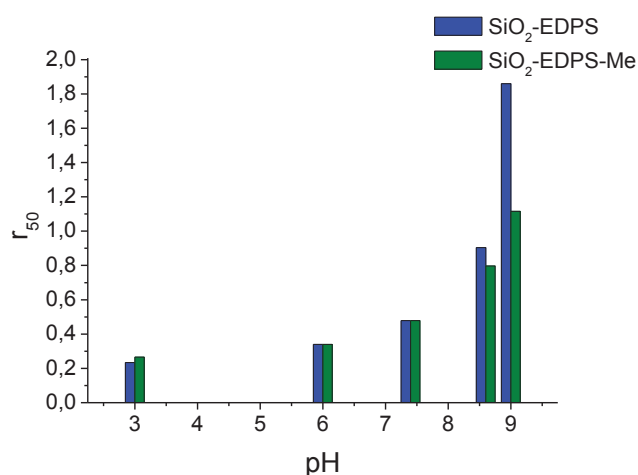


FIGURE 2.2-2 Amount of nanoparticles needed to complex 50 % of DNA during a cosedimentation assay (r_{50}). It changes in relation to the pH and differs for differently modified nanoparticles. Fewer quaternized nanoparticles than EDPS modified nanoparticles are needed to complex the same amount of DNA at basic pHs.

We observed that fewer quaternized nanoparticles were needed to complex the same amount of DNA at basic pHs 8.6 and 9 (see **FIGURE 2.2-2**). This observation can be explained by the fact that the charges present on the surface of quaternized nanoparticles are independent of the pH although they are progressively screened by Si-O⁻ ions, which is the reason why with increasing pH they complex less DNA. On the other hand the positive charges on EDPS-modified nanoparticles are pH dependent. Their charges are provided by protonated amine groups, which with the increase of the pH deprotonate gradually.

The adsorption of DNA strands to quaternized and EDPS modified silica surfaces were also investigated by QCM-D measurements (see **FIGURE 2.2-3**). Silica-coated quartz crystals were surface modified as previously described and 950 μ L of DNA solution with a concentration of 100 μ g/mL was injected. The measurements were implemented under the same conditions as the cosedimentation assays: the salt concentration stayed constant at 150 mM whereas the different measurements were accomplished at varying pHs.

When injecting DNA on an aminated silica surface a dissipation shift of $2.8 \cdot 10^{-6}$ and a frequency shift of -19.7 Hz were measured, which corresponds to the adsorption of 348.7 ng of DNA on a silica surface bearing solely primary and secondary amines (see **FIGURE 2.2-3 A**, graph on the left). When measuring at pH 7.4 on a quaternized surface we observed a frequency shift of -22.6 Hz and a dissipation shift of $3.8 \cdot 10^{-6}$ corresponding to 400 ng of DNA which was adsorbed to the surface as a soft viscoelastic layer (see **FIGURE 2.2-3 A**, graph on the right).

In contrast to quaternized surfaces the ability of EDPS modified surfaces to attract DNA decreases significantly with the increase in pH. At pH 8.6 a frequency shift of -9 Hz was observed corresponding to the adsorption of 159.3 ng of DNA; the dissipation shift of $2.2 \cdot 10^{-6}$ is relatively high and shows that a soft viscoelastic layer of DNA is adsorbed to the quartz crystal (see **FIGURE 2.2-3 B**, graph on the left). For the adsorption of DNA on a quaternized surface at pH 8.6 a frequency shift of -19.9 Hz and dissipation shift of $2.6 \cdot 10^{-6}$ were observed corresponding to the adsorption of 354 ng of DNA (see **FIGURE 2.2-3 B**, graph on the right). The values of both graphs indicate the loss of charges of the aminated or quaternized surfaces at higher pHs leading to a lower capacity to attract DNA electrostatically. In addition we noted that the loss of charges is less important on quaternized surfaces on which we adsorb the double DNA amount than on the aminated SiO₂ surfaces.

At pH 9 the aminated surface bearing primary and secondary amines has almost completely lost its potential to adsorb DNA. We observed a frequency shift of -1.6 Hz after the injection of DNA on an EDPS modified surface, which indicates the adsorption of only 28.3 ng of DNA (see **FIGURE 2.2-3 C**, graph on the left). In contrast, for the adsorption of DNA on a silica surface bearing quaternary ammonium ions at pH 9 a frequency shift of -19.5 Hz and dissipation shift of $2.8 \cdot 10^{-6}$ were observed (see **FIGURE 2.2-3 C**, graph on the right). According to the Sauerbrey law 345 ng of DNA adsorbed on the quaternized surface. The ability of the quaternized surface to interact with DNA seems nearly unchanged and decreased by only 55 ng compared to what was adsorbed at pH 7.4.

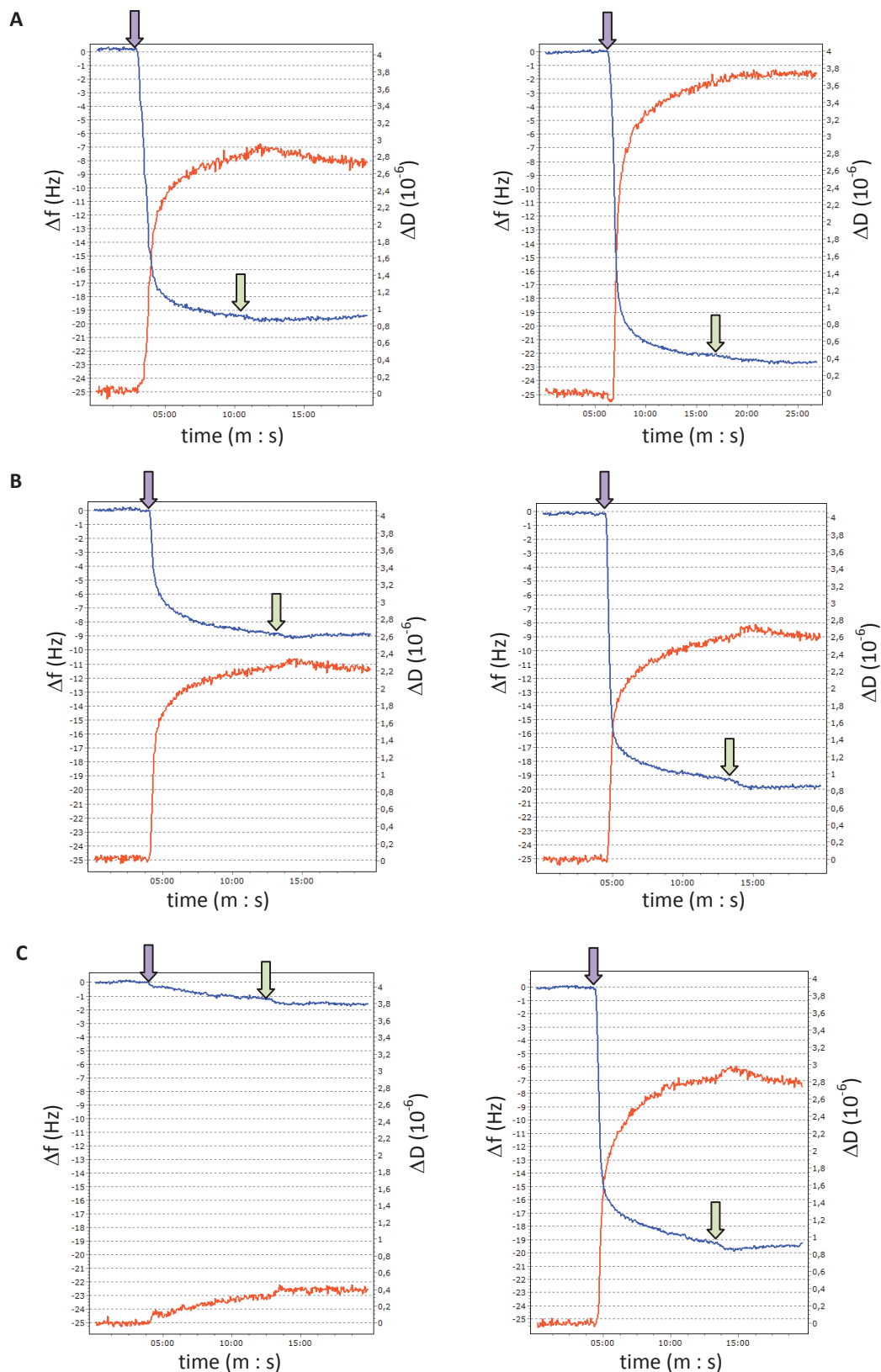


FIGURE 2.2-3 The presented graphs display the adsorption of DNA on EDPS modified (**left**) and quaternized surfaces (**right**) by QCM-D in the presence of 150 mM salt at different pHs **A:** pH 7.4 **B:** pH 8.6 **C:** pH 9. The graphs monitor Δf shifts (blue line) and ΔD shifts (orange line). DNA injections are marked by violet arrows; the injection of buffer is indicated by green arrows.

The decrease of the DNA binding on EDPS-modified silica surfaces with increasing pH can be explained by the fact that the zeta potential of an aminated surface decreases to nearly zero at pH 9. Furthermore the electrostatic interactions taking place between the modified surfaces and adsorbed DNA are not only decreased due to the increase in the pH, but also screened by the salt ions present. The negative charges of DNA are screened by the Na⁺ ions present. Meanwhile even at pH 9 we observed a slight adsorption of DNA on surfaces bearing primary and secondary amines. This observation might be explained by the fact that the interactions taking place between the modified surfaces and DNA at basic pHs are not only of electrostatic conduct. Most likely van der Waals interactions are also taking place and result in the binding of DNA to the aminated silica surfaces at basic pHs.

The advantages of the pH-independence of the charges of quaternary ammonium groups can be pointed out when we regard the capacity of quaternary ammonium group bearing gold nanoparticles to bind DNA. Quaternary ammonium group bearing gold nanoparticles were employed to bind DNA by Rotello and coworkers^[5,35-37], who synthesized mixed monolayer-protected gold clusters (MMPCs) functionalized with octanethiol and (11-mercaptoundecyl)-N,N,N-trimethylammonium bromide (MUTAB) (see FIGURE 2.2-4). To compare the capacity of quaternized silica nanoparticles and gold nanoparticles bearing quaternary ammonium groups gold nanoparticles of 10 nm diameter were synthesized^[38] and stabilized in ethanol using the macromolecule polyvinylpyrrolidone (PVP) before thiolation with MUTAB in accordance with PROTOCOL 2.2-1.

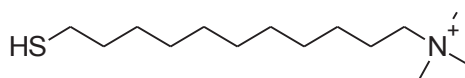


FIGURE 2.2-4 Chemical structure of (11-mercaptoundecyl)-N,N,N-trimethylammonium bromide (MUTAB)

PROTOCOL 2.2-1 Functionalization of gold nanoparticles via the formation of a self assembled monolayer of MUTAB

Previously synthesized gold nanoparticles^[38] stabilized in water by adsorbed citrate molecules were incubated in a solution of polyvinylpyrrolidone (PVP, 10 g/L) for 12 hours. After the completion of the place-exchange reaction of citrate molecules and PVP, released citrate and excrescent PVP polymers were eliminated by centrifuging the PVP-coated nanoparticles twice at 15000 g for 30 minutes in water. The nanoparticles were then redispersed in absolute ethanol. $6.6 \cdot 10^{-4}$ mol of (11-Mercaptoundecyl)-N,N,N-trimethylammonium bromide was added per m² of the nanoparticle surface area and the mixture was incubated for 12 hours. After completion of the ligand exchange reaction the particles coagulated in EtOH and were subsequently decanted. The supernatant was withdrawn and the particles were washed twice in absolute EtOH. Subsequently the nanoparticles were redispersed in ultrapure water (18.2 MΩ) and the remaining alcohol was evaporated at 40 °C.

The DNA-binding-capacity is more pH independent (see **FIGURE 2.2-5**) than the binding capacity of quaternized silica nanoparticles due to the fact that the zeta potential of modified silica nanoparticles is decreased by negatively charged silanolate groups at alkaline pHs remaining on the modified silica.

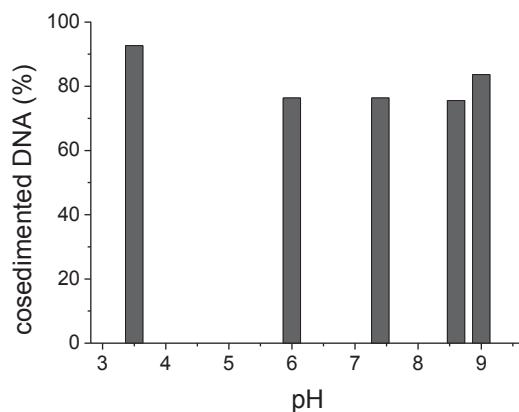


FIGURE 2.2-5 Diagram showing the pH independence of the capacity to bind DNA from gold nanoparticles bearing quaternary ammonium groups.

To estimate the impact that remaining amine and silanolate residues have on the DNA-binding-capacity of quaternized silica nanoparticles we implemented DNA cosedimentation assays with MUTAB-bearing gold nanoparticles (AuNQ) which do not suffer from the presence of such residues. It can be seen that the gold nanoparticles bind DNA more efficiently than the quaternized SiO₂-EDPS-Me nanoparticles (see **FIGURE 3.1-1**).

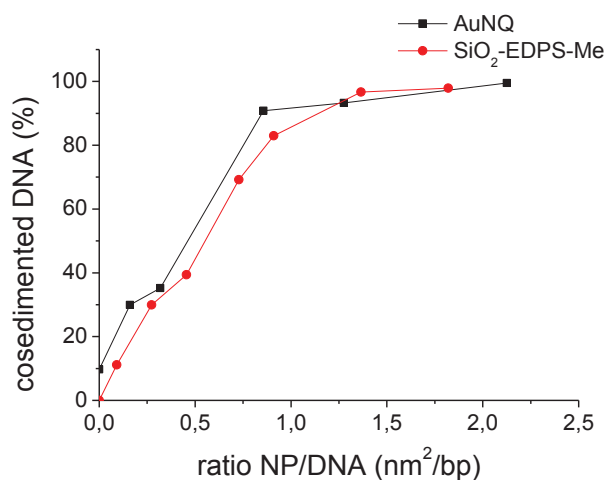


FIGURE 2.2-6 Cosedimentation assay comparing the capacity of gold nanoparticles (AuNQ) and silica nanoparticles (SiO₂-EDPS-Me), both functionalized to bear quaternary ammonium groups on their surface.

Nevertheless, we are aware of the fact that the number of charges and the number of quaternary ammonium groups per m² present on silica or gold nanoparticles differ. To quantify the MUTAB molecules forming the self-assembled monolayer on the surface of gold nanoparticles a colorimetric dosage with Ellman's reagent 5,5'-dithiobis-2-nitrobenzoic acid (DNTB) was implemented at 412 nm (see protocol in Annex 1). The colorimetric assay makes it possible to determine the presence of

3 μmol MUTAB molecules per m^2 of the particle surface. For quaternized silica nanoparticles we estimated the presence of 4.3 μmol quaternary ammonium groups per m^2 (see SECTION 3.2, chapter II). Subsequently the observation that gold nanoparticles adsorb more DNA per nm^2 of particle surface area at pH 7.4 underlines the importance of electrostatic interactions for binding DNA on quaternary ammonium group bearing nanoparticles and the loss of efficiency from which quaternized silica nanoparticles must suffer due to the presence of negatively charged silanolate groups, even at moderate pHs.

2.3 Salt concentration as a parameter influencing the adsorption of DNA to cationic surfaces

Considering the fact that the salt concentration influences the effective charge of modified silica surfaces as well as the rigidity and conformation of a DNA strand, we studied the adsorption of DNA on modified silica surfaces in relation to the salt concentration of the medium in which the supramolecular assembly of DNA on a cationic nanoparticle takes place (see FIGURE 2.3-1). Cosedimentation experiments were implemented at pH 7.4 at salt concentrations of 50 mM, 150 mM, 300 mM and 1 M NaCl.

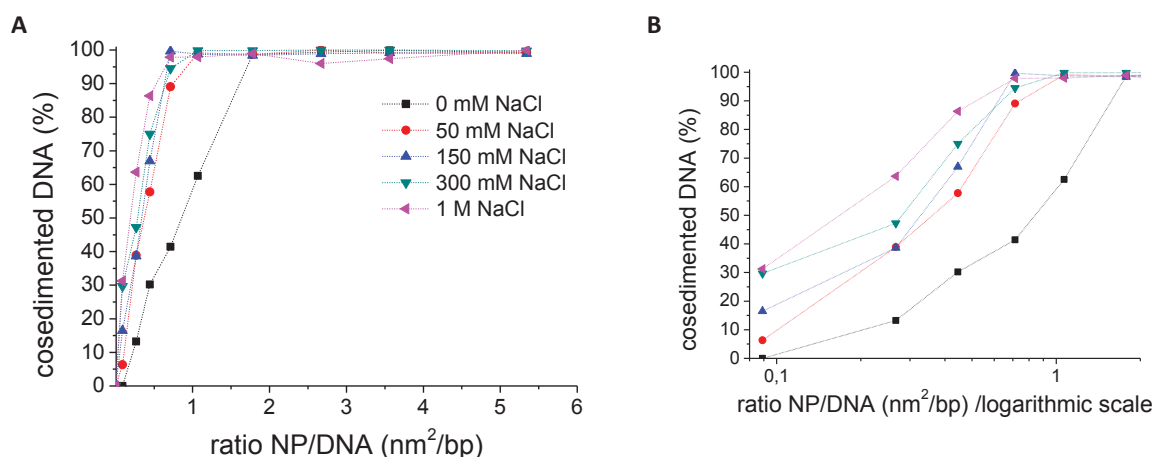


FIGURE 2.3-1 The cosedimentation of DNA by modified nanoparticles varies in relation to the salt concentration. **A:** Cosedimentation of DNA with EDPS-modified nanoparticles in 10 mM HEPES buffer at pH 7.4 and varying salt concentration. **B:** Zoom in graph A in the range from 0.1 nm^2/bp to 1 nm^2/bp .

The cosedimentation experiments showed that with increasing salt concentration fewer nanoparticles are needed to complex 100 % of the present DNA. The decrease of DNA rigidity in the presence of salt seems to benefit its complexation with nanoparticles. We also investigated the adsorption of DNA on modified silica surfaces by QCM-D measurements. The frequency and dissipation shifts measured during the adsorption of DNA strands on an EDPS-modified, silica-coated crystal are shown in FIGURE 2.3-2. In the absence of salt the observed frequency shift of -6 Hz indicates the adsorption of 106 ng DNA on the EDPS modified surface of the crystal and a low dissipation shift of $0.2 \cdot 10^{-6}$. With increasing salt concentration frequency and dissipation shifts increase. Injections of DNA in the presence of 5 mM and 10 mM NaCl lead to adsorption of 173.5 and 180.5 ng of DNA. The adsorbed

DNA layers cause a dissipation of $0.95 \cdot 10^{-6}$ and $1.25 \cdot 10^{-6}$, indicating that at these salt concentrations a relatively compact layer is formed. An intermediate quantity of DNA is adsorbed in the presence of 25 mM NaCl. We observed a frequency shift of -14.5 Hz indicating that 256.6 ng of DNA is adsorbed. Nevertheless the dissipation of this layer of $2.5 \cdot 10^{-6}$ is double the dissipation observed at 5 mM or 10 mM and already ten times higher than the dissipation measured for a DNA layer formed in the absence of salt. A further increase of the salt concentration to 50 mM, 100 mM or 150 mM leads to an adsorption of even higher DNA amounts of about 318.6 ng per layer assembled in the presence of 50 mM and 100 mM NaCl (Δf -18 Hz) and 350.5 ng of DNA in the layer formed at a salt concentration of 150 mM (Δf -19.8 Hz). QCM-D measurements of all these three layers display a dissipation of $2.8 \cdot 10^{-6}$, indicating that the DNA strands building up the layers possess a similar and minor rigid conformation.

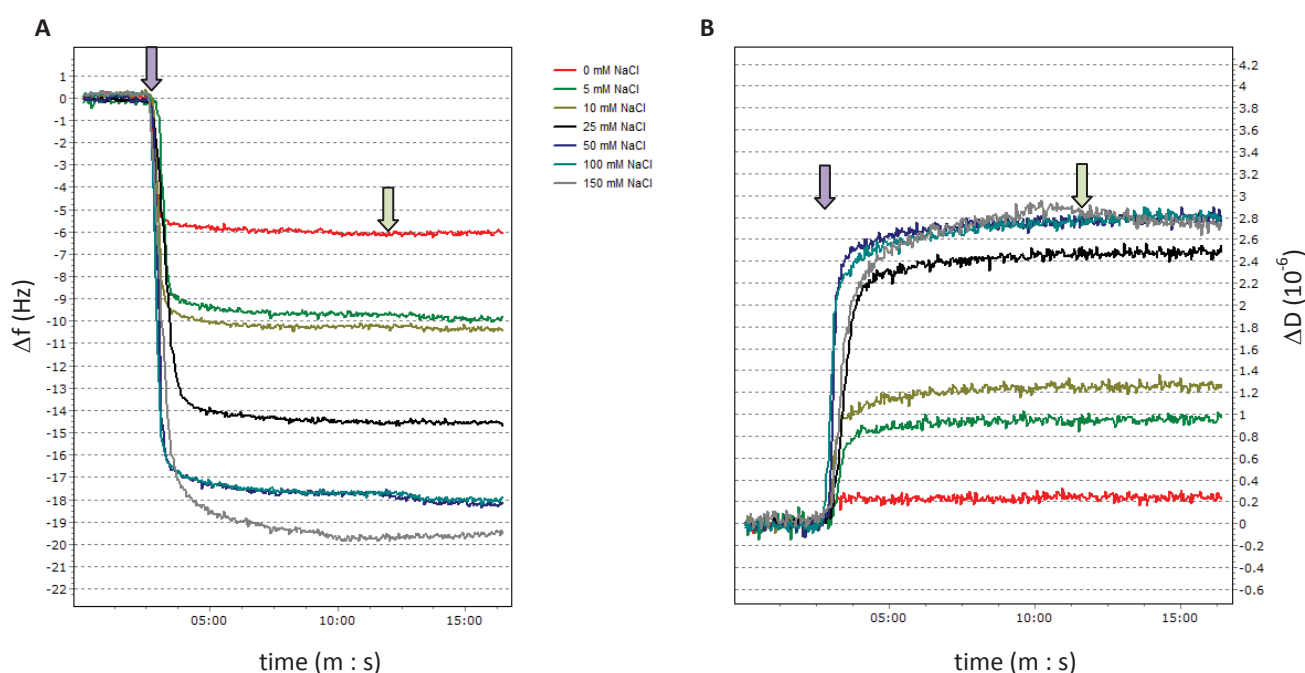


FIGURE 2.3-2 Adsorption of DNA macromolecules on EDPS-modified quartz crystals at varying salt concentrations from 0-150 mM NaCl. DNA injections are signaled by violet arrows, buffer injections by green arrows. **A:** Frequency shifts Δf_7 observed during the adsorption of DNA; the amount of DNA adsorbed increases with the increase of the salt concentration. **B:** Dissipation shifts ΔD_7 observed during the adsorption of DNA on EDPS; DNA layers assembled increasing the salt concentration become less compact and more viscoelastic.

The frequency and dissipation shifts measured during the adsorption of DNA strands on a quaternized silica-coated crystal are shown in **FIGURE 2.3-3**. In the absence of salt the observed frequency shift of -4.5 Hz indicates the adsorption of only 70.8 ng of DNA on the quaternized surface of the crystal and no dissipation shift. Less DNA is adsorbed in comparison to the DNA layer on aminated nanoparticles, but the layer which is formed is fully rigid and extremely compact. As observed before, frequency and dissipation shifts increase with increasing salt concentration. Nevertheless the differences between the frequency shifts at different salt concentration are more pronounced.

Supramolecular assemblies of DNA formed in the presence of 5 mM and 10 mM NaCl lead to frequency shifts of -8.8 Hz and -11 Hz, which corresponds to 155.8 ng and 194.7 ng of adsorbed DNA. The adsorbed DNA layers cause a dissipation of $0.9 \cdot 10^{-6}$ and $1.6 \cdot 10^{-6}$, indicating that at a salt concentration of 10 mM a less compact layer is formed. At a salt concentration of 25 mM a higher quantity of DNA is adsorbed than on EDPS-modified nanoparticles. We observe a frequency shift of -16.1 Hz indicating that 295.6 ng of DNA are adsorbed, which is a difference of 39 ng in comparison to the DNA adsorption on EDPS modified crystals at the same salt concentration. The dissipation shift of the layer increases in relation to the increase of adsorbed mass to $2.9 \cdot 10^{-6}$. A further increase in the salt concentration to 50 mM, 100 mM or 150 mM leads to an adsorption of even higher DNA amounts of about 323.9 ng DNA adsorbed in the presence 50 mM NaCl (Δf -18.3 Hz), 387.6 ng of DNA adsorbed at 100mM NaCl (Δf -21.9 Hz), and 400 ng of DNA in the layer formed at a salt concentration of 150 mM (Δf -22.6 Hz). QCM-D measurements of these three layers display a dissipation of $2.95 \cdot 10^{-6}$ (50 mM NaCl), $3.7 \cdot 10^{-6}$ (100 mM NaCl) and $3.9 \cdot 10^{-6}$ (150 mM NaCl). Subsequently DNA seems to be adsorbed in a coiled, viscoelastic conformation. We observed that above a salt concentration of 10 mM the amounts of DNA adsorbed to quaternized surfaces are in general slightly higher than the amounts of DNA adsorbed at aminated surfaces under the same conditions.

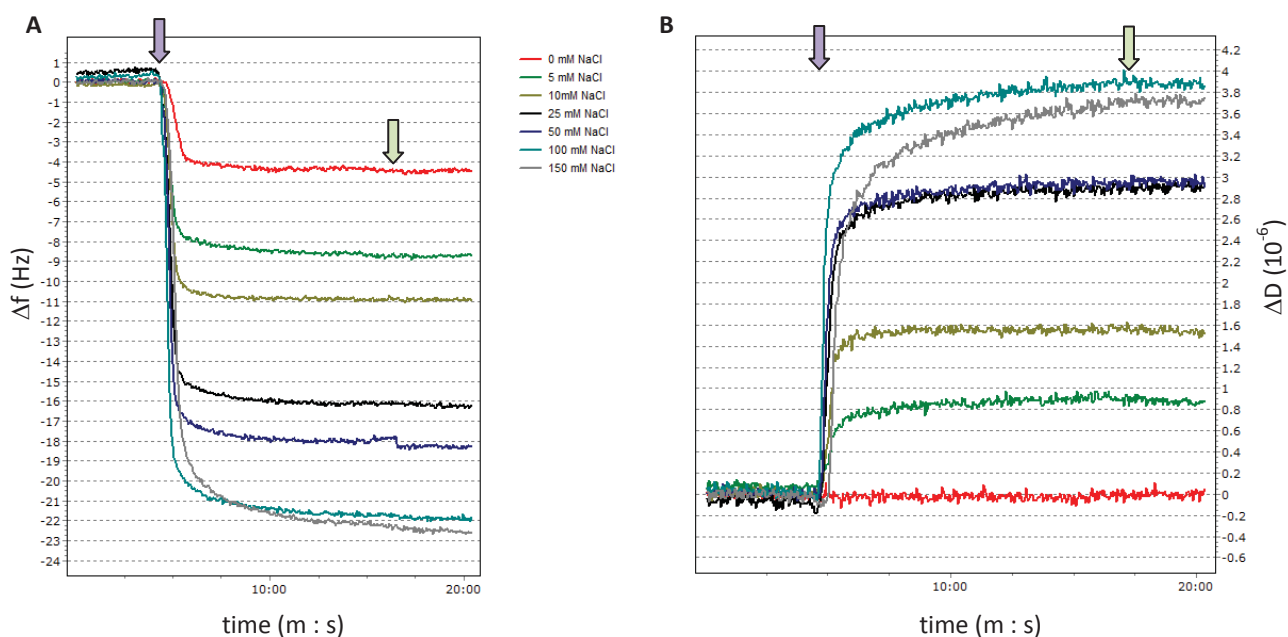


FIGURE 2.3-3 Adsorption of DNA macromolecules on quaternized silica-coated quartz crystals at varying salt concentrations from 0 mM to 150 mM NaCl. DNA injections are signaled by violet arrows, buffer injections by green arrows. **A:** Frequency shifts Δf , observed during the adsorption of DNA; the amount of DNA adsorbed increases with the increase in the salt concentration. **B:** Dissipation shifts ΔD , observed during the adsorption of DNA. When the salt concentration increases the adsorbed DNA layers become less compact and less rigid.

It is known that DNA loses its rigidity in the presence of salt due to the fact that the present Na^+ ions screen the charges of the phosphate groups in the DNA backbone, which subsequently repulse each

other less and do not maintain their maximal interdistance any more^[28,39]. Therefore DNA strands adsorbing to the modified silica surfaces do not exist in the same conformation at varying salt concentrations. Whereas DNA strands will be available in a stiff and linear conformation, the addition of small amounts of salt to concentrations of 5, 10 or 25 mM already leads to less rigid strands, which are more disposed to folding. At high salt concentrations such as 50, 100 or 150 mM of NaCl adsorbed DNA exists in more and more coiled conformations (see FIGURE 2.3-4).

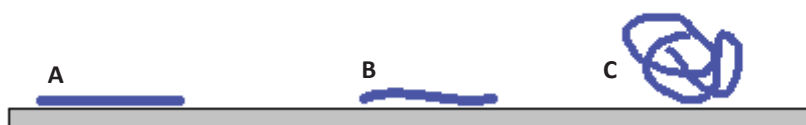


FIGURE 2.3-4 DNA strands exist at different conformations depending on the salt concentration present during the assembly of the surface of a modified QCM-D crystal. **A:** In the absence of salt DNA is present as a stiff, linear strand forming a thin, rigid layer on a cationic surface. **B:** At low salt concentrations (5, 10, 25 mM) DNA strands are less rigid and more flexible, leading to the assembly of less structured and more viscoelastic layers of DNA on cationic surfaces. **C:** At high salt concentrations (50, 100, 150 mM) DNA strands appear in coiled, raveled conformations. They adsorb on cationic surfaces, forming highly viscoelastic layers.

The adsorption of DNA at different salt concentrations on aminated nanoparticles has been observed by Cryo-TEM microscopy^[40] (see FIGURE 2.3-5).

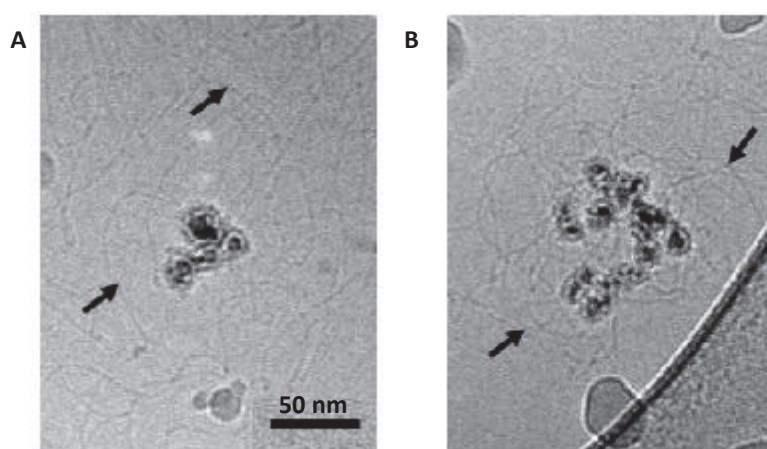


FIGURE 2.3-5 Cryo-TEM pictures of plasmidic DNA interacting with aminated $\gamma\text{-Fe}_2\text{O}_3\text{@SiO}_2$ core-shell nanoparticles at different concentrations of NaCl^[40]. DNA strands exist at different conformations depending on the salt concentration. **A:** In the absence of salt DNA is present as a stiff, linear strand (indicated by black arrows) and interacts partly with the nanoparticles surfaces. **B:** In the presence of 150 mM NaCl the negative charges of the DNA backbone are partly screened and DNA strands (indicated by black arrows) have been displayed as assembled around aminated nanoparticles in coiled, raveled conformations.

The strong influence of cationic counterions on the conformation of DNA adsorbing on mica surfaces has been demonstrated by Nguyen and coworkers^[41,42], who showed that the presence of different monovalent or bivalent cations extensively determines the thickness and viscosity of a DNA layer adsorbed to a mica-coated QCM-D crystal, as well as the nature and strength of the interactions

leading to the DNA assembly. The presence of ions can also influence the hybridization of short DNA oligomers as well as their stability as shown by Zhu and coworkers^[43] who investigated the damaging of adsorbed DNA by heavy metal ions such as cerium.

Subsequently the increase in the amount of DNA adsorbed with increasing salt concentrations can be explained by the fact, that linear rigid DNA strands can cover the crystal surfaces forming a relatively uniform layer. At high salt concentrations ravel of DNA adsorb to the modified silica surfaces; due to its ability to fold and coil, a DNA strand does not need to be fully adsorbed to a cationic surface. Its partial adsorption leads to the existence of a thicker, fluffy DNA cushion, where a part of each strand is freely moving in the cushion (see **FIGURE 2.3-4**). Because of their partly adsorption more DNA strands can undergo electrostatic interactions to a cationic surface.

This behavior of DNA is well known and has also been observed by QCM-D studies of DNA layers of short strands adsorbed on polyethyleneimine cushions^[44]. Furthermore the screening of the negative charges of DNA by Na⁺ ions penetrating the DNA layers permits the adsorption of loosely bound DNA interacting with neighboring strands by van der Waals interactions. Johnston et al.^[45] showed that DNA layers of short strands (60 bp) adsorbed to a polyethyleneimine layer in the presence of high salt concentration (200-700 mM NaCl) lost about 55 % of the adsorbed DNA when the salt concentration was lowered to 100 mM and 30 % further below this concentration.

2.4 Conclusions

In recapitulating the results obtained up to now we noted that under the influence of salt DNA layers adsorbed to quaternized or EDPS modified surfaces change their compactness, thickness and viscoelasticity. DNA layers formed on quaternized surfaces in the absence of salt are thinner than DNA layers formed on aminated surfaces under the same conditions, but are extremely rigid, which may indicate that DNA strands are adsorbed to quaternized surfaces more tightly than on EDPS-modified surfaces. For both surfaces the increase of the salt concentration leads to the adsorption of higher amounts of DNA forming less compact, viscoelastic layers, which contain not only DNA but also salt ions and water molecules between the semi-rigid strands. In the process it becomes clear that above a concentration of 10 mM NaCl at the same salt concentration higher amounts of DNA are adsorbed to the quaternized surfaces than on aminated surfaces. This observation is probably due to the fact that quaternized surfaces possess a higher amount of cationic charges, so that in spite of the screening of their overall charges by the salt which is present the quaternized surfaces possess still sufficient charges to attract negatively charged DNA macromolecules.

Nanoparticles bearing quaternary ammonium groups on their surface may have a further advantage which enhances their ability to bind DNA. Goodman et al.^[5] demonstrated that gold nanoparticles modified with quaternary ammonium groups bearing short hydrophobic alkyl chains such as butyl chains interact favorably with DNA compared to less hydrophobic quaternizing chains. The more hydrophobic character of quaternized surfaces compared to aminated surfaces is advantageous to their

interaction with DNA. This effect is also used for the conception of DNA-intercalating substances such as SYBR green possessing quaternary ammonium groups, which intercalate to DNA grooves^[46,47]. Nevertheless the hydrophobic interactions between quaternary ammonium groups bearing three methyl groups and DNA are relatively small^[5], but the implementation of longer alkyl chains on the quaternized amines might further enhance the ability of quaternized nanoparticles to bind DNA.

Furthermore we noted that the increase in the pH reduces the capacity of quaternized nanoparticles to adsorb DNA less than is the case for aminated nanoparticles. EDPS-modified silica surfaces on the contrary suffer from the fact that the presence of the cationic charges, due to protonated amine functions, is highly dependent on the pH. With increasing pH, aminated surfaces mainly lose all their charges. This fact diminishes their potential for binding DNA electrostatically on their surface at physiological pH, and may explain why DNA labeled with aminated nanoparticles is released in the cytosol, where the presence of salts additionally decreases their surface potential.

3. TOWARDS THE ASSEMBLY OF NANOPARTICLE LABELED LIPOPLEXES.

The aim of our project is the development of a multimodal nanoparticle for the labeling of DNA in lipoplexes. Lipoplexes include condensed and compact, rod-like assembled DNA. Due to their high density of positive charges they are able to neutralize the negative charges of the DNA-backbone. DNA has been observed as rods organized in the lipidic sheets separated from each other by a specific distance resulting in a one-dimensional lattice of DNA chains through one bilayer^[48,49]. The distance between the different DNA-rods is in general much larger than their diameter. In the sandwiched organization of multiple bilayers the DNA-bilayer arrangement forms a two-dimensional smectic phase^[50] (see **FIGURE 3.0-1**). Hexagonally organized structures of cylinders consisting of DNA rods coated with a lipid monolayer do also exist^[51].

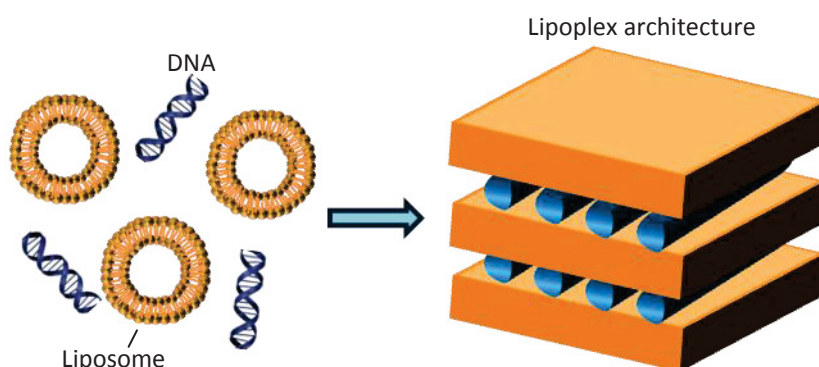


FIGURE 3.0-1 Formation of a lipoplex via self assembly: Cationic liposomes and DNA organize to build lipoplexes, which show a characteristically ordered structure. Condensed rod-like assembled DNA (blue) is ordered between lipidic bilayers (orange).

When they are interacting negatively charged DNA and cationic liposomes equalize their charges. Theoretically lipoplexes are formed until they reach their point of zero charge. In fact over 90 % of the charges coming from the DNA backbone are neutralized, which makes it possible to observe the DNA in a condensed state^[39]. However, it has been observed that charge-neutral lipoplexes are of minor stability. Without stabilization by charge-induced repulsive forces the lipoplexes tend to collide and stick together due to attractive van der Waals (vdW) forces. To form more stable lipoplexes we need to place the assembly conditions either in an excess of DNA to form negatively charged lipoplexes or in an excess of liposomes leading to positively charged complexes^[48,50].

The spherical, monodisperse complexes remain stable and usable for about three months. During this storing period their transfection efficiency persists on a high level^[48]. The lipoplexes formed have the considerable advantage that they tend to pass through the membranes of cells of interest easily. The DNA-lipid complexes interact with the membranes of tissue cells due to their cationic lipidic formulation, which favors interaction with the negatively charged lipidic cell membranes.

The driving force for the supramolecular self assembly of lipoplexes is the partial release of counterions surrounding DNA strands (equalizing 76 % of their charge^[52]) and the surface of the charged liposomes. But the free energy gain pushing the assembly in the described structure is achieved not only due to increased entropy but is also caused by the partial counterion release. Secondly it is due to a lower electrostatic repulsion of the counterions entering the complex^[53]. Subsequently the formation of lipoplexes is mainly undergone in the presence of salt at concentrations of about 150 mM NaCl, which has the further advantage that the DNA strands are more flexible.

3.1 Following of the adsorption of cationic liposomes on DNA layers formed on modified silica surfaces by QCM-D

In aiming to incorporate silica nanoparticles modified with quaternary ammonium ions into these DNA lipid structures we were interested in characterizing the interactions between DNA-covered modified silica surfaces with cationic lipids in the expectation of identifying assembly conditions which facilitate the inclusion of quaternized multimodal silica nanoparticles in lipoplexes. For this purpose we examined the attraction of cationic DOTAP liposomes on the DNA layers formed on modified surfaces at different salt concentrations by QCM-D measurements with a pH fixed at 7.4. DOTAP liposomes were injected on DNA layers which had previously formed on aminated or quaternized surfaces to follow the interactions occurring between DNA adsorbed to the modified crystals in different conformations and vesicles of a cationic lipid which can serve as a transfection agent^[52].

The frequency and dissipation shifts measured during the injection of DNA strands and subsequently DOTAP on an EDPS-modified silica coated crystal are shown in **FIGURE 3.1-1**. Whereas the frequency and dissipation shifts caused by the adsorption of DNA were discussed in section 2.3 we now survey the frequency and dissipation shifts caused by the subsequent adsorption of DOTAP on the previously

accumulated DNA layers. In the absence of salt we observed a frequency shift of 31.9 Hz and a dissipation shift of $2.3 \cdot 10^{-6}$ after the injection of DOTAP vesicles. At 5mM NaCl concentration we observed a frequency shift of 41 Hz and a dissipation shift of $1.7 \cdot 10^{-6}$, a Δf of 43.3 Hz and a ΔD of $1.4 \cdot 10^{-6}$ at 10 mM NaCl, a Δf of 51.3 Hz and a ΔD of $1.65 \cdot 10^{-6}$ at a salt concentration of 25 mM (see FIGURE 3.1-1 A, B).

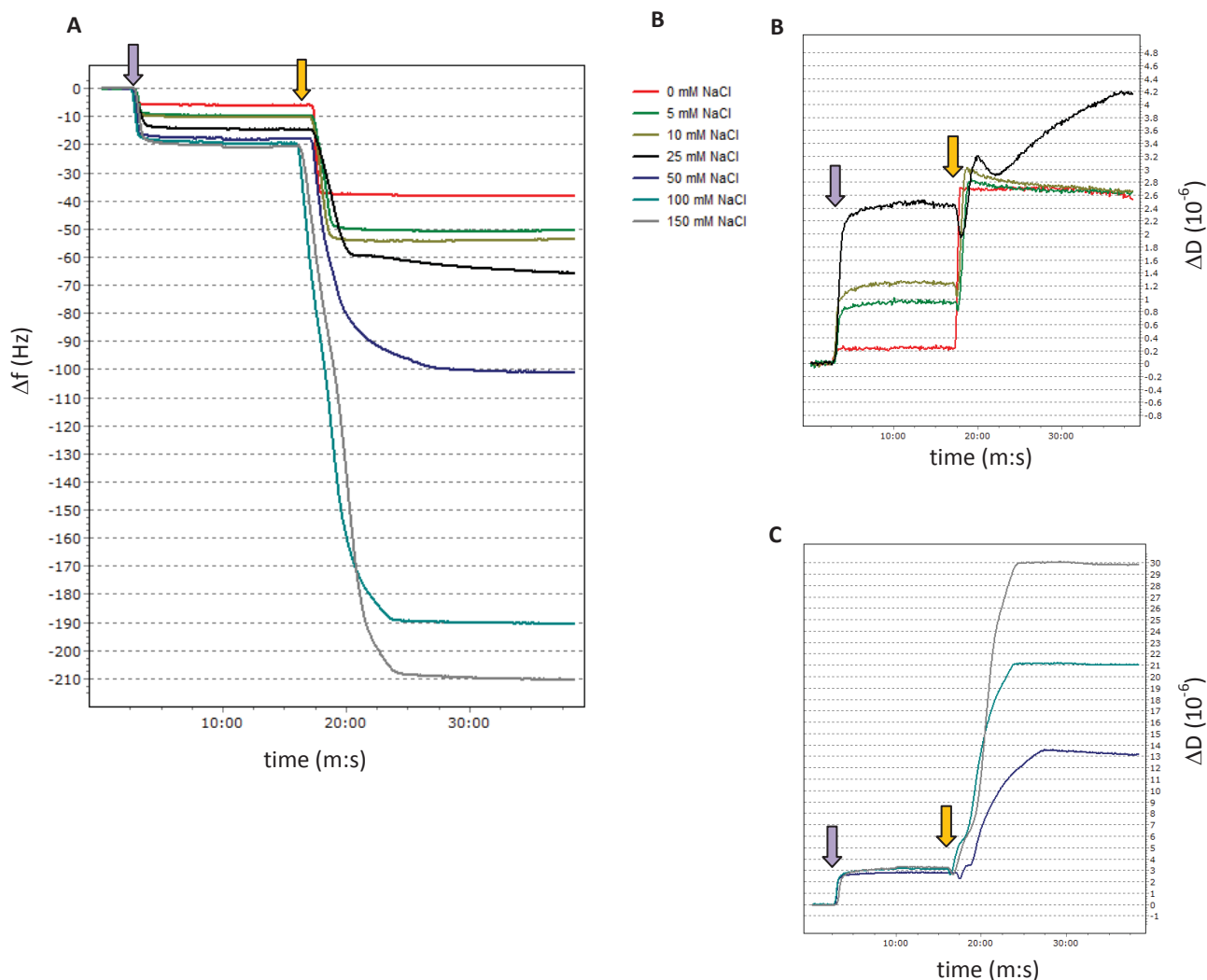


FIGURE 3.1-1 Formation of supramolecular assemblies of DNA and DOTAP liposomes on EDPS-modified quartz crystals at varying salt concentration from 0-150 mM NaCl. DNA injections are signaled by violet arrows, DOTAP injections by yellow arrows. Buffer injections have been accomplished after each sample injection, but aren't signaled. **A:** Frequency shifts Δf , observed during the adsorption of DNA and DOTAP. **B, C:** Dissipation shifts ΔD , observed during the adsorption of DNA and DOTAP at different scales.

At higher salt concentrations above 25 mM frequency and dissipation shifts are considerably higher. We observed a frequency shift of -189.2 Hz at a concentration of 150 mM NaCl, a frequency shift of -170.9 Hz at 100 mM NaCl and a frequency shift of -82.8 Hz for the adsorption of DOTAP on DNA in the presence of 50 mM NaCl. We observed high dissipation shifts of $10.4 \cdot 10^{-6}$ at 50 mM NaCl, $17.9 \cdot 10^{-6}$ at 100 mM NaCl and $26.5 \cdot 10^{-6}$ at 150 mM NaCl concentration respectively (see

FIGURE 3.1-1 B, C). With an increasing amount of DNA we adsorb higher amounts of lipids and form agglomerates which are more and more viscoelastic. The extremely high dissipation shifts illustrate the formation of huge, soft accumulations of DNA and lipids, but these are so high that the Sauerbrey law no longer applies. We obtain qualitative information about the situation of the adsorbed DNA-lipid agglomerates rather than quantitative informations about the adsorbed mass.

We observed the evolution of frequency and dissipation shifts after the injection of DOTAP vesicles on DNA layers which previously formed on quaternized surfaces. The frequency and dissipation shifts measured during the supramolecular self assembly of DNA strands on a Me-EDPS-modified silica coated crystal are shown in FIGURE 3.1-2.

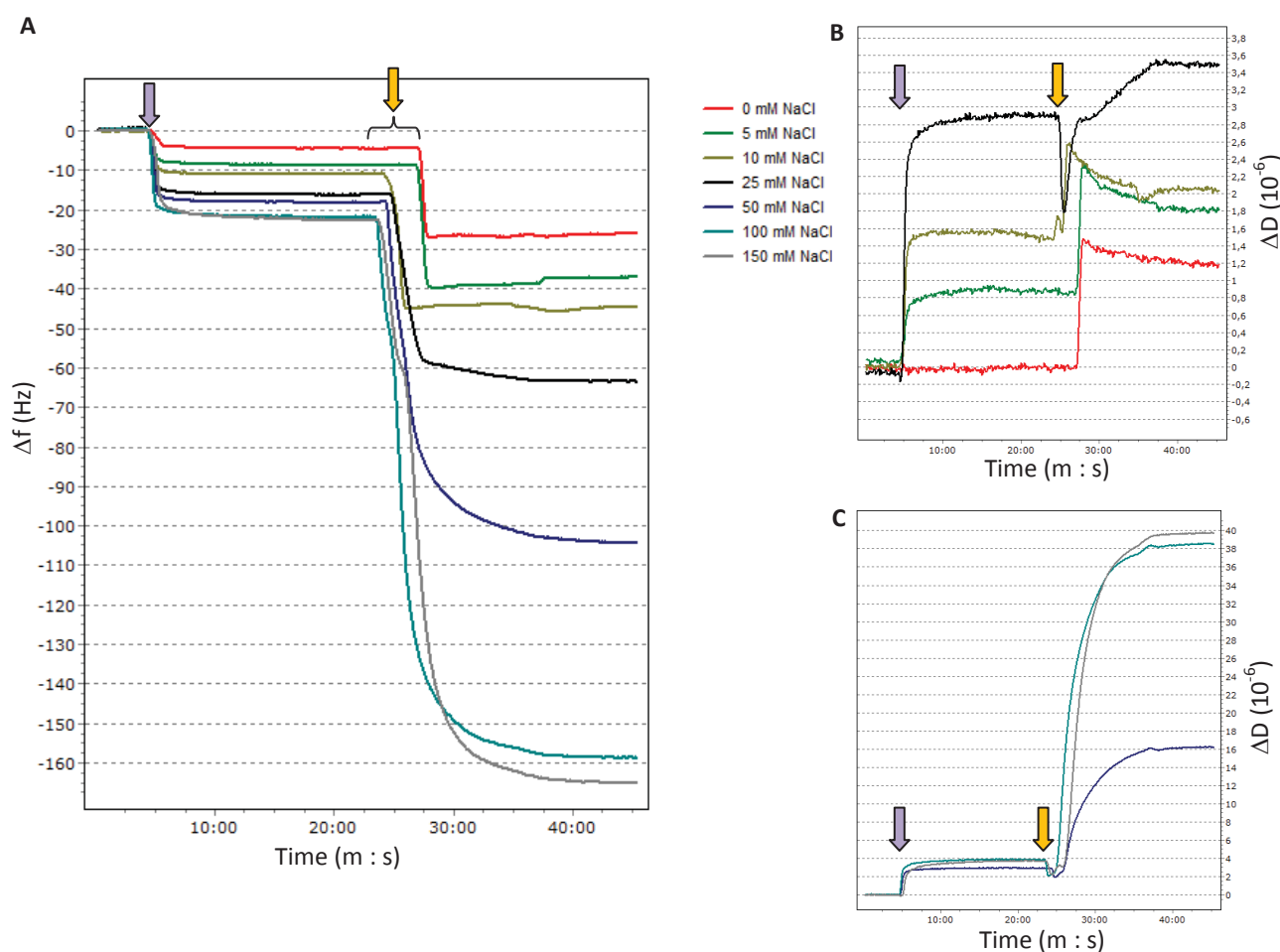


FIGURE 3.1-2 Adsorption of DNA and DOTAP liposomes on quaternized, Me-EDPS-modified quartz crystals at varying salt concentration from 0-150 mM NaCl. DNA injections are signaled by violet arrows, DOTAP injections by yellow arrows. Buffer injections were implemented after each sample injection, but aren't signaled. A: Frequency shifts Δf , observed during the adsorption of DNA and DOTAP. B, C: Dissipation shifts ΔD , observed during the adsorption of DNA and DOTAP on two different scales.

At lower salt concentrations the observed frequency and dissipation shift are more moderate. We observed a frequency shift of -21.3 Hz in the absence of salt, -29 Hz at 5 mM NaCl, -34 Hz at 10 mM NaCl and -47.5 Hz at a concentration of 25 mM NaCl. The corresponding dissipation shifts are very

low in comparison to the shifts observed at higher salt concentrations. At a salt concentration of 25 mM we observed a dissipation shift of $0.6 \cdot 10^{-6}$, at 10 mM NaCl of $0.4 \cdot 10^{-6}$, at 5 mM NaCl of $0.9 \cdot 10^{-6}$ and in the absence of salt of $1.2 \cdot 10^{-6}$ (see FIGURE 3.1-2 A, B).

On quaternized surfaces we observed a frequency shift of -142.5 Hz at 150 mM NaCl, -136.8 Hz at 100 mM NaCl and of -86 Hz at 50 mM NaCl concentration (see FIGURE 3.1-2 A). We adsorb high amounts of liposomes, which can interact with DNA forming DNA-lipid complexes and be adsorbed in the form of vesicles, until the surfaces were completely covered with positively charged lipids and no further interaction took place. At the same time the dissipation increased at extremely high values. We observed dissipation shifts of $13.2 \cdot 10^{-6}$ at 50 mM NaCl, $34.7 \cdot 10^{-6}$ at 100 mM NaCl and $35.8 \cdot 10^{-6}$ at the maximal salt concentration of 150 mM (see FIGURE 3.1-2 C). The dissipation values were 6 to 18 times higher than those previously observed for a monolayer of vesicles adsorbed to a silica surface (see FIGURE 1.1-5), indicating that the assemblies formed contain more than one layer of vesicles and are certainly affected by the fact that the DNA layers on which the assemblies took place had already been adsorbed as a viscoelastic and fluffy layer (see FIGURE 3.1-3).

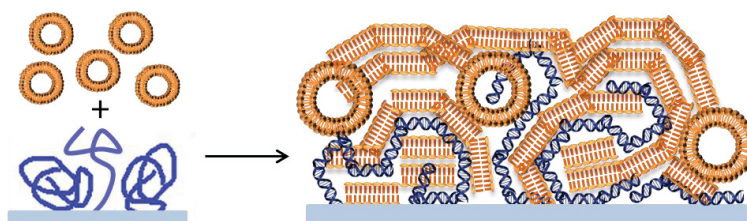


FIGURE 3.1-3 Schematic illustration of a viscoelastic agglomerate which may form on a modified silica surface in the presence of salt. DNA is present on the surface in a coiled conformation, and a multilayer of lipids and vesicles forms due to electrostatic interactions.

It is interesting to note that the dissipation decreases at the first contact of DNA with lipid vesicles, which indicates an interaction of liposomes with the flexibly adsorbed DNA. The decrease in dissipation shows that this first interaction leads to a rigidification of the assembled system and might correspond to a condensation of DNA strands by the cationic lipids added. We observed this particular decrease of dissipation at the first contact of DNA with cationic lipids as soon as we reached a concentration of 25 mM NaCl. This type of dissipation decrease is not observed at lower salt concentrations, which is probably due to the fact that the DNA layers adsorbed to the surfaces are already constituted of DNA strands present in a rigid conformation when they start to interact with cationic liposomes.

The differences in frequency shifts and dissipation shifts between DNA/DOTAP assemblies observed on quaternized and EDPS-modified surfaces at low concentrations of salt seem to confirm the observations implemented for the formation of DNA layers, which we observed to be very compact and rigid on quaternized surfaces. The conformation of the DNA layer seems to particularly influence its subsequent interactions with cationic liposomes. The most rigid layer of DNA forms on quaternized silica surfaces in the absence of salt. On this layer DOTAP molecules adsorb, inducing a frequency shift of -21.3 Hz accompanied by relatively low dissipation shift. In view of the fact that a

supported lipid bilayer of DOTAP on silica shows a frequency shift of about -20 Hz^[17] the observed frequency shift of -21.3 Hz might therefore indicate the formation of a supported lipid bilayer of DOTAP on the rigid DNA support.

It is known that lipid bilayers form on polymer-based cushions. Lipidic bilayers of different composition have been formed on layers of polysaccharide polyelectrolytes as chitosan and hyaluronic acid^[54], cellulose polymer supports^[55] or layers consisting of molecules such as poly(ethylene oxide) or oligopeptides^[56]. By forming a supported lipid bilayer of DOTAP on DNA as we suggested we subsequently expect that we will be able to form a DNA/DOTAP multilayer containing DOTAP SLBs. Tabaei et al.^[57] implemented the formation of a lipid/DNA/lipid multilayer on silica by the use of cholesterol conjugated oligonucleotide duplexes (chol-DNA-chol, 27 bp), which are anchored on the formed lipid bilayers by their cholesterol groups. Consequentially the formation of an alternating DNA/lipid multilayer should be feasible if the DOTAP layer previously formed on the rigid DNA support is present as a well-organized, rather rigid supported lipid bilayer. To verify this hypothesis we injected further DNA and subsequently further DOTAP liposomes to test if the formation of a supplementary DNA a second supported lipid bilayer is possible.

For this purpose, in the absence of salt we measured the frequency and dissipation shifts during further adsorption of DNA strands and subsequently DOTAP on a quaternized silica-coated crystal bearing a layer of DNA and lipids which had previously formed, as shown in **FIGURE 3.1-4**.

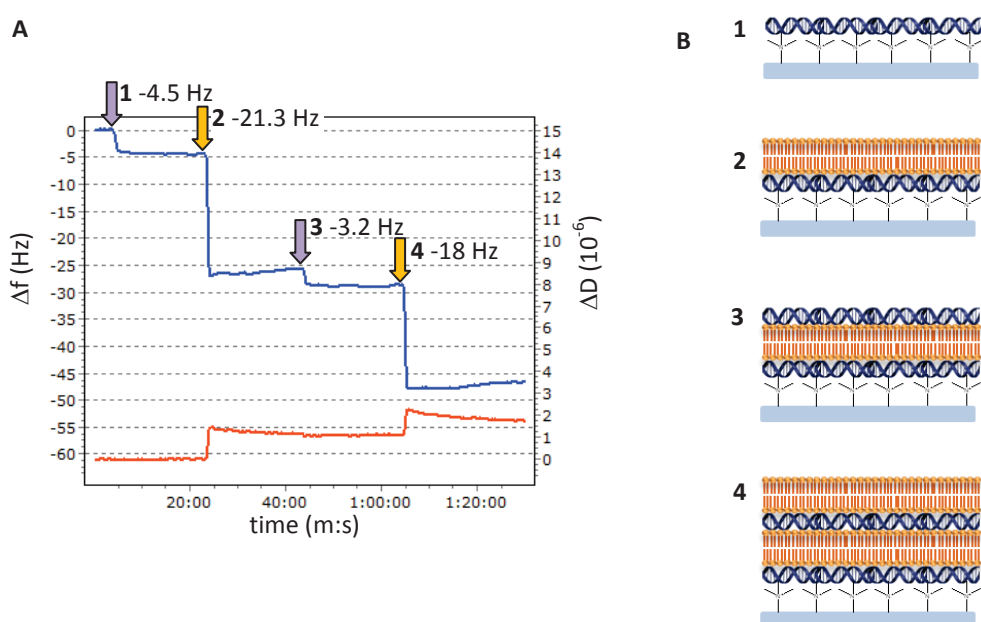


FIGURE 3.1-4 QCM-D measurement makes it possible to follow the formation of a DNA-DOTAP multilayer which consists of rigid DNA layers supporting lipid bilayers. **A**: The QCM-D graph shows that DNA/DOTAP multilayers are formed on quaternized silica surfaces at salt concentrations of 0 mM and at pH 7.4. DNA injections are signaled by violet arrows, DOTAP injections by yellow arrows. Buffer injections (HEPES 10 mM, pH = 7.4) were implemented after each sample injection, but are not signaled. **B**: Schematic illustration of the well-organized layers forming on a quaternized silica surface in the absence of salt.

When injecting an additional sample of DNA on a DNA/DOTAP layer formed in the absence of salt we observed the adsorption of DNA to the present lipidic layer indicating that DOTAP molecules form an even well organized bilayer. We monitored a frequency shift of 3.2 Hz and a decrease in dissipation of $-0.1 \cdot 10^{-6}$. The decrease in dissipation shows that the adsorbed DNA is present in a completely rigid conformation and is probably condensed to the lipid bilayer. A subsequent injection of DOTAP liposomes led to a frequency shift of -17.8 Hz and a dissipation increase of $0.68 \cdot 10^{-6}$. Both shifts indicate that the formation of a further DOTAP bilayer on the condensed DNA takes place. Frequency shifts **2** and **4** monitored (see FIGURE 3.1-4) after the injection of DOTAP on the DNA layers show values of -21 Hz and -18 Hz, which are near to the ideal frequency shift of -20 Hz observed for the formation of a supported lipid bilayer, indicating that the formation of a DNA-lipid multilayer consisting of rigid DNA layers and supported lipid bilayers occurred. Furthermore it is interesting to observe that the injection of DNA on a lipid layer does not lead to an increase in the dissipation of the multilayer although it increases its mass. This fact indicates that DNA is condensed due to electrostatic interactions with the cationic lipid layer.

At a salt concentration of 5 mM the adsorption of a DNA layer on the previously formed DNA/DOTAP cushion is also possible. But already the first lipid layer adsorbed on DNA induces a frequency shift of -28.5 Hz which is too high to correspond to a supported lipid bilayer. Subsequent to the injection of DNA a frequency shift of 8.5 Hz accompanied by a dissipation shift of $0.4 \cdot 10^{-6}$ was monitored. In contrast to the previous observation a following injection of DOTAP led instead to the formation of a lipid layer whose formation we followed by the observation of a frequency shift of -27.1 Hz and a simultaneous dissipation shift of 1.4 Hz (see FIGURE 3.1-5). The frequency shift of -27.1 Hz was already 1.35 times higher than the shift of -20 Hz corresponding to a supported lipid bilayer of DOTAP. It did not correspond to the signal of a supported lipid bilayer.

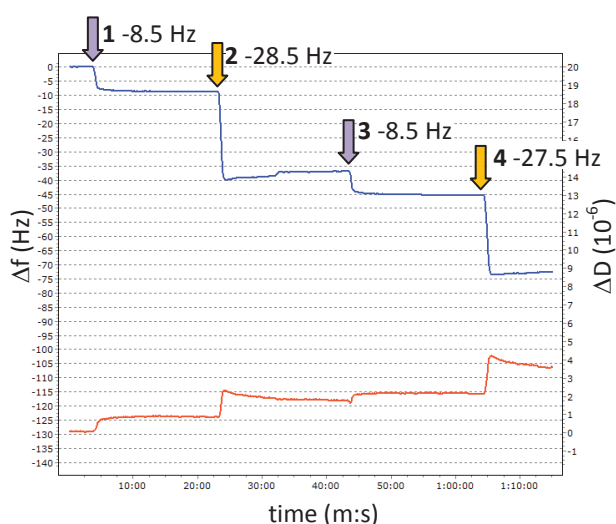


FIGURE 3.1-5 At a salt concentration of 5 mM NaCl the observed frequency shifts of the lipid layers within the DNA-lipid multilayer adsorbed on a quaternized silica surface do not correspond to the signals expected for supported lipid bilayers. DNA injections are signaled by violet arrows, DOTAP injections by yellow arrows. Buffer injections (HEPES 10 mM, pH = 7.4) were implemented after each sample injection but are not signaled.

We also implemented the formation of DNA/DOTAP multilayers on an aminated EDPS-modified surface to compare the values of the frequency shifts corresponding to the adsorption of DOTAP layers within the DNA-lipid layers with those which we observed on quaternized surfaces (see FIGURE 3.1-6).

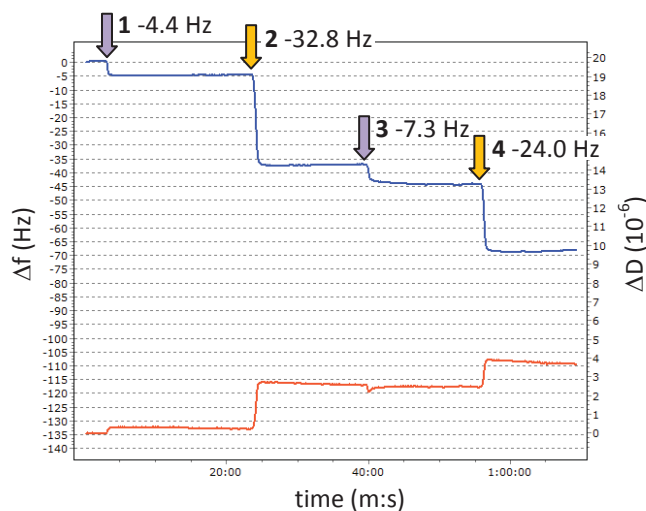


FIGURE 3.1-6 In the absence of salt the observed frequency shifts of the lipid layers within the DNA-lipid multilayer adsorbed on an aminated surface do not correspond to the signals expected for supported lipid bilayers. DNA injections are signaled by violet arrows, DOTAP injections by yellow arrows. Buffer injections (HEPES 10 mM, pH = 7.4) were implemented after each sample injection but are not signaled.

After the injection of DOTAP vesicles on a previously formed DNA layer we observed frequency shifts of -32.8 Hz and -24 Hz, which are too high to correspond to the shift of a supported lipid bilayer of DOTAP. The fact that we solely observed the formation of supported lipid bilayers of DOTAP on DNA layers adsorbed to a quaternized surface in the absence of salt whereas under the same conditions we did not observe the formation of supported lipid bilayers on EDPS-supported DNA probably results from the adsorption of a more rigid DNA layer on quaternized surfaces. The conformation of DNA apparently decides the way in which DOTAP lipids adsorb to the surface. It is most likely that DNA strands are better adsorbed and condensed on quaternized surfaces and more tightly bound at low concentrations of salt because of the maximization of electrostatic interactions under these conditions.

3.2 Investigation of the formation of lipoplexes including nanoparticle labeled DNA

To investigate the ability of quaternized nanoparticles to label DNA included to lipoplexes we executed initial trials to assemble DNA and cationic lipids with quaternized or aminated nanoparticles. To maximize the difference between quaternized and aminated nanoparticles we carried out all the experiments at pH 8.6, where the differently modified nanoparticles possess clearly distinguished zeta potentials which will show an impact on their ability to interact with DNA. The formation of

lipoplexes was implemented using the cationic transfection agent bis(guanidinium)-tris(2-aminoethyl)aminecholesterol (BGTC) and the phospholipid 1,2-di-(9Z-octadecenoyl)-*sn*-glycero-3-phosphoethanolamine (DOPE). Lipoplexes of this composition have been shown to facilitate the transfection of DNA and siRNA with particular efficiency^[6,58]. The assemblies of nanoparticle labeled lipoplexes were accomplished in line with **PROTOCOL 3.2-1**:

PROTOCOL 3.2-1 Formation of lipoplexes containing DNA, cationic lipids and surface modified silica nanoparticles at pH 8.6

To 46.84 μL containing 0.3 μg DNA and 5 μL borate buffer (100 mM, pH 8.6) 1.16 μL of an aqueous dispersion of quaternized nanoparticles (1.721017 NPs/L) was added under careful agitation. Subsequently 2 μL of lipids of a desired composition (BGTC/DOPE, 2.5 mM) was added. The final volume of the mixture was 50 μL .

Lipoplexes have been visualized by transmission electron microscopy with the help of negative stains or by Cryo-TEM within the group of O. Lambert at the CBMN research center. To avoid the formation of nanoparticle/DNA aggregates before the addition of the cationic lipids, a nanoparticle/DNA ratio of 0.5 nm^2/bp was fixed during the assembly process. All assembly processes were carried out in borate buffer (10 mM) at pH 8.6 and at a salt concentration of 150 mM using herring sperm DNA and cationic liposomes, which were added in a considerable excess. During these tests liposomes of a lipid composition of BGTC and DOPE were used. **FIGURE 3.2-1** shows the TEM micrograph of an assembly of DNA, quaternized nanoparticles and BGTC/DOPE liposomes. We observed the incorporation of the modified nanoparticles into lipid agglomerations resembling lipoplexes.

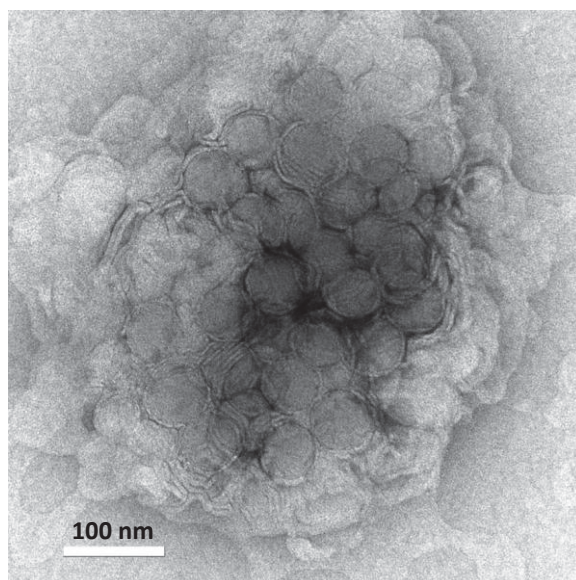


FIGURE 3.2-1 TEM image of an NP/lipoplex agglomeration assembled at 150 mM NaCl in borate buffer (10 mM, pH 8.6) using Me-EDPS-modified nanoparticles, herring sperm DNA and BGTC/DOPE liposomes. The specimen is stained with uranyl acetate.

Comparing Cryo-TEM micrographs of the DNA/NP/lipid agglomerations formed either with quaternized nanoparticles (FIGURE 3.2-2 A) or with aminated nanoparticles (FIGURE 3.2-2 B) under the same conditions (HEPES 10mM, pH 8.6, 150 mM NaCl), we observed that the quaternized nanoparticles are in contact with lipoplex resembling structures probably consisting of DNA and BGTC/DOPE. In contrast we detected the formation of supported lipid bilayers on the EDPS-modified nanoparticles. We conclude that the basic pH and the high salt concentration prevent an efficient adsorption of DNA to aminated nanoparticles and lead to the formation of a cationic SLB due to van der Waals forces.

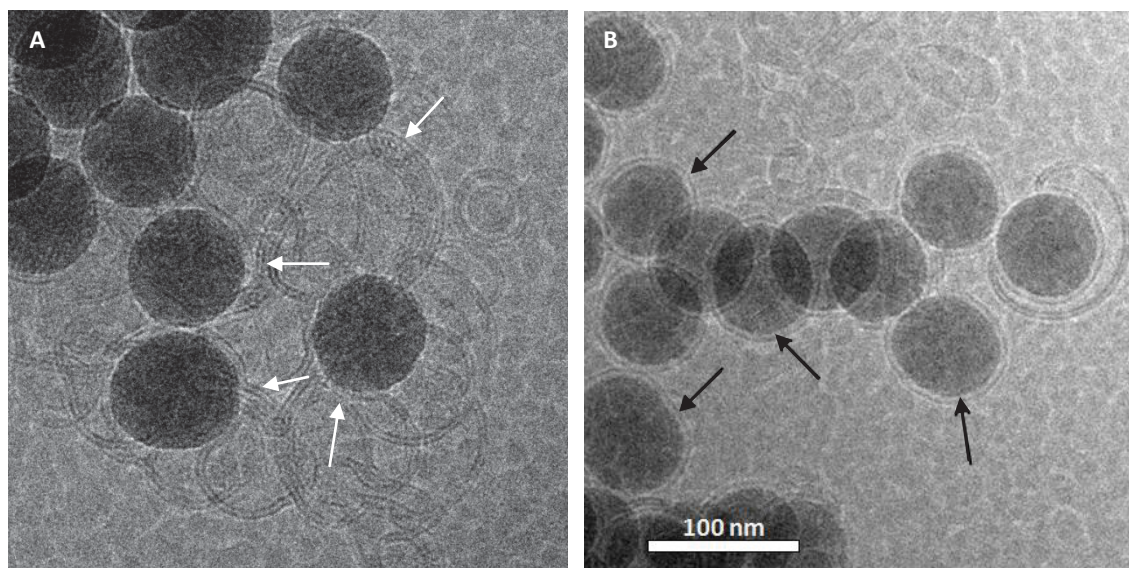


FIGURE 3.2-2 Cryo-TEM image of an NP/lipoplex agglomeration assembled at 150 mM NaCl in borate buffer (10 mM, pH 8.6) using **A**: Me-EDPS-modified nanoparticles or **B**: EDPS-modified nanoparticles, herring sperm DNA and BGTC/DOPE liposomes. In picture **A** lipoplex resembling structures are indicated by white arrows. Supported lipid bilayers observed on EDPS modified nanoparticles are indicated by black arrows in picture **B**.

Although the implementation of the formation of nanoparticle labeled lipoplexes in the presence of salt at pH 8.6 was appropriated to display the difference between aminated and quaternized nanoparticles it was not considered to be the best condition to form nanoparticle labeled lipoplexes. We tested further conditions for the formation of lipoplexes containing nanoparticle-labeled DNA. We implemented the formation of lipoplexes in the presence of 150 mM NaCl and also in the absence of salt at pH 6.5 in 10 mM MES buffer by mixing herring sperm DNA, quaternized nanoparticles and DOTAP vesicles (see **PROTOCOL 3.2-2**).

PROTOCOL 3.2-2 Formation of lipoplexes containing DNA, cationic lipids and surface modified nanoparticles at pH 6.4

10 μ L of an aqueous dispersion of quaternized silica nanoparticles (varying concentration) was added under careful agitation to a volume of 90 μ L aqueous solution containing 5 μ g DNA and 10 μ L MES buffer (100 mM, pH 6.5, 0mM or 150 mM NaCl) in order to obtain NP/DNA complexes at different NP/DNA ratios (nm^2/bp). The final volume is 100 μ L. Subsequently the volume was separated by pipetting 30 μ L of the mixture to different wells of a multiwell plate. Then 0.63 μ L,

1.26 μL or 1.89 μL of liposome dispersion (DOTAP, 10 mg/mL) was added to obtain mixtures with $S_{\text{LB}}/S_{\text{NP}}$ ratios of 2:1, 4:1 or 6:1. Some assemblies were also undergone using quaternized silica nanoparticles and MUTAB-coated gold nanoparticles, which were added to the DNA containing solution with a silicaNP/goldNP ratio of 1:10.

FIGURE 3.2-3 shows the different lipoplex preparations which were implemented in a multiwell plate.

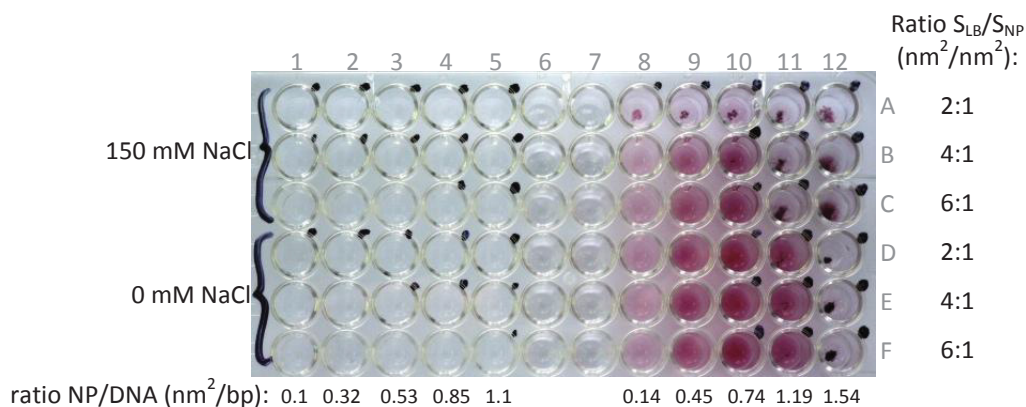


FIGURE 3.2-3 Photographed picture of different nanoparticle-labeled lipoplex assemblies implemented in a multiwell plate. The wells from 1 to 5 contain lipoplexes formed in the presence of quaternized silica NPs. The wells 8 to 12 contain lipoplexes labeled with modified silica and gold NPs. Coagulated samples are indicated by a black point.

Depending on the used ratios the formed NP/DNA/lipid agglomerates stayed dispersed or flocculated as indicated by the black points next to the concerned samples. Gold nanoparticles permit a better visualization of the flocculated states shown in FIGURE 3.2-3. We observed that the samples coagulate in relation to the NP/DNA and the $S_{\text{LB}}/S_{\text{NP}}$ ratios. The assemblies coagulate with increasing NP/DNA ratio and with decreasing $S_{\text{LB}}/S_{\text{NP}}$ ratio. The samples C3 and F3 were observed by TEM and Cryo-TEM (see FIGURE 3.2-4). On Cryo-TEM pictures we observed lipid bilayers less distinct than in FIGURE 3.2-2 because the DOTAP molecules do not contain a phosphate groups and are subsequently less electron-dense than DOPE containing LBs.

In the presence of salt we observed the formation of supported lipid bilayers of DOTAP on the quaternized nanoparticles (see FIGURE 3.2-4 A, C, E; SLBs are indicated by black arrows). The formation of a SLB of DOTAP on a quaternized nanoparticle may be due to the presence of negatively charged DNA which allies the two positively charged compounds but may also occur without the presence of DNA because the cationic charges of lipids and nanoparticles were screened by chloride ions. Subsequently van der Waals interactions promoted the formation of a SLB. We also observed the formation of lamellar lipoplex type structures as indicated by white arrows. On Cryo-TEM pictures we could distinct DNA rods enclosed to two concentric lipid bilayers. Such lipoplex ultrastructures have been previously observed^[6]. They occur independently from the quaternized nanoparticles in the saline medium. They were located individually in the medium, adsorbed to quaternized nanoparticles or completely surrounding those in a circular form (see FIGURE 3.2-4 A, C).

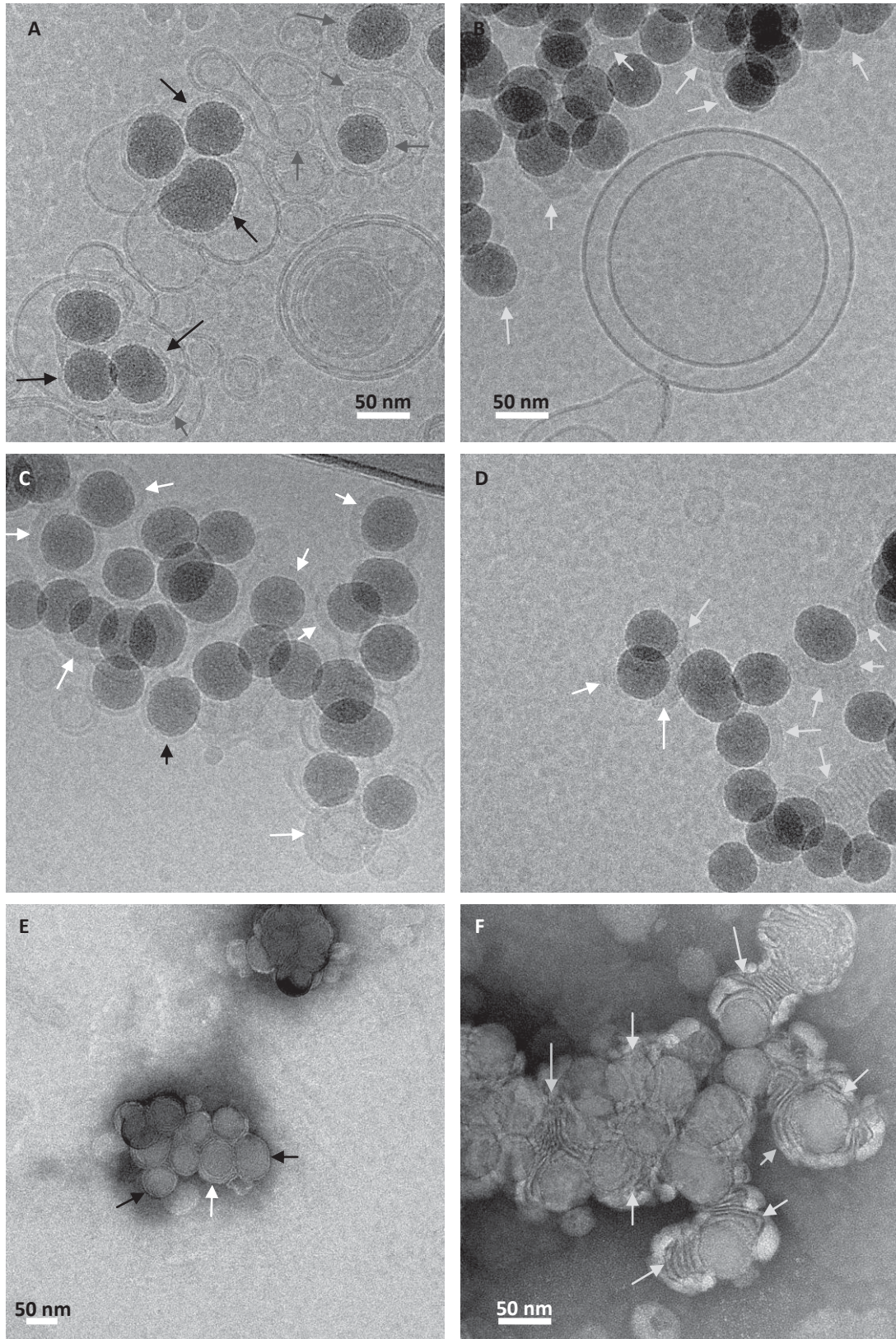


FIGURE 3.2-4 Cryo-TEM (**A, B, C, D**) and uranyl acetate stained TEM (**E, F**) images of NP/lipoplex agglomerations (ratio NP/DNA = $0.53 \text{ nm}^2/\text{bp}$, ratio NP surface area/lipid surface = 1:6) formed at pH 6.5 in 10 mM MES buffer at 150 mM NaCl (**A, C, E**) or without NaCl (**B, D, F**). Different assemblies occur: SLBs are indicated by black arrows, lamellar lipoplex structures are indicated by white arrows (circular, concentric structures) and grey arrows (planar structures). All Cryo-TEM pictures are at the same scale. See further pictures in Annex 5.

In the absence of salt we implemented the formation of nanoparticle-labeled lipoplexes in conditions which promoted the electrostatic interactions between quaternized nanoparticles, DNA and the positively charged DOTAP vesicles. The formation of supported lipid bilayers was not observed anymore. This indicates that their formation in the presence of 150 mM NaCl was mainly due to van der Waals forces. In contrast to what we observed for liposomes near to quaternized nanoparticles on the Cryo-TEM picture in **FIGURE 3.2-4 A** a liposome near to a quaternized nanoparticles shown in **FIGURE 3.2-4 B** does not even change its curvature, because no interaction took place.

We could distinct lamellar lipoplex structures of DNA/lipid multilayers adsorbing on quaternized nanoparticles or surrounding them completely. These lipoplexes exhibit angular and planar morphologies which are indicated by light-grey arrows (see **FIGURE 3.2-4 B, C, D**). Such lipoplex ultrastructures were previously observed^[48]. Although lipoplexes formed at 150 mM and those formed in the absence of salt consist both of a multilamellar L_{α}^C structures^[51] they showed different morphologies. The planar lipoplexe layers which were formed in the absence of salt seem to be more compact than the circular lipoplexes which we were formed at 150 mM NaCl concentration.

The fact that DNA layers observed in the circular lipoplexes at 150 mM NaCl (see **FIGURE 3.2-4 A**) seem to require more space than DNA layers inbetween planar lipoplexes (see **FIGURE 3.2-4 B**) may be explained by the fact that the space between DNA rods increases if they are surrounded not only by cationic lipids but also by salt counterions. This observation corresponds to what we observed on quaternized QCM-D crystals on which we monitored the formation of compact DNA/SLB multilayers in the absence of salt and the adsorption of less rigid and less compact DNA/lipid multilayers in the presence of salt.

The results encouraged us to test the assembly of nanoparticle/DNA/lipid complexes using quaternized silica nanoparticles and a second kind of nanoparticles at the same time. For the purpose of forming lipoplexes containing DNA, which is labeled by two different kinds of nanoparticles as we have illustrated in Chapter I **FIGURE 4.3-4**, we implemented lipoplexe formations in the presence of quaternized silica and MUTAB-coated gold nanoparticles. The NP/DNA/lipid assemblies formed in sample F8 (see **FIGURE 3.2-3**) were displayed by TE microscopy (see **FIGURE 3.2-5 A**) under the use of uranyl acetate as a stain.

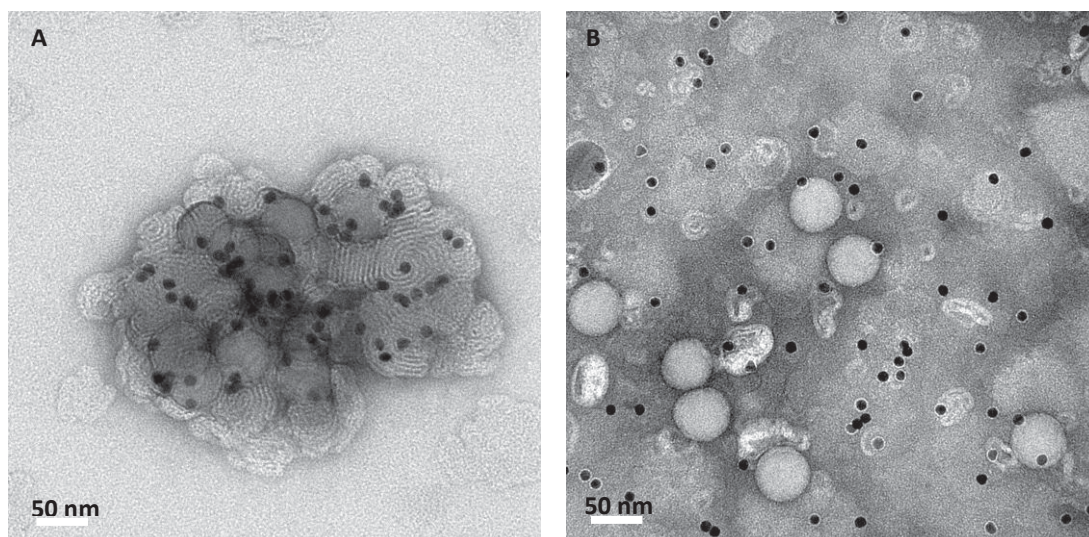


FIGURE 3.2-5 TEM pictures of assemblies implemented at pH 6.5 in the absence of salt but using two different kinds of quaternary ammonium group bearing nanoparticles. **A:** TEM picture of a NP/DNA/lipid agglomeration formed of quaternized silica nanoparticles, MUTAB-coated gold nanoparticles, herring sperm DNA and DOTAP vesicles (ratio silica NP/DNA = 0.1, ratio silica NP/gold NP 1:10, ratio silica NP surface/lipid surface 1:6). **B:** TEM picture of a control sample containing quaternized silica NPs, MUTAB-coated gold NPs and DOTAP lipids which were mixed in the same ratios as described for sample shown in picture **A** but in the absence of DNA. See further pictures in Annex 5.

We detected that as we prospected it was possible to form lipoplexes where DNA was labeled by two kinds of quaternized nanoparticles (see **FIGURE 3.2-5 A**). To obtain a control sample quaternized silica nanoparticles, MUTAB-coated gold nanoparticles and DOTAP vesicles were mixed under the same conditions but in the absence of DNA to demonstrate that the presence of DNA is necessary to form the observed assemblies. We observed that the formation of such nanoparticle labeled lipoplexes did not take place in the absence of DNA (see **FIGURE 3.2-5 B**).

In recapitulating the experiments implemented to form nanoparticle labeled lipoplexes we can see that we were able to label DNA in lipoplexes with our newly modified silica nanoparticles.

3.3 Conclusions and prospects

This third chapter reported the efforts implemented to study the interactions between quaternized nanoparticles and DNA or phospholipids in comparison to aminated silica nanoparticles.

In the first part we showed that we did not observe an improvement in interactions between negatively charged DOPS vesicles and quaternized surfaces in comparison to SiO₂ surfaces only modified with primary and secondary amine groups. Whereas we achieved the formation of a supported lipid bilayer of DOPS on SiO₂ surfaces bearing primary and secondary amine groups we did not observe the formation of a supported lipid bilayer on a quaternized surface under the same operating conditions. The quaternized nanoparticles do not seem to be optimized to interact with phospholipids and even at basic pHs such as pH 9 the fact that quaternized surfaces keep far more charges than aminated ones was not sufficient to induce the rupture of DOPS vesicles. This observation can most likely be

explained by the fact that DOPS liposomes are highly negatively charged and strongly repulse each other in the absence of salt.

In contrast quaternized silica surfaces seem to be more suitable for interacting with DNA than aminated silica surfaces. At alkaline pHs quaternized nanoparticle surfaces adsorb higher quantities of herring sperm DNA than aminated nanoparticle surfaces. We demonstrated that to complex the same amount of DNA at pH 9 an amount of quaternized nanoparticles is needed which represents only $\frac{3}{5}$ of the quantity of aminated nanoparticles employed. In addition QCM-D measurements showed that quaternized surfaces are more suitable for adsorbing DNA in the presence of 150 mM of salt even at alkaline pHs such as pH 8.6 and pH 9.

Cosedimentation assays showed that with increasing salt concentration the same amount of modified nanoparticles are able to complex higher amounts of DNA. QCM-D measurements confirmed these observations and demonstrated that this result is due to a change in the DNA conformation. At higher salt concentrations DNA strands are more flexible due to a partial screening of the charges of the deoxyribosephosphate backbone and adsorb as viscoelastic ravel. DNA adsorbing to quaternized surfaces at low salt concentrations has been shown to adsorb in a more rigid conformation than DNA which adsorbed on aminated surfaces under the same conditions. Furthermore we achieved the formation of supported lipid bilayers of DOTAP on DNA cushions condensed on quaternary ammonium bearing silica surfaces under conditions promoting the electrostatic interactions between lipids and DNA. DNA-lipid multilayers which formed on aminated surfaces did not contain lipid layers in the form of a supported lipid bilayer. This observation indicates an improved condensation of DNA on quaternized surfaces.

We observed the formation of lipoplex structures including DNA-labeling quaternized nanoparticles when cationic lipids, DNA and quaternized nanoparticles were brought in contact with each other. The formation of nanoparticle/DNA/lipid complexes was possible in the presence of 150 mM salt at alkaline pH of 8.6, although this was not possible while using aminated silica nanoparticles. This fact demonstrates the different ability of the two surfaces to undergo electrostatic interactions in an alkaline environment. The formation of nanoparticle labeled lipoplexes has been shown to be successful at pH 6.5. We observed the formation of lipoplexes with different morphologies in the presence and in the absence of salt. We aim to continue self assembly experiments to identify the ideal conditions for the formation of nanoparticle-labeled cationic lipoplexes.

The results of this third chapter demonstrate that the adsorption of DNA on the modified nanoparticles was mainly caused by electrostatic interactions. Nevertheless the affinity of modified nanoparticles with DNA does not only depend on electrostatic interactions. The specificity of modified silica surfaces may be enhanced by a further modulation of the hydrophilic-hydrophobic balance of quaternized surfaces. The implementation of more hydrophobic butyl or phenyl groups replacing a part of quaternizing methyl groups is one strategy to be followed in aiming a further improvement of DNA binding. Furthermore the implementation of guanidinium groups on modified surfaces might enhance the capacity of functionalized nanoparticles to label DNA. Guanidinium

groups possess a pKa of 12.5 and are mainly responsible for interactions existing between DNA and arginine rich histone proteins which condense DNA in the chromosomes.

The implementation of the modification process allowing the quaternization of primary and secondary amine groups on EDPS-coated silica nanoparticles was shown to significantly improve the interaction of quaternized nanoparticles with DNA compared to nanoparticles which are only aminated. As a consequence of this study we are now able to functionalize multimodal silica nanoparticles with quaternary ammonium groups for the labeling of DNA. We aim to display DNA labeled by quaternized hybrid nanoparticles during their transfection by cationic lipids *in vitro* and *in vivo* and forward our research in collaboration with biologists. Microscopic studies could reveal if the newly modified nanoparticles stay bound to labeled DNA during its migration through the cytosol.

REFERENCES

- [1] M. A. Markowitz, G. Deng, B. P. Gaber, *Langmuir* **2000**, *16*, 6148–6155.
- [2] M. A. Markowitz, G. Deng, M. C. Burleigh, E. M. Wong, B. P. Gaber, *Langmuir* **2001**, *17*, 7085–7092.
- [3] S. Jayasundera, M. Zeinali, J. B. Miller, L. M. Velea, B. P. Gaber, M. A. Markowitz, *J. Phys. Chem. B* **2006**, *110*, 18121–18125.
- [4] C. Jin, L. Han, S. Che, *Angew. Chem. Int. Ed.* **2009**, *48*, 9268–9272.
- [5] C. M. Goodman, N. S. Chari, G. Han, R. Hong, P. Ghosh, V. M. Rotello, *Chem. Biol. Drug. Des.* **2006**, *67*, 297–304.
- [6] O. Le Bihan, R. Chèvre, S. Mornet, B. Garnier, B. Pitard, O. Lambert, *Nucleic Acids Res.* **2011**, *39*, 1595–1609.
- [7] J. A. Virtanen, K. H. Cheng, P. Somerharju, *PNAS* **1998**, *95*, 4964–4969.
- [8] S. Mornet, O. Lambert, E. Duguet, A. Brisson, *Nano Lett.* **2005**, *5*, 281–285.
- [9] R. P. Richter, A. R. Brisson, *Biophys J* **2005**, *88*, 3422–3433.
- [10] T. J. Zwang, W. R. Fletcher, T. J. Lane, M. S. Johal, *Langmuir* **2010**, *26*, 4598–4601.
- [11] F. Höök, J. Vörös, M. Rodahl, R. Kurrat, P. Böni, J. Ramsden, M. Textor, N. Spencer, P. Tengvall, J. Gold, et al., *Colloids Surf. B* **2002**, *24*, 155–170.
- [12] F. Höök, B. Kasemo, T. Nylander, C. Fant, K. Sott, H. Elwing, *Anal. Chem.* **2001**, *73*, 5796–5804.
- [13] K. A. Melzak, S. Moreno-Flores, A. E. López, J. L. Toca-Herrera, *Soft Matter* **2011**, *7*, 332–342.
- [14] R. Richter, *The Formation of Solid Supported Lipid Membranes and Two Dimensional Assembly of Proteins.*, Université Bordeaux I, **2004**.
- [15] Q-sense, **2013**.
- [16] G. Sauerbrey, *Z. Physik* **1959**, *155*, 206–222.
- [17] R. Richter, A. Mukhopadhyay, A. Brisson, *Biophys. J.* **2003**, *85*, 3035–3047.
- [18] M. Rodahl, B. Kasemo, *Review of Scientific Instruments* **1996**, *67*, 3238–3241.
- [19] S. Trépout, Etude de l'assemblage du système d'efflux membranaire MexAB-OprM impliqué dans la résistance aux antibiotiques chez *Pseudomonas aeruginosa* : caractérisation combinée par Microbalance à cristal de quartz avec mesure de dissipation et cryo-tomographie électronique, thesis, **2008**.
- [20] C. A. Keller, B. Kasemo, *Biophys. J.* **1998**, *75*, 1397–1402.
- [21] R. P. Richter, J. Lai Kee Him, B. Tessier, C. Tessier, A. R. Brisson, *Biophys. J.* **2005**, *89*, 3372–3385.
- [22] I. Reviakine, A. N. Morozov, F. F. Rossetti, *J. Appl. Phys.* **2004**, *95*, 7712–7716.
- [23] D. D. Lasic, *Liposomes: From Physics to Applications*, Elsevier, **1993**.
- [24] A. Moscho, O. Orwar, D. T. Chiu, B. P. Modi, R. N. Zare, *PNAS* **1996**, *93*, 11443–11447.
- [25] D. D. Lasic, *Liposomes in Gene Delivery*, Taylor & Francis, **1997**.
- [26] R. P. Richter, A. Brisson, *Langmuir* **2004**, *20*, 4609–4613.
- [27] J.-O. Carlsson, R. V Bucur, *Sens. Actuators B: Chem.* **1996**, 91–95.
- [28] L. D. Williams, L. J. Maher 3rd, *Annu. Rev. Biophys. Biomol. Struct.* **2000**, *29*, 497–521.
- [29] D. Voet, J. G. Voet, C. W. Pratt, A. Beck-Sickinger, *Lehrbuch der Biochemie*, Wiley VCH Verlag GmbH, **2010**.
- [30] M. N. V. Ravi Kumar, M. Sameti, S. S. Mohapatra, X. Kong, R. F. Lockey, U. Bakowsky, G. Lindenblatt, H. Schmidt, C. M. Lehr, *J. Nanosci. Nanotechnol.* **2004**, *4*, 876–881.
- [31] C. Kneuer, M. Sameti, E. G. Haltner, T. Schiestel, H. Schirra, H. Schmidt, C. M. Lehr, *Int. J. Pharm.* **2000**, *196*, 257–261.
- [32] P. C. Ross, S. W. Hui, *Gene Ther.* **1999**, *6*, 651–659.
- [33] J. R. Paulson, U. K. Laemmli, *Cell* **1977**, *12*, 817–828.
- [34] C. Pichon, C. Gonçalves, P. Midoux, *Adv. Drug Deliv. Rev.* **2001**, *53*, 75–94.
- [35] P. S. Ghosh, C.-K. Kim, G. Han, N. S. Forbes, V. M. Rotello, *ACS Nano* **2008**, *2*, 2213–2218.
- [36] C. M. McIntosh, E. A. Esposito 3rd, A. K. Boal, J. M. Simard, C. T. Martin, V. M. Rotello, *J. Am. Chem. Soc.* **2001**, *123*, 7626–7629.
- [37] K. K. Sandhu, C. M. McIntosh, J. M. Simard, S. W. Smith, V. M. Rotello, *Bioconjugate Chem.* **2002**, *13*, 3–6.
- [38] Renault, Baudrimont, Mesmer-Dudons, Gonzalez, Mornet, Brisson, *Gold Bulletin* **2008**, *41*, 116–126.
- [39] V. B. Teif, K. Bohinc, *Prog. Biophys. Mol. Biol.* **2011**, *105*, 208–222.

- [40] O. Le Bihan, *Etude Par Microscopie Électronique Des Mécanismes D'action de Vecteurs Synthétiques Pour Le Transfert de Gènes*, Université Bordeaux 1, **2009**.
- [41] T. H. Nguyen, M. Elimelech, *Biomacromolecules* **2007**, *8*, 24–32.
- [42] T. H. Nguyen, K. L. Chen, M. Elimelech, *Biomacromolecules* **2010**, *11*, 1225–1230.
- [43] L. Zhu, Y. Gao, H. Shen, Y. Yang, L. Yuan, *J. Anal. Chem.* **2005**, *60*, 780–783.
- [44] A. Y. Yang, R. J. Rawle, C. R. D. Selassie, M. S. Johal, *Biomacromolecules* **2008**, *9*, 3416–3421.
- [45] A. P. R. Johnston, H. Mitomo, E. S. Read, F. Caruso, *Langmuir* **2006**, *22*, 3251–3258.
- [46] H. Zipper, H. Brunner, J. Bernhagen, F. Vitzthum, *Nucleic Acids Res.* **2004**, *32*, e103–e103.
- [47] A. I. Dragan, R. Pavlovic, J. B. McGivney, J. R. Casas-Finet, E. S. Bishop, R. J. Strouse, M. A. Schenerman, C. D. Geddes, *J. Fluoresc.* **2012**, *22*, 1189–1199.
- [48] A. R. Thierry, V. Norris, F. Molina, M. Schmutz, *Biochim. Biophys. Acta* **2009**, *1790*, 385–394.
- [49] C. Marchini, D. Pozzi, M. Montani, C. Alfonsi, A. Amici, H. Amenitsch, S. Candeloro De Sanctis, G. Caracciolo, *Langmuir* **2010**, *26*, 13867–13873.
- [50] J. O. Rädler, I. Koltover, T. Salditt, C. R. Safinya, *Science* **1997**, *275*, 810–814.
- [51] C. R. Safinya, *Curr. Opin. Struct. Biol.* **2001**, *11*, 440–448.
- [52] G. S. Manning, *J. Chem. Phys.* **1969**, *51*, 924–933.
- [53] R. Bruinsma, *Eur. Phys. J. B* **1998**, *4*, 75–88.
- [54] K. Mulligan, Z. J. Jakubek, L. J. Johnston, *Langmuir* **2011**, *27*, 14352–14359.
- [55] M. Tanaka, M. Tutus, S. Kaufmann, F. F. Rossetti, E. Schneck, I. M. Weiss, *J. Struct. Biol.* **2009**, *168*, 137–142.
- [56] M. Tanaka, E. Sackmann, *Nature* **2005**, *437*, 656–663.
- [57] S. R. Tabaei, P. Jönsson, M. Brändén, F. Höök, *J. Struct. Biol.* **2009**, *168*, 200–206.
- [58] L. Desigaux, M. Sainlos, O. Lambert, R. Chevre, E. Letrou-Bonneval, J.-P. Vigneron, P. Lehn, J.-M. Lehn, B. Pitard, *Proc. Natl. Acad. Sci. U.S.A.* **2007**, *104*, 16534–16539.

OVERALL CONCLUSION

The literature research presented in chapter I drew up the need of multimodal nanoparticles for the labeling of DNA to follow its transfection. A therapeutic gene can be transfected complexed with transfection agents such as cationic lipids in the form of lipoplexes. In order to validate the efficiency of such transfection agents the DNA transfection has to be followed from the extracellular matrix to the nucleus. Several publications outlined the advantages of multimodal silica nanoparticles, in whose matrix different materials such as fluorescing dyes, metal, semiconductor or metal oxide nanoparticles can be enclosed, to be used as nanomarkers for bioimaging applications. The generation of quaternary ammonium groups, which strongly interact with DNA, on silica surfaces seemed to be a fruitful strategy to surface-functionalize multimodal silica nanoparticles for the labeling of DNA. Such nanoparticles allow the following of the transfection of DNA at different scales for the purpose of elucidating the mechanisms of gene transfection.

The work presented in chapter II dealt with the optimization of the chemical surface functionalization of silica nanoparticles with quaternary ammonium groups. Two synthesis strategies have been explored:

- a) A direct modification of silica with the quaternary ammonium group containing organosilane derivatives (TMAPS and TBAPS).
- b) A two step process of silica nanoparticles via a first modification with the primary and secondary amine groups containing organosilane derivative (EDPS) and a subsequent quaternization of the amine groups via an alkylation with iodomethane.

The first modification process led to the obtainment of silica nanoparticles bearing quaternary ammonium groups, which possess their isoelectric point at pH 8.5, due to the presence of silanolate groups remaining on the surface and influencing the overall surface potential. The amount of organo-silane, the catalyst, duration and temperature of the thermal treatment of the modification process were varied to optimize the density of the coated polysiloxane films. The understanding of the influence of the pH on the formation of silane layers on silica surfaces led to the choice of acetic acid as optimal catalyst. We demonstrated that this modification strategy is suitable to modify silica nanoparticles with quaternary ammonium groups, but we could not achieve a TMAPS- or TBAPS-coating sufficiently dense to obtain modified nanoparticles sufficiently charged to act as DNA labeling tool in a physiological environment. As a major problem we identified the tendency of quaternary ammonium groups to electrostatically interact with silanolate groups present on the surface of colloidal silica. The formation of ionic bonds between quaternary ammonium groups and residual silanolates before and after the completion of the implemented silanization process diminishes the success of the coating process.

Subsequently we carried out a two-step modification process using the silane coupling agent EDPS for silanization, which contains two amine groups. In contrast to ionic bonds forming between quaternary

ammonium and silanolate groups van der Waals bonds formed between primary amines and silanolate groups can be abrogated during thermal treatment under vacuum. This fact enables the surface modification of nanoparticles with aminosilanes to produce nanoparticles possessing their isoelectric point above pH 9. The following alkylation of amine groups with iodomethane permitted the implementation of quaternary ammonium groups on the aminated silica surfaces.

The setting up of the second surface modification process permitted to obtain quaternary ammonium group bearing nanoparticles possessing a relatively high graft density of the functionalizing silane. The determination of the optimal solvent and base used during the quaternizing Menshutkin reaction allowed to maintain colloidal stability of the nanoparticles during the modification process. A quaternization process transforming at least 60 % of the overall amine groups into quaternary ammonium groups was developed. This process led to the obtainment of silica nanoparticles bearing quaternary ammonium groups, which possess their isoelectric point at about pH 10.5. In contrast to nanoparticles quaternized by the first modification process their colloidal stability is guaranteed under physiological conditions. The second modification process is therefore suitable for the purposes of functionalizing multimodal silica nanoparticles with quaternary ammonium groups and of using them as DNA-labeling tools.

The optimization of the surface modification protocols in chapter II permitted the study of the interactions between quaternized nanoparticles and DNA in comparison to aminated silica nanoparticles and silica surfaces as shown in chapter III. Cosedimentation assays and QCM-D measurements showed that quaternized surfaces adsorb higher quantities of DNA than aminated silica surfaces at basic pHs. DNA adsorbed to quaternized surfaces at low salt concentrations has been shown to exist in a more rigid conformation than DNA adsorbed to aminated surfaces, indicating an improved condensation of DNA on quaternized surfaces. The results of the this last part demonstrated that the ability of modified nanoparticles to bind DNA depends not only on electrostatic interactions but also on the existence of hydrogen-bonding, van der Waals interactions or hydrophobic interactions. It may be enhanced by a further modulation of the hydrophilic-hydrophobic balance of quaternized surfaces. The alkylation reaction of amine groups on premodified silica may be implemented using reagents as iodobutane or iodophenyl to replace a part of quaternizing methyl groups by more hydrophobic groups. Furthermore it might be interesting to implement the generation of guanidinium groups on the premodified surfaces. They are known to possess a pKa of 12.5 and to be responsible of interactions between DNA and arginine-rich histone proteins. Therefore we assume that their presence might enhance the capacity of functionalized nanoparticles to label DNA. Nonetheless, the implementation of the modification process of the quaternization of EDPS-coated nanoparticles is significantly ameliorating the interaction of such nanoparticles with DNA compared to nanoparticles which are only aminated.

We demonstrated that the obtainment of lipoplexes including DNA-labeling quaternized nanoparticles in the presence of 150 mM salt is possible even at basic pH of 8.6, although this is not possible when using aminated silica nanoparticles. We showed that at the lower pH of 6.5 in the presence of salt the

formation of nanoparticle-labeled lipoplexes and also the formation of supported lipid bilayer on quaternized nanoparticle surface take place. We identified the formation of circular, lamellar lipoplexes which can be in contact with quaternized nanoparticles. By carrying out QCM-D measurements we could show the formation of supported lipid bilayers on condensed DNA cushions formed on quaternary ammonium modified silica surfaces, which is favored under conditions promoting the supramolecular self assembly of lipids and DNA via electrostatic interactions. This observation is in agreement with the display of planar, lamellar lipoplexe structures, which form at pH 6.5 in the absence of salt, by Cryo-TEM and TEM imaging. We showed that we are also able to form dually labeled lipoplexes by the simultaneous use of MUTAB-coated gold and quaternized silica nanoparticles.

Nanoparticles bearing quaternary ammonium groups are highly charged at pH 7.4 and keep more positive charges on their surface even in a salty environment such as the cytosol. The generation of quaternary ammonium groups on a multifunctional nanoparticle might therefore solve the problem that lipoplex transfected DNA labeled by aminated nanoparticles could not be followed until its internalization into the cell nucleus. This study allowed us to implement a process of surface modification on silica nanoparticles in order to enclose them in lipoplexe structures by complexation with DNA. Due to the versatility of the silanization this surface modification process can be applied on more sophisticated silica nanoparticles, such as multimodal silica nanoparticles containing fluorescent dyes, magnetic or plasmonic nanoparticles, and also on other metal oxide surfaces. In the near future such bioimaging tools, which could allow displaying the DNA transfection from tissular to subcellular scales, will be used to validate the efficiency of transfection agents in *in vitro* and *in vivo* situations.

ANNEX

Annex 1: Characterization protocols

Determination of Si Concentration by Inductively Coupled Plasma (ICP)

To determine the concentration of silica present in a sol, four portions of 500 μL of the sol were dried in a weighted aluminum cup. The weight of the dried extract was used to determine an approximate concentration of silica in the sol in g/L. Then the sol was diluted to a silicium concentration of 3 g/L, and 100 μL were taken and dissolved by the addition of 400 μL of hydrofluoric acid (40% w/v). The homogeneous silicium-containing solution was neutralized by adding 9.5 mL of NH_4OH (1M). The silicium concentration of a prepared sample was dosed by inductively coupled plasma (ICP) and converted to the concentration of silica of our sol. The preparation of the samples for ICP was undergone in plastic Eppendorf tubes to avoid the falsification of the silica content by the dissolution of glass recipients.

Dynamic light scattering (DLS)

To 1 mL of a chosen solvent 20 μL of a sol ($3.5 \cdot 10^{17}$ NPs/L) was added. 800 μL of the dilute particle sol was introduced to the VASCO particle size analyzer from Cordouan Technologies. The laser intensity of the 658 nm laser diode was adjusted and the sample was cooled to a temperature of 20 °C. The refractive index and viscosity of the solvent as well as the refractive index of the particles in the solvent concerned were entered into the software NanoQ, which pilots the further measurements. A real time signal was measured; acquisitions were implemented every 30 seconds if the noise of the signal did not exceed 1.06 %. 80 measurements were accomplished to determine size distribution and the polydispersity index of the nanoparticles by the cumulants method.

Transmission electron microscopy TEM

On a carbon-film covered copper grid 5 μL of a diluted particle solution (dilution factor 100 to 1000) was deposited. Particles were allowed to adsorb to the grid for two minutes, after which the remaining solution was collected by the aid of fine coarse filter paper. A series of TEM micrographs was recorded with the Philips CM120 microscope at 120 kV, with the Ultra scan USC1000 2Kx2K camera. Particle sizes were analyzed with the help of the ImageJ program, which permits the processing (functions used: median filter, enhanced contrast), transformation of the recorded micrographs to binary pictures of separated particles (functions used: make binary, threshold, watershed) and the analysis of the particles (function used: analyze particles) to determine their Feret diameter.

Diffuse reflectance infrared fourier transform spectroscopy (DRIFT)

2 mL of a nanoparticle sol was dried at 80 °C under vacuum. 9 mg of the dried sample was added to 281 mg of equally dried KBr (spectroscopy grade). The mixture was pestled in an agate mortar and the powder was deposited on the sample holder. The sample was then introduced to the Bruker IFS

Equinox 55 spectrometer and measured in a Selector Graseby Specac reflection cell. Thirty minutes after the installation of the sample in the cell an infrared spectrum was recorded by the acquisition of 128 measurements.

Nuclear magnetic resonance spectroscopy (NMR)

1.5 mL of aqueous nanoparticle sols was centrifuged for 10 min. at 13000 ppm in 2 mL Eppendorf cups. The supernatant was removed and the particles were dried by the deposition of open Eppendorf cups upside down on a filter paper for thirty seconds. The particles were then redispersed in 500 μ L D_2O . The sample should be concentrated and show about 7000 m^2 of surface area per liter to permit the recording of a 1H NMR spectrum. All spectra were recorded in a Bruker NMR spectroscope at 400 MHz by the acquisition of 128 measurements.

Conductometry

Conductivity measurements were carried out using the Bioblock Scientific conductivity meter 93008. A titration solution of $AgNO_3$ (0.1 M) was prepared and stored protected from light. Immediately after quaternization 2 mL of a sol containing nanoparticles dispersed in water after the accomplishment of two washing steps in ultrapure water is prelevated. The conductivity of the sol is measured while $10 \pm 0.1 \mu$ L of the prepared $AgNO_3$ solution is gradually added with an Eppendorf micropipette. When all halide ions in the solution have been consumed and precipitated with the added Ag^+ ions as $AgHal$, additional Ag^+ ions contribute to the conductivity of the solution leading to an increase in the gradient of the measured conductivity profile. The change of the gradient marks the titration end point, permitting us to calculate the halide concentration of the sol.

Thermogravimetric analysis (TGA) and coupled mass spectrometry (MS)

25 mg of nanoparticles previously dried at 80 °C under vacuum was placed in a platine crucible, which was positioned on a MTB18 SETARAM thermobalance. TGA measurements were effected under an oxygen flux with a temperature increase from 25 °C to 650 °C by increasing heat of 2 °C/min. TGA measurements could be coupled to a Pfeiffer Balzer mass spectrometer. The quadrupolar spectrometer detects mass fragments of 0 to 300 m/z , which were released during the heating process.

Zetametric measurements

50 mL of a dilute aqueous solution of a nanoparticle sol at a concentration of about $3.4 \cdot 10^{16}$ NPs/L was prepared. The pH of the solution was adjusted by the addition of HCl (0.01M) or NaOH (0.01M). At the desired pH 5 mL of the sample was collected. After pH equilibration of for 12 hours the zeta potential of the nanoparticles in the prepared samples was measured using the Malvern Zetasizer 3000HS. The pHs of the samples were verified after the measurement of the zeta potential.

Cleaning of QCM-D crystals

Silica coated QCM-D crystals can be cleaned after surface modification by immersion in 10 mL of a mixture of $H_2O:H_2O_2:NH_3$ (5:1:1) heated at 70 °C for 5 minutes. The cleaning protocol has the

advantage to be rapid and efficient, but the inconvenient to decrease the thickness of the silica coating of the quartz crystal. The so cleaned quartz crystals were therefore of a limited life time and could be used for about 5 modification/cleaning cycles. A second cleaning method is the cleaning of the modified crystals by 45 min of UV-ozone treatment. The method takes much more time than the first one, but has the advantage to be much gentler and allows the use of SiO₂ coated QCM-D crystals for about 10 modification/cleaning cycles. All SiO₂ coated quartz crystals suffer from the dissolution of silica in salt containing media and their exposition to capillary flows peeling SiO₂ entities of the surfaces.

Spectrophotometric dosage of phosphate molecules

Concentrations of prepared liposome dispersions containing phospholipids were determined by a colorimetric dosage of molybdate complexes of phosphate. 200 µL of phospholipid containing solutions (0.5 mg/mL) were prepared and twice 100 µL of the sample were injected into two borosilicate tubes. The samples were dried in a destruction block at 180 °C. Then 300 µL of perchloric acid (70 % w/v) were added, the tubes were sealed with glass pearls and placed in the destruction block at 180 °C for thirty minutes. If the solutions remained colored after this treatment they were placed in the destruction block for further 15 minutes heating at 180 °C. Subsequent 1.4 mL of ultrapure water (18.2 MΩ) was added to each tube and the mixture is vortexed. In the following 200 µL of a solution of ammonium molybdate (2.5 % w/v) and 200 µL freshly prepared ascorbic acid (10 % w/v) were added under vortexing. The samples were placed in a water bath preheated at 100 °C during 5 minutes, then immediately cooled in an ice bath. The absorbance of the samples was measured at 797 nm using an UV-VIS spectrometer to determine the concentration of the samples.

Simultaneously the dosage was implemented for eight borosilicate tubes containing 0, 5, 10, 20, 40, 60, 80 or 100 nanomoles of NaH₂PO₄ to obtain a calibration diagram permitting the determination of the phosphate concentration of the sample.

Spectrophotometric determination of the thiol concentration with Ellman's reagent

50 µl of NaBH₄ (2 M) was added to a 50 µl of a sol containing MUTAB-modified gold nanoparticles at a concentration of $1.72 \cdot 10^{17}$ nanoparticles per liter. After incubation for 30 minutes the sample was centrifuged at 8000 g for 10 minutes. 90 µl of the supernatant were taken, paying attention not to withdraw the pellet. 90 µl of HCl (1 M) were added and the sample was incubated for 30 minutes. Subsequently the sample was degazed via the application of a vacuum during sonication for 30 minutes. 1.77 ml of degazed borate buffer (pH 8.0, 0.2 M) was added to the sample. Then 50 µL of Ellman's reagent (5,5'-dithiobis-(2-nitrobenzoic acid), 10 mM) was added. Thiols react with DNTB, cleaving its disulfide bond to give 2-nitro-5-thiobenzoate (NTB). The presence of one mole of thiol leads to the release one mole of NTB (extinction coefficient of $13.800 \text{ M}^{-1} \cdot \text{cm}^{-1}$) which is quantified using a spectrophotometer. After 15 minutes incubation the absorption was measured at 412 nm and the concentration of NTB was calculated via the Lambert-Beer equation. At the same time two control samples were prepared one containing Ellman's reagent and ultrapure water and the second

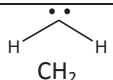
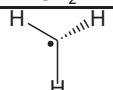
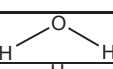
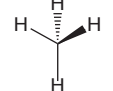
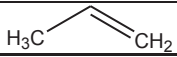
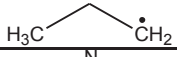
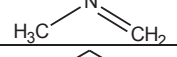
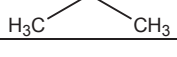
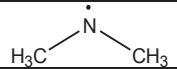
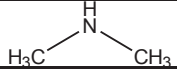
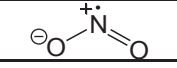
containing Ellmann's reagent, NaBH₄ and HCl and equally dosed by measuring the absorption of the control samples at 412 nm.

Annex 2: Tables

TABLE 0-1 Scheduling presentation of the observed vibration bands on colloidal silica and TMAPS, EDPS and EDPS-Me modified nanoparticles. ν – stretching vibrations, δ – bending vibrations, ρ – rocking vibrations.

Vibration band (cm ⁻¹)	Colloidal silica	TMAPS modified NPs	EDPS modified NPs	EDPS-Me modified NPs
3400 - 3700	$\nu(\text{OH})$ strong, broad	✓	✓	✓
2989	$\nu_{\text{asym}}(\text{CH}_x)$ medium	✓	✓	✓
2950	$\nu(\text{NCH}_x)$ medium		✓	✓
2903	$\nu_{\text{sym}}(\text{CH}_x)$ medium	✓	✓	✓
1984	Shoulder, typical silica overtone	✓	✓	✓
1872	Typical silica overtone	✓	✓	✓
1688	$\delta(\text{H}_2\text{O})$ shoulder	✓	✓	✓
1631	$\delta(\text{H}_2\text{O})$ weak, enclosed water	✓	✓	✓
1477 - 1479	$\delta(\text{N}^+\text{CH})$ weak, sharp		✓	✓
1452	$\delta(\text{NCH})$ weak, sharp		✓	
1418	$\delta(\text{CN}^+)$ weak, sharp		✓	✓
1395	$\delta(\text{CN})$ weak, sharp		✓	
1190	$\nu_{\text{asym}}(\text{SiOSi})$ shoulder	✓	✓	✓
1108	$\nu_{\text{asym}}(\text{SiOSi})$ strong, sharp	✓	✓	✓
938	$\nu_{\text{sym}}(\text{SiOSi})$ strong	✓	✓	✓
803	$\delta(\text{SiOSi})$ strong	✓	✓	✓
561	cyclic(SiOSi) medium	✓	✓	✓
468	$\rho(\text{SiOSi})$ strong, sharp	✓	✓	✓

TABLE 0-2 Scheduling presentation of the detected mass fragments^[41] of differently modified silica nanoparticles.

Fragment	m/z	z=2	z=3	TMAPS M _{graft} 101 g/mol	TBAPS M _{graft} 101 g/mol	EDPS M _{graft} 101 g/mol	EDPS-Me EtOH/H ₂ O M _{graft} 101 g/mol	EDPS-Me EtOH/H ₂ O/NaCl M _{graft} 101 g/mol
C	12	6	4	✓	✓		✓	✓
CH	13	6.5	4.3	✓				✓
	14	7	4.7	✓				
	15	7.5	5	✓			✓	✓
OH	17	11.9	5.7	✓	✓	✓	✓	✓
	18	9	6	✓	✓	✓	✓	✓
	18	9	6	✓	✓	✓	✓	✓
HC≡CH	26	13	8.7	✓	✓	✓	✓	✓
H ₂ C=CH [•]	27	13.5	9	✓	✓	✓	✓	✓
N ₂	28	14	9.3	✓	✓	✓		✓
CO	28	14	9.3	✓	✓	✓		✓
H ₂ C=CH ₂	28	14	9.3	✓	✓	✓		✓
H ₃ C—CH ₂ [•]	29	14.5	9.7	✓	✓	✓	✓	✓
H ₃ C—CH ₃	30	15	10	✓	✓	✓		
NO	30	15	10	✓	✓	✓		
O ₂	32	16	10.7	✓				
³⁵ Cl	35	17.5	11.7	✓				✓
HCl	36	18	12	✓				
³⁷ Cl	37	111.9	12.3	✓				✓
H ₂ C=C=NH	41	20.5	13.7	✓			✓	
	42	21	14				✓	✓
	43	21.5	14	✓	✓		✓	✓
	43	21.5	14	✓	✓		✓	✓
	44	22	14.67	✓	✓	✓	✓	✓
O=C=O	44	22	14.67	✓	✓	✓	✓	✓
	44	22	14.67	✓	✓	✓	✓	✓
	45	22.5	15	✓	✓	✓	✓	✓
	46	23	15.3	✓				
	47	23.5	15.7					✓

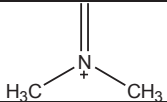
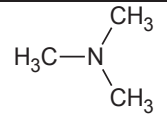
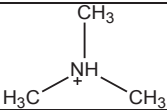
$\text{CH}_3\text{-Cl} (^{35}\text{Cl})$	50	25	16.7	✓	✓		✓	
$\text{CH}_3\text{-Cl} (^{37}\text{Cl})$	52	26	17.3	✓	✓		✓	
	58	29	19.3				✓	
	59	29.5	19.7					✓
	60	30	20					✓
I	127	63.5	42.3				✓	
CH_3I	142	71	47.3				✓	

TABLE 0-3 Summary of the different surface modifications of silica nanoparticles with TMAPS implemented under variety of nTMAPS, catalyst, pH, temperature T and duration t of the thermal treatment.

Condition	nTMAPS ($\mu\text{mol}/\text{m}^2$)	Catalyst	pH	$T_{(\text{thermal treatment})}$ ($^{\circ}\text{C}$)	$t_{(\text{thermal treatment})}$ (hours)
001	2.5	Acetic acid	4.5	100	2
002	5	Acetic acid	4.5	100	2
003	15	Acetic acid	4.5	100	2
004	30	Acetic acid	4.5	100	2
005	60	Acetic acid	4.5	100	2
006	100	Acetic acid	4.5	100	2
007	120	Acetic acid	4.5	100	2
008	150	Acetic acid	4.5	100	2
009	100	NH_4OH	11.9	100	2
010	100	H_3PO_4	2	100	2
011	100	HCl	1	100	2
012	100	HNO_3	1	100	2
013	100^{Δ}	Acetic acid	4.5	100	2
014	100	1) H_3PO_4 * 2) NH_4OH **	2 11.9	100	2
015	100	1) Acetic acid * 2) NH_4OH **	4.5 11.9	100	2
016	100	1) NH_4OH * 2) Acetic acid ***	11.9 4.5	100	2
017	100	Acetic acid	4.5	130	2
018	100	Acetic acid	4.5	150	2
019	100	HNO_3	1	130	2
020	100	HNO_3	1	150	2

021	100	NH ₄ OH	11.9	130	2
022	100	NH ₄ OH	11.9	150	2
024	100	H ₃ PO ₄	2	130	2
025	100	H ₃ PO ₄	2	150	2
026	100	Acetic acid	4.5	50	2
027	100	Acetic acid	4.5	50	12
028	100	Acetic acid	4.5	100	12
029	100	NH ₄ OH	11.9	100	12

* during hydrolysis/condensation of TMAPS and the adsorption of polysiloxane oligomers to silica overnight

**transfer to an alkaline reaction medium just before the thermal treatment in glycerol

*** transfer to an acidic reaction medium just before the thermal treatment in glycerol

^Δ added drop wise during five hours

TABLE 0-4 Summary of the different surface modifications of silica nanoparticles with TBAPS.

Condition	nTBAPS ($\mu\text{mol}/\text{m}^2$)	Catalyst	pH	T _(thermal treatment) (°C)	t _(thermal treatment) (hours)
030	100	NH ₄ OH	11.9	100	2
031	100	Acetic acid	4.5	100	2
032	100	H ₃ PO ₄	2	100	2
033	100	HNO ₃	1	100	2
034	100	Acetic acid	4.5	130	2
035	100	Acetic acid	4.5	150	2

TABLE 0-5 Conditions tested to implement the quaternization of EDPS-modified silica nanoparticles.

Condition	Solvent	Base	t _{RT} (hours)	t _{70°C} (hours)
036	Acetonitrile	K ₂ CO ₃	12	1
037	Acetonitrile	NEt ₃	12	1
038	EtOH/Acetonitrile (1:3)	K ₂ CO ₃	12	1
039	EtOH/Acetonitrile (1:3)	NEt ₃	12	1
040	EtOH	K ₂ CO ₃	12	1
041	EtOH	NEt ₃	12	1

Annex 3: Calculations

The calculation of the grafting density of the sample using 60 μmol TMAPS to modify 50 nm sized silica colloids (cond. 005, see TGA in CHAPTER 2, FIGURE 2.3-1) provides an example for the calculations implemented to calculate the surface densities of TMAPS-coated nanoparticles.

For the sample examined by TGA we determine:

$$m_i = 24.57 \text{ mg} \quad \Delta m_{25-160^\circ\text{C}} = -2.05 \% \rightarrow m_{160^\circ\text{C}} = 24.0653 \text{ mg}$$

$$\Delta m_{160-650^\circ\text{C}} = 11.84 \% \rightarrow \Delta m_{160-650^\circ\text{C}} = 2.909 \text{ mg}$$

The calculated mass loss includes the loss of water and ethoxy residues enclosed into the matrix of the amorphous silica nanoparticles. For this purpose a TGA of the used silica colloids was implemented to determine the quantity of mass loss due to water and ethoxy residues. For the sample of colloidal silica we determined:

$$m_i = 25.03 \text{ mg} \quad \Delta m_{160-650^\circ\text{C}} = 5,5 \% \rightarrow \Delta m_{160-650^\circ\text{C}} = 1.377 \text{ mg}$$

The mass loss per mg of silica is of:

$$0.056 \text{ mg}_{\Delta m_{160-650^\circ\text{C}}} \text{ per mg}_{m_{160^\circ\text{C}}}$$

For the sample of TMAPS-modified silica the mass loss due to the loss of water and ethoxy residues $\Delta m_{160-650^\circ\text{C}(H_2O)}$ corresponds approximately to 1.354 mg. To calculate the surface density of the organic graft on the modified nanoparticles this loss is subtracted from the total mass loss:

$$\begin{aligned} \Delta m_{160-650^\circ\text{C}(graft)} &= \Delta m_{160-650^\circ\text{C}(total)} - \Delta m_{160-650^\circ\text{C}(H_2O)} \\ &= 2.909 \text{ mg} - 1.354 \text{ mg} = 1.555 \text{ mg} \end{aligned}$$

In the following the surface density of TMAPS on the modified nanoparticles is calculated via EQUATION 2.3-1, CHAPTER 2:

$$\begin{aligned} d_{graft} &= \frac{\Delta m_{160-650^\circ\text{C}(graft)}}{S_S \times m_{160^\circ\text{C}} \times M_{TMAP+Cl}} = \frac{1.555 \text{ mg}}{60 \frac{\text{m}^2}{\text{g}} \times 24.0653 \text{ mg} \times 136.45 \frac{\text{g}}{\text{mol}}} \\ &= 7.90 * 10^{-6} \text{ mol/m}^2 \end{aligned}$$

EQUATION 0-1 Sample calculation of the surface density of TMAPS grafted silica.

To calculate the amount of quaternary ammonium groups, which may be formed by the quaternization of the primary or the secondary amine of an EDPS graft, we executed a TGA analysis of quaternized nanoparticles (cond. 041, see TGA in CHAPTER 2, FIGURE 3.2-4).

For the sample examined by TGA we determined:

$$m_i = 49.2 \text{ mg} \quad \Delta m_{25-160^\circ\text{C}} = -1.26 \% \rightarrow m_{160^\circ\text{C}} = 411.982 \text{ mg}$$

$$\Delta m_{160-650^\circ\text{C}} = 11.056 \% \rightarrow \Delta m_{160-650^\circ\text{C}} = 5.4396 \text{ mg}$$

The calculated mass loss includes the loss of water and ethoxy residues and EDPS

grafts of the previously modified silica nanoparticles. For this purpose a TGA of the used silica colloids was carried out to determine the quantity of mass loss due to water, ethoxy residues and grafted EDPS. For the sample of EDPS coated colloidal silica we determined:

$$m_f = 50.63 \text{ mg} \quad \Delta m_{160-650^\circ\text{C}} = 9.783 \% \rightarrow \Delta m_{160-650^\circ\text{C}} = 4.953 \text{ mg}$$

The mass loss per mg of silica is subsequently of:

$$0.099 \text{ mg}_{\Delta m_{160-650^\circ\text{C}}} \text{ per mg}_{m_{160^\circ\text{C}}}$$

For the sample of quaternized silica the mass loss due to the loss of water and ethoxy residues $\Delta m_{160-650^\circ\text{C}(H_2O)}$ corresponds approximately to 4.8096 mg. To calculate the surface density of the organic graft on the modified nanoparticles this loss is subtracted from the total mass loss:

$$\begin{aligned} \Delta m_{160-650^\circ\text{C}(graft)} &= \Delta m_{160-650^\circ\text{C}(total)} - \Delta m_{160-650^\circ\text{C}(H_2O)} \\ &= 5.4396 \text{ mg} - 4.8096 \text{ mg} = 0.63 \text{ mg} \end{aligned}$$

We estimate that averaged 2.5 methyl groups are necessary to implement one quaternary ammonium group on an EDPS graft (either two methyl groups to quaternize a secondary or three methyl groups to quaternize a primary amine), which will be accompanied by one iodide counterion. In what follows the surface density of quaternary ammonium groups on the modified nanoparticles is calculated via EQUATION 2.3-1, CHAPTER 2:

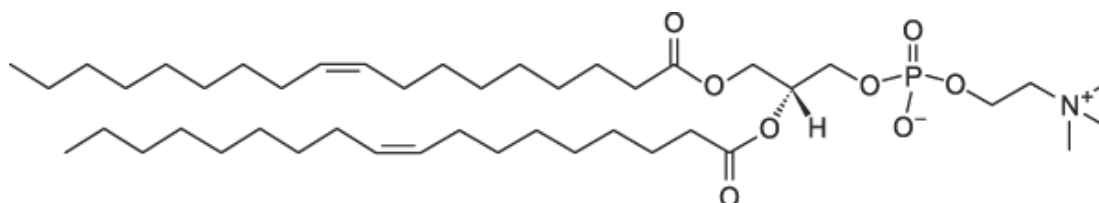
$$\begin{aligned} d_{graft} &= \frac{\Delta m_{160-650^\circ\text{C}(graft)}}{S_s \times m_{160^\circ\text{C}} \times M_{2.5 Me + I - 1.5 H}} = \frac{0.63 \text{ mg}}{60 \frac{\text{m}^2}{\text{g}} \times 24.0653 \text{ mg} \times 162.9 \frac{\text{g}}{\text{mol}}} \\ &= 2.6 \times 10^{-6} \text{ mol/m}^2 \end{aligned}$$

EQUATION 0-2 Calculation of the amount of quaternary ammonium groups present on modified silica nanoparticles after the quaternization of EDPS with iodomethane.

Annex 4: IUPAC names and structures of lipids and cationic transfection agents

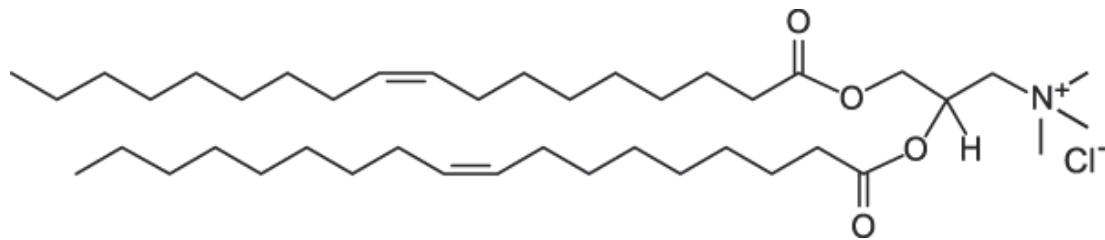
DOPC 1,2-dioleoyl-*sn*-glycero-3-phosphocholine

$C_{44}H_{84}NO_8P$, exact mass 785.593



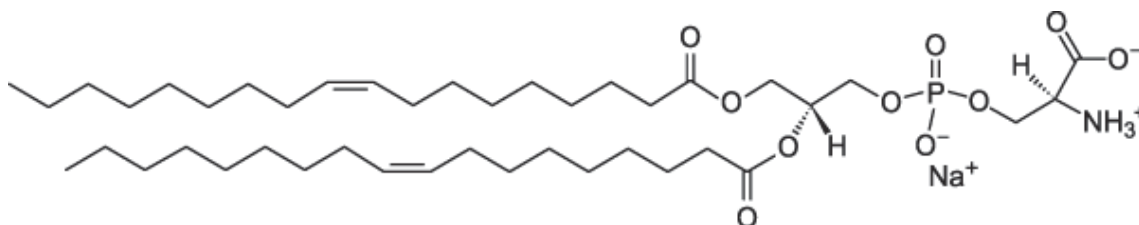
DOTAP 1,2-dioleoyl-3-trimethylammonium-propane

$C_{42}H_{80}NO_4Cl$ chloride salt, exact mass 697.578



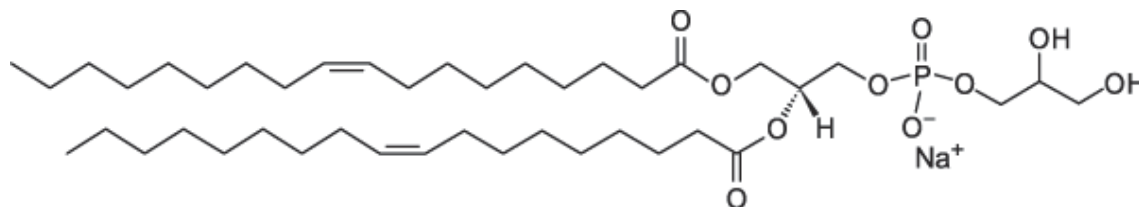
DOPS 1,2-dioleoyl-*sn*-glycero-3-phospho-L-serine

$C_{42}H_{77}NO_{10}PNa$ sodium salt, exact mass 809.518



DOPG 1,2-dioleoyl-*sn*-glycero-3-phospho-(1'-*rac*-glycerol)

$C_{42}H_{78}O_{10}PNa$ sodium salt, exact mass 796.523



DOPE 1,2-dioleoyl-*sn*-glycero-3-phosphoethanolamine

$C_{41}H_{78}NO_8P$, exact mass 743.547

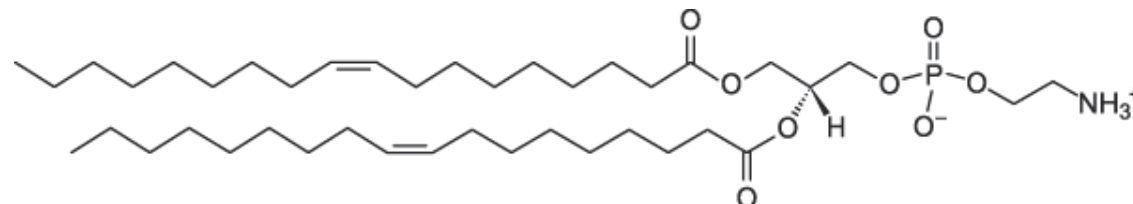


FIGURE 0-1 Molecular formular, structure and molar weight of lipids used in these chapter.

BGTC bis(guanidinium)-tris(2-aminoethyl)amine cholesterol

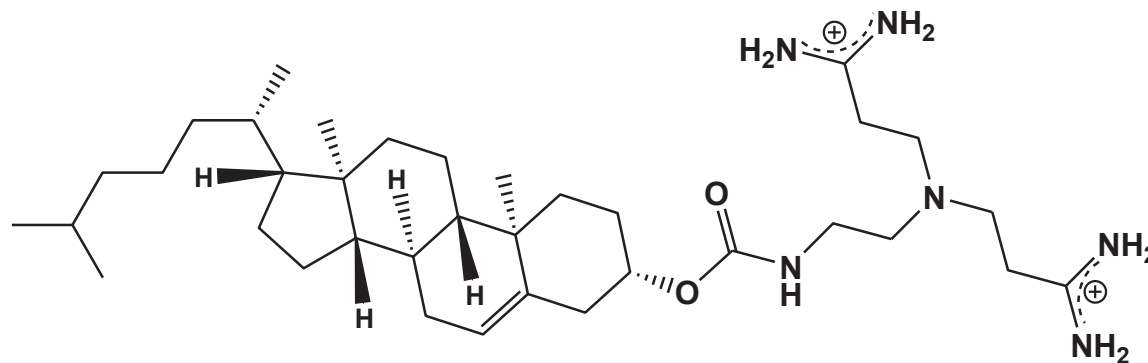


FIGURE 0-2 Cationic transfection agent used for the formation of lipoplexes

Annex 5: Supplementary Cryo-TEM and TEM pictures

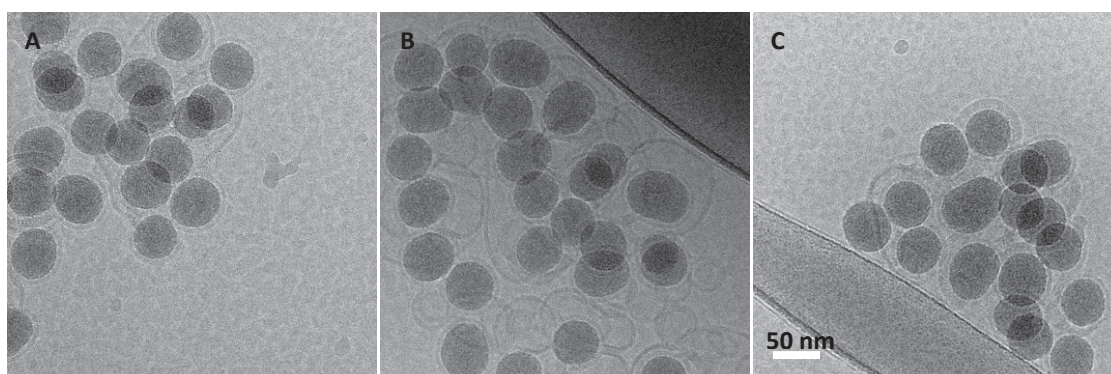


FIGURE 0-1 Cryo-TEM pictures of nanoparticle/DNA/lipid agglomerates formed at pH 6.5 in the presence of 150 mM NaCl (sample C3, see chapter 3, **FIGURE 3.2-3**). We observe the formation of SLBs and concentric, lamellar lipoplex structures on quaternized silica NPs. All Cryo-TEM pictures are at the same scale.

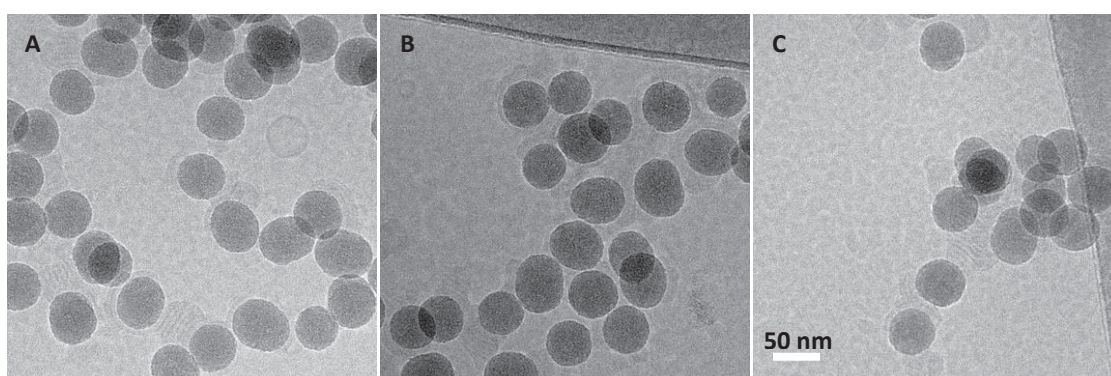


FIGURE 0-2 Cryo-TEM pictures of nanoparticle/DNA/lipid agglomerates formed at pH 6.5 in the presence of 0 mM NaCl (sample F3, see **CHAPTER 3, FIGURE 3.2-3**). We observe the formation of planar, lamellar lipoplex structures on quaternized silica NPs. All Cryo-TEM pictures are at the same scale.

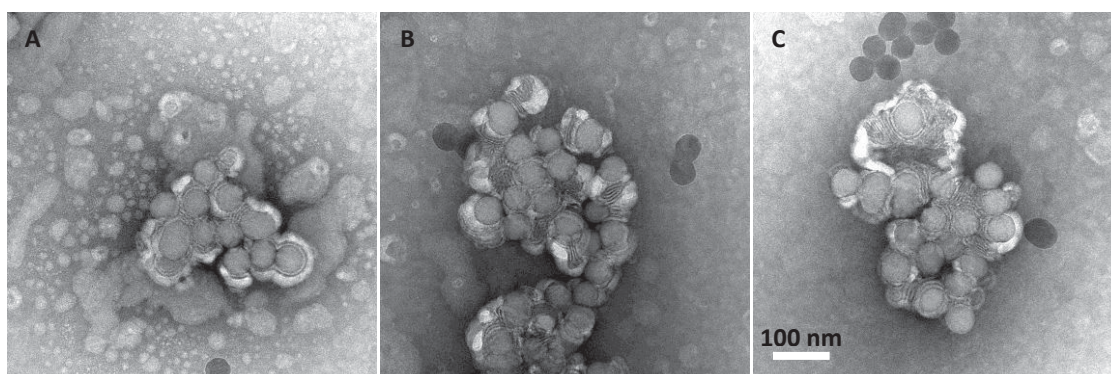


FIGURE 0-3 TEM pictures of nanoparticle/DNA/lipid agglomerates formed at pH 6.5 in the presence of 0 mM NaCl (sample F3, see **CHAPTER 3, FIGURE 3.2-3**). The specimen was stained with uranyl acetate. We observe the formation of planar, lamellar lipoplex structures on quaternized silica NPs as equally observed by Cryo-TEM. All TEM pictures have the same scale.

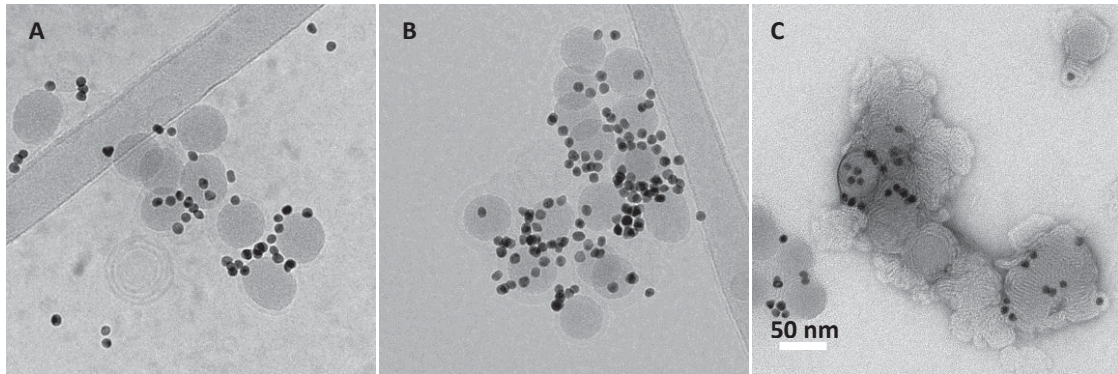


FIGURE 0-4 Cryo-TEM (A, B) and TEM (C) pictures of nanoparticle/DNA/lipid agglomerates formed at pH 6.5 in the presence of 0 mM NaCl (sample F8, see CHAPTER 3, FIGURE 3.2-3).

We observe the formation of lipoplex structures including quaternized silica NPs and MUTAB-coated gold nanoparticles. Both Cryo-TEM pictures have the same scale. The specimen observed

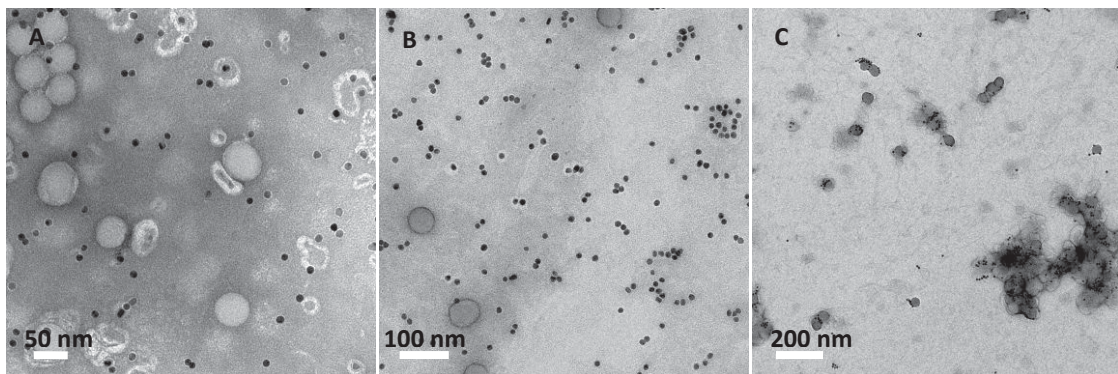


FIGURE 0-5 Silica and gold nanoparticles bearing quaternary ammonium groups incubated with DOTAP vesicles in the absence of salt (A) and at 150 mM NaCl (B). The nanoparticles are evenly distributed. C: TEM picture of nanoparticle/DNA/lipid agglomerates formed at pH 6.5 in the presence of 0 mM NaCl (sample F8, see CHAPTER 3, FIGURE 3.2-3). The silica and gold nanoparticles are located at the same place indicating that they interact with DNA and are located in lipoplexes. All specimens were stained with uranyl acetate.

CHEMICAL SURFACE MODIFICATION OF SILICA NANOPARTICLES FOR THE LABELING OF DNA IN LIPOPLEXES.

ABSTRACT

Silica nanoparticles are ideal platforms for the conception of bioimaging tools serving for the elucidation of the mechanisms of gene transfection via lipoplex structures. The purpose of the present study is the development of a chemical surface modification for the generation of quaternary ammonium groups on silica nanoparticles permitting the obtainment of highly positively charged silica colloids which strongly attract DNA by electrostatic interactions. Two modification strategies to generate quaternary ammonium groups on silica are presented a) a direct silanization using quaternary ammonium groups containing silane derivatives and b) a modification of silica nanoparticles via a first modification with an amine group containing silane derivative and a subsequent quaternization of the amine groups via an alkylation with iodomethane. Different physicochemical methods were employed (cosedimentation assays, quartz crystal microbalance with dissipation monitoring measurements, TEM and Cryo-TEM imaging) to analyze interactions between quaternized surfaces, DNA and lipids. A preliminary study was carried out which shows the capacity of the synthesized nanoparticles to label DNA in lipoplexes.

Key words: silica, nanoparticle, quaternary ammonium group, surface functionalization, silanization, DNA-labeling, gene transfer, lipoplex, quartz crystal microbalance with dissipation monitoring

RÉSUMÉ

Les nanoparticules de silice sont des plateformes idéales pour la conception d'outils de bioimagerie afin d'étudier les mécanismes de transfert de gènes par des lipoplexes. L'objectif de notre étude est le développement d'une modification chimique de surface permettant d'obtenir des colloïdes de silice chargés positivement susceptible de lier de l'ADN par des interactions électrostatiques. Deux stratégies pour la génération de groupements ammonium quaternaires sur des nanoparticules de silice sont présentées a) une silanisation directe par l'utilisation d'un agent de couplage silanique contenant un groupement ammonium quaternaire et b) un procédé en deux étapes mettant en jeu une modification de surface chimique par des aminosilanes primaires et secondaires suivie d'une alkylation des amines par l'iodométhane. Différentes méthodes physico-chimiques (essais de cosédimentation, des expériences de microbalance à cristal de quartz avec mesure de dissipation et d'imagerie MET et Cryo-MET) ont été utilisées pour mettre en évidence et caractériser les interactions entre les biomolécules et les surfaces quaternisées. Des études préliminaires ont montrées les capacités de marquage de lipoplexes par de telles nanoparticules.

Mots clés: silice, nanoparticule, ammonium quaternaire, fonctionnalisation de surface, silanisation, marquage d'ADN, transfert de gènes, lipoplexe, microbalance à cristal de quartz avec mesure de dissipation